CetZ1 in Cell Shape control of Haloarchaea:

Understanding the Functional Divergence of Tubulin Superfamily Proteins

Kariyawasam W. T. Roshali Thavindra de Silva

A thesis submitted in fulfilment of the requirements for the degree of Doctor of Philosophy

The ithree Institute and School of Life Sciences, University of Technology Sydney

November 2019

CERTIFICATE OF ORIGINAL AUTHORSHIP

I, Kariyawasam W. T. Roshali Thavindra de Silva declare that this thesis, is submitted in fulfilment of the requirements for the award of PhD, in the School of Life Sciences/ Faculty of Science at the University of Technology Sydney.

This thesis is wholly my own work unless otherwise reference or acknowledged. In addition, I certify that all information sources and literature used are indicated in the thesis.

This document has not been submitted for qualifications at any other academic institution.

This research is supported by the Australian Government Research Training Program.

Production Note:
Signature removed prior to publication.

Signature

Date: 02/09/2019

TABLE OF CONTENT

Certificate of Original Authorship iii
List of Figures viii
List of Tables xi
Abbreviations xii
Publications and Conference Proceedings xiv
Acknowledgement xv
Abstract xvi

1 Introduction....18
1.1 Overview of the research problem....19
1.2 Cytoskeleton....20
1.3 Tubulin superfamily proteins....22
1.4 Microtubules....23
1.4.1 Relationship of tubulin structure and conformation with the function....24
1.4.2 Microtubule dynamics and regulation....28
1.4.3 Microtubule isoforms and post-translational modifications....33
1.5 Cell division in bacteria by FtsZ....34
1.5.1 FtsZ Polymerisation and structure....34
1.5.2 FtsZ controls prokaryotic cell division....35
1.6 Tubulins in archaea....39
1.6.1 Archaea....39
1.6.2 FtsZ and divergent tubulin superfamily members in archaea....41
1.6.3 Cell-structure-related euryarchaeota tubulin/FtsZ proteins (CetZ) in *Haloferax volcanii*....42
1.7 Aims of the present study....48
2 General Materials and Methods....49
2.1 Bacterial strains and plasmids....50
2.2 Growth media....51
2.3 Chemicals, reagents and solutions....53
2.4 Growth conditions and preparation of *E. coli* cells....55
2.4.1 Normal growth conditions for *E. coli*....55
2.4.2 Preparing chemically competent cells of *E. coli*....55
2.4.3 Preparing electrocompetent cells of *E. coli*....55
2.5 Transformation of *E. coli*....56

2.5.1 *E. coli* transformation by heat shock....56
2.5.2 *E. coli* transformation by electroporation....56
2.6 General growth conditions for *Haloferax volcanii*....57
2.7 *Haloferax volcanii* transformation....57
2.8 Common genetic techniques....58
2.8.1 Measuring DNA concentration and storage....58
2.8.2 Extraction of gDNA and plasmid DNA....58
2.8.3 Demethylation of plasmid DNA....58
2.8.4 Agarose gel electrophoresis....59
2.8.5 Polymerase chain reaction (PCR)....59
2.8.6 General cloning protocol....60
2.8.7 Sanger sequencing....61
2.9 General protein analysis techniques....61
2.9.1 Sodium dodecyl sulfate polyacrylamide gel electrophoresis (SDS-PAGE)....61
2.9.2 Western Blot....62
2.10 Common techniques used to analyse different cellular parameters....63
2.10.1 Imaging cell shapes using microscopy....63
2.10.2 Cell circularity analysis....64
2.10.3 Cell volume and cell count analysis by Coulter counter....64
3 Conditional Pleomorphology and Differentiation in the Model Archaeon *Haloferax volcanii*....65
3.1 Abstract....67
3.2 Introduction....67
3.3 Results....69
3.3.1 *H. volcanii* growth and pleomorphology in nutrient-limited batch culture....69
3.3.2 Improved growth of *H. volcanii* in TE-supplemented media....71
3.3.3 *H. volcanii* forms rods during the onset of growth in culture....73
3.3.4 The interplay between conditions controlling *H. volcanii* morphological development....75
3.3.5 Microfluidic flow chamber visualization of *H. volcanii* cellular development....76
3.3.6 Potential role of secreted signals in cell elongation during early growth....78
3.3.7 Reversibility and specificity of the TE-starvation cell elongation response....78

3.3.8 The requirement of tubulin-like protein CetZ1 for rod cell formation in batch culture 79
3.4 Discussion 82
3.5 Materials and Methods 85
3.5.1 Archaeal strains 85
3.5.2 Culture media and general growth conditions 85
3.5.3 Nutrient depletion in liquid cultures 86
3.5.4 Time-course studies of rod development 86
3.5.5 Microscopy 87
3.5.6 Coulter cytometry 88
3.5.7 Western blotting 88
4 Characterisation of CetZ1 localisation in *Haloferax volcanii* morphogenesis using a new knockout strain and fluorescent protein fusion 89
4.1 Introduction 91
4.1.1 *Haloferax volcanii* gene knockout system 91
4.1.2 The discovery of CetZ1 function in cell shape control 92
4.1.3 Previous studies of CetZ1 localisation in *Haloferax volcanii* 94
4.1.4 Designing functional fusion proteins in biology 95
4.1.5 Aims and the content of the results chapter 99
4.2 Results 100
4.2.1 Design, construction and complementation of CetZ1 knockout strains . 100
4.2.2 Design, construction and complementation of CetZ1 fluorecent protein fusions 109
4.2.3 The localisation of CetZ1 in *Haloferax volcanii* during morphogenesis 118
4.3 Discussion 125
4.4 Methods 128
4.4.1 Construction of plasmids containing the knock-out regions 128
4.4.2 Construction of knockout strains 129
4.4.3 Construction of vectors with CetZ1 fluorescent protein fusion 130
4.4.4 Testing the complementation of CetZ1 fluorescent fusion proteins 132
4.4.5 Motility assay 132
4.4.6 Early-log phase rod assay 133
5 Chapter 05: *In vivo* characterisation of CetZ1 function via site-directed mutagenesis 134
5.1 Introduction 135

5.2 Results 137
5.2.1 Use of CetZ1 site-directed mutants for identification of structural components in CetZ1 important for *Haloferx volcanii* motility and morphogenesis .. 137
5.2.2 CetZ1 localisation dynamics in the point mutants 146
5.3 Discussion 155
5.4 Methods 158
5.4.1 Construction of point mutants 158
5.4.2 Construction of fluorescent fusion proteins of CetZ1 point mutants 160
5.4.3 Early-log phase rod development 160
5.4.4 Live cell imaging 160
5.4.5 Cell volume and cell count analysis by Coulter counter 161
6 Analysis of *In Vitro* Interactions of CetZ1 162
6.1 Introduction 163
6.1.1 Models for subunit polymerisation 163
6.1.2 The polarity of the cytoskeletal filaments 165
6.2 Results 168
6.2.1 Optimisation of CetZ1 purification 168
6.2.2 Optimised condition for CetZ1 polymerisation 172
6.2.3 *In vitro* polymerisation of selected CetZ1 point mutants 178
6.2.4 CetZ1 aggregated multimers can directly bind to the lipids 181
6.3 Discussion 185
6.4 Methods 188
6.4.1 Overproduction of the protein and preparation of the cell lysate 188
6.4.2 The purification of untagged CetZ1 189
6.4.3 Purification of archaeal membrane lipids and liposome preparation 189
6.4.4 Ultracentrifuge co-sedimentation assay 190
6.4.5 Ultracentrifuge co-pelleting assay 191
6.4.6 90^0 Light scattering assay 191
6.4.7 Malachite Green GTPase assay 192
7 Discussion 194
7.1 External signals that induce the *H. volcanii* rod formation 195
7.2 CetZ1 in modulating *H. volcanii* cell shape 198
8 Appendix: Supplementary Data 201
9 References 208

List of Figures

Figure 1.1: *Three main types of cytoskeletal components in cells.* 21
Figure 1.2: *Important structural features in tubulin heterodimer.* 24
Figure 1.3: *Straight and bent conformations of tubulin dimers and models proposed for the role of GTP in adapting these conformations into the microtubule lattice.* 26
Figure 1.4: *The structure of the γ- tubulin ring complex (γ- TuRC).* 28
Figure 1.5: *The effect of β:T238A mutation on microtubule dynamics.* 31
Figure 1.6: *Z ring formation in Haloferax volcanii, the model haloarchaeon used in this study.* 36
Figure 1.7: *An overview of cell division (left) apparatus and cell elongation (right) apparatus.* 37
Figure 1.8: *Different cell shapes in haloarchaea.* 40
Figure 1.9: *A phylogenetic overview of tubulin superfamily.* 43
Figure 1.10: *Evidence indicating CetZ1 is not essential for cell division, and it is needed for the shapeshift form plate shape to rod shape.* 44
Figure 1.11: *Current evidence that displays CetZ1 cytoskeletal dynamics.* 45
Figure 1.12: *Evidence showing CetZ1 can assemble into a quaternary structure.* 47
Figure 3.1: *Effects of nutrient depletion on H. volcanii growth and morphology in liquid culture.* 70
Figure 3.2: *Media supplementation with trace elements (TE) solution improves growth and cell shape uniformity in H. volcanii.* 72
Figure 3.3: *H. volcanii forms rods during the early stages of growth at low ODs in liquid batch culture.* 73
Figure 3.4: *Assays for H. volcanii reversible morphological transitions during the growth cycle.* 74
Figure 3.5: *Time-lapse microscopy of H. volcanii (H98 + pTA962) with and without trace elements.* 77
Figure 3.6: *CetZ1 is essential for rod development during early-growth after colony resuspension and during TE-depletion.* 80
Figure 4.1: *Summary of H. volcanii gene knockout system based on pyrE2 genetic marker.* 92
Figure 4.2: *Motility and cell shape comparison of WT and cetZ1 knockout cells.* 93
Figure 4.3: *CetZ1 localisation in the WT background.* 94
Figure 4.4: *Effect of linker rigidity on FRET efficiency and the separation between a CFP and YFP fusion protein.* 97
Figure 4.5: *Schematic representation of the cetZ1 (HVO_2204) deletion construct.* 101
Figure 4.6: *Schematic representation showing the steps in the construction of new cetZ1 knockout strains.* 103
Figure 4.7: *Diagnostic tests to confirm the ΔcetZ1 strains* 104
Figure 4.8: *Complementation of CetZ1 function in cetZ1 in-frame and out-of-frame knockouts compared to H. volcanii H26 (WT) strain.* 106

Figure 4.9: *Complementation of rod cell formation by cetZ1 overexpression (4 mM tryptophan) during mid-log growth and cetZ1 WT level expression (2 mM tryptophan) during early-log phase rod assay in the cetZ1 in-frame knockout strain.* 108
Figure 4.10: *Plasmid design of the fluorescent vectors.* 111
Figure 4.11: *Screening of IF ΔcetZ1 complementation by the fluorescently labelled CetZ1.* 113
Figure 4.12: *The fluorescent (left) and phase-contrast (right) images of the cells from the early-log phase assay in Hv-YPCab+2 mM tryptophan for all CetZ1 fusions with G linker in IF ΔcetZ1.* 115
Figure 4.13: *Comparison of the complementation of ΔcetZ1 by CetZ1-mTurquoise2 fusions and the original GFP fusion; pIDJL40.CetZ1.* 117
Figure 4.14: *The localisation of new CetZ1-mTurquoise2 in motile rods and during supplementary expression.* 119
Figure 4.15: *CetZ1 localisation during early-log phase assay and trace elements (TE) depletion assay.* 121
Figure 4.16: *CetZ1 localisation imaged by 3D-SIM.* 122
Figure 4.17: *Selected time frames showing CetZ1 localisation dynamics during morphogenesis.* 123
Figure 5.1: *Locations of the CetZ1 point mutations designed to disrupt the lateral interaction, membrane interaction and GTP contact.* 138
Figure 5.2: *Expression and motility assays of strains expressing CetZ1 point mutants.* 141
Figure 5.3: *Cell shapes observed in ID181 expressing the indicated CetZ1 site-directed mutants (on pTA962) in the TE depletion assay.* 143
Figure 5.4: *Rod formation by CetZ1 point mutants in the early-log phase assay.* 144
Figure 5.5: *CetZ1-mTurquoise2 localisation during early-log phase assay for point mutants that displayed decreased motility.* 147
Figure 5.6: *CetZ1-mTurquoise2 localisation during early-log phase assay for point mutants that displayed normal motility.* 149
Figure 5.7: *Comparison of distances of CetZ1 localisations to the cell edge in different point mutants.* 151
Figure 5.8: *A comparison of the aspect ratio of the localisations in the double mutant (R726E, K277E) and G108S to the that of WT CetZ1.* 153
Figure 6.1: *A schematic showing the differences in subunit assembly between* 164
Figure 6.2: *The two possible kinetic polarities for polymer growth. Tubulin shows the first top-end growth kinetics in which subunits add to the GTP-bound end of the polymer.* 166
Figure 6.3: *The optimisation of the protein purification buffer with different additives.* 169
Figure 6.4: *Buffer optimisation improved CetZ1 purification.* 170
Figure 6.5: *SDS-PAGE analysis of the collected fractions from Ion Exchange and subsequent Gel Filtration.* 171
Figure 6.6: *Optimisation of CetZ1 (12 μM) in vitro polymerisation condition using 90^0 light scattering assay.* 173
Figure 6.7: *The effect of pH on CetZ1 (12 μM) polymerisation.* 174
Figure 6.8: *Analysis of CetZ1 GTP dependent polymerisation.* 175
Figure 6.9: *CetZ1 displays cooperative polymerisation.* 176

Figure 6.10: *Malachite Green Phosphate assay cannot detect CetZ1 GTPase activity.* 177
Figure 6.11: *Comparison of gel filtration chromatograms between (A) WT CetZ1 and CetZ1 point mutants, (B) CetZ1.M-loop, (C) CetZ1.E218A resulted during their purification.* 179
Figure 6.12: *Analysis of the polymerisation of CteZ1 point mutants, CetZ1, M-loop and CetZ1.E218A, via light scattering assay.* 180
Figure 6.13: *Haloferax volcanii lipids.* 181
Figure 6.14: *Analysis of CetZ1 lipid-binding via ultracentrifuge co-sedimentation assay.* 183

- **Supplementary Data Figure 1.** Reversal and specificity testing of TE starvation. *H. volcanii* (H98 + pTA962) colonies from Hv-Ca agar were resuspended in Hv-Ca liquid medium.
- **Supplementary Data Figure 2.** Effect of spent media on *H. volcanii* cell shape during on-set rod formation.
- **Supplementary Data Figure 3.** Inclusion body formation depending on the cells' history of starvation.
- **Supplementary Data Figure 4.** The growth differences in *H. volcanii* during TE depletion.
- **Supplementary Data Figure 5.** The CetZ1 localisation concerning the local curvature of the cell.
-
- **Supplementary Video 1.** *H. volcanii* cell shape change in Hv-Cab (+TE).
- **Supplementary Video 2.** *H. volcanii* cell shape change in Hv-Ca (-TE).
- **Supplementary Video 3.** *H. volcanii* cell shape change in Hv-YPC (-TE).
- **Supplementary Video 4.** *H. volcanii* cell shape change in Hv-YPCab (+TE).
- **Supplementary Video 5.** The localisation of CetZ1-mTq2 expressed in ID181 during early-log phase assay.
- **Supplementary Video 6.** The localisation of CetZ1-mTq2 expressed in ID181 during early-log phase assay.
- **Supplementary Video 7.** The localisation of CetZ1.R276E, K277E-mTq2 expressed in ID181 during early-log phase assay.
- **Supplementary Video 8.** The localisation of CetZ1.G108S-mTq2 expressed in ID181 during early-log phase assay.
- **Supplementary Video 9.** The localisation of CetZ1.C-terminal tail mutant-mTq2 expressed in ID181 during early-log phase assay.
- **Supplementary Video 10.** 3D-SIM images showing localisation of CetZ1-mTq2 expressed in ID181 during early-log phase assay.
- **Supplementary Video 11.** Z-stack of a 3D-SIM images showing localisation of CetZ1.G108G-mTq2 expressed in ID181 during early-phase assay.

List of Tables

Table 2.1 General Bacterial Strains Used in the Present Work 50
Table 2.2 General Archaea Strains Used in the Present Work 50
Table 2.3 General Plasmids Used in This Work 51
Table 2.4 Commonly Used Bacterial Growth Media 51
Table 2.5 Commonly Used Archaea Growth Media 52
Table 2.6 Commonly Used Chemicals in the Present Work 53
Table 2.7 Buffers and General Solutions Used in This Work 54
Table 2.8 Ingredients of SDS-PAGE Gels 62
Table 4.1 Primers Used for Amplification of Flanking Regions of *cetZ1* Deletions 128
Table 4.2 Primers Used in Diagnostic PCR of *cetZ1* Deletion Strains 129
Table 4.3 Sequences of the Three Types of Linkers Used in This Study 130
Table 4.4 Primer Sequences Used for GFP Amplification and the Plasmid Sequence Confirmations 131
Table 5.1 Rod Formation of ID181 by CetZ1 with Point Mutations During Early-log Phase Assay 145
Table 5.2 Primers used to amplify the CetZ1 point mutations 159
Table 6.1 Protein Concentration Gradient used in Malachite Green Phosphate Assay 192

ABBREVIATIONS

AMP	Ampicillin
Å	Angstrom
BSA	Bovine Serum Albumin
BLAST	Basic local alignment search tool
DNA	deoxyribonucleic acid
g	Gram
GFP	Green fluorescent protein
GTP	Guanosine triphosphate
GDP	Guanosine diphosphate
h	Hour(s)
kb	Kilo base pair(s)
kDa	Kilodalton(s)
min	Minute(s)
ml	Millilitre(s)
MQW	Milli-Q water
OD	Optical Density
PBS	Phosphate Buffered Saline
PCR	Polymerase Chain Reaction
psi	Pounds per square inch
mRNA	Messenger Ribonucleic acid
M	Molar concentration
Mm	Millimolar concentration

MWCO	Molecular weight cut-off
n	nano
NCBI	National Centre for Biotechnology Information
RT	Room Temperature
rpm	Revolutions per minute
r.m.s.d	Root-mean-square deviation
SDS-PAGE	Sodium dodecyl sulfate polyacrylamide gel electrophoresis
sec	sec
TBS	Tris Buffered Saline
TEMED	N,N,N',N'-tetramethylethylenediamine
Tris	Tris(hydroxymethyl)methylamine
w	Weight
WT	Wild Type
v	Volume
µ	Micro

PUBLICATIONS AND CONFERENCE PROCEEDINGS

Journal Publications:

- **de Silva, R.T**, Halim, M. F., Pohlschroder, M., Duggin, I. G., 'Cell shape differentiation in *Haloferax volcanii'* Applied Environmental Biology (manuscript to be submitted).
- Liao, Y., Ithurbide, S., **de Silva, R. T**, Erdmann, S., Duggin, I. G. et al. (2018) 'Archaeal cell biology: diverse functions of tubulin-like cytoskeletal proteins at the cell envelope', Emerging Topics in Life Sciences. doi: 10.1042/etls20180026.

Conference Proceedings:

- **de Silva R.T**. Ithurbide S.I., Duggin I.G. (2019) "CetZ1 in cell shape control of haloarchaea: Understanding the functional divergence of tubulin superfamily protein" at Motile and Contractile Systems Gordan Research Conference, USA (**oral and poster presentation**).
- **de Silva R.T**. Ithurbide S.I., Duggin I.G. (2019) "CetZ1 in cell shape control of haloarchaea: Understanding the functional divergence of tubulin superfamily protein" at ASMMicrobe19, American Society of Microbiology, USA (**late breaker poster presentation**).
- **de Silva R.T**. Ithurbide S.I, Duggin I.G. (2018) "Metal starvation triggers CetZ1-depedent cell shape changes in haloarchaea" at Combio 2018, Sydney, Australia (**oral presentation**).
- **de Silva R.T**. Ithurbide S.I, Duggin I.G. (2018) "Metal starvation triggers CetZ1-dependent cell shape changes Haloferax volcanii" at Molecular biology of archaea: From mechanisms to ecology (MBoA6), EMBO Workshop, Vienna, Austria (**poster presentation**).

ACKNOWLEDGEMENT

I would like to convey my sincere thanks to all those who encouraged me and supported me in completing my research timely. First and foremost, I am deeply grateful to my supervisor A/Prof. Iain Duggin for all the opportunities, guidance, and support in my progression through the PhD. I deeply enjoyed all the insightful discussions. You have been an excellent mentor.

My warmest thanks to all my lab mates for making a wonderful vibe to work. I am grateful to Yan Liao, Greg Iosifidis, Taylor Corocher and Carly Italiano for proofreading my thesis. Also, I really enjoyed collaborating with Solenne Ithurbide to make the archaeal world colourful with a new set of fluorescent plasmids. The support received from my labmates, Tamika Blair, Dora Pittrich and Vinaya Shinde are much appreciated.

I would like to extend my thanks to UTS Microbial Imaging Facility. The MIF director A/Prof. Louise Cole and Dr Michael Johnson, for giving me excellent training and Dr Christian Evenhuis for his invaluable help in data analysis.

I am also grateful to ithree Director, Prof. Liz Harry, for her invaluable guidance which helped me to shape my research career, Dr Chris Rodrigues for giving me insightful advice to improve my research and to all my friends at the ithree institute. I must thank Shima Vahdat, Meggie Leung and Shannon Hawkins for making sure that all administrative works are completed timely. My appreciation also extends to Prof.Mecky Pohlschröder from the University of Pennsylvania for collaborating with our research.

I am grateful to all my thesis reviewers for spending their time reviewing my thesis. My warm thanks are due to Ransalu for his indispensable support. Thank you for your patience and encouragement. Last, but not least, I am also greatly indebted to my parents and friends for their affection.

K.W.T. Roshali Thavindra de Silva, ithree Institute, The University of Technology Sydney, 02 September 2019.

ABSTRACT

Cell shape dynamics are important for cell survival. Eukaryotic cytoskeletal protein tubulin plays essential roles in internal structure organisation and cell shape. However, the prokaryotic tubulin homologue, FtsZ, controls the assembly and function of the division ring. The origin of this functional disparity is still unclear. A third group of the tubulin superfamily, CetZ, has been recently identified in archaea and shows characteristics in common with both the tubulin and FtsZ. A conserved member, CetZ1, is required for cell shape changes (from plate to rod) during the development of motile cells in the archaeon, *Haloferax volcanii* (Duggin *et al*., 2015).

The present study has defined additional culture conditions—metal nutrients depletion and early-log growth—that result in rod development, which has opened new ways of understanding cellular differentiation in archaea. A new Δ*cetZ1* strain, which can be complemented by resupply of CetZ1 on a plasmid, was also constructed. Using these culture conditions and Δ*cetZ1*, a functional CetZ1-mTurquoise2 fusion was identified after screening numerous fluorescent proteins and linker-peptide combinations. It displayed a patchy and dynamic localisation in discoid cells, then, during rod formation, displayed short dynamic filaments along the edges of the cell's long axis. During cell division, CetZ1 localises at the envelope around the division furrow; this differed significantly from FtsZ localisation pattern.

By using the CetZ1 and CetZ2 crystal structures as a guide, mutants were constructed to probe the functions and interactions of CetZ1 in *H. volcanii*. Mutation in the predicted CetZ1 membrane-interaction and self-association domains prevented rod development. The former displayed filament-like localisation detached from the cell edges, whereas the latter did not localise *in vivo*, consistent with the predictions. The GTPase mutants of CetZ1 prevented rod development but caused more intense and less dynamic localisation suggesting regulation of characteristic GTP-dependent dynamics is critical to CetZ1 function. CetZ1 *in vitro* studies revealed GTP-dependent polymerisation and these polymers were destabilised in predicted self-association mutant. Moreover, a mutation in the C-terminal tail displayed a decreased membrane localization.

These structure-function studies suggest CetZ1 forms polymers that has its longitudinal interactions controlled via the GTPase activity and the lateral interactions mediated by a

region similar to tubulin ‘M-loop’. The dynamic localisation of CetZ1 to the cell edges via the C-terminal tail region is essential to modulate the cell shape. Finally, these discoveries support the notion that cell shape control by tubulin superfamily proteins could have predated the emergence of eukaryotic tubulins.

CHAPTER 1
INTRODUCTION

1.1 Overview of the research problem

The cytoskeleton is a complex composite of filaments and tubules which can be found in every cell of all living organisms. Prime roles among the diverse range of functions of the cytoskeleton include maintaining cell shape, cell division, and intracellular transportation (Nogales, 2001). Eukaryotic tubulin plays a pivotal role in exerting all of these functions while prokaryotic tubulin homolog FtsZ is essentially required for cytokinesis. In addition, the mechanism of action and the higher-order quaternary structures of these eukaryotic and prokaryotic tubulin homologs are remarkably different. Prokaryotic FtsZ forms a ring structure at the mid cell called "Z ring", which contains loosely assembled protofilaments. The number of protofilaments can be variable (Osawa, Anderson and Erickson, 2008). The treadmilling of this "Z ring" drives the peptidoglycan synthesis at the septum (Yang *et al.*, 2017) and probably provides the constrictive force to exert the cytokinesis (Mukherjee and Lutkenhaus, 1998, Ramirez-diaz *et al.,* 2019). Eukaryotic tubulin exists in the form of complex and organised structures called microtubules. Microtubules exist as a protein meshwork inside the cell and arrange into a spindle during mitosis to help chromosomal segregation (Minc, Burgess and Chang, 2011). Furthermore, tubulin displays complex regulation mechanisms and dynamics to exert a diverse range of structural roles (Dráber and Dráberová, 2012). Since evolution is a gradual process, the gaps between this abrupt change in tubulin superfamily proteins are still unclear (Osawa and Erickson, 2006).

We believe the recently discovered archaeal tubulin superfamily protein CetZ1, could be the "missing link" of this cytoskeletal evolution as it shares common features with both FtsZ and tubulin. The current project aims at characterising the function of archaeal cytoskeletal protein CetZ1 as a part of understanding the evolution of tubulin from FtsZ. Furthermore, to design new biological molecules with useful applications, studying the function and evolution of molecules will advance our knowledge to understand how nature designed these simple molecules prior to the emergence of eukaryotic cells. Moreover, the cell cytoskeleton is one of the major drug targets in designing anti-cancer (Kavallaris, 2010) drugs and antibiotics. The common features shared between archaeal and eukaryotic cytoskeleton reveal a possibility of using archaea as a simplified model organism for *in vivo* cytoskeletal studies of complex eukaryotic systems and drug development. Additionally, unveiling further details about archaea has intrigued scientists

due to its significance in earth's geochemical cycling and biotechnological applications (Jarrell *et al.*, 2011).

1.2 Cytoskeleton

Although the term "cytoskeleton" implies a steady structure that holds the integrity of cells, it is charachterized by highly dynamic filaments that coordinate with each other to maintain the structure and dynamics of the cells by consuming the energy of NTPs. Eukaryotic cells display the most advanced cytoskeleton among the three domains of life, and the complexity of the cytoskeleton increases as it proceeds higher into the tree of life, with the cytoskeleton of human cells being one of the most complex. The eukaryotic cytoskeleton consists of three main components, microtubules, microfilaments and intermediate filaments. Coordination of these protein components together with the motor proteins such as kinesin and dynein maintains the structural integrity of the cell (Wickstead and Gull, 2011).

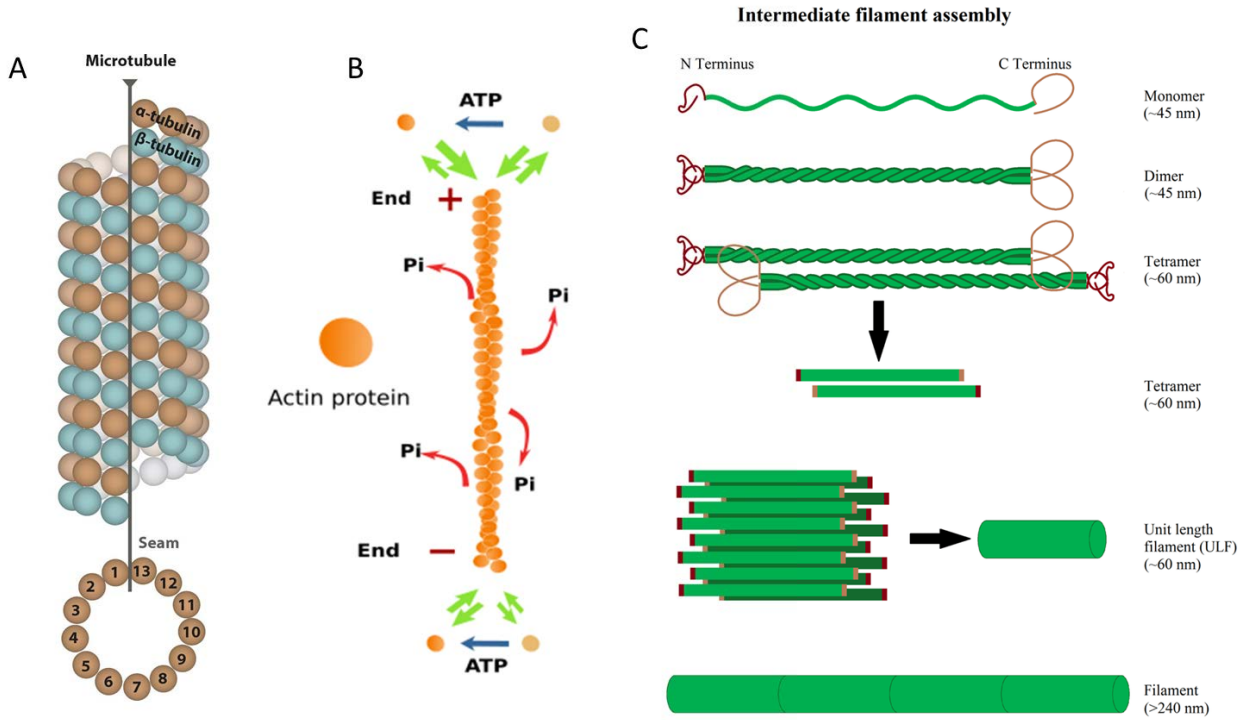

Figure 1.1: *Three main types of cytoskeletal components in cells.*

(A) Microtubules, a hollow cylinder formed typically by 13 protofilaments αβ heterodimer (diameter of the outer cylinder is ~24 nm). (B) Spiral chain arrangement of actin molecules in actin protofilament. (C) Monomer structure of the basic subunit of intermediate filaments (top), monomers arranged into a coiled-coil dimer (second row), tetramer formed by intertwined coil-coiled dimers (third row). Below that is a schematic of a unit length filament (ULF) in which eight tetramers have coiled into a rope-like structure. Finally, consolidation of ULFs into an intermediate filament. Taken from (Deng et al., 2017, Pollard et al., 2016, Hohmann and Dehghani, 2019).

Microtubules are typically made up of thirteen tubulin protofilaments of α, and β tubulin heterodimers organised into a hollow straw (Figure 1.1) shaped filament (Nogales *et al.*, 1999). Microfilaments are a second major type of cytoskeletal filaments in eukaryotic cells, formed by ATP-dependent polymerisation of a globular protein called actin (Figure 1.1). Actin filaments that have a spiral chain arrangement bind with myosin motor proteins in muscle cells to exert muscle contraction. Microfilaments are important in maintaining cell shape and for cell movement (Dominguez and Holmes, 2011). The basic subunit of the third group of cytoskeletal proteins, intermediate filaments are a tetramer of a coiled-coil dimer of filamentous subunits. The structure of an intermediate filament contains eight tetramers coiled into a rope-like structure (Figure 1.1). The type of polypeptide subunit in intermediate filaments depends on the cell type (Strelkov,

Herrmann and Aebi, 2003). These intermediate filaments provide mechanical stability to cells (Leube and Schwarz, 2015). Another filament-forming cytoskeletal component that has been discovered only in eukaryotic animal cells is septin. Unlike other eukaryotic cytoskeletal proteins, septin is unable to form long-range filaments. They are usually sensitive to the positive local curvature of the cells and help to assemble other cytoskeletal protein complexes at these points (Mostowy and Cossart, 2012, Beber *et al.*, 2019).

Despite the weak sequence homology, the bacterial cytoskeleton contains the counterparts of each of the eukaryotic cytoskeleton protein types. The most conserved and ubiquitous bacterial proteins, FtsZ and MreB, are the bacterial homologues of tubulin and actin, respectively (Erickson, 1997, Van den Ent, Amos and Löwe, 2001). In addition to FtsZ, two other microtubule-forming tubulin homologues (BtubA and BtubB) were found in *Prosthecobacter* species, and these proteins are closely related to the eukaryotic tubulin. However, this bacterium might have acquired the microtubule genes via horizontal gene transfer (Schlieper *et al.*, 2005). Bacterial intermediate filaments such as crescentin and FilP were later discovered in some bacterial species (Bagchi *et al.*, 2008). As the present study is focused on probing the function of CetZ1, i.e. a protein belonging to a new family of tubulin-like proteins in archaea, the subsequent sections will focus on the current findings on structure and dynamics of eukaryotic, bacterial and archaeal tubulins and the biological processes driven by these proteins.

1.3 Tubulin superfamily proteins

Tubulin superfamily proteins are primarily involved in controlling cell division. Although tubulin superfamily proteins are widespread across all domains of life, a few examples can be identified that have sustained cell division without any tubulin homologues present in them (e.g., *Desulfurococcales*, *Thermoproteales*) (Ettema and Bernander, 2009). Tubulin superfamily proteins can be identified by the high primary amino acid sequences conservation at the GTP contact site (T1, T4, H6 and T7). Therefore, the GTPase activity of these proteins is highly conserved and is essential for function (Mukherjee and Lutkenhaus, 1998). During protein polymerisation, GTP molecules are bound between

the two subunits and subsequently hydrolyses when the two subunits are in contact. Thus, tubulin superfamily proteins are described as GTPase Activating Proteins (GAPs).

Furthermore, the monomers of tubulin superfamily proteins display a common protein fold that usually contains two distinct C-terminal and N-terminal domains separated by a central helix. They also display a structural similarity to the Rossmann-fold di-nucleotide binding proteins and small GTPases of the Ras superfamily (Snyder *et al.*, 2010). A disordered C-terminal tail region usually crucial for the protein function can also be noticed in the tubulin superfamily proteins. Although these proteins share a common backbone, there are a few differences in the exact crystal structure. For example, tubulin lacks the N-terminal extension to the core GTP binding domain present in FtsZ (Lowe and Amos, 1998). Furthermore, the polymeric structures of these proteins also display differences that are reflected in the way they function. Therefore, the following sections describe the structure of eukaryotic and bacterial tubulin superfamily proteins, the behaviour of these polymers (based on *in vivo* and *in vitro* studies), regulation mechanisms during polymerisation, and briefly describe how these proteins regulate important biological functions.

1.4 Microtubules

Tubulins exist in the cell in the form of microtubules, which are non-covalent polymers build-up from αβ heterodimers as its basic subunit (Gregoretti, 2007). Microtubules inside the cells can be described as an "organised mesh" as they position the cytoplasmic organelles at correct locations. Motor proteins that walk on the microtubules are used to transport cargo inside the cell (Kapitein *et al.*, 2010). In dividing cells, microtubules from the mitotic spindle which aligns the chromosomes at the division plane and subsequently pull them to segregate into two daughter cells. Additionally, microtubules contribute to cell motility by forming axonemes of the flagella and cilia (Satir and Christensen, 2007). The functionally important microtubule dynamics are primarily governed by its intrinsic properties inherent by the structural features, conformational changes of the tubulin subunits and the post-translational modifications The interactions with regulatory

proteins that occur during the microtubule growth cycle also play a crucial role. The following sections will describe the specific examples of how these factors affect microtubule dynamics according to the current understanding.

1.4.1 Relationship of tubulin structure and conformation with the function

Tubulin subunits exist in a heterodimeric form of α and β tubulins in cells. Although, α and β tubulin share only ~51% amino acid sequence similarity, the crystal structures determined (3.7 Å resolution) from zinc-induced and taxol stabilised proteins indicate that these subunits share a very similar protein fold (Löwe *et al.*, 2001). Both α and β subunits can bind to the GTP.

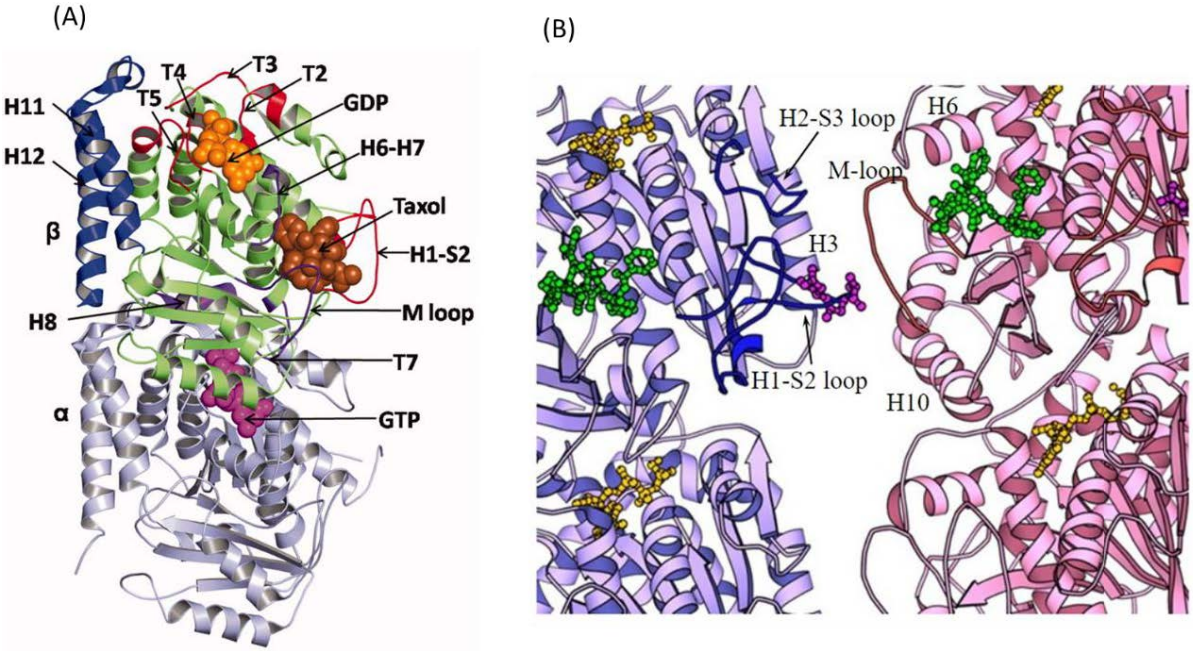

Figure 1.2: *Important structural features in tubulin heterodimer.*

(A) Tubulin heterodimeric structure resolved from electron crystallography. A GTP molecule is located in a pocket formed by the flexible loops T1-6 on the top surface of each monomer. Additionally, the T7 region at the bottom surface has close contact with the GTP molecule. (B) Lateral interaction between tubulin subunits via the M-loop region. The M-loop sticks out to the H1-S2 loop and H3 region of the next subunit. Taken from https://slideplayer.com/slide/8808418/ (Kenneth H. Downing, Lawrence Berkeley National Laboratory) [15/08/2019].

The conserved GTP binding pocket in the tubulin subunit is formed by the collection of nucleotide-binding N-terminal domain loops T1-T6 and, the top end of the central helix H7 (Figure 1.2) (Löwe *et al.*, 2001). However, the buried conformation of the GTP binding site (N-site) in the α tubulin makes the GTP molecule nonexchangeable (Figure 1.2). Therefore, the subunit interface between α and β subunits are quite stable, and they exist as heterodimers. The GTP bound to the partially exposed active site (E-site) of β tubulin, however, is exchangeable. Therefore, heterodimers with GTP bound to the E-site are required for the microtubule polymerisation. The amino acids in the H8 and T7 loop (between H8 and H7) are also highly conserved (Dougherty *et al.*, 2001) (Löwe *et al.*, 2001). This region at the bottom surface of the subunit allows a direct contact with the GTP molecule (Figure 1.2), supporting the idea that its evolutionary conservation is due to its functional importance in the GTPase activity of these proteins (Anders and Botstein, 2001b). Usually, the C-terminal tail region of tubulins are rich with acidic residues. Also, the C-terminal tail is not well resolved in the crystal structure due to its intrinsically disordered nature. However, many studies indicate these regions are highly important for function (mainly for the binding of motor proteins and microtubule-associated proteins) (Freedman *et al.*, 2011).

Microtubule dynamics are mainly driven by the conformational changes that occur in the αβ dimer subunits.

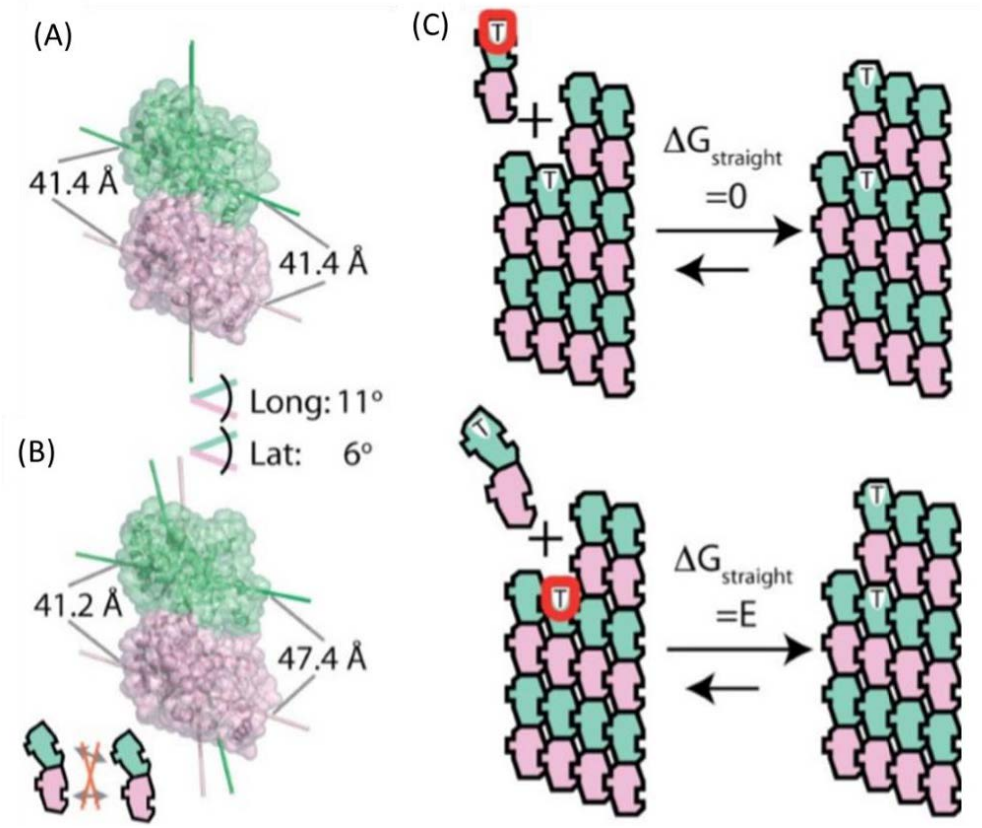

Figure 1.3: *Straight and bent conformations of tubulin dimers and models proposed for the role of GTP in adapting these conformations into the microtubule lattice.*

(A) The straight conformation of tubulin in which longitudinal and lateral axes of α and β tubulins are aligned with each other. (B) The curved conformation of the heterodimer in which the longitudinal axis one monomer is shifted by 11° from the other and the lateral axis is shifted by 6°. (C) A comparison of two models by which tubulin subunit can incorporate into the microtubule lattice. The top one shows the GTP (red circle) bound to tubulin can exert an allosteric effect to change the tubulin heterodimer into the straight conformation, thereby reducing the energy barrier. The bottom model proposes tubulin subunits incorporate into the microtubule in a GTP-bound curved conformation. As this is energetically unfavourable, the GTP bound to the microtubule (red circle) stabilises the straight conformation by exerting a stronger contact. Adapted from (Rice, Montabana and Agard, 2008).

The free GTP bound subunits that are at the relaxed state has ~11° kinks at the intradimer surface (Figure 1.3) (Rice *et al.*, 2008). Based on the studies carried out using mammalian tubulins (Zhang *et al.*, 2015, Alushin *et al.*, 2014), dimer subunits adapt to a straight conformation upon polymerisation, thus introducing strain energy to the microtubule lattice. The subsequent conformational change of α-tubulin into a compact form promotes

the hydrolysis of GTP into GDP shortening the microtubule lattice. The distribution of the subunits with each of these conformations and the exact nucleotide state (GDP vs GDP-Pi) of the compact conformation is poorly understood (Wang and Nogales, 2005, Alushin *et al.*, 2014).

The different energy states featured by the microtubule lattice either trigger growth or shrinkage of the microtubule. To explain the exact conformation by which tubulin incorporates into the microtubule, two models (Figure 1.3), the allosteric model and the lattice model, have been proposed. In the former model, subunits are taken up in straight conformation (energetically favourable) and the later model, subunits are added in the curved confirmation (overcoming the energy barrier of straightening the subunit). However, using kinetic simulations, it has been shown that the lattice model is highly plausible in which tubulin acts as a bent spring until an additional force is applied by the microtubule bound GTP (Rice *et al.*, 2008).

Lateral interactions also play a crucial role in maintaining microtubule structure and polymer dynamics. The M-loop structure (residues 276- 286 in α-tubulin and 272–285 in β-tubulin) located between S7 and H9 (Keskin *et al.*, 2002) plays a crucial role in stabilising the lateral interaction of microtubules (Prota *et al.*, 2013). The M-loop is capable of movement without disrupting its interactions with H1-S2 loop and H3 regions in the next subunit. Therefore, a variation between 10-15 tubulin protofilaments in a microtubule can be evident in different types of cells. However, as the lateral interactions are highly conserved (<1 Å variation), a bundle of 13 protofilaments is the most commonly observed microtubule type in eukaryotic cells (Chrétien, Flyvbjerg and Fuller, 1998). Furthermore, the conformation of the M-loop suggests that destabilisation of the lateral interactions triggers the catastrophe, thereby transitioning the compact conformation of the microtubule lattice to revert into the curved low energy state. The H3 helix, the region that M-loop interacts with on the adjacent subunit, is located next to the GTP γ-phosphate contact site, loop T3 (Figure 1.2). Therefore, conformational change at the H3 helix following destabilisation in the lateral interactions could effect a conformation change in the longitudinal interactions, thereby promoting depolymerisation (Nogales *et al.*, 1999).

1.4.2 Microtubule dynamics and regulation

The development of high-resolution microscopy, together with fluorescence labelling techniques have now unravelled the mechanisms of tubulin dynamics in eukaryotic cells. Microtubule dynamics are energy consuming, yet an evolutionarily conserved process in the cell. Adding αβ heterodimers to the polymer uses the energy stored in GTP molecules. The polymerisation process comprises two phases: nucleation and elongation. Although microtubule de novo synthesis is possible, the high sensitivity of the nucleation kinetics to the free tubulin concentration in the solution indicates this process is an energetically unfavourable reaction (Voter and Erickson, 1984, Kuchnir Fygenson *et al.*, 1995). *In vivo*, this energy barrier is overcome by initiating nucleation on an already existing microtubule end or using templates such as the γ- tubulin ring complex (γ- TuRC).

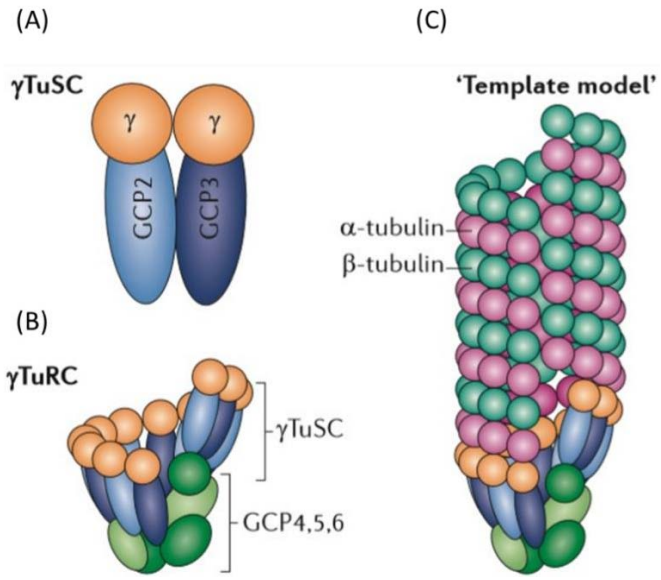

Figure 1.4: *The structure of the γ- tubulin ring complex (γ- TuRC).*

(A) The structure of γ- tubulin small complex (γ- TuSC). GCP2 and GCP3 are highly conserved among most eukaryotic cells. (B) The structure of γ- TuRC. A ring-like template is formed complexing γ- TuSC with GCP 4,5 and 6. (C) The widely accepted nucleation model where αβ heterodimers nucleate on a γ- TuRC template. Adapted from (Kollman et al., 2011).

γ- TuRC is a conical shaped ring of γ-tubulins arranged at the microtubule organising centre (MTOC) and this acts as a template for microtubule polymerisation. During mitosis

in eukaryotes, the organisation of microtubules into a spindle is initiated on the spindle pole body (SPOD). This is formed by assembling γ- tubulin with spindle pole complex proteins called Spc97 and Spc98 also known as γ- tubulin complex proteins (GCP2 and 3) which together forms γ- tubulin small complex (γ- TuSC) (Figure 1.4). In some organisms, this complex is further modified into γ- TuRC by complexing with a few additional proteins, GCP 4-6 (Figure 1.4) (Kollman *et al.*, 2011). Having a template for nucleation decreases the critical tubulin concentration needed for the microtubule polymerisation. However, lag time is evident (Tovey and Conduit, 2018) when nucleation occurs from γ- TuRC suggesting that nucleation is favoured at a tapered end of an existing microtubule over γ- TuRC that has a straight conformation. The reason for such an effect could be because the curved conformation of tubulin dimers is energetically favourable while nucleating on γ- TuRC might require an unfavourable step of straightening of this conformation (Tovey and Conduit, 2018).

Recent discoveries suggest that the microtubule-associated proteins (MAPs) such as kinesin, microtubule polymerases and depolymerase also play an important conformation-specific regulatory role in microtubule dynamics. For example, the microtubule polymerase, XMAP215 which identifies and binds to the curved conformation of the dimer subunit promotes the addition of tubulin subunits at the initial stages of nucleation (Brouhard *et al.*, 2008). MAPs such as TPX2 and doublecortin (DCX) bind to the subunits with the curved conformation and stabilise the subunit-subunit interface to accelerate nucleation. TPX2 is a well-studied anti-catastrophe factor (an agent that stops the switching from growth to shrinking of microtubules) of the mitotic spindle. TPX2 can interact directly with γ- TuRC to reduce the lag time of nucleation, and promote branching nucleation where nucleation occurs from the side of an existing microtubule (Alfaro-Aco, Thawani and Petry, 2017). On the contrary, the presence of MAP, such as MCAK, contributes to the lag time during nucleation because it prefers the curved conformation of tubulin subunit (Alfaro-Aco *et al.*, 2017, Wang *et al.*, 2017).

Microtubules establish a polarity across the cell as it has a minus-end attached to the MTOC at the nucleus, and a fast-growing plus end towards the periphery of the cell. And due to the intrinsic polarity of the heterodimer obtained via having an E-site and an N-site, β tubulin is always situated at the plus end of the microtubule while α tubulin is at the minus end (Lüders and Stearns, 2007). Therefore, during nucleation γ-tubulin starts

an interaction with the α-tubulin. However, this interaction at the α and γ tubulin surface is much weaker than the interaction at the α and β tubulin surface (Thawani *et al.*, 2018).

The growing microtubule is stabilised by anchoring the minus end to the centrosome and forming a GTP cap at the plus end. Although the exact features of the cap are poorly understood, it contains about 100 GTP bound subunits which help recruit the end binding (EB) proteins and MAPS (Maurer *et al.*, 2012). The EB proteins regulate microtubule dynamics and are highly conserved in eukaryotic cells. They bind to the microtubule via by recognising conformational changes that occur when the microtubule lattice changes from GTP bound state to GDP bound state. The subunits between MTOC and the GTP cap have their GTP molecules hydrolysed into GDP due to the intrinsic GTPase activity of tubulin. Stochastic loss of the GTP cap following microtubule elongation results in depolymerisation and catastrophe of the microtubule. The polymers can either undergo complete catastrophe or sometimes the shrinking polymers can be rescued. This non-equilibrated dynamic state of the polymers is known as the dynamic instability of the microtubule (Burbank and Mitchison, 2006, Rickman *et al.*, 2017). Dynamic instability is the most important attribute of the microtubules that ultimately functions to provide the forces needed for the cellular functions. Since microtubule dynamics are stochastic events, exact structure and dynamics of the microtubule end, prior to the catastrophe, is vaguely understood. According to the current understanding, the ends are curved during catastrophe with varying degree of curvatures and the end is also tapered with an approximate distance of 124 nm between the longest filament and the fully closed microtubule (Guesdon *et al.*, 2016).

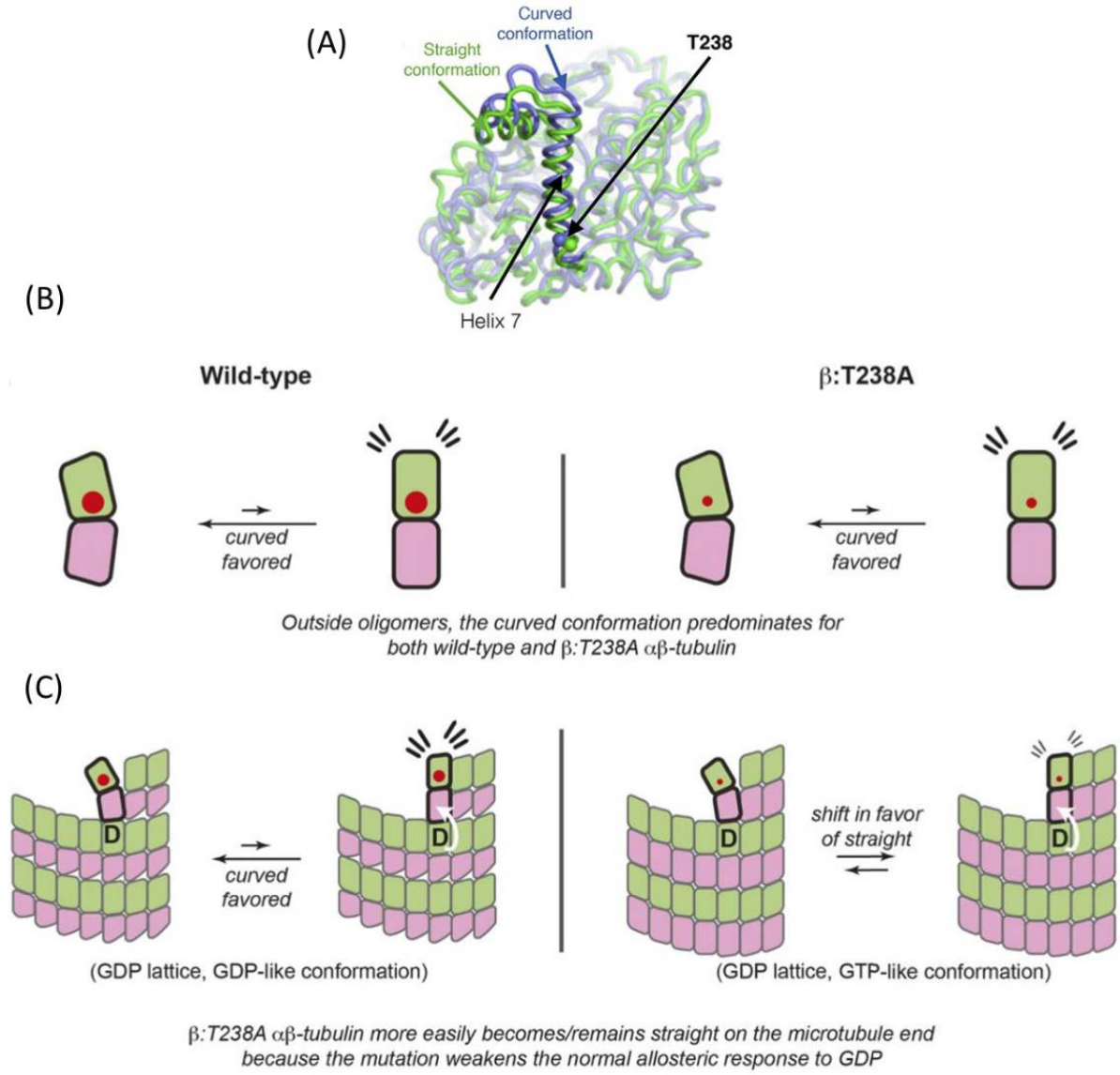

Figure 1.5: *The effect of β:T238A mutation on microtubule dynamics.*

(A) The buried position of the mutation β:T238A located on the H7 region of the β-tubulin that suppresses the nucleotide-dependent conformational changes. The two conformations of β-tubulin: straight (green) and curved (blue). (B) Effect of β:T238A mutation in the tubulin oligomers. It does not display a remarkable difference in the conformation compared to the WT (curved confirmation if preferred). (C) Effect of β:T238A mutation for the subunit in the microtubule conformation. The mutation favours the straight conformation of the subunit independent of the nucleotide status. Adapted from (Geyer et al., 2015).

The catastrophe of the microtubules is regulated by the different types of MAPS that act on the different conformations in dynamic states of the microtubule. From a study carried

out using yeast EB protein, Mal3, it has been shown that an increase in the concentration of EB proteins increases the frequency of catastrophe by decreasing the size of the stabilising cap (Bieling *et al.*, 2007). The conformation preferred by EBs have been investigated by studying the EB protein affinity for polymers containing GTP analogues (Alushin *et al.*, 2014, Maurer *et al.*, 2011). Polymers created with non-hydrolysable GTPγS usually resemble the GDP-Pi bound (compact) state of the microtubule while polymers with guanosine-5′-[(α,β)-methyleno]triphosphate (GMPCPP) resemble the GTP bound (straight) conformation. The higher affinity of EB proteins to microtubules polymerised with GTPγS suggests EB protein binding prefers microtubules with the compact conformation (Maurer *et al.*, 2011). Furthermore, the compact conformation allows EB proteins to position their binding sites properly, thus promoting catastrophe via increasing the GTPase activity.

The allosteric effects of nucleotide state for EB protein binding independent of the conformational change in the microtubule lattice has been tested by analysing the binding affinity of well-studied EB1 with the β-tubulin mutant, β:T238A (Geyer *et al.*, 2015). This β:T238A mutation does not affect GTPase activity and it suppresses the nucleotide-dependent conformational changes when the subunits are bound to the microtubule lattice, thus promoting the lattice to maintain the straight conformation even when in the GDP bound state (Figure 1.5). The increased EB protein binding to the mutant tubulin lattice with GDP provides evidence that GDP could exert an allosteric effect to regulate the frequency of microtubule catastrophe (Geyer *et al.*, 2015).

Rescue of catastrophe, which contributes to the characteristic dynamic instability of the microtubule, is often seen *in vivo* more than *in vitro* (Moriwaki and Goshima, 2016). The rescue also demands energy comparable to nucleation. This is overcome by another family of MAPs called CLASPs which can bind to an intermediate conformation of the peeling protofilaments via a region called TOG domain and facilitate rescue by reducing the energy requirement (Al-Bassam *et al.*, 2010). These recent discoveries (Geyer *et al.*, 2015) demonstrate that in addition to the intrinsic properties and the conserved structural features of the tubulin, the conformation-specific interactions of MAPs play a crucial role in regulating microtubule dynamics.

1.4.3 Microtubule isoforms and post-translational modifications

Microtubules are mosaic noncovalently linked filaments. Microtubule arrays display considerable diversity, and exert different functions in different cells. For instance, neurons contain stable microtubule bundles to promote molecular transport via motor proteins, the mitotic spindle has dynamic filaments to generate force, and the discoid shape of platelet cells are maintained by a microtubule ring arranged underneath the cell membrane. The mosaic nature of microtubules is evident by the presence of different isoforms and the post-translational modifications. There are eight α-tubulins and nine β-tubulins in humans (Ludueña and Banerjee, 2009). The differences in these isotypes are usually located on the last few residues (~15 amino acids) of the C-terminal tail. The exact stoichiometry and the expression level of these isotypes varies depending on the cell type and the development stage of the cell. Although the arrangement of these isotypes might act as recognition sites for regulatory protein binding, thus altering the regulation of microtubule dynamics, little is known about the details of these isotypes (Roll-Mecak, 2015).

Additionally, post-translational modifications such as acetylation, tyrosination, detyrosination, glycylation and phosphorylation decorate the microtubule ends which then could act as a recognition site for the cellular effectors (Sirajuddin, Rice and Vale, 2014). All the modifications usually occur at the C-terminal tail region except acetylation which happens at the inner surface (favourably at Lys40 residue) of the microtubule. Furthermore, the post-translational modifications change the electrostatic properties of the microtubule surface, thus regulating their dynamics by facilitating the molecular interactions, such as binding of MAPs and changing the bulk properties of the cytoplasm around them. The type of modification differs depending on the cell type and the function or growth phase of the microtubule within the same cell. For example, the mitotic spindle has three types of microtubules originating from the centrosome. The kinetochore microtubules that attach to a kinetochore of a chromosome are detyrosinated. The aster microtubules that attach to the cell cortex and are oriented away from spindle centre are tyrosinated. The middle polar microtubules that do not attach to chromosomes are detyrosinated, glutamylated and acetylated. These different types of microtubules work together during different phases of mitosis to achieve the correct chromosome segregation. However, cellular regulation mechanisms that drive these selective post-

translational modifications in the microtubules are poorly understood (Song and Brady, 2015, Yu, Garnham and Roll-Mecak, 2015).

1.5 Cell division in bacteria by FtsZ

1.5.1 FtsZ Polymerisation and structure

All major eukaryotic cytoskeleton components have counterparts in the prokaryotic cytoskeleton, and these homologous proteins have been conserved. A main component of the prokaryotic cytoskeleton is the tubulin homologue, FtsZ which can be found in the cytoplasm of bacteria, archaea, mitochondria and chloroplasts (Lowe and Amos, 2000). FtsZ is a GTPase (length of the monomer is 40 Å) which polymerises into protofilaments with a head-to-tail arrangement by hydrolysing the GTP molecule bound to the GTP binding site in the subunit below. The formation of GTP dependent longitudinal interaction formation is quite similar between tubulin and FtsZ. Conserved catalytic amino acid residues N207, D209 and D212 in the bottom surface (T7 region) of the FtsZ subunit are shown to be involved in the conserved GTPase function (Adams and Errington, 2009). The crystal structure of *Methanocaldococcus jannaschii* FtsZ bound to GDP was the first structure resolved of a tubulin superfamily protein. The crystal structure revealed the strong structural homology between FtsZ and tubulin, and clearing the uncertainty due to the weak primary sequence homology. The structure also showed that the pocket formed by the highly conserved T1, T2, T3 and T4 flexible glycine-rich loops on the top surface are directly in contact with the phosphate groups of the GTP molecule in FtsZ and all tubulin superfamily proteins. In FtsZ, GTP hydrolysis has not shown to exert an apparent conformational change in the crystal structure that could trigger depolymerisation (Lowe, 1998). However, recent developments in cryo-EM revealed subtle compaction in the GTP binding pocket when bound to GDP which results in the weakening of the longitudinal interactions (Alushin *et al.*, 2014). While most of the GTP contact regions are located on the N-terminal domain, the globular C-terminal domain covers a larger part of the molecule and plays an important role in FtsZ function. The protruded M-loop region between S7 and H9 in the tubulin C-terminal domain facilitates

microtubule lateral interactions and is quite small in FtsZ (Löwe and Amos, 2017). However, surface loops in the FtsZ C-terminal domain are known to be important in self-association. The FtsZ structure also contains a central helix (H7) that separates the two globular domains, and C-terminal and N-terminal extensions that stick out of the structure. The N-terminal extension (Figure 1.9) is a characteristic feature in FtsZ among other tubulin superfamily proteins (Lowe and Amos, 1998). The function of the N-terminal extension is obscure. C-terminal tail extensions are usually poorly resolved in crystal structures due to high flexibility and lack of tertiary structure. In FtsZ, the C-terminal tail is important for molecular binding such as the proteins that mediate membrane binding. It has been shown that the length of this tail region can vary depending on the type of species, thus acting as a biological spacer when its tethered to the membrane (Osawa and Erickson, 2005).

1.5.2 FtsZ controls prokaryotic cell division

The filaments of the prokaryotic cytoskeleton are usually directly associated with the cell envelope, unlike the long-range internal network of fibres throughout the cell seen in eukaryotes, and these cytoskeletal filaments play an important role in controlling the shape, division and overall structural integrity. FtsZ is essential in the formation of the division ring which forms during cytokinesis in bacteria, archaea, chloroplasts and mitochondria of some protists. FtsZ is the first to localise at the division site, and its protofilaments bundle into a ring-like structure called the “Z ring” which marks the mid-cell position (Figure 1.6) and serves as a scaffold for other division proteins during cell division (Adams and Errington, 2009). Time-lapse imaging of cells expressing FtsZ tagged with Green Fluorescence Protein (GFP-FtsZ) and fluorescence recovery after photobleaching (FRAP) studies, indicate that dynamic assembly and disassembly FtsZ protofilaments provide the constrictive force to foster correct cell division (Anderson *et al*, 2004).

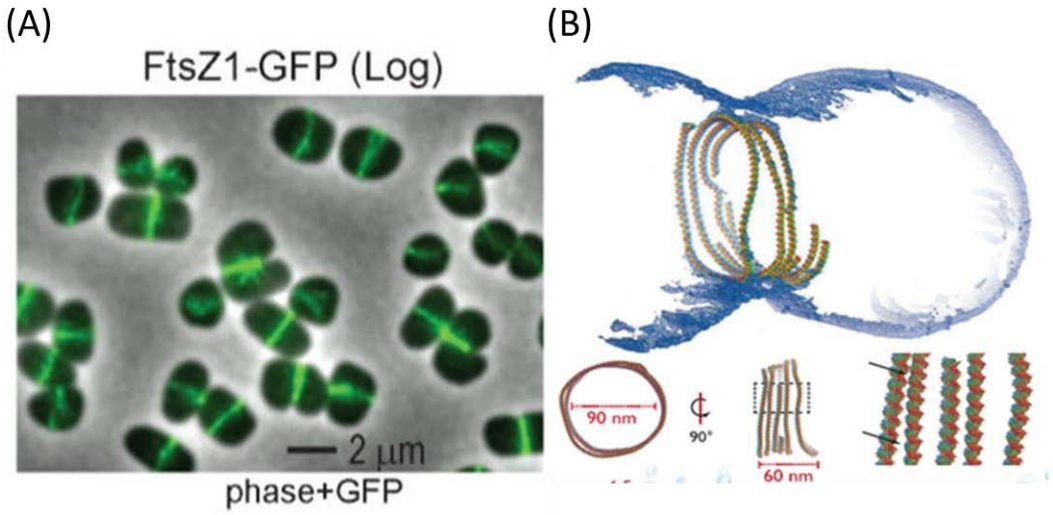

Figure 1.6: *Z ring formation in Haloferax volcanii, the model haloarchaeon used in this study.*

(A)The image shows log-phase cells expressing FtsZ1 tagged with GFP. (B) Sub-atomic model of FtsZ constricting a liposome. The figures below indicate the constricting ring has a 90 nm width and 60 nm thickness. Variability in the inter-protofilament distances of the Z ring is indicated in this model. Taken from (Duggin *et al.*, 2015, Piotr Szwedziak *et al.*, 2014).

In *E. coli*, the polymerisation of FtsZ is regulated by a group of proteins called Zap proteins: Zap A-E. Zap A-D proteins help to stabilise the Z ring to aid cell division, while Zap E destabilises the Z ring to reduce cell division in hostile environments (Marteyn *et al.*, 2014).

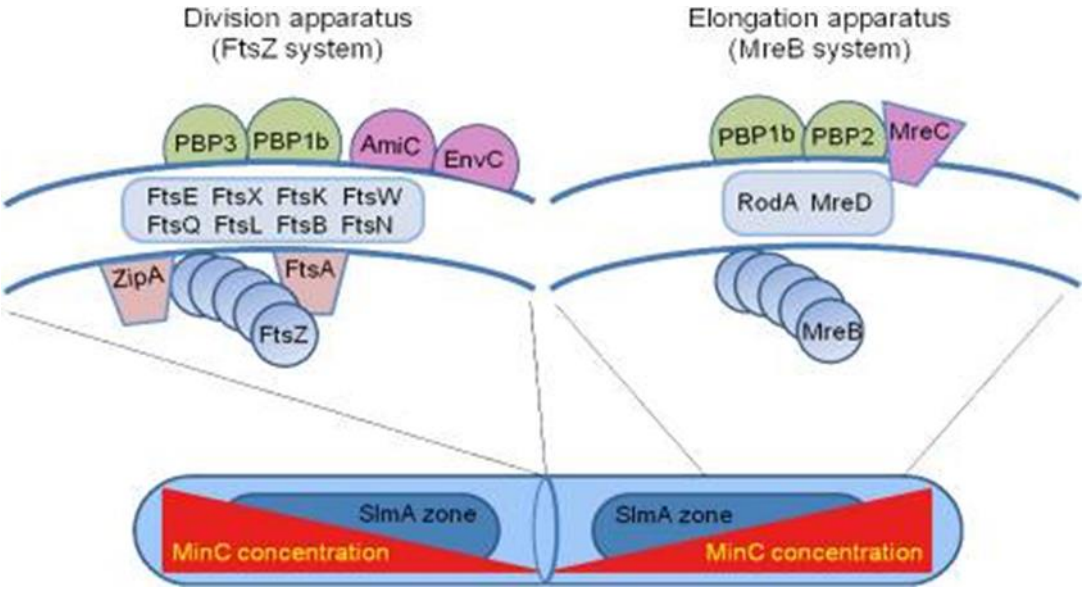

Figure 1.7: *An overview of the cell division (left) apparatus and the cell elongation (right) apparatus.*

Schematic showing the proteins associated with FtsZ and MreB to tether them into the plasma membrane and exert their activity. The bottom figure indicates the distribution of division and elongation regulatory proteins along with the cell. Adapted from (Young, 2010).

FtsZ protofilaments are tethered to the membrane at the division site through actin-like ATPase protein FtsA and ZipA (Adams and Errington, 2009). ZipA also helps to stabilise the Z ring. FtsA promotes the recruitment of other cell division associated proteins FtsK and FtsW at the divisome (Figure 1.7) (Wang and Lutkenhaus, 1998, Vishniakov and Borkhsenius, 2007). FtsK, which carries an N-terminal membrane domain and a large C-terminal cytoplasmic domain is a DNA translocase that helps in correct chromosomal segregation before cell division. FtsW is a peptidoglycan polymerase which promotes the division septum formation when in contact with the penicillin-binding protein III (Fraipont *et al.*, 2011). Following the localisation of FtsW, the proteins that are involved in chaperoning and regulating the division machinery assembly such as FtsQ and FtsL are recruited at the Z ring (Schmidt *et al.*, 2004). Finally, the transpeptidases, FtsI and FtsN, are recruited to facilitate peptidoglycan synthesis at the septum (Schmidt *et al.*, 2004). All these accessory proteins, FtsQ, FtsL, FtsI and FtsN are periplasmic proteins that are anchored to the plasma membrane, and their functions are only vaguely understood. Unlike these accessory proteins, FtsZ is the most conserved protein in prokaryotes and found to be present in some species that lack a cell wall. Therefore, the

poorly understood accessory proteins are assumed to be involved in septal peptidoglycan synthesis rather than cytokinesis. Furthermore, in vitro studies have demonstrated that FtsZ is capable of exerting a constrictive force on liposomes (Figure 1.6) independent of other cytoplasmic and periplasmic proteins associated with the divisome (Chen and Erickson, 2005). Although our understanding of bacterial cell division by FtsZ has vastly improved over the last few years, the constriction initiation and disassembly of the Z ring during the division is still abstruse.

Generally, the regulation of cell division and cell shape are closely interconnected. Under normal conditions, the divisome is assembled after the cell reaches a certain size, thereby resulting in homogeneous cell shapes and sizes in the daughter cells. Mutation in FtsZ which disrupts the cell division process causes unusual filamentous growth or lethal effects in bacteria (Addinall, Erfei and Lutkenhaus, 1996). MreB and Min CDE are considered as main spatial regulators of prokaryotic cell division (B D Corbin, Yu and Margolin, 2002). MreB, which is the eukaryotic actin homologue, controls elongation of the cell envelope. During this process, long MreB fibrils enfold around the inner lining of the envelope of rod-shaped bacteria to aid cell wall synthesis (Mauriello *et al.*, 2010). Cell length is determined by the frequency of cell division. Z ring formation is regulated by molecular processes that inhibit FtsZ assembly. For instance, the Min system in bacterial cells ensures that division occurs only at mid-cell by creating a MinC (MinC is a negative regulator of FtsZ ring assembly) gradient along the cell. This is achieved by the other two Min proteins MinD and MinE. MinC concentration ascends from the centre to poles of the cells, thereby facilitating the correct positioning of the Z ring at mid-cell. MinD oscillates from one pole to the other of the cell, preventing the membrane interaction of FtsZ via FtsA at cell poles. MinE oscillates at the centre of the cell to repel MinC and D, thereby preventing cell division before the cell reaches its full growth stage (Rothfield, Taghbalout and Shih, 2005). However, the poor conservation of *minE* suggests there might be other topological regulators that co-exist that help to ensure correct Z ring positioning (Nakanishi *et al.*, 2009).

Nucleoid occlusion is another mechanism that regulates cell division. This happens via proteins called SlmA (*E. coli*) (Bernhardt and de Boer, 2005) and Noc (*Bacillus subtilis*), which inhibit division in regions of the cell containing DNA, thereby ensuring that cell division occurs between chromosomes (nucleoids) after they have replicated and segregated completely (Wu and Errington, 2004). Although the appearance of the Z ring

coincides with the termination of DNA replication, no direct signal for Z ring assembly has been identified so far. However, some studies have demonstrated FtsZ assembly can occur before nucleoid separation or when there is no nucleoid or directly over the nucleoid (Rodrigues and Harry, 2012). These observations suggest that both the nucleoid occlusion and Min system collectively decide the correct positioning of the Z ring. Although the exact Z ring architecture is poorly understood, its structural integrity is important for correct cell division. For example, a study of the temperature-sensitive FtsZ mutant strain *ftsZ26* of *E. coli* showed that it produced a spiral FtsZ assembly and a corresponding spiral constriction of cells (Addinall and Lutkenhaus, 1996).

1.6 Tubulins in archaea

Archaea possesses many divergent tubulin superfamily proteins and often contain multiple homologues of these proteins. Some archaea do not have any tubulin present in them. The following sections introduce the important features of archaea and the function of diverse tubulin superfamily members in them.

1.6.1 Archaea

Archaea are single-cell microorganisms, which can be found in a broad range of habitats, including harsh environmental conditions such as hypersaline lakes (Charlesworth and Burns, 2015). They are thought to be related to some of the earliest life on earth. Archaea were classified with bacteria until it was realised that they differed fundamentally, in features such as the absence of peptidoglycan layer in cell envelopes and the sequences of the synthetic machinery of the cell—DNA, RNA and protein polymerases (Albers and Meyer, 2011, Lindås *et al.*, 2008). Even though the chromosomes of Archaea are circular dsDNA, like Bacteria, their fundamental processes such as translation and transcription are remarkably similar with eukaryotes. Genome analysis revealed that archaea have several features in common with eukaryotes, thus creating a model organism to explore convoluted eukaryotic systems. Another unique feature that has been identified in archaea is the lipid composition of the plasma membrane that is significantly different from

membrane lipids in eukaryotes and bacteria. In eukaryotes and bacteria, the glycerol head of the phospholipid is bound to an unbranched fatty acid chain through an ester linkage, while in archaeal plasma membrane, branched isoprene chains are linked to glycerol via an ether linkage (Albers and Meyer, 2011). Although there could be a few instances where bacteria and eukaryotes form ether bonds in phospholipids, the stereochemistry/chirality of the archaeal ether bond is unique for archaea. The archaeal ether linkage is with a sn-glycerol-1-phosphate moiety while bacterial ester bond formation occurs with sn-glycerol-3-phosphate (Albers and Meyer, 2011).

Many archaeal species have been identified, which can be classified into five main phylogenetic groups: Nanoarchaeota, Euryarchaeota, Thaumarchaeota, Crenarchaeota and Lokiarchaeota. The present study uses the halophilic archaeal species *Haloferax volcanii* (Phylum Euryarchaeota, Class Halobacteria, Family Haloferacaceae), which is one of the best studied archaeal species, and widely used as a model organism, thus availing its primary biochemical and genomic data. *H. volcanii* have flat plate-shaped cells. However, in some circumstances, they tend to change shape into rods, and the trigger for this metamorphosis is unclear. Some haloarchaea such as *Haloquadratum walsbyi* (Burns *et al.*, 2007, Bolhuis *et al.*, 2006) displays a uniquely thin, square cell shape that is maintained during cell division (Figure 1.8).

Typically, many archaea have a myriad of cell shapes in nature, and the reason behind why such shapes developed is still obscure.

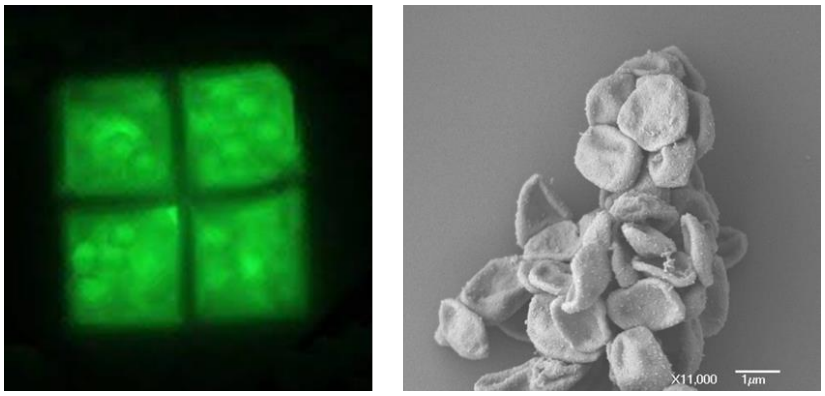

Figure 1.8: *Different cell shapes in haloarchaea.*

The first image shows the dividing cell of Haloquadratum walsbyi which has a unique square shape and the second image shows the pleomorphic flat shape of Haloferax volcanii (Dyall-Smith et al., 2011, H . volcanii image was taken from https://biobabel.wordpress.com/tag/haloferax-volcanii/ [22/08/2019]).

Exploring archaeal cytoskeletons might shed light on finding the reason and underlying mechanisms for these different cell shapes. Archaea also show greater diversity among the most widespread cytoskeletal proteins found in all three domains, including diverse homologues from the actin and tubulin superfamilies (Löwe and Amos, 2017).

1.6.2 FtsZ and divergent tubulin superfamily members in archaea

Archaea display a high diversity of tubulin superfamily proteins, and they have diverse functions as well. The cell division gene *ftsZ* is ubiquitous and highly conserved in bacteria. Cell division of most archaea is also controlled by FtsZ. However, two FtsZ homologues—FtsZ1 and FtsZ2—which localise into the mid cell to form the Z ring (similar to the bacterial FtsZ) can often be noticed in many archaea (Duggin *et al.*, 2015). The studies carried with FtsZs in *H. volcanii* support the hypothesis that FtsZ1 might be important in the initial Z ring formation and FtsZ2 recruitment while FtsZ2 might be playing an important role in exerting the constriction (Duggin unpublished data). Archaea also possess deeply branched tubulin superfamily proteins. For example, some archaea have highly divergent FtsZ-like group 1 proteins (FtsZL1) (Makarova and Koonin, 2010) which have unusually long homologous N-terminal extensions to the core GTP-binding domain (in *Crenarchaeota*). They also have an aberrant domain arrangement where the C-terminal domain is replaced with a large poorly understood domain. The function of FtsZL1 remains obscure. Although FtsZL1 in archaea forms a phylogenetically distinct group, the level of diversity is far higher among FtsZ1 proteins of Bacteria. However, it is distributed among many archaeal species (in *Methanomicrobia*, *Halobacteria* and *Thermococci* Classes). In fact, FtsZL1 has been identified in Crenarchaeota which do not have any other apparent tubulin superfamily member (Natale *et al.*, 2000, Lindas *et al.*, 2008). Cell division in Crenarchaeota is driven by a protein complex homologue of the eukaryotic Endosomal Sorting Complex Required for Transport (ESCRT)-III complex called Cdvb. (ESCRT)-III which is also present in the group *Thaumarchaeota* (Ettema and Bernander, 2009). Some *Thaumarchaeota*, in particular, *Nitrosopumilis maritimus*, have an additional tubulin homologue called artubulins which are phylogenetically related closely to the eukaryotic tubulin, thus predicting the origin of eukaryotic tubulins.

In these species, both (ESCRT)-III and artubulin might work cooperatively to effect cell division.

Archaea also possesses a conserved group of tubulin superfamily proteins called CetZ that belongs to a distinct, separate branch in the family tree. So far, the CetZs have been widely studied in the model haloarchaeon *Haloferax volcanii*, and are described below.

1.6.3 Cell-structure-related euryarchaeota tubulin/FtsZ proteins (CetZ) in *Haloferax volcanii*

Generally, different orthologous groups of FtsZ and tubulin proteins possess a strong amino acid sequence similrity which allows us to categorise them into two distinct groups of proteins in the tubulin superfamily. A recent study on FtsZ homologues in *Pyrococcus kodukuruensis* identified a phylogenetically independent group of tubulin superfamily proteins from archaeal and bacterial FtsZs which were later named as Cell-structure-related *Euryarchaeota* Tubulin/FtsZ homologs, and the CetZs are mainly distributed among *Euryarchaeota* (Chinen *et al.*, 2000). According to multiple sequence alignments, *H. volcanii* possesses eight tubulin superfamily protein homologues, and only two of them show a close sequence similarity with FtsZ. Moreover, these FtsZ homologues, FtsZ1 and FtsZ2, displayed a direct involvement in cell division (Baumann and Jackson, 1996, Hartman *et al.*, 2010, Duggin *et al.*, 2015). The remaining six tubulin superfamily protein homologues in *H. volcanii* shared an unique sequence homology of CetZs (Figure 1.9) (Duggin *et al.*, 2015).

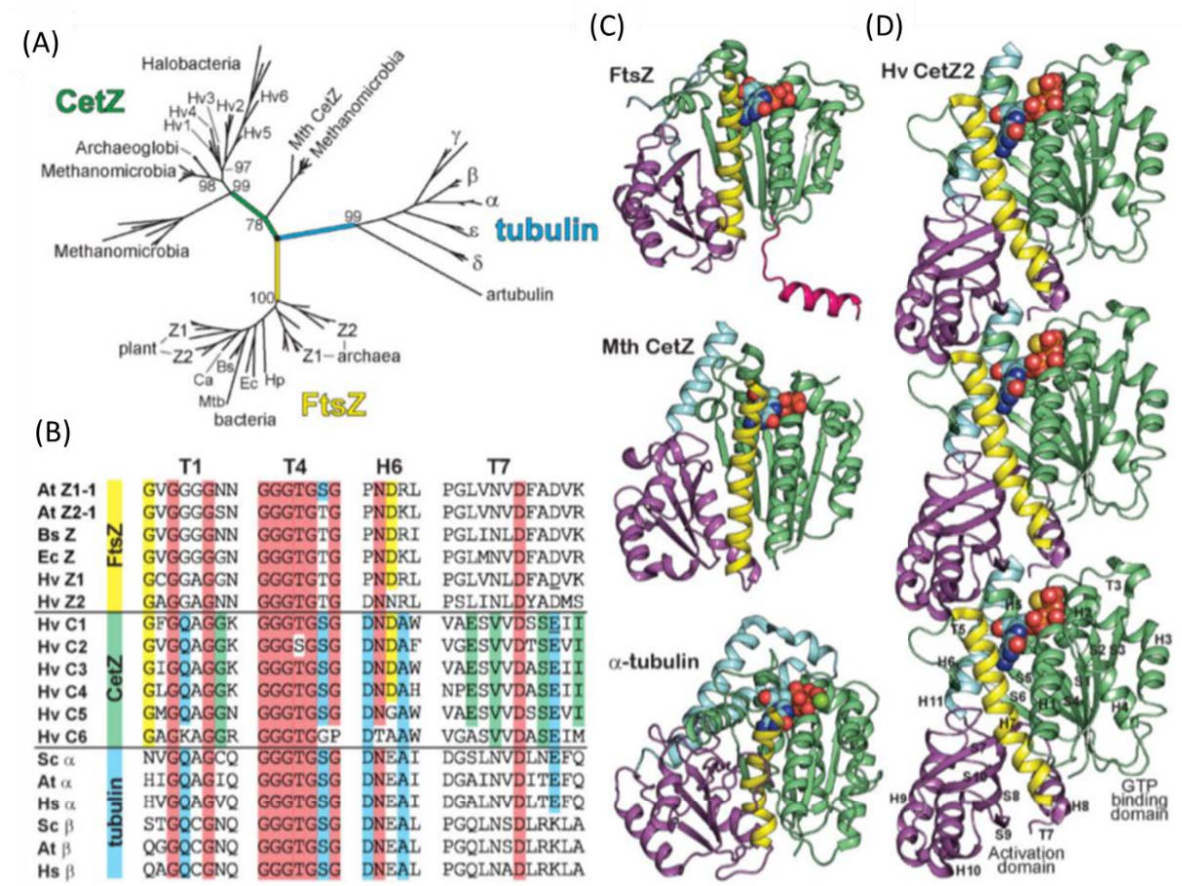

Figure 1.9: *A phylogenetic overview of tubulin superfamily.*

(A) Phylogenetic tree reconstruction of the tubulin superfamily based on protein sequences. Brach length indicates the degree of difference of protein sequences, with major groups labelled. (B) Amino-acid sequence alignments at the GTPase active site, comparing sequence conservation of CetZs (green) with FtsZ (yellow) and tubulins (blue). Universal conservation is indicated by red shading. (C) Structural comparison between different tubulin/FtsZ superfamily proteins; FtsZ, MthCetZ and α-tubulin (D) Protofilament of CetZ2-GTP. C-terminal α helix (H11) of CetZ2 structure is significantly analogous to that of α-tubulin unlike disordered C-terminal of FtsZ. Taken from (Duggin et al., 2015).

In addition to the distinctive amino acids in the CetZs, they also share a common structural and primary amino acid sequence with both tubulin and FtsZ independently (Figure 1.9). Concerning the basic protein fold, the crystal structure resolved for the CetZ1 monomer in the model archaeon *H. volcanii* revealed a remarkable similarity to FtsZ. (overall Cα r.m.s.d 2.9 Å for FtsZ and CetZ1). For instance, the conformation of the T3 loop, which is the primary contact of the γ- phosphate of GTP in both CetZ1 and CetZ2, is substantially identical to that of FtsZ (Duggin *et al.*, 2015). However, the

primary amino acid sequences in the conserved regions reveal that CetZs are more comparable with tubulins than FtsZs. For instance, the conserved aspartate in the "T7 loop" of FtsZ that activates the γ- phosphate by a nucleophilic attack is glutamate in both tubulin and CetZ. Also, the T1 apex which interacts with T7 loop in tubulin has a glutamine residue in both tubulin and CetZ while this is absent in FtsZ. Moreover, the sixth position of the tubulin/FtsZ "signature" motif GGGTGS/TG is serine in both tubulins and CetZ proteins while it is a threonine in FtsZ (Duggin *et al.*, 2015). The guanine recognition site in the H7 loop contains asparagine in both CetZ and tubulin while it is an aspartate in FtsZ (Duggin *et al.*, 2015). The greater sequence homology between CetZs and tubulins makes them attractive to study in Archaea because they represent simpler models to understand the more eukaryotic cytoskeleton.

Although tubulins have a diverse range of functions, the primary function of all tubulin superfamily proteins that have been analysed so far is cell division.

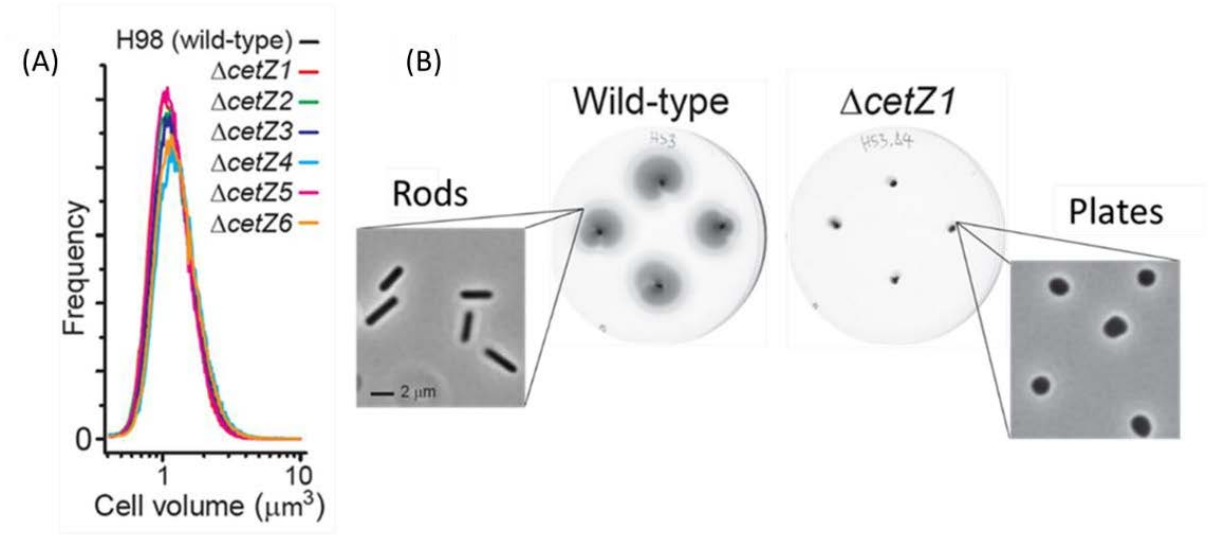

Figure 1.10: *Evidence indicating CetZ1 is not essential for cell division, but is needed for plate shape to rod shape.*

(A) Comparison of cell volumes of all cetZ knockouts in mid-log phase to the cell volume of WT. (B) Motility comparison between WT and cetZ1 knockout. Phase-contrast images show the cell shapes of cells in the motile halo. Taken from (Iain G Duggin *et al.*, 2015).

The comparable cell volume (Figure 1.10) changes during systematic testing of *cetZ* gene knockouts suggests that CetZ proteins are not essential in cell division. Interestingly,

knocking out the *cetZ1* gene blocked the ability of cells to change shape from fllat plates to rods, thereby inhibiting *H. volcanii* swimming motility (Figure 1.10). Although *H. volcanii* can exhibit different types of motility behaviour, rods are the fast swimmers (Duggin *et al.*, 2015).

The cytoskeleton of a cell typically acts as a force generator to maintain the vast range of structural dynamics such as cell motility and division. Therefore, dynamic localisation is a signature attribute of the cytoskeleton proteins that have been investigated so far.

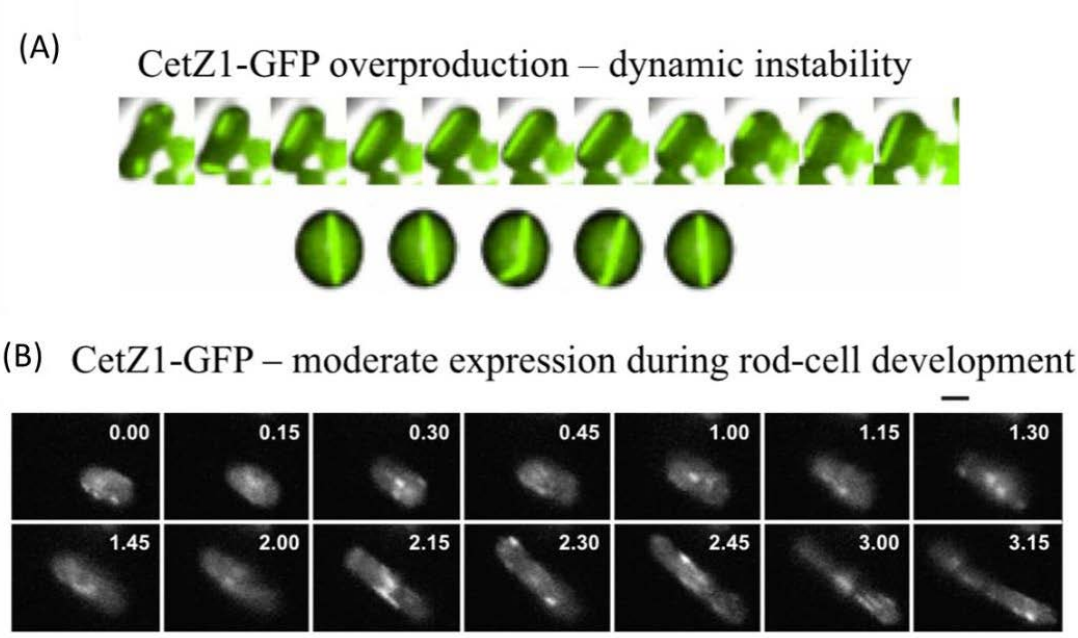

Figure 1.11: *Current evidence that displays CetZ1 cytoskeletal dynamics in H. volcaii.*

These localisation studies were carried out by expressing partially functional CetZ1-GFP fusion in a WT H26 background. (A) Formation of a dynamic filament structure during CetZ1-GFP overproduction. (B) The localisation dynamics of CetZ1-GFP during a plate to rod shape transition. Taken from (Liao et al., 2018).

During *H. volcanii* shape transition, CetZ1 tagged with Green Fluorescence Protein (GFP) expressed in a WT background displayed a highly dynamic localisation implicating an important cytoskeletal role of CetZ1 in modulating the cell shape (Figure 1.11). Further analysis revealed expressing a GTPase-defective CetZ1 (CetZ1.E218A) failed in both exerting motility and rod cell development. The mutation instead resulted in jagged and irregular-shaped cells. This indicates having a GTPase dependent

polymerisation and depolymerisation is essential for the rod shape development; thus, the increase in the cellular motility of *H. volcanii*. Moreover, supporting that CetZ1 can form dynamic cytoskeletal structures, overexpression of CetZ1.GFP in a WT background displayed a formation and retraction (Figure 1.11) of protein filaments, which resembles the typical dynamic instability of a cytoskeletal structure. However, this CetZ1.GFP fusion was only partially functional, as the expression of this fusion protein was unable to induce rod formation in the WT background, limiting its use in further characterisation of CetZ1 function (Duggin *et al.*, 2015). The exact purpose of the remaining CetZ paralogues in *H. volcanii* is yet unclear. Although inhibition of GTPase activity in CetZ2 resulted in a similar morphological response as the CetZ1.E218A, no notable morphological or growth effects have been observed in strains carrying mutations in the other CetZ paralogues. Furthermore, the low level of CetZ2 protein expression inside cells suggests this protein has a redundant function in cell shape control.

In eukaryotes, functional tubulin exists in the form of microtubules, while the prokaryotic tubulin homologue FtsZ is unable to form an ordered quaternary structure.

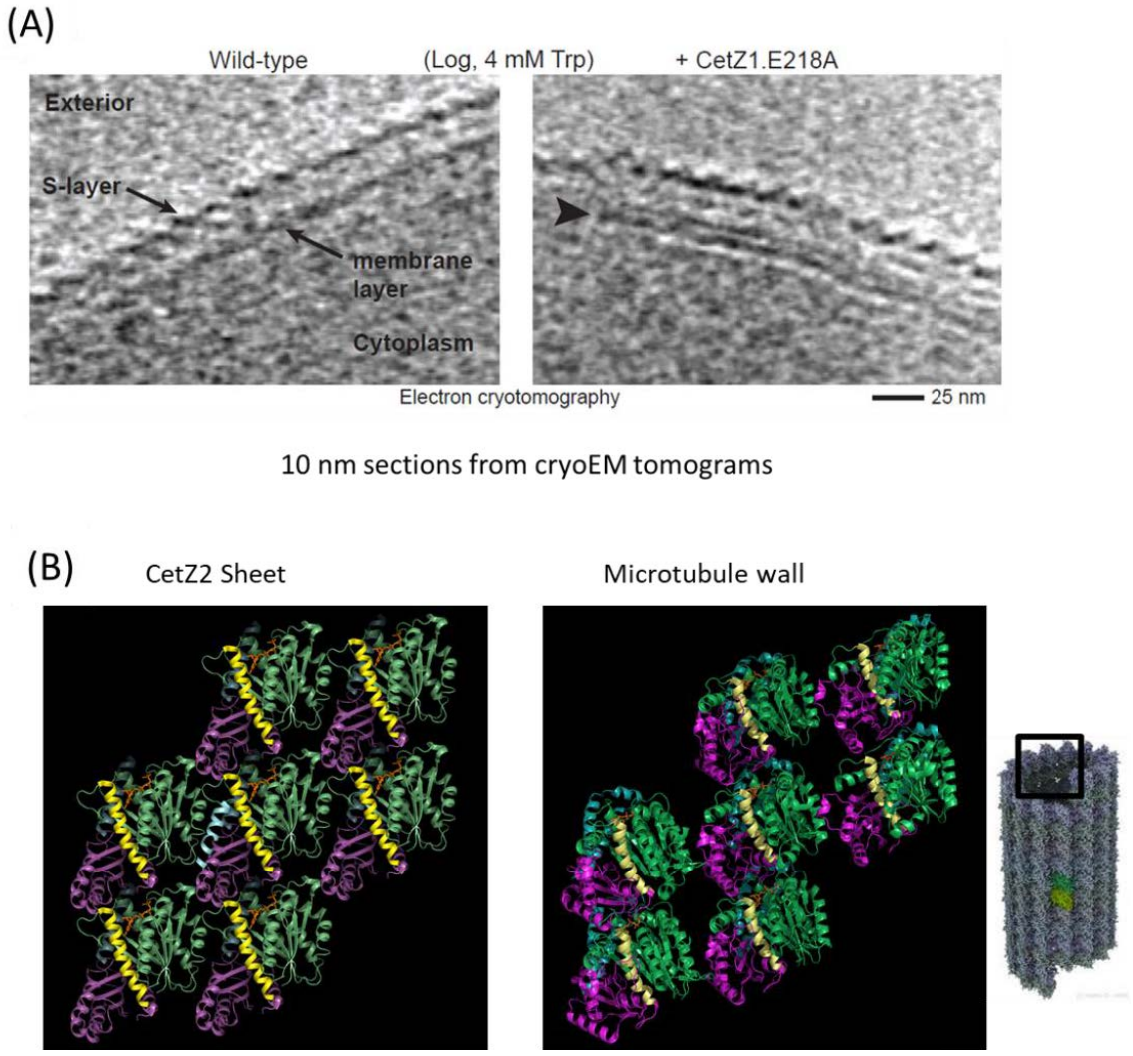

Figure 1.12: *Evidence showing CetZ1 can assemble into a quaternary structure.*

(A) A cryo EM tomogram showing formation of an additional layer beneath the cell membrane when CetZ1.E218A was overexpressed. (B) A comparison of the subunit arrangement of CetZ2 sheet-like crystal structure and the crystal structure of the microtubule wall. Taken from (Duggin *et al.*, 2015, *Nogales et al., 1999).*

Formation of a possible higher order cytoskeletal structure was evident in CetZ1 from an electron microscopic analysis which indicated an additional layer near the plasma membrane as a 300 nm patch during the overexpression of the GTPase mutant CetZ1.E218A (Figure 1.12). Furthermore, CetZ2, the closest paralogue of CetZ1 (shares 51% sequence similarity), resolved as a sheet-like structure which resembles the subunit arrangement in the microtubule wall (Figure 1.12). However, further investigations by screening the functional importance of lateral interactions and cryo-EM imaging of CetZ1 polymers are needed to confirm these initial observations. Although there is a preliminary

understanding of CetZ1 function, the insights of structure-function relationships of CetZ1 protein remain as predictions based on what is known about tubulin and FtsZ. Furthermore, functional aspects of CetZ1 such as the cues that trigger the CetZ1 function and its molecular interactions are vaguely understood.

1.7 Aims of the present study

In the present study, primarily the following questions were addressed.

1) What are the environmental signals that trigger CetZ1 dependent morphogenesis?
2) What are the important regions in the CetZ1 structure that determine its function in modulating the cell shape?

Furthermore, the currently available motility assay is not the best method to measure CetZ1 function, as the cell shape can be highly variable depending on the sample collection position in the motile halo. Addressing the first question provided additional functional assays that could be used to measure CetZ1 function. In particular, this thesis describes the culture conditions that develop CetZ1 dependent rods in a liquid medium, which improved the ability to quantify CetZ1 function (Chapter 3). Moreover, efforts were taken to overcome the current limitations, such as the inability of the current *cetZ1* knockout strain to rescue *cetZ1* function and the limited functionality of the CetZ1-GFP fusion to quantify CetZ1 function, and the results will be described in this thesis (Chapter 4). Finally, the data for the experiments carried out to investigate the important structural features and interactions via site-directed mutagenesis will be presented (Chapter 5 and 6). As reviewed in the above introductory section, prokaryotic and eukaryotic tubulin homologues are vastly different in their higher-order structures, mechanism of action and regulation. The structural characterisation present in this study will provide the foundation to understand the intermediate stages that occurred during the evolution of tubulin superfamily proteins.

CHAPTER 2
GENERAL MATERIALS AND METHODS

2.1 Bacterial strains and plasmids

Tables 2.1, 2.3 and 2.3 list the general *E. coli* strains, archaeal strains, and plasmids used in this work respectively (archaeal strains and plasmids produced in this work will be described where appropriate). All *E. coli* strains and archaeal strains were stored as stationary phase cultures, with 20% (v/v) glycerol at -80ºC. Archaeal strains harbouring plasmids were stored with 20% (v/v) glycerol at -80ºC.

Table 2.1 General Bacterial Strains Used in the Present Work

Species	Strain	Relevant genotype	Reference/Source
E. coli	C2925	K12 mutant strain without (*dam- dcm-*) methyltransferase	NEB
E. coli	C41(DE3)	*E. coli B F- ompT gal dcm hsdSB* (*rB- mB-*)(DE3)	Jan Lowe MRC Cambridge UK
E. coli	DH5α	*fhuA2* Δ(*argF-lacZ*)*U169 phoA glnV44* ϕ80 Δ(*lacZ*)M15 *gyrA96 recA1relA1 endA1 thi-1 hsdR17*	Invitrogen

Table 2.2 General Archaea Strains Used in the Present Work

Species	Strain	Relevant genotype	Reference/Source
Haloferax volcanii	H26	Δ*pyrE2*	T. Allers
Haloferax volcanii	H98	Δ*pyrE2* Δ*hdrB*	T. Allers
Haloferax volcanii	ID59	(H98) Δ*cetZ1*	Duggin *et al.,* 2015

Table 2.3 General Plasmids Used in This Work

Plasmid	Relevant features	Reference/Source
pTA131	pBluescript II containing *pyrE2* under ferredoxin promoter. *Amp* resistance gene	T. Allers
pTA962	Expression vector. *tnaA* promoter. *pyrE2*, *hdrB* markers and *Amp* resistance gene	T. Allers
pIDJL40	GFP-fusion expression vector based on pTA962	Duggin *et al*., 2015
pHis17	Protein overexpression vector. T7 promoter, *Amp* resistance gene	Cordell and Löwe, 2001
pUC57	Unspecified promoter. Contains Amp resistance gene.	GenScript

2.2 Growth media

Bacterial and archaeal growth media used in this study are listed in Tables 2.4 and 2.5 respectively. All heat-stable media were sterilised by autoclaving, and heat-sensitive media were sterilised by 0.2 μm membrane filtration*.

Table 2.4 Commonly Used Bacterial Growth Media

Medium	Constituents
2TY	1.6% (w/v) tryptone, 1% (w/v) yeast extract, 0.5% (w/v) NaCl
LB	25 g of LB broth base (1% (w/v) tryptone, 0.5% (w/v) yeast extract, 0.05% (w/v) NaCl) in 1 L of MQW
LB agar	25 g of LB broth in 1 L of MQW, 1.5% (w/v) bacteriological agar
SOC	2 % (w/v) Tryptone, 0.5 % (w/v) Yeast Extract, 10 mM NaCl, 2.5 mM KCl, 10 mM $MgCl_2$. Following was added after autoclaving 20 mM Glucose in MQW

Table 2.5 Commonly Used Archaea Growth Media

Medium	Constituents
30% BSW	24% (w/v) NaCl, 3% (w/v) $MgCl_2.6H_2O$, 3.5% (w/v) $MgSO_4.7H_2O$, 0.7% (w/v) KCl, 0.02 M Tris-Cl (pH7.4), 0.005M $CaCl_2$
100x Trace elements solution (TE)	EDTA 0.5% (w/v), 4.9 mmol $FeCl_3$, 0.37 mmol $ZnCl_2$, 0.074 mmol $CuCl_2$, 0.077 mmol $CoCl_2$, 0.16 mmol H_3BO_3, 12.7 mmol $MnCl_2$, 0.065 mmol $NiSO_4$, 0.041 mmol $Na_2MoO_4.2H_2O$
1000x vitamins solution (vitamins)	0.1% (w/v) Thiamine, 0.01% (w/v) Biotin
HvCab	60% (v/v) 30%BSW, 0.5% (w/v) Casamino acid (CAA), 1% (v/v). Following were added after autoclaving. 100x Trace element solution, 0.1% (v/v) 1000x vitamins solution, pH 7.4
HvYPC	60% (v/v) 30%BSW, 0.1% (w/v) Casamino acid, 0.5% (w/v) Yeast extract, 0.1% (w/v) Peptone, pH 7.4
Regeneration solution	60% (v/v) 30%BSW, 0.1% (w/v) Casamino acid, 0.5% (w/v) Yeast extract, 0.1% (w/v) Peptone, 15% (w/v) Sucrose, pH 7.4
Spheroplast dilution solution	76% (v/v) 30% BSW, 15% (w/v) Sucrose
Transformants dilution solution	60% (v/v) 30% BSW, 15% (w/v) Sucrose

2.3 Chemicals, reagents and solutions

Most chemicals and reagents used in this work were analytical reagent (AR) grade. These chemicals and the companies they were obtained from are listed in table 2.6. Commonly used aqueous buffers and solutions in this work are listed below in Table 2.7.

Table 2.6 Commonly Used Chemicals in the Present Work

Chemical	Source
Acrylamide	GE Healthcare, Sweden
Agarose	Bioline, Australia
Ampicillin	Genlantis, USA
Bio-Rad Pre-Stained Protein Standard	Bio-Rad, USA
Betaine	Sigma-Aldrich, USA
Chemiluminescence Kit	Thermo-Fischer Scientific, USA
Coomassie Briliant Blue R-250	Sigma-Aldrich, USA
Difco^{TM} LB Broth Base (Luria-Bertani)	Thermo-Fischer Scientific, USA
DMSO	New England Biolabs, UK
Gel-Red	Biotinum
Glycerol	Sigma-Aldrich, USA
GTP	Sigma-Aldrich, USA
Oxoid^{TM} Agar (Bacteriological Agar No1)	Thermo-Fischer Scientific, USA
Trichloroacetic acid	Sigma-Aldrich, USA
Tween 20	Sigma-Aldrich, USA

Table 2.7 Buffers and General Solutions Used in This Work

Buffer/Solution	Constituents
1x PBS	150 mM potassium phosphate, 50 mM Tris-Cl, pH 7.4
4 x SDS-PAGE loading buffer (SDS-LB)	250 mM Tris-Cl, 8% (w/v) SDS, 40% (v/v) Glycerol, 20% (v/v) 2-β Mercaptoethanol, 0.4% (w/v) Bromophenol Blue, pH 6.8
Blocking solution	5% (w/v) Diploma skim milk powder in TBST
Buffered Spheroplasting solution	1M NaCl, 27 mM KCl, 50mM Tris.HCl, 15% (w/v) Sucrose, pH 8.5
Coomassie Destain	20% (v/v) Ethanol, 10% (v/v) Acetic acid
Coomassie Stain	50% (v/v) Ethanol, 10% (v/v) Acetic acid, 0.5% (w/v) Coomassie brilliant Blue R
Ponceau Stain	0.1% (w/v) Ponceau, 5% (v/v) Acetic acid
SDS-PAGE Running Buffer	25 mM Tris, 190 mM Glycine, 0.1% (w/v) SDS, pH 8.3
TAE	40 mM Tris-Cl, 20 mM acetate, 1 mM EDTA, pH 8.6
TB	1 mM EDTA, 183 mM KCl, 47 mM NaCl, 1mM Phenylmethylsulfonyl fluoride, 10 mM Tris-Cl, pH6.8
TBE	89 mM Tris-Cl, 89 mM boric acid, 2.5 mM EDTA, pH 8.3
TBST	150 mM NaCl, 50 mM Tris-Cl 0.01% (v/v) Tween 20, pH 7.4
Unbuffered Spheroplasting solution	1 M NaCl, 27 mM KCl, 15% (w/v) Sucrose, pH 7.5
Western Blot Transfer Solution	50 mM Tris, 384 mM Glycine, 20% (v/v) Methanol

2.4 Growth conditions and preparation of *E. coli* cells

2.4.1 Normal growth conditions for *E. coli*

E. coli strains (Table 2.1) were cultured by streaking a loop full of bacteria from a frozen glycerol stock on to LB agar (Table 2.4) (with appropriate antibiotics) and incubated overnight at 37°C. A single colony from the above agar plate was used to inoculate LB (Table 2.3) broth (with appropriate antibiotics). This liquid culture was then incubated at 37°C with shaking (150 rpm).

2.4.2 Preparing chemically competent cells of *E. coli*

The desired *E. coli* culture (Table 2.1) was grown overnight as outlined in 2.4.1. This culture was used to inoculate a fresh sterile SOB (Table 2.3) medium at A (600 nm) = 0.0025 at 18ºC for 24 h with 200-250 rpm shaking. At A (600 nm) ≈ 0.6, the cells were pelleted (3000 rpm, 10 min) at 4ºC. Then the cells were gently resuspended in $1/6^{th}$ of the initial volume of ice-cold TB. The resuspended cells were incubated on ice for 10 mins with gentle swirling. The cells were pelleted again at 4ºC as mentioned above. The cells were resuspended in $1/6^{th}$ of the initial volume of ice-cold 7% (v/v) DMSO in TB and incubated on ice for 10 min. The cell suspension was aliquoted into pre-chilled sterile tubes and frozen immediately by throwing into a liquid nitrogen bath. These tubes were then stored at -80ºC.

2.4.3 Preparing electrocompetent cells of *E. coli*

The desired *E. coli* strain (Table 2.1) was grown up to mid-log phase (A (600 nm) 0.5-1) as outlined in 2.4.1. Cells were pelleted at 6000 rpm for 15 min at 4 ºC. Then the cells were washed by resuspending them in an equal volume of sterile water and centrifuged as in step 1. This washing step was repeated 2 more times with ½ the initial volume of sterile water and 1/50th of the initial volume of 10% (v/v) glycerol in sterile water,

respectively. Cells resuspended in 10% (v/v) glycerol were aliquoted and stored at -80ºC.

2.5 Transformation of *E. coli*

Negative controls without DNA in the reaction mixture were treated identically in the below protocols.

2.5.1 *E. coli* transformation by heat shock

Plasmid DNA (1 -5 µl) was mixed with pre-chilled chemically competent *E. coli* cells (50 µl) and incubated the mix on ice for 30 min. These cells were heat-shocked by placing in a 42ºC heat block for exactly 1 min, then cells were put back on the ice for 2 min. SOC (0.9 ml) (Table 2.3) was added and the mixture incubated at 37ºC for 60 min with shaking (200 rpm). 0.1 ml of this culture was spread onto a LB agar (Table 2.3) plate (with appropriate antibiotics) and incubated at 37ºC overnight.

2.5.2 *E. coli* transformation by electroporation

Pre-chilled electrocompetent cells (40 µl) were mixed with 1-2 µl of plasmid DNA in a low ionic strength buffer. The mix was kept on ice for 1 min. Then this was transferred into a cold 0.2 cm electroporation cuvette. A pulse of 12.5 kV/cm with a time constant of 4.5-5 msec was applied (The pulse generator was set to the 25 µF capacitors, 2.5 kV and 200 Ω). SOC (1 ml) (Table 2.3) was added immediately and the electroporated cell suspension was transferred to a different tube to incubate at 37ºC for 1 h with shaking (200 rpm). Each cell suspension (0.1 ml) was spread onto a LB agar (Table 2.3) plate with appropriate antibiotics.

2.6 General growth conditions for *Haloferax volcanii*

H. volcanii strains (Table 2.2) were cultured by streaking a loop full of archaea from a frozen glycerol stock on to Hv-YPC agar (Table 2.5) (with appropriate nutrient supplements) and incubated 3-5 days at 45°C. A single colony from the above agar plate was used to inoculate Hv-YPC broth (Table 2.5) (with appropriate nutrient supplements). This liquid culture was then incubated at 45°C with shaking (150 rpm) (Robinson *et al.*, 2005).

.

2.7 *Haloferax volcanii* transformation

H. volcanii was grown as outlined in 2.6 overnight until the OD (600 nm) reached 0.2-1.0 (10 ml culture was used for 4 transformations). The 10 ml culture was centrifuged at 6000 rpm for 8 min at R.T. The pellet was gently resuspended in 2 ml of buffered spheroplasting solution (Table 2.7) and centrifuged at 6000 rpm for 8 min at R.T. The pellet was gently resuspended in 800 µl of buffered spheroplasting solution (Table 2.7). This cell suspension (200 µl/ single transformation) was added to a tube containing 20 µl of 0.5 M EDTA, pH 8 and mixed immediately by inverting the tube several times. The mixture was left at R.T for 10 min. Meanwhile, DNA was prepared by mixing 10 µl (≈1 µg) of unmethylated plasmid DNA, 15 µl of unbuffered spheroplasting solution (Table 2.7) and 5 µl of 0.5 M EDTA (pH 8). After 10 min, the above DNA preparation was mixed gently with the spheroplasts and incubated at R.T for 5 min. After 5 mins, 250 µl of 60% (v/v) PEG600 in unbuffered spheroplasting solution (Table 2.7) was added to each transformation reaction and mixed immediately by gently shaking the tube horizontally. This was incubated at R.T for 30 min. Spheroplast dilution solution (1.5 ml) (Table 2.5) was added and centrifuged at 6000 rpm for 8 min at R.T. The pellet was resuspended in 1 ml of regeneration solution (Table 2.5) and the tubes were left undisturbed at 45ºC for 1 h. Then the pellet was resuspended gently and returned to incubation at 45ºC for further 4 h, with shaking at 200 rpm. After 4 h, the cells were pelleted at 6000 rpm for 8 min at R.T and resuspended in 1 ml of transformant dilution solution (Table 2.5). The cell suspension (100 µl) was spread on to an agar plate with the

appropriate selective medium. These agar plates were incubated at 45ºC inside a plastic bag to avoid drying for 3-5 days. Negative controls with no DNA were treated identically.

2.8 Common genetic techniques

2.8.1 Measuring DNA concentration and storage

DNA concentrations were measured by Nanodrop 100 spectrophotometer (Thermo Fisher Scientific, Australia) with transmission at 260 nm. All DNA samples were stored at -20ºC.

2.8.2 Extraction of gDNA and plasmid DNA

gDNA was extracted from a stationary phase *H. volcanii* culture grown as outlined in 2.6 using the Bioline Isolate II genomic DNA preparation kit as per manufacturer's instructions.

A single *E. coli* (Table 2.1) colony resulted from a transformation described in 2.5 was grown in LB broth (Table 2.4) with appropriate antibiotics as outlined in 2.4.1. This culture was then used to extract plasmid DNA as "minipreps" using the Bioline Isolate II plasmid DNA preparation kits (Bioline Isolate II, Australia) as per the manufacturer's instructions for high-copy plasmid isolation.

2.8.3 Demethylation of plasmid DNA

The plasmid of interest was transformed into *E. coli* c2925 (Tale 2.1) as outlined in 2.5.2. A single colony was grown in LB broth (Table 2.4) with appropriate antibiotics as outlined in 2.4.1. This culture was then used to make a "miniprep" as described in 2.8.2.

2.8.4 Agarose gel electrophoresis

Generally, 1% agarose gels with TBE (Table 2.7) were used in this study except during DNA gel purification (0.7% (w/v) agarose gel with TAE (Table 2.7) was used). Gels were pre-stained by adding 0.5 µl of Gel Red or Ethidium Bromide per 50 ml of agarose solution and cast on a horizontal wide "mini gel" apparatus (8.0 × 13.5 cm; 60 ml gel) or a standard gel apparatus (13.5 × 14.5 cm; 100 mL gel). DNA samples (~50 ng) containing 1x loading buffer (New England Biolabs) were loaded into the wells and run at 100 V for 60 min in an electrophoresis chamber containing TBE (Table 2.7). During DNA gel purification, the gel was run at 60 V for 2 h in TAE buffer (Table 2.7). These gels were visualised via UV light (254 nm) using a transilluminator (Ingenius3; Syngene) and imaged using a charge-coupled device camera (Synoptics CAM-FLXCM; Syngene). In DNA gel purification, the correct band was cut from the gel and the DNA was isolated using Bioline Isolate II PCR clean up kit as per the manufacturer's instructions.

2.8.5 Polymerase chain reaction (PCR)

PCR was mainly used to amplify genes of interest from genomic DNA for subsequent cloning and to confirm gene is knockouts. The primers were purchased as lyophilised single-stranded oligonucleotides by Macrogen and Integrated DNA Technologies (IDT). Primers were prepared by dissolving them in x1 TE buffer to a final concentration of 100 µM. The sequences of the primers will be indicated in relevant chapters. In this work, both Phusion and Q5 High-Fidelity (HF) DNA Polymerases (New England Biolabs) were used depending on the reaction efficiency for a given enzyme. The reactions were prepared on ice and carried out as per the manufacturer's (New England Biolabs) instructions specified under each polymerase.

When using Phusion High-Fidelity DNA Polymerase, reaction mixtures (50 µl total volume with nuclease-free water) were prepared containing 1x Phusion GC buffer, 200 µM dNTPs, 0.5 µM reaction specific forward primer, 0.5 µM reaction specific reverse primer, ~50 ng genomic DNA (from 2.8.2), 1 M Betaine and 1 unit of Phusion HF DNA Polymerase. The reactions were subjected to following temperature cycle using a thermal cycler: initial denaturation at 98 ^{o}C for 30 s, then 30 cycles with 98 ^{o}C for 10 s, annealing

temperature (specific for the reaction) for 30 s and 72ºC for 30 s per kb, final extension at 72ºC for 10 min and then hold at 4ºC.

For Q5 High-Fidelity DNA Polymerase the same above protocol was used with following exceptions: total reaction volume was 25 µl, 1x Q5 high GC enhancer was used instead of Betaine and 0.5 units of polymerase was used per reaction. Reaction products were examined by agarose gel electrophoresis (2.8.4).

2.8.6 General cloning protocol

Plasmids were constructed using the below general protocol using different vectors and inserts which will be mentioned in relevant chapters. Unless specified, all enzymes and buffers were purchased from New England Biolabs.

1.1.1.1 Restriction enzyme digestion

A 50 µl reaction mixture containing 5 µl of reaction buffer/Cutsmart buffer, 1 µg of DNA and 10 units of restriction enzymes of interest was prepared on ice. If the DNA sample was a PCR product (from 2.8.5), it was cleaned up using Bioline Isolate II PCR clean up kit as per the manufacturer's instructions. The reaction mix was incubated at 37ºC for 1h.

1.1.1.2 Antarctic Phosphatase (AP) treatment

If the digested DNA was a plasmid, 1 µl of Antarctic phosphatase was added and incubated for further 1 h. The digested DNA was either gel-purified or cleaned up using Bioline Isolate II PCR clean up kit as per the manufacturer's instructions.

1.1.1.3 Ligation

A 20 µl reaction mixture with vector: insert ratio 1:3 was prepared. The reaction consisted of T4 ligase (1 µl), T4 ligase buffer (2 µl), and vector DNA >50 ng. This was incubated at 16^{o}C overnight.

The ligation mix was transformed into an *E. coli* strain (Table 2.1) as described in 2.5. Plasmids "minipreps" were prepared as given in 2.8.2. Subsequent small-scale digestion analysis (2.8.6.1) with the same restriction enzymes used for cloning followed by gel electrophoresis (2.8.4) was used to screen the correct clones. These clones were further confirmed by Sanger sequencing (2.8.7)

2.8.7 Sanger sequencing

The sequence of the inserts made mainly by PCR amplification was confirmed using sanger sequencing. Purified DNA samples were sent to the Australian Genome Research Facility (AGRF) with appropriate primers (10 pmol/µl) for sequencing. The data were viewed using Finch TV software version 1.40 and Clustal Omega was used for multiple sequence alignment.

2.9 General protein analysis techniques

2.9.1 Sodium dodecyl sulfate polyacrylamide gel electrophoresis (SDS-PAGE)

SDS-PAGE was used in this work multiple times to perform western blotting, during protein purification and in-vitro studies. Resolving and stacking gels were prepared by mixing the ingredients shown in Table 2.8. Ammonium persulphate and TEMED were added immediately before pouring the gel into the gel casting apparatus. Once the resolving gel was solidified, the stacking gel was poured on top of it and the appropriate comb was inserted immediately, avoiding any trapped air bubbles. After the gel solidified, it was placed in a Bio Rd Mini-PROTEAN System and was filled the inner tank

completely and outer tank filled up to 2 with 1x running buffer (Table 2.7). 10 µl of protein samples containing 1x sample buffer (Table 2.7) were loaded on to the gel along with pre-stained blue protein standard (New England Biolabs). The gel was run at a constant current of 20 mA per gel for 60 min. Once the run was completed, the gel was stained with Coomassie stain (Table 2.7) unless proceeding to the western blotting. Then the gel was de-stained with by Coomassie de-stain solution (Table 2.7)

Table 2.8 Ingredients of SDS-PAGE Gels

Resolving gel 12% w/v (for 10 ml)	Stacking gel 4% w/v (for 5 ml)
3 ml Acrylamide solution (40%)	500 µl Acrylamide solution (40% v/v)
2.5 ml 1.5 M Tris-Cl (pH 8.8), 0.4% w/v SDS	1.25 ml 0.5 M Tris-Cl (pH 6.8), 0.4% w/v SDS
100 µl Ammonium persulphate (10% w/v frozen stock)	50 µl Ammonium persulphate (10% w/v - frozen stock)
10 µl TEMED	5 µl TEMED
4.4 ml MQW	3.2 ml MQW

2.9.2 Western Blot

Western blots were used to confirm gene knockouts and test the expression of proteins from cloned genes. Resolving gels were run as described in 2.9.2 and used for protein transfer. A “sandwich” for electro-transfer was prepared placing the nitrocellulose membrane (Protran) on the anode side and the gel on the cathode side. The membrane and the gel were immediately sandwiched between 2 wet filter papers and then a couple of wet sponge pads. A pipette was rolled over the sandwich to remove any air bubbles trapped between the layers. The sandwich was placed in the electrode chamber (Bio-Rad) and the tank topped up with cold transfer buffer (Table 2.7). Electro transfer was carried

out at 100 V for 1 h. Once the transfer was completed, the unit was disassembled and the total protein on the membrane was tested by submerging the membrane in Ponceau stain (Table 2.7). If the protein transfer was good, the membrane was incubated in the blocking solution (Table 2.7) at 4^{o}C overnight. On the next day, the membrane was washed with water and incubated with the primary antibody (diluted with TBST (Table 2.7) appropriately) at R.T for 1 h on a rocking platform. The membrane was washed 3 times (5 min each) with TBST (Table 2.7). After washing, the membrane was incubated with the appropriately diluted secondary antibody at R.T for 1 h in a rocking platform. Then the membrane was washed again 5 times (5 min each) with TBST (Table 2.7). Finally, the membrane was incubated with a 50:50 mixture of Super Signal West Pico PLUS Chemiluminescent Substrate ("enhanced" luminol/stabilised H_2O_2) reagents (Thermo Fisher Scientific, Australia) as per manufacturer's instruction. The membrane was immediately imaged with a chemiluminescence gel-doc, Amersham Imager 600 (GE Biosciences).

2.10 Common techniques used to analyse different cellular parameters

2.10.1 Imaging cell shapes using microscopy

For most microscopic imaging, a 2 µl sample of culture (concentrated as necessary) was placed directly onto a slide prepared with a 170 µm thick, 1% (w/v) agarose pad containing 18% (w/v) BSW. A number 1.5 coverslip was then placed on top. Phase-contrast images were acquired with the Zeiss Axio Plan 2 system with a 1.4 NA phase-contrast objective (Carl Zeiss, Germany). Super-resolution imaging for circularity analysis was performed with Delta Vision (DV) Elite Super-Resolution Microscope (SRM) and DV OMX SRM (Applied Precision Inc., a GE Healthcare Company, Issaquah, USA).

2.10.2 Cell circularity analysis

In this study, cell circularity changes were primarily analysed in several experiments. Phase-contrast images were analysed using MicrobeJ, an ImageJ plug-in (Adrien Ducret, 2016). In this plug-in, medial axes are generated from smoothed particle contours using a skeletonisation algorithm. The circularity ($4\pi \times \text{area} / \text{perimeter}^2$) is measured on the interpolated contour generated using the particle medial axis and the specified value of the width measured along the medial axis. Values may range between 0 and 1.

2.10.3 Cell volume and cell count analysis by Coulter counter

A coulter counter was used to measure the cell volume and cell count in several archaeal strains. Culture samples were diluted (x1000) with 18% (w/v) BSW (Table 2.5), and then, analysed with a Multisizer 4 Coulter Counter (Beckman Coulter) in the constant volume mode (1 ml), with a 30 mm aperture tube and 18% BSW as the electrolyte. A 2 mm bead standard (Beckman Coulter), diluted in 18% (w/v) BSW, was used for prior calibration.

.

CHAPTER 3

CONDITIONAL PLEOMORPHOLOGY AND DIFFERENTIATION IN THE MODEL ARCHAEON *HALOFERAX VOLCANII*

DISCLOSURE

This chapter was written in a manuscript format for submission to the Journal of Applied Environmental Biology by American Society of Microbiology for publication under the title "Cell shape differentiation in *Haloferax volcanii*". I certify that I carried out significant work presented in this manuscript.

- Roshali T. de Silva and Iain G. Duggin conceived the project idea and designed the experiments for metal depletion
- Mechthild Pohlschroder initially observed the rods during *H. volcaii* early growth
- Roshali T. de Silva and Iain G. Duggin designed all the experiments presented
- Roshali T. de Silva performed all the experiments presented.

3.1 Abstract

Some microbes are pleomorphic—showing multiple distinct shapes in a single culture—whereas others may display specific conditional differentiation. Here we show that the rods and other more complex elongated forms commonly observed in mid-logarithmic batch cultures of the model archaeon *Haloferax volcanii* are a response to limited trace-element nutrients. Growth was improved in both complex and defined media by the inclusion of eight supplemental trace elements. During steady mid-log growth in these supplemented media, *H. volcanii* existed as the plate-shaped cell type. However, in both batch and microfluidic-flow cultures, we observed an additional morphological response during the early stages of growth in culture, in which plate cells transitioned into well-defined rods. Conditioned growth medium, supplemented with fresh nutrients, partially inhibited rod development during early-log growth, suggesting that secreted signals control differentiation. Rod development under all conditions tested was dependent on the tubulin-like protein CetZ1. Our results show that *H. volcanii* morphology is highly sensitive to both nutritional and culture-dependent signals, suggesting that the various morphologies would have multiple functions in different conditions experienced by *H. volcanii* in its hypersaline habitats. These responses may serve as experimental models for studies of archaeal morphological development.

3.2 Introduction

Archaea exhibit some of the most diverse and unusual microbial cell morphologies. Cell shapes range from rods and cocci to striking triangles and squares. However, little is known about the mechanisms and environmental cues that dictate archaeal cell morphology, or the regulation of transitions between cell morphologies. The model haloarchaeon, *Haloferax volcanii*, when first isolated, was described as mainly disk-shaped cells, with cell shape and size varying significantly (Mullakhanbhai and Larsen, 1975). In routine liquid cultures of *H. volcanii*, both irregular disk (plate) and rod morphologies may be observed (Mullakhanbhai and Larsen, 1975).

The conditions that influence *H. volcanii* cell shapes and the relative abundance of the distinct types are not well understood, and specific signals have not been identified. In *H.*

volcanii biofilms, substantial elongation (filamentation) has been observed in a subpopulation of cells (Mullakhanbhai and Larsen, 1975). Furthermore, *H. volcanii* forms rods in swimming-motility soft-agar, such that rods are observed at the forefront of expanding colonies of swimming cells (Duggin *et al.*, 2015). The tubulin-like cytoskeletal protein CetZ1 is required for *H. volcanii* rod-formation and the normal rate of motility, suggesting a connection between morphology and motility that may be expected based on improved hydrodynamics or directional movement of rods (Duggin *et al.*, 2015).

The surface (S-)layer glycoprotein (SLG) is considered the main constituent of the *H. volcanii* cell wall and is important for cell shape maintenance and envelope integrity (Rodrigues-Oliveira *et al.*, 2017). The biosynthetic machinery involved in the assembly and modification of SLG also affects *H. volcanii* cell shape. Mutations in the peptidase archaeosortaseA (ArtA), which is required for the C-terminal processing of a subset of surface proteins, including lipid attachment to SLG, cause a greater frequency of rod-shaped cells (Abdul Halim *et al.*, 2016). This appears to be only partly due to a lack of SLG processing by ArtA, suggesting that other activities of ArtA influence cell shape too.

While some of the components influencing rod-formation in *H. volcanii* are being identified, a better understanding of the conditions under which *H. volcanii* forms rods or other shape types will be valuable to the ongoing study of archaeal cell biology. Furthermore, the conditions underlying the striking pleomorphology in routine cultures of *H. volcanii* have not been previously identified. In this study, we identify these conditions and show that both nutritional and culture-dependent signals can trigger CetZ1-dependent morphological switching in *H. volcanii*. By doing so, we have defined culture conditions for these responses that may serve as experimental models for studies of morphological development in *H. volcanii*.

3.3 Results

3.3.1 *H. volcanii* growth and pleomorphology in nutrient-limited batch culture

Commonly used media for *H. volcanii*, Hv-Ca and Hv-YPC, consists of macronutrients for heterotrophic growth in a base of 18% (w/v) buffered primary sea-water salts (Allers *et al.*, 2004). Hv-Ca is a defined medium with Casamino acids as the carbon and energy source, and typically provides a slower growth rate and yield than the complex Hv-YPC medium, which contains yeast extract, peptone and Casamino acids added to the 18% salts base. Both media are known to produce pleomorphic cells, displaying different shape types (primarily rods or irregular discoidal 'plates') in the same culture.

We initially noticed inconsistent growth yields of *H. volcanii* in Hv-Ca prepared in different laboratories or with different sources of reagents. Since these media are normally not supplemented with trace elements (Allers *et al.*, 2004), and a range of metal ions are typically required by cells at low or trace concentrations to act as essential cofactors needed in enzymatic reactions, we added a solution of eight compounds as a source of trace-elements (containing Fe, Zn, Cu, Co, Mn, Ni, Mo and B) to the Hv-Ca medium. A vitamins solution (Allers *et al.*, 2004) was also added. As detailed below, the new medium (named "Hv-Cab") greatly improved the growth rate, yield and reproducibility of *H. volcanii* cultures. Hv-Cab liquid cultures produced plate-shaped cells in steady mid-log growth at relatively high cell densities, in which rod-shaped cells are infrequent (Duggin *et al.*, 2015).

To identify any growth or morphological changes associated with omission of the primary nutrient sources in Hv-Cab, mid-log *H. volcanii* cells were transferred to specific nutrient-omitted media, which were prepared with highly pure reagents to minimize contaminating sources of nutrients (particularly trace elements). Growth and cell morphology were monitored over three successive passages under each of these nutrient-depleted conditions. Transfer to media without the carbon and energy source, Casamino acids (CAA) caused cells to rapidly cease growth, as expected (Figure 3.1A, maroon data-points). Exclusion of the vitamins had a minor effect on the maximum OD that was consistent throughout the three successive culture passages (Figure 3.1A-C). However, cultures without supplementary trace elements showed successively greater reductions in

both growth rate and yield with each passage, such that by the third passage growth was very poor, and the culture barely reached a maximal OD of ~0.3 (Figure 3.1C).

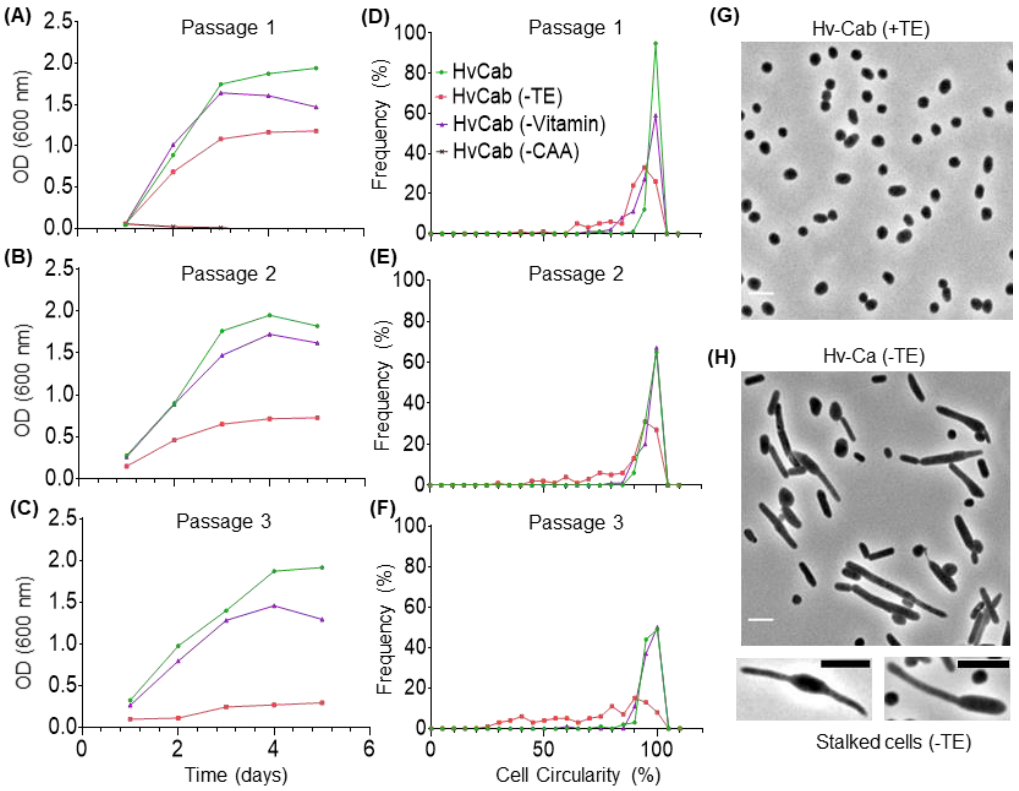

Figure 3.1: *Effects of nutrient depletion on H. volcanii growth and morphology in liquid culture.*

Strain H98+pTA962 was initially grown to mid-log phase in Hv-Cab, and then was washed and resuspended in fresh Hv-Cab or in media excluded for one of the major nutrient components, i.e. trace elements (TE, red data-points), vitamins (biotin and thiamine, purple triangles), or casamino acids (CAA, maroon triangles). (A) Culture growth was monitored by measuring the OD (600 nm) over 5-days. Cells from day-5 of the first dilution were then diluted (1/100) into the respective nutrient-depleted media and incubated and monitored the same way for a further 5 days (B). Cells from the second dilution (day-5) were again diluted (1/100) into the respective nutrient-depleted media and then incubated for five more days (C). Cells imaged by phase-contrast microscopy at day-5 (final data point) in each of the cultures (A-C) by determining the circularity of cell outlines (N = 100, randomly selected cells), shown as a corresponding histogram (D-F). G and H shows the phase-contrast images of cells in (G) Hv-Cab (+TE) and (H) Hv-Ca (-TE) on day-5 of the third passage (a representative image of the cells analysed in histogram F). TE depletion also resulted in formation of stalks like structures in some cells. The scale bar represents the length of 5 µm.

Cells were observed by phase-contrast microscopy at day 5 (stationary phase) after all three of the culture passages, and the cell shapes were analyzed by automated measurement of the circularity of cell outlines; these data were then plotted as histograms of cell circularity, expressed as a percentage compared to a perfect circle (Figure 3.1D-F). Under these conditions, the Hv-Cab cultures contained almost exclusively plate-shaped cells that had near-circular cell outlines; however, the trace-elements-depleted cultures showed striking cell elongation, which became more extensive in each successive passage (Figure 3.1H). Cells depleted of trace elements showed complex features accompanying the extensively elongated rod shapes, including rods that showed variable widths along their lengths, including some cells exhibiting substantial stalks of variable length and width (Figure 3.1H).

3.3.2 Improved growth of *H. volcanii* in TE-supplemented media

Previous studies have shown that in rich media, such as Hv-YPC (Allers *et al.*, 2004), elongated and irregular cell morphologies can exist together with the plate-shaped cells, which also show a moderate irregularity in shape. Trace elements are expected to be present in Hv-YPC, originating primarily from the yeast extract. We investigated the possibility that trace elements may yet be somewhat limiting in Hv-YPC, giving rise to the strong pleomorphology seen in this medium, by supplementing it with the trace-elements (TE) solution. By analogy to the Hv-Ca/Hv-Cab media terminology introduced above, we refer to the TE-supplemented version of the medium as “Hv-YPCab”.

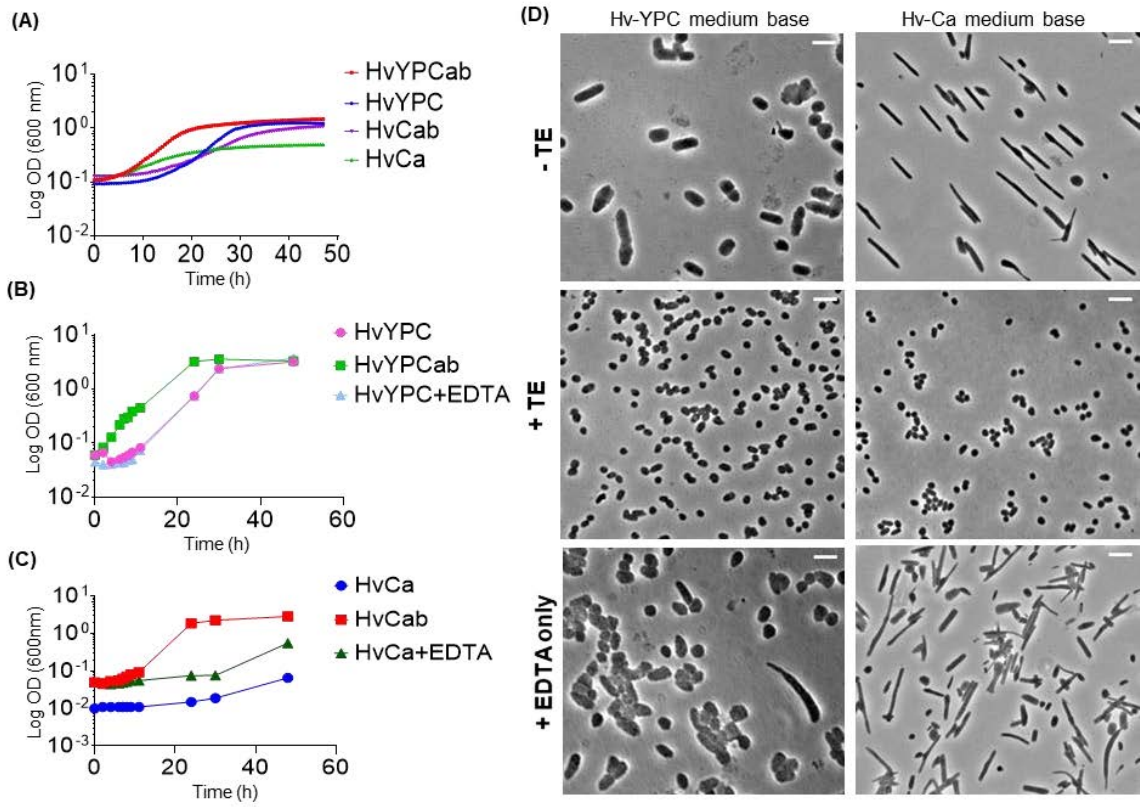

Figure 3.2: *Media supplementation with trace elements (TE) solution improves growth and cell shape uniformity in H. volcanii.*

(A) Growth curves in microtiter plate format. H. volcanii cells from stationary phase batch culture, in HvCab, was washed with 18% BSW three times and then inoculated to a final OD of 0.1 into media with or without TEs. Growth (42 ^{0}C with 200 rpm shaking) was then monitored in a Tecan Spark microtiter plate spectrophotometer. (B) Growth curves in tube-culture format, started from steady mid-log (for 4 days) cultures in the respective media, comparing Hv-YPC medium with the same media supplemented with either the complete TE solution (i.e. Hv-Cab) or the EDTA component only. (C) Tube-culture experiments, as per panel (B) except based on Hv-Ca medium. The Hv-Ca culture was started at ~10-fold lower cell density than the other two (as on 4th day the culture displayed a very poor growth). (D) Cells sampled after 40 h were imaged by phase-contrast microscopy. All scale bars represent 5 µm.

The onset of growth and the culture growth rate was noticeably faster with Hv-YPCab medium, compared to Hv-YPC, in both microtiter-plate (Figure 3.2A) and culture-tube formats (Figure 3.2B). As expected, growth was also substantially improved in Hv-Cab compared to Hv-Ca (Figure 3.2A, 3.2C). Furthermore, microscopy revealed that cells were almost uniformly the plate morphotype in Hv-YPCab cultures and showed none of the longer rods or filaments with stalks previously noted in non-TE-supplemented

medium (Figure 3.2D). The cell size was also smaller in both TE-supplemented media compared to the original media (Figure 3.2D). No significant change was observed when EDTA (at the same concentration and pH as present in the TE solution) was added to the medium; culture growth, cell size and morphology were unaffected compared to Hv-YPC alone, demonstrating that the cells were reacting specifically to the concentration of the trace-element compounds that differ between the original and the supplemented media.

3.3.3 *H. volcanii* forms rods during the onset of growth in culture

We have noticed that *H. volcanii* cells placed in fresh medium at low cell densities can develop into an obvious rod-shaped morphology during initial growth stages, whereas cells at late stages of growth or in colonies from agar plates are primarily plate-shaped. As may be seen in Figure 3.3, cells resuspended in fresh liquid medium from colonies were plate-shaped immediately upon resuspension. However, after incubation of the cultures overnight, the cells were observed to be primarily rod-shaped, for example, when sampled at an OD(600 nm) of 0.05 (Figure 3.3). By the time the culture had reached OD = 0.3, many plate-shaped cells were observed, although rod-shaped cells could still be observed to varying degrees, possibly due to differences in the size of starting inoculum in different cultures. At higher OD values later in the culture growth, the cells were observed to be almost exclusively the plate-shaped cell type (Figure 3.3).

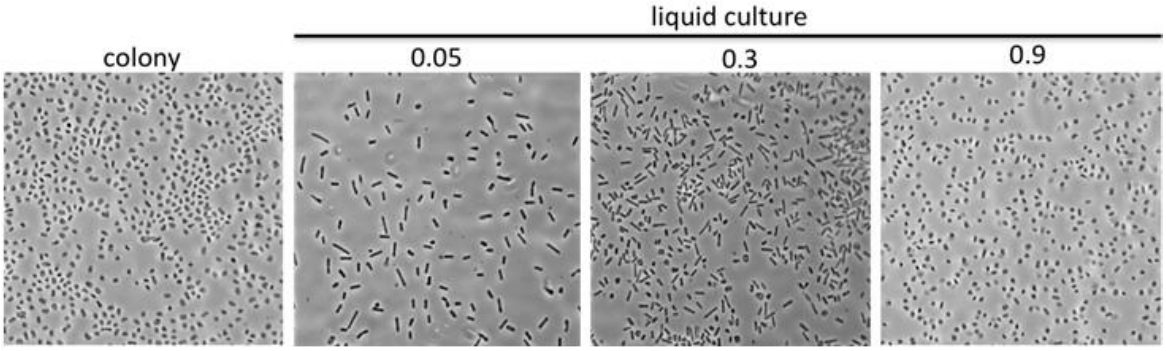

Figure 3.3: *H. volcanii forms rods during the early stages of growth at low ODs in liquid batch culture.*

A fresh colony of H. volcanii (H98 + pTA963) was used to inoculate liquid medium and then next morning cells were sampled when culture reached OD values of 0.05, 0.3, and 0.9, and were observed by phase-contrast microscopy.

In order to thoroughly characterise the development of *H. volcanii* during the batch-culture growth cycle, we monitored the culture growth rate and cell morphology in various growth media at frequent time points throughout the growth cycle. *H. volcanii* was initially grown for four days on the appropriate solid media to allow colony growth, and then sufficient colonies were picked and resuspended in the equivalent liquid medium, and the OD was adjusted to 0.05, to start the culture at a measurable and reproducible density. Culture growth (OD and cell number), cell volumes (Coulter cytometry) and morphology (microscopy) were monitored over time in the new media described above, both with or without supplemental trace elements (Figure 3.4).

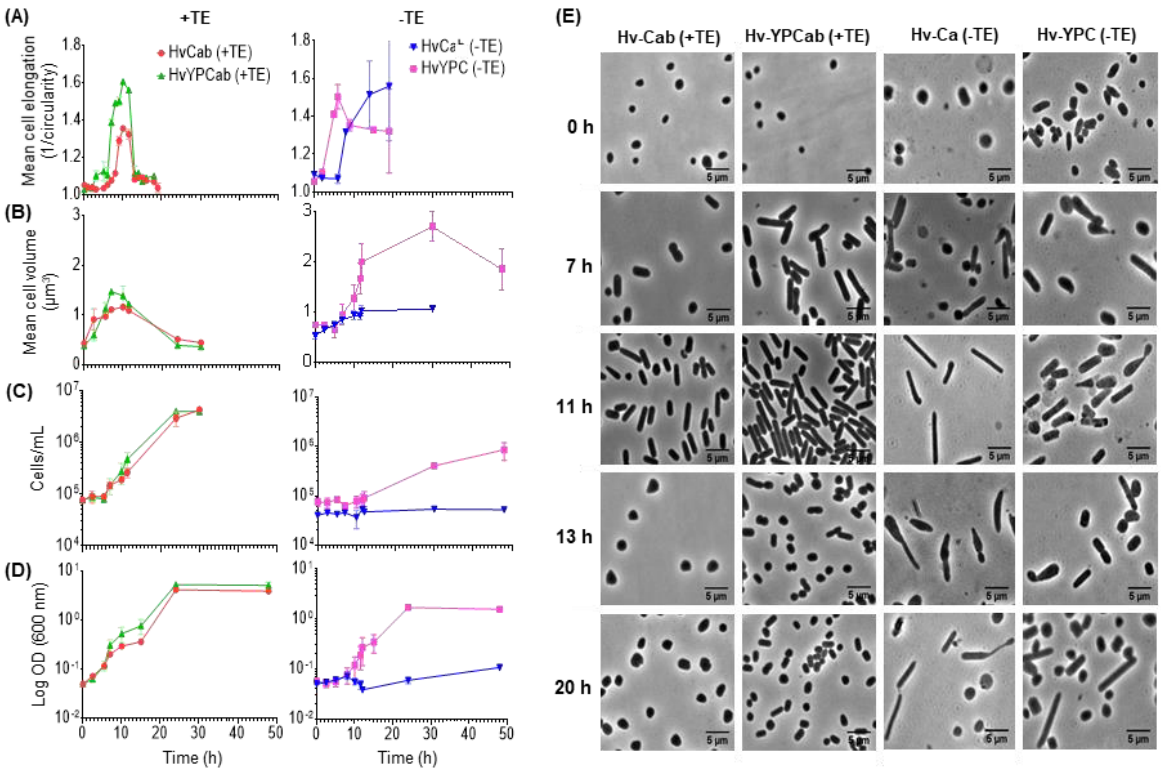

Figure 3.4: *Assays for H. volcanii reversible morphological transitions during the growth cycle.*

Samples of H. volcanii (H98 + pTA962), grown in the indicated liquid media (after inoculation from colonies obtained from 4-days of growth on the equivalent solid agar medium), were withdrawn at time-points for microscopy (A), Coulter cytometry determination of cell volumes (B) and counts (C), and OD measurements (D). The microscopy analysis in panel (A) shows mean cell elongation (expressed as inverse circularity) of 250 randomly selected cells at each time point. Error bar indicate the standard deviation of the mean of duplicates.

In both Hv-Cab and Hv-YPCab media, cell volume and culture growth (OD) increased from the start of the experiments (Figure 3.4B, 3.4D) and the cell number began to increase after ~7 h delay (Figure 3.4C), reflecting biomass increase rather than cell number increase in these cultures. This corresponded approximately to the onset of rod development, as seen in the representative images of the cells (Figure 3.4E), which were analysed by measuring the mean cell elongation (1/circularity) at the time points indicated (Figure 3.4A). In both media (+TE), a peak of rod development was observed commencing ~7 h after inoculation, reaching a maximum mean cell elongation after ~10 h, and then from 13 h onwards, plate cells were again almost exclusively prevalent (Figure 3.4a, +TE); the peak was greater in Hv-YPCab than in Hv-Cab. The timing of rod development and subsequent conversion back to plates approximately corresponded to an increase and then a decrease in the mean cell volume, respectively (Figure 3.4B), suggesting that rod development accompanies the first few generations of growth, whereas the reversion to plates accompanies cell division, which reduces the mean cell volume several generations later. These responses to resuspension/dilution in fresh liquid medium are consistent with a culture density-dependent signal (e.g. secreted compound), or physical or cell-cell contact sensing mechanisms.

3.3.4 The interplay between conditions controlling *H. volcanii* morphological development

To begin investigating the interplay between the conditions we have identified above that control *H. volcanii* morphology, the effects of TE-starvation in the above colony-resuspension (rod-development) assay were studied. Cells were first grown into the mid-log phase in the respective +TE medium, and then they were separated from the medium, washed, and then plated on the respective -TE agar medium. After growth on the agar, cells were resuspended in -TE liquid medium to start the time-course. In both Hv-Ca and Hv-YPC, cells resuspended from colonies immediately appeared as plate-shaped cells (Figure 3.4A, 3.4E -TE), despite the lack of trace elements in the agar (and visibly poor growth of colonies on this Hv-Ca agar), suggesting that the morphological effect of growth on agar (producing the plate morphotype) is dominant over the influence of trace element starvation.

As expected, the Hv-Ca (-TE) cultures showed very poor overall growth, whereas Hv-YPC cultures grew quite well by comparison (Figure 3.4C, 3.4D, -TE). Cells became noticeably elongated by 5 h (Hv-YPC) or 8 h (Hv-Ca) of incubation, and they continued to show substantial elongation (and increased cell volume) for at least 20 h, displaying a myriad of unusual irregular cell shapes (Figure 3.4A, 3.4B, 3.4E). These results indicate that TE-starvation in liquid culture masks any rod-development signals (or the clear detection of their effects) associated with the transient appearance of rods observed during early growth in the +TE cultures (Figure 3.4).

3.3.5 Microfluidic flow chamber visualization of *H. volcanii* cellular development

We next sought to directly visualize morphological development during the early stages of growth in liquid culture. Cells resuspended from colonies were loaded into incubated microfluidic chambers for time-lapse microscopy. Time-series of rod-cell development in complete medium (+TE) are shown in Figure 3.5A and Figure 3.5B, and the complete time series is available in Supplementary Videos 1 and 4. These data show that plate cells can initially grow and divide once or twice as plates, and then transition into the rod form as cells grow and continue to divide as rods for several generations. We observed that rods generally persisted during incubation in the microfluidic culture system (particularly evident in Hv-YPCab), compared to the sharp peak of rods seen in batch culture (Figure 3.4A). The microfluidic flow system would continuously remove any putative secreted signals, and the chamber surfaces directly contact the cells, which are also exposed to different shear forces.

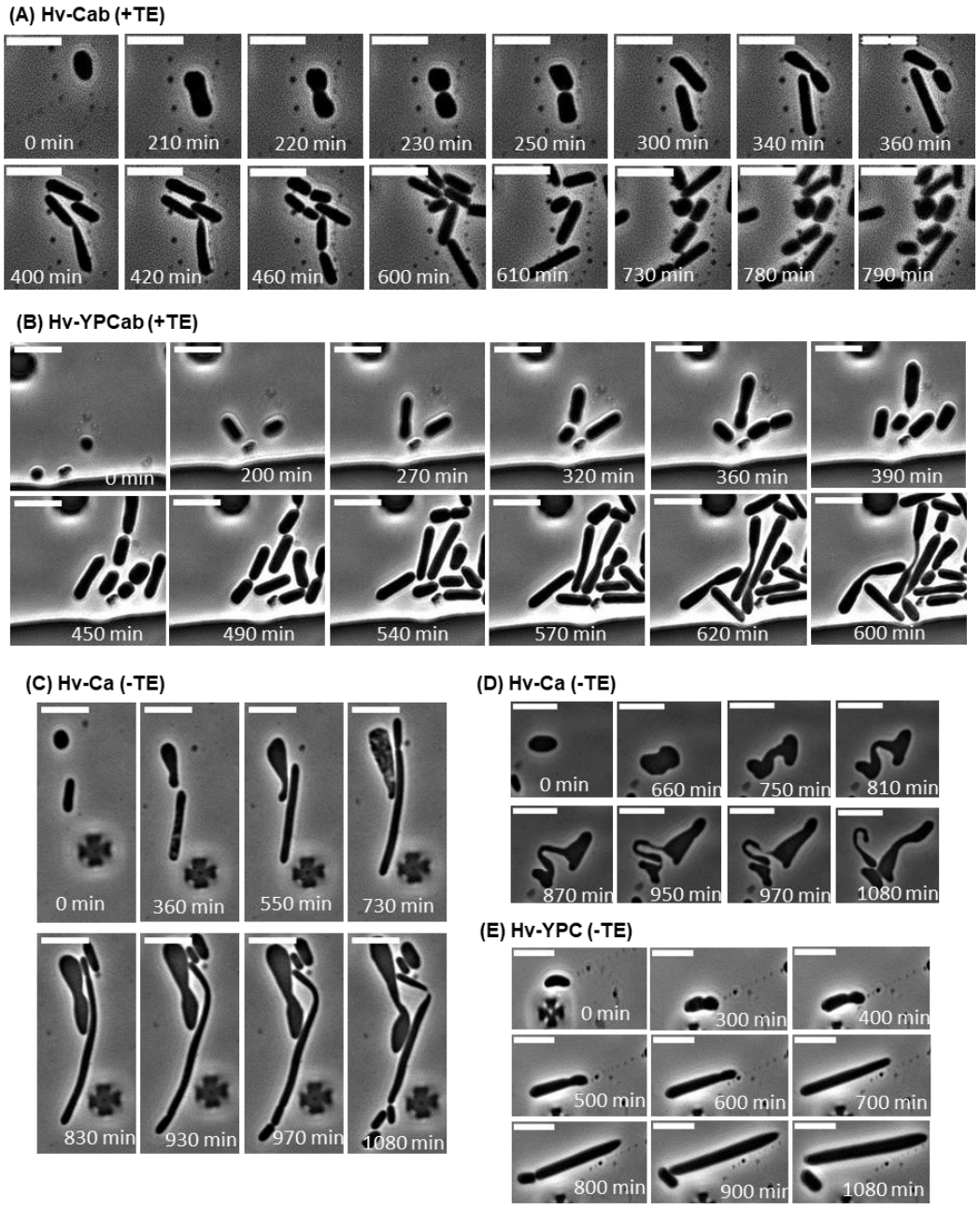

Figure 3.5: *Time-lapse microscopy of H. volcanii (H98 + pTA962) with and without trace elements.*

Microfluidic chambers were loaded with cells and phase-contrast images were collected at 10 min intervals during perfusion (2 psi for 20 h). (A) Selected time frames showing initial growth after resuspension in Hv-Cab (+TE). (B) Selected time frames during microfluidic culture in Hv-YPCab (+TE). (C) Selected time frames showing the substantial cell elongation observed Hv-Ca (-TE) and a highly-asymmetric division event. (D) Another field of cells cultured in Hv-Ca (-TE) showing slow growth and striking morphologies, including the generation of a "mermaid" cell, which shows a distinctive highly-curved tail. (E) Selected time frames of cell elongation in Hv-YPC (-TE).

Microfluidics experiments run with -TE conditions revealed striking morphological responses (Figure 3.5C, 3.5D, 3.5E, and Supplementary Videos 2 and 3), including highly asymmetric division in extensively elongated cells (Figure 3.5C), and the generation of some bizarre shapes (Figure 3.5D). Overall, these results show that the microfluidic culture system is well suited to microscopy studies of *H. volcanii* morphology and development, in the context of both early-growth rod development, and trace element depletion.

3.3.6 Potential role of secreted signals in cell elongation during early growth

Based on the hypothesis that the onset of rod formation during the early log phase is caused by a change in the concentration of a culture density-dependent (quorum sensing) signal, the effect of cell-free ('conditioned') culture medium isolated from a late-log culture on cell shape was tested. *H. volcanii* colonies were used to inoculate the respective conditioned media, and then cell circularity changes were compared with the cells inoculated into fresh media. There was a moderate decrease in rod formation during the "rod peak" time in conditioned Hv-YPCab medium compared to the fresh media (Supplementary Data Fig. S2) . The statistical significance of this test was calculated using a non-parametric Kolmogorov–Smirnov test. In Hv-YPCab-based cultures, the cell circularities in spent media and fresh media were significantly different ($p<0.01$) at 6h, 8h and 10h; however, the Hv-Cab-based cultures were not significantly different. These observations suggest that accumulation of an externally secreted quorum-sensing signal might influence the cell shape transitions under certain conditions (e.g. from rod to plate cells as culture density increases).

3.3.7 Reversibility and specificity of the TE-starvation cell elongation response

To investigate the reversibility of TE-starvation in the Hv-Ca cultures, TEs were added at 15 h incubation after colony resuspension either by direct addition of the TE stock, or by dilution of the Hv-Ca culture (1:100) into Hv-Cab, Hv-Cab with 10x concentrated TE, or Hv-Ca as a control. In all three media conditions containing additional TE, cells

reverted to the plate morphotype over 12 h (Supplementary Data Fig. S1), which is a similar duration required for the appearance of elongated cells upon colony resuspension in Hv-Ca (Figure 3.4A, -TE), showing that the starvation is readily reversible by resupply of the trace element nutrients.

The role of individual components of the TE solution on *H. volcanii* cell shape was screened by testing a series of five TE solutions omitting either the Co, Cu, Fe, Mn or Zn. None of the individual 'drop-out' TE media at 15 h post-resuspension matched the degree of cell elongation observed under -TE conditions (Supplementary data Fig. S1D). However, Fe and particularly Co drop-out media appeared to cause a moderate cell elongation response, suggesting that *H. volcanii* may respond proportionally to cumulative effects from different elements, rather than on just one of these particular elements.

3.3.8 The requirement of tubulin-like protein CetZ1 for rod cell formation in batch culture

CetZ is a family of cytoskeletal protein from the tubulin superfamily protein found in the Euryarchaeota, and are particularly abundant in haloarchaea. In *H. volcanii*, there are six CetZ homologues, and a distinct function was identified for the most conserved member of this family, CetZ1, which was found to be required for motile rod-cell development (Duggin *et al.*, 2015). We analysed the rod-development capacity of strains carrying a CetZ1 knock-out or expressing a dominant-negative mutation (CetZ1.E218A) in the different media conditions identified in the present study. The CetZ1.E218A mutant disrupts the GTP-dependent polymerisation of the protofilament, resulting in hyper-stabilisation of protofilaments, which inhibits CetZ1 function.

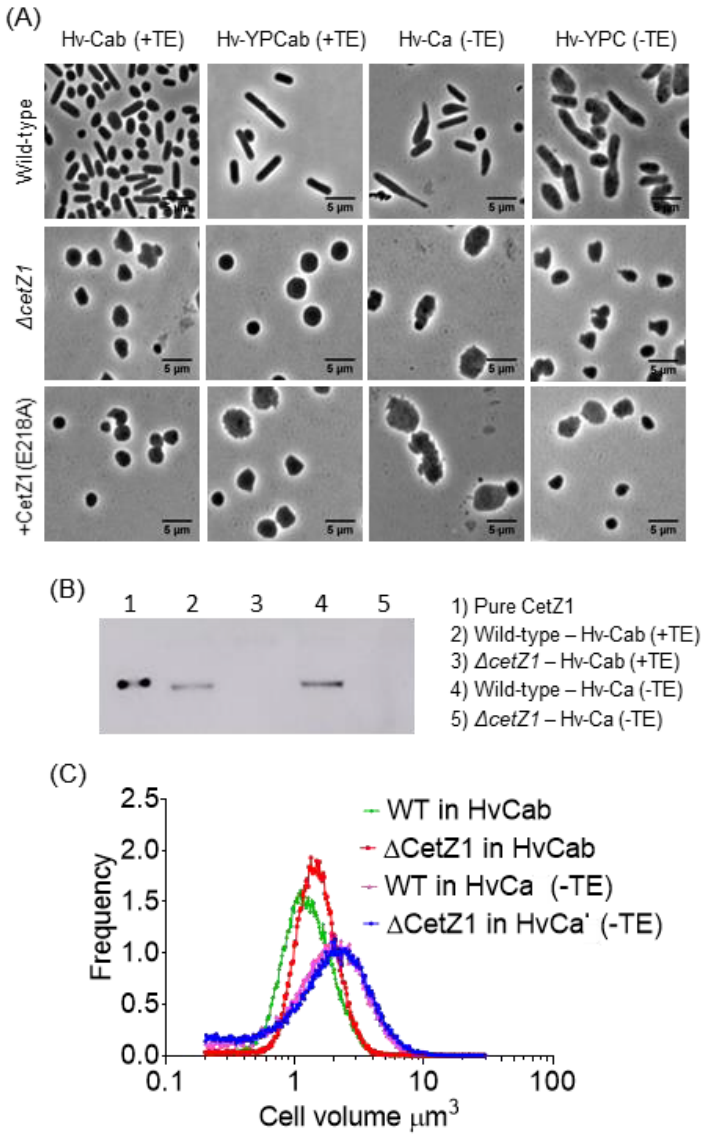

Figure 3.6: *CetZ1 is essential for rod development during early-growth after colony resuspension and during TE-depletion.*

(A) Phase-contrast images of wild-type (H98 + pTA962), the CetZ1 knock-out (H98.ΔcetZ1 (ID59) + pTA962), and the point mutation (H98 + pTA962-cetZ1.E218A) at 10 h post-resuspension of colonies in the indicated media. (B) Western blot detection of CetZ1 in the wild-type and CetZ1 knock-out strains at 15 h post-resuspension in the indicated media. (C) Coulter cytometry histograms comparing cell volume distributions of the wild-type and CetZ1 knock-out strains at 15 h post-resuspension in Hv-Cab and Hv-Ca (-TE).

Both strains failed to form rods in Hv-Cab, Hv-YPCab and in the corresponding TE-depleted media conditions compared to the wild-type control (Figure 3.6). Furthermore, the CetZ1.E218A mutant displayed irregular, jagged cell shapes, consistent with previous

observations of the consequences of this mutant's overexpression (Duggin *et al.*, 2015). Western blotting indicated that there was no substantial difference in the cellular amounts of CetZ1 during TE-depletion-induced rod formation compared to the TE-supplemented media (Fig. 3.6B). Although the CetZ1 knock-out cells were significantly different in shape compared to the wild-type cells under these conditions (Fig. 3.6A), the cell volumes of both strains were very similar (Figure 3.6C). However, the cell volume distribution of both WT and CetZ1 KO in Hv-Ca (-TE) were larger than the cell volumes in Hv-Cab, consistent with the previous results (Figure 3.4B) and showing that CetZ1 does not substantially affect cell volume under these conditions.

3.4 Discussion

It was previously shown that, in soft agar assays of cellular motility, *H. volcanii* cells change from a discoid or plate shape into a rod shape during the development of swimming motility (Duggin *et al.*, 2015). However, the soft-agar motility assay is not a robust method for ongoing studies of cell-shape differentiation in *H. volcanii* because the soft agar is difficult to separate from the cells, and cell yields are low. Furthermore, the fraction of rod-shaped cells observed in these assays is sensitive to the precise location from which cells are withdrawn (only the outermost ring of advancing cells are near-uniformly rod shaped (Duggin *et al.*, 2015)), which can result in substantial variation of the cell shape with different samples from the same colony of swimming cells. The present study reports new liquid-culture methods of observing rod-development, based on the discoveries reported here that *H. volcanii* undergoes rod-cell development in response to resuspension in fresh medium, and by depletion of trace-element nutrients. The latter also produces more complex cell shapes, most notably rod-shaped cells that exhibit striking stalks of variable length and width, emanating from one or both cell poles (Figure 3.2). Both rod-shape and stalk development were dependent on the conserved tubulin-like cytoskeletal protein, CetZ1 (Figure 3.6). We defined protocols to observe the development of rods in liquid cultures, based on these responses (Figure 3.4), which are applicable and adaptable in the ongoing study of *H. volcanii* cell differentiation as a model for archaeal development.

We showed that the commonly used *H. volcanii* media, Hv-Ca and Hv-YPC, are limited in their supply of trace-element nutrients (Figure 3.2). When high-purity reagents are used, Hv-Ca in particular gives very poor growth, and the cells respond by substantial cell elongation and stalk development (Figure 3.1). Our preliminary observations had showed that the sources of the reagents used for preparing the media substantially and unpredictably influenced growth and cell morphology; for example, in addition to the nutritional effects described above, we had noticed that the use of one lower-grade source of NaCl inhibited the rod development observed after culture resuspension in all other media tested. In response to these observations, we introduce two new media here, Hv-Cab and Hv-YPCab, which are supplemented with a solution of 8 metal salts that enhance the reproducibility and growth performance (rate and yield) of *H. volcanii* cultivation (Figure 3.2). Furthermore, these media produce consistent cell shapes (Figure 3.2D), in

contrast to the highly pleomorphic cultures (showing a mixture of distinct cell morphotypes) obtained with the original Hv-Ca and Hv-YPC media (Allers *et al.*, 2004, Delmas, Duggin and Allers, 2013). The pleomorphology of *H. volcanii* commonly seen in laboratory cultures therefore appears to be primarily a response to trace nutrient limitation.

H. volcanii responded to the set of 8 trace-elements generally, rather than being responsive to the specific depletion of one of either of the relatively more abundant elements added: Co, Cu, Fe, Mn or Zn (Supplementary Data Figure 1). Why would general trace-element limitation trigger the development of *H. volcanii* rod cells or stalks? Some of the factors that are related to morphological changes in bacteria are nutrients, cell attachment and biofilm formation, motility/chemotaxis, predation and polar differentiation (Young, 2007). Starvation of multiple nutrients causes viable cell shape changes in a marine *Vibro* species, resulting in pleomorphic cell populations that stayed viable for extended periods, suggesting that the morphological heterogeneity may offer a survival advantage (Stretton *et al.*, 1997). In *Caulobacter crescentus*, phosphate starvation triggers stalk extension, which is thought to improve surface area for nutrient uptake (Klein *et al.*, 2013, Wagner *et al.*, 2006). During severe trace-element starvation, *H. volcanii* develop as rods and many cells produce stalks, thus showing resemblance to the above examples of bacterial conditional pleomorphology and stalk growth.

While both rod development and stalk formation can occur together in *H. volcanii* in response to TE-starvation, the observation that stalk-less rod cells form in response to motility conditions (i.e. crowding or nutrient limitation) without the stalk formation indicates that these responses can be separate under some circumstances. However, both rod development and substantive stalk formation during TE-starvation were dependent on the CetZ1 cytoskeletal protein (Figure 3.6), indicating that the two morphological processes have some mechanisms in common.

To enhance the survival in unfavourable environmental conditions such as starvation, high temperature and inhibitory chemicals, bacteria often secrets a myriad of secondary metabolites, such as bacteriocins. This type of quorum sensing is an advanced communication means developed in bacteria to progress signals between cells. Generally, it helps in the movement of bacterial cells away from inhibitory molecules and propagation towards the favourable conditions such as nutrients — chemotaxis. Moreover, it has been found that *H. volcanii* secretes quorum sensing molecules similar

to bacterial Acyl Homoserine Lactone (Megaw and Gilmore, 2017). We believe the additional cell differentiation during early log phase described in this study as a result of a quorum-sensing response. This hypothesis is supported by the delayed rod reversal observed in the CellASIC microfluidic system where signalling molecules can be washed out by the continuous flow of the media. Moreover, cell circularity measures carried out using the conditioned media displayed a reduction in rod cell formation during on-set rod peak. However, some of the cells were still able to form rods under this condition suggesting on-set rod formation is not solely caused by quorum sensing.

In addition to the externally secreted molecules, many cell types display mechanosensing to the signals such as shear rate, shear stress and surface attachment. The mechanosensing could also trigger changes in the cell cytoskeleton thus changing the cell shape (Shemesh *et al.*, 2015, Sanfilippo *et al.*, 2019). Although the microfluidic chambers are continuously perfused with the media, the cells are not directly exposed to the fluid flow. Instead, the replenishment of the nutrients and the removal of the waste products inside the microchambers occur via diffusion. Therefore, in contrast to the batch cultures on a spinning platform, the cells experience less shear stress in a microfluidic system. Also, the cells in the microfluidic chambers are partially immobilised compared to the cells in batch culture. We hypothesise these altered mechano-stress conditions could contribute to the enhanced rod formation effect observed in the microfluidic system in addition to the dilution of a quorum-sensing signal. The cell shape is a highly sensitive attribute in *H. volcanii,* and changes in the cell shape can be triggered in response to changes in the intercellular or extracellular environment. All the tests in the present study were carried out in *H. volcanii* H98 cells with pTA962 plasmid (Allers *et al.*, 2010); thus the normal biosynthesis was replenished in the cell. However, it has been shown that ability form rods are reduced in the *H. volcanii* strains that have interrupted biosynthesis of uracil and tryptophan (Halim *et al.*, 2016).

3.5 Materials and Methods

3.5.1 Archaeal strains

Haloferax volcanii H26 (ΔpyrE2) or H98 (ΔpyrE2 ΔhdrB) (7), containing the pHV2-based plasmid pTA962 (8), were used as wild-type strains. *H. volcanii* ID59 (4), transformed with pTA962, was the cetZ1 knockout strain used (based on H98). For expression of cetZ1.E218A (dominant-inhibitory mutant), *H. volcanii* H98+pTA962-cetZ1.E218A was used.

3.5.2 Culture media and general growth conditions

Media were based on the Hv-Ca and Hv-YPC media commonly used for *H. volcanii* (7). In this study, we used defined sources of reagents, which we have found is important for reproducibility. For solid media, Bacteriological Agar (Oxoid LP0011)(10 g/L), was dissolved in the volume of water required for the media by heating in a microwave oven, before mixing with appropriate concentrated stock solutions of pre-heated media reagents (listed below) and autoclaving. Water for all media was obtained from an ultrapure (18.2 MOhm.cm) water purification system (Sartorius).

Hv-Ca medium (7) contained: 144 g/L NaCl (Sigma S6191), 21 g/L $MgSO_4.7H_2O$ (Sigma M1880), 18 g/L $MgCl_2.6H_2O$ (Sigma M2393), 4.2 g/L KCl (Sigma P5405), 12 mM Tris-HCl (pH 7.4) (Sigma RDD008, buffered with AR grade HCl), 3 mM $CaCl_2$ (Sigma C5670), and 5 g/L Casamino Acids (Oxoid LP0041). The medium was then autoclaved. Once cool, a filter-sterilized vitamins concentrated stock solution (1000x), containing 1 g/L thiamine (Sigma T1270) and 0.1 g/L biotin (Sigma B4639), was added (1 ml per L of medium). To prepare Hv-Cab medium, a trace-elements concentrated stock solution (100x) was also added (10 mL per L of medium). The 100x trace-elements stock solution contained: 5 g/L $Na_2.EDTA.2H_2O$ (Sigma E1644), 0.8 g/L $FeCl_3$ (Sigma 157740), 0.05 g/L $ZnCl_2$ (Sigma 793523), 0.01 g/L $CuCl_2$ (Sigma 751944), 0.01 g/L $CoCl_2$ (Sigma 232696), 0.01 g/L H_3BO_3 (Sigma B6768), 1.6 g/L $MnCl_2$ (Sigma 328146), 0.01 g/L $NiSO_4$ (Sigma 656895), and 0.01 g/L $Na_2MoO_4.2H_2O$ (Sigma M1003); the pH of the solution was adjusted to 7.0 with NaOH (AR grade, Sigma), and then the obvious brown

precipitate that formed on neutralization was removed by 0.2 µm sterile filtration. Stock solutions were stored at room temperature in sterile aliquots.

Hv-YPC medium was prepared as per the Hv-Ca medium above, except the supplementary vitamins and trace-elements were omitted, the Casamino acids were used at a concentration of 1 g/L, and 5 g/L Yeast Extract (Oxoid LP0021) and 1 g/L Peptone (Oxoid LP0037) were included. To prepare "Hv-YPCab" medium, the 100x trace-elements stock solution was added (10 mL per L of medium) to Hv-YPC after autoclaving and cooling.

Most cultures (5 ml) were grown in sterile 50 mL Falcon tubes, incubated at 45°C with shaking at 200 rpm in a GFL 1092 rotary-shaking water bath (the tube's lid was maintained loosened) unless otherwise indicated. *H. volcanii* was initially grown on solid medium followed by continuous growth in liquid medium (diluted once per day), to maintain steady logarithmic growth prior to sampling, which was only done after the culture had been growing steadily in continuous log-phase for at least 2 days.

3.5.3 Nutrient depletion in liquid cultures

To examine the growth effects of omitting individual media components (Figure 3.1), *H. volcanii* was first grown into a steady log phase in Hv-Cab medium. When the OD (600 nm) reached 0.5, a sample was withdrawn and the cells were washed 3 times by centrifugation at 5000 rpm in a microcentrifuge for 5 min, followed by resuspension of the cell pellet in same volume of 18% buffered saltwater (BSW), which was prepared as the buffered salts solution described above for Hv-Ca medium, omitting Casamino acids. The resuspended cells were then diluted (1:100) separately into fresh Hv-Cab medium (control), or Hv-Cab prepared without addition of vitamins, trace elements, or Casamino acids.

3.5.4 Time-course studies of rod development

In order to obtain a standardised way of observing rod cells, and analysing rod-development, time course studies of the early stages of liquid culture growth were carried

out (Figure 3.4). The *H. volcanii* strain was streaked onto an agar plate made from the same medium as chosen for the assay (e.g. Hv-YPCab), and then the plate was incubated in sealed humidified bag at 45°C for 4 days. Colonies were collected from the surface with a microbiological loop, and suspended in 5 ml of the liquid medium, sufficient to give an OD (600 nm) > 0.05. The OD was immediately adjusted to 0.05 by dilution with fresh pre-warmed medium, marking the start of the time-course. Samples were withdrawn as required for microscopy or other analyses (Figure 3.4).

To observe trace element limitation over a time-course (Figure 3.4), cells were first grown into steady log phase growth in Hv-Cab medium at 45°C, with shaking at 200 rpm (5 mL culture). A sample of the culture was withdrawn and centrifuged at 5000 rpm for 5 min in an Eppendorf microcentrifuge. The supernatant was discarded, and the cells were then washed by re-suspending the pellet in 0.1 mL of 18% BSW. The wash was repeated three times, and then the cells were finally re-suspended in 0.1 mL 18% BSW and then spread onto Hv-Ca agar plate(s). The plate(s) were placed into a plastic bag and incubated at 45°C for 4 days. Liquid Hv-Ca (5 mL) was added to the plate surface, and the cells were re-suspended. The OD (600 nm) was adjusted to 0.05 with Hv-Ca medium, to start the time course (45°C at 200 rpm incubation).

3.5.5 Microscopy

Samples were prepared by mounting a 2 µl volume of culture (concentrated where necessary by centrifugation and gentle resuspension) onto a slide prepared with a ~170 µm thick, 1% agarose pad containing 18% BSW (4). Phase-contrast images were acquired with a Zeiss AxioPlan2, or a V3 Delta Vision Elite (Applied Precision Inc., a GE Healthcare Company, Issaquah, USA) microscope, with 1.4 NA phase-contrast objectives. Images were analysed using the MicrobeJ plug-in for ImageJ (9). The cell circularity ($4\pi \times \text{area} / \text{perimeter}^2$) was measured on the interpolated contour generated using the particle medial axis and the specified value of the width measured along the medial axis. Circularity values range between 0 and 1. Cell elongation was calculated as the inverse of the circularity.

For live-cell imaging, a CellASIC ONIX microfluidics system with bacterial (B04A-03) plates was used with a Nikon Ti inverted microscope equipped with an incubated stage

(42°C). The four flow chambers were initially washed (at 5 psi for 5 min) with 1 mg/mL Bovine Serum Albumin (BSA) in phosphate-buffered saline followed by 18% BSW. Cells were loaded into the chambers as per the manufacturer's instructions, and the chambers were perfused with medium at 2 psi for 20 h, with time-lapse images recorded at 10 min intervals.

3.5.6 Coulter cytometry

Culture samples were diluted (1/1000) with 18% w/v BSW and then analysed with a Multisizer 4 Coulter cytometer (Beckman-Coulter) as described previously in Section 2.9.2.

3.5.7 Western blotting

Western blotting was carried out, as described previously in Section 2.10.3.

Acknowledgements

We are grateful for use of the equipment and technical support of the UTS Microbial Imaging Facility.

CHAPTER 4

CHARACTERISATION OF CETZ1 LOCALISATION IN *HALOFERAX VOLCANII* MORPHOGENESIS USING A NEW KNOCKOUT STRAIN AND A FLUORESCENT PROTEIN FUSION

DISCLOSURE

I certify that I carried out significant work presented in this manuscript. The section on the designing and construction of the fluorescent vectors presented in this chapter was a project carried out in collaboration with Dr Solenne Ithurbide. Contributions for this project were as follows

- Roshali T. de Silva and Iain G. Duggin conceived the project idea and designed all the experiments presented.
- Solenne Ithurbide designed the fluorescent vectors.
- Roshali T. de Silva constructed the fluorescent vectors, performed the functional assays presented.

4.1 Introduction

Cell shape dynamics play an important role in cell survival. However, little is known about the cell shape regulation in archaea. The recently discovered tubulin superfamily protein CetZ1 indicated a cell shape control function in *Haloferax volcanii,* the haloarchaea used in this study. Mainly it supports the cell shapeshift from plate (flat and round) shape to rod shape. However, further characterisation is needed to understand how CetZ1 modulates cell shape in *H. volcanii*. Having a *cetZ1* knockout strain that can complement *cetZ1* and a functional CetZ1 fluorescent fusion protein are important elements in characterising *cetZ1* function. Therefore, the primary goal of the study present in this chapter was to achieve the above mentioned two elements and characterise CetZ1 localisation during morphogenesis.

The next sections describe the genetic modification system that was used to create a *cetZ1* gene knockout and the previous attempts that have been taken to characterise CetZ1 localisation. Moreover, as we improved the function of CetZ fluorescent protein fusion by using a peptide linker, the previous studies that provided the basis for this approach will be discussed in the next sections.

4.1.1 *Haloferax volcanii* gene knockout system

Haloferax volcanii is widely used as a model organism for molecular genetic studies as it has an efficient transformation system, several shuttle vectors, selectable markers, known genome sequence, and a powerful system for genetic modification of the genome (Allers *et al.*, 2004). In the present study, the *pyrE2* gene marker system is used to transform the cells of a uracil auxotroph (Δ*pyrE2*), deficient in orotate phosphoribosyltransferase (Bitan-Banin, Ortenberg and Mevarech, 2003). Homologous recombination, which naturally occurs in *Haloferax*, is used to integrate a plasmid with the desired sequence and *pyrE2* genetic marker into the *H. volcanii* genome, in the first step known as "pop-in" (Figure 4.1). The transformed cells can be selected by culturing the cells in media that have no uracil. In the second step, the "pop-out" recombination, the desired knockout strains can be selected by plating them on media with uracil and 5-Fluoroorotic acid (5

FOA). The cells which do not have the *pyrE2* gene (pop-outs) are resistant to 5-FOA (Allers *et al.*, 2004, Allers *et al.*, 2010). Depending on the position of the pop-out recombination, the resulting clones will contain either the original wild-type sequence or the desired mutation contained on the original plasmid (Figure 4.1). These strains may be identified by using diagnostic PCR analysis.

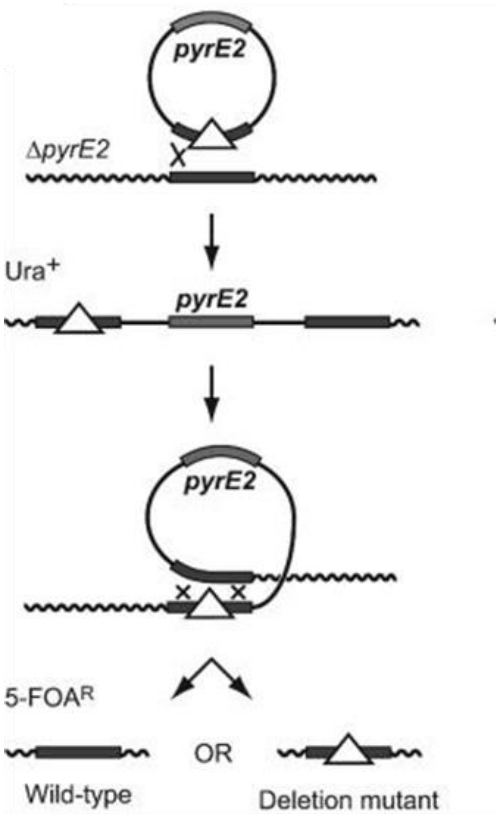

Figure 4.1: *Summary of H. volcanii gene knockout system based on pyrE2 genetic marker.*

A suicide plasmid (i.e. non-replicative) containing a uracil selection marker and the flanking regions of the desired mutation could incorporate into the H. volcanii chromosome via homologous recombination. The subsequent pop-out of the plasmid could result in two genetic outcomes: WT and the mutant. A diagnostic PCR identifies mutants. The image was adapted from (Allers et al., 2004).

4.1.2 The discovery of CetZ1 function in cell shape control

To the best of our knowledge, a functional analysis of CetZ proteins in *H. volcanii* has only been reported once in the study by Duggin *et al.*, 2015. This study has shown CetZ1,

one of the six CetZ homologues, is essential for the phenotypic differentiation of cells from plate shape to rod shape (Duggin *et al.*, 2015). Rods help in the swimming motility of *H. volcanii* (Duggin *et al.*, 2015).

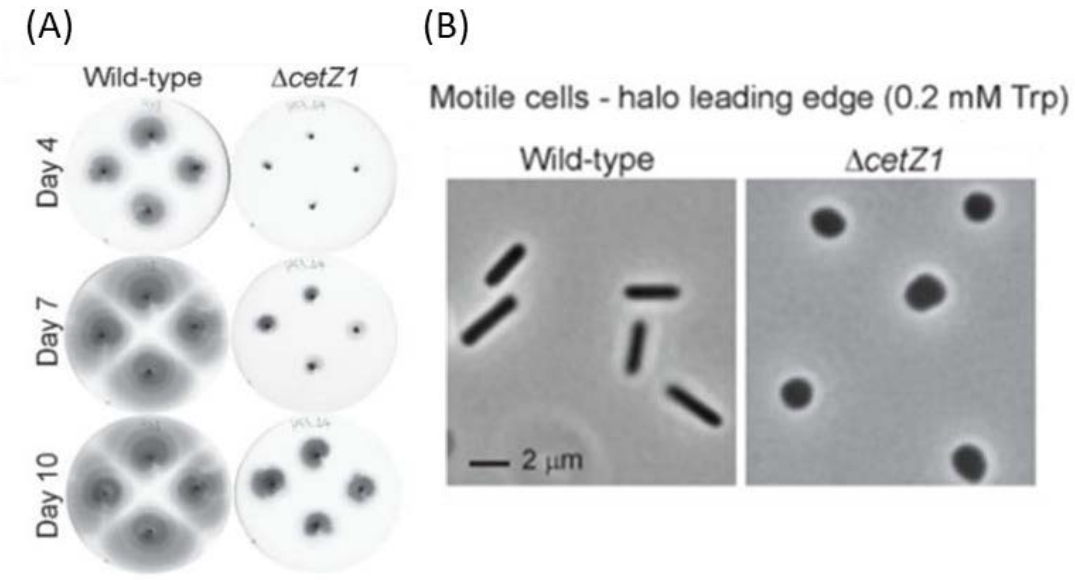

Figure 4.2: *Motility and cell shape comparison of WT and cetZ1 knockout cells.*

(A) Compares the spread of colonies in soft agar medium over ten days in WT and the ΔcetZ1. The spreading of the colony indicates the cell's ability to swim. (B) shows the cell shapes in the leading edge of the spreading colony in WT and the ΔcetZ1 (Duggin et al., 2015).

In a motile halo of a spreading *H. volcanii* colony in soft agar medium, the cells displayed a rod-shaped morphology while the rest of the cells in the colony were plate-shaped. Knocking out *cetZ1* resulted in a severe defect in motility (Figure 4.2). The *cetZ1* knockouts were unable to form rods, whereas the overexpression of CetZ1 induced the rod formation in the WT background. Inhibition of rod formation in the WT cells, when the GTPase mutant CetZ1.E218A was expressed further implies CetZ1 plays a crucial role in modulating the cell shape. However, the *cetZ1* knockout strain, ID59 (Duggin *et al.*, 2015), could not be complemented by a plasmid copy of *cetZ1* making it unsuitable for further characterisation of CetZ1 function by studying the localisation and the structure-function relationships. This chapter describes the design of a new *cetZ1* knockout strain that can be complemented.

4.1.3 Previous studies of CetZ1 localisation in *Haloferax volcanii*

According to the previous localisation studies carried out in *H. volcanii* H98 wild type background, CetZ1 displayed a very dynamic cell envelope associated localisation. However, the well-developed rods in the motile halo of the motility assay showed a less dynamic end-capped localisation as single or multiple foci. These localisation studies were carried out using CetZ1 fusions of three different fluorescent proteins, smRSGFP, the A206K mutant of smRS-GFP (blocks GFP self-association) and mCherry, which were expressed under a tryptophanase inducible promoter (Large *et al.*, 2007). All these CetZ1 fusions exhibited a comparable localisation pattern (Figure 4.3) (Duggin *et al.*, 2015).

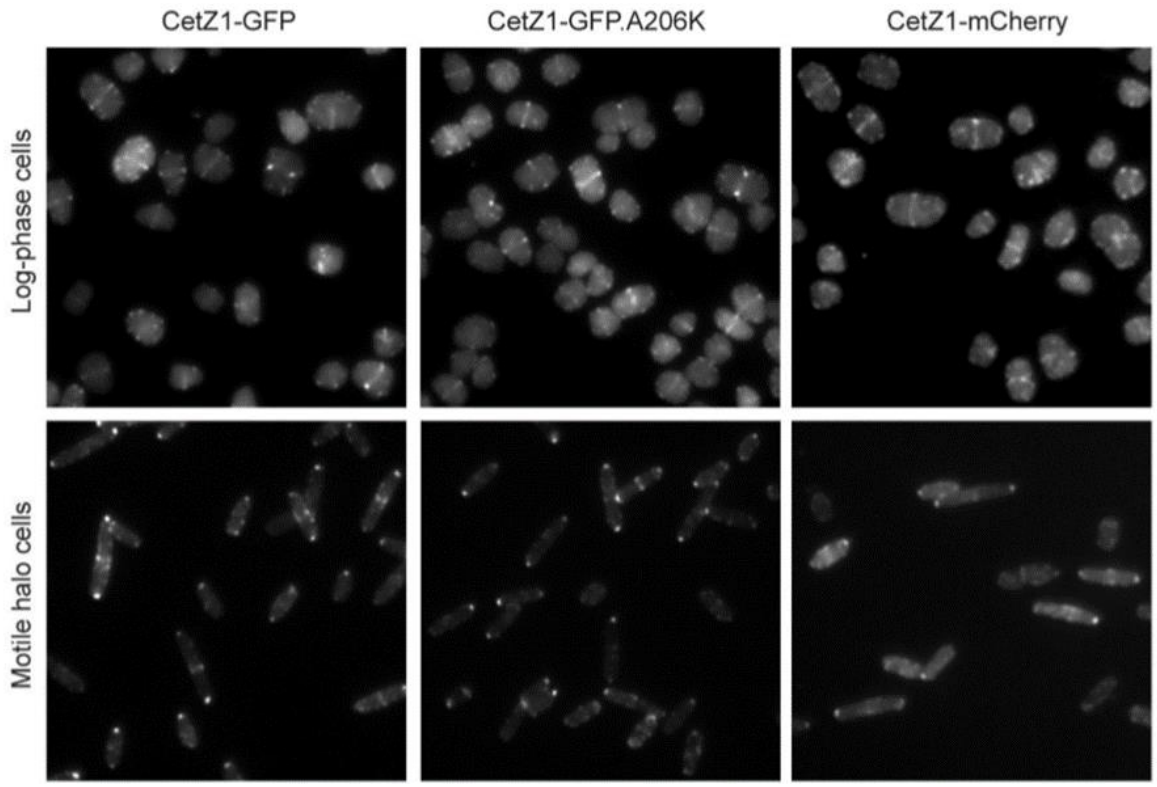

Figure 4.3: *CetZ1 localisation in the WT background.*

The localisation of CetZ1 fusions with GFP, GFP.A206K and mCherry in cells during log-phase (top row) and rod cell in the motile halo (bottom row) (Duggin et al., 2015).

A signature attribute of cytoskeletal filaments that are important for the function is its dynamic instability. Cytoskeletal filaments grow by polymerising its subunits, and after reaching a certain length, it begins the depolymerisation which breaks down the polymer. Sometimes a growing polymer can pause and restart the polymerisation. Furthermore, a depolymerising polymer with peeling protofilaments can sometimes be rescued. This stochastic growth and shrinkage behaviour of filaments is known as dynamic instability (Mitchison and Kirschner, 1984). Although the CetZ1-GFP fusion formed dynamic filaments (formation and retraction of filaments) during overproduction that resembles the typical behaviour of tubulin superfamily polymers, it was unable to induce the rod cell formation (in WT cells) like the untagged CetZ1 suggesting this fusion was not fully functional. Therefore, the present study aimed to screen a new CetZ1 fluorescent fusion protein by utilising the methods that have been shown to improve the function of fusion proteins.

4.1.4 Designing functional fusion proteins in biology

Despite the difficulty in constructing a fully functional fusion protein (Moore *et al.*, 2017), as tethering an alien protein could result in unpredictable effects on the protein's function such as mislocalisation, aggregation, or degradation, these fusion proteins often have many applications in biology. Fluorescent fusion proteins are frequently used to understand protein localisation and dynamics in a cell. The utilisation of a linker between the two proteins has been shown to be advantageous in improving the function of protein fusions. Protein complexes found in nature often consist of such linkers and properties of these natural linkers have been used as a guide to design the linkers for the synthetic fusion proteins (George and Heringa, 2003, Argos, 1990). Several attributes such as length, hydrophobicity, amino acid residues, and secondary structure of the linker contribute to the proper design of the fusion protein (Chen, Zaro and Shen, 2013). In natural protein complexes, the increased rigidity of the linker is preferred as it could help to decrease the non-native interactions between the linker and the active protein domains, thus improving the separation of the connecting proteins (Argos, 1990). Linkers with the amino acid proline increase the stiffness of the linker, thereby ensuring the structural integrity and the proper biological activity of individual proteins in many natural multi-

domain proteins. Therefore, proline is a favoured choice in many natural linkers (Turner *et al.*, 1993, Bhandari *et al.*, 1986). Also, Threonine and Glutamine are commonly detected in natural linkers among a few other preferred polar uncharged or charged amino acids (Argos, 1990, George and Heringa, 2003). The secondary structure of the linker also plays an important role in constructing a functional multi-domain protein. While the rigidity of the non-helical natural linkers is improved by the presence of proline residues, having an α-helical secondary confirmation could also increase the rigidity regardless of the constituent amino acids due to hydrogen bonds between helical turns to make a closely packed α-helix (Amet, Lee and Shen, 2009). Moreover, fast assembly of the helical linker helps to reduce the interactions between active protein domains and the linker, thus establishing the correct folding of the protein (Aurora *et al.*, 1997).

Several synthetic linkers have been designed over the years combining the properties of natural linkers to achieve a desired biological function. These linkers can be categorised into three types: flexible linkers, rigid linkers and *in vivo* cleavable linkers. In the present study we made use of the properties of rigid linkers and flexible linkers to create a CetZ1 fluorescent fusion protein. Most (George and Heringa, 2003) natural linkers are rigid linkers as this efficiently separates connecting proteins reducing any interruption to their function. A synthetic rigid linker with the amino acid sequence $A(EAAAK)_nA$ (n = 2-5) has shown an effective functional separation of connected proteins (Arai *et al.*, 2001). Fluorescent resonance energy transfer (FRET) analysis had indicated reduction in FRET efficiency with the increase in the length of the linker when two fluorescent proteins (cyan/CFP and yellow/YFP) were fused via the above rigid linker (Figure 4.4).

Additionally, the FRET efficiency in a fusion protein with a rigid linker is lower than the same in a fusion protein with a flexible linker of the same length (Li *et al.*, 2016). The length of the linker can be optimised to gain maximum biological activity. However, increasing the length of the linker could exacerbate the probability of proteolytic cleavage. Similar to the natural linkers, the synthetic linkers achieve the rigidity either by forming a helical conformation (Eg: $A(EAAAK)_nA$) or by using multiple proline residues in the linker.

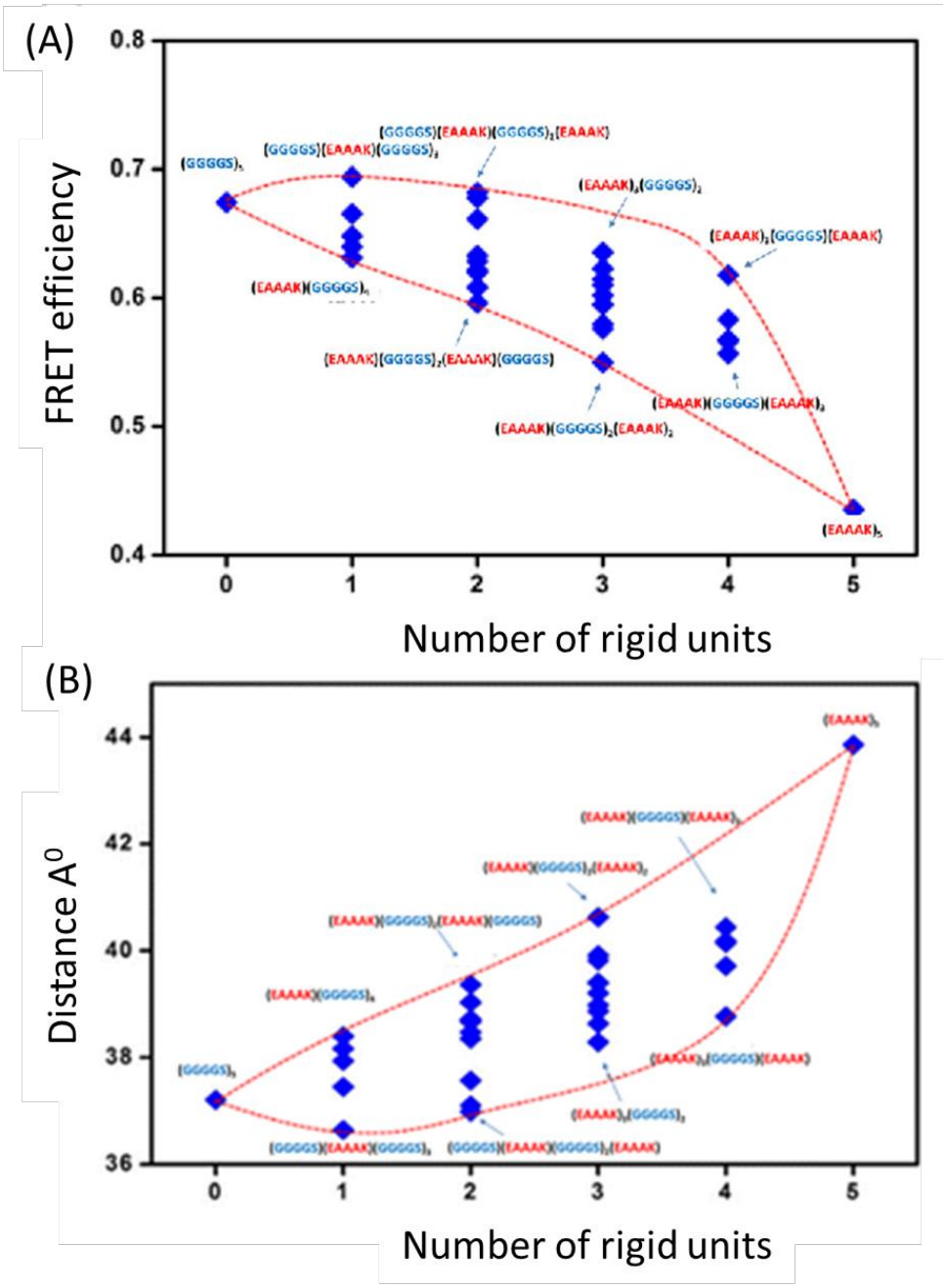

Figure 4.4: *Effect of linker rigidity on FRET efficiency and the separation between a CFP and YFP fusion protein.*

This study by Li et al., 2016 tested 32 different fusions, and each blue data point indicates a fusion with a unique linker. Linker sequences are shown for the data points marked by an arrow (red sequence- rigid unit, blue sequence- flexible unit). The red dashed line of graph (a) shows the change in FRET efficiency with the rigidity of the linkers and the that of the graph (b) shows the distance or the separation between CFP and YFP with the rigidity of the linker. The image adapted from (Li et al., 2016).

Flexible linkers are used in situations where a certain degree of mobility of active domains is required for the proper biological function. It could act as a passive linker to maintain the useful interaction between the proteins. Flexibility is primarily achieved by incorporating small nonpolar or polar amino acids into the linker. The commonly used flexible linker—referred to here as the "GS linker"—$(GGGGS)_n$—is rich in glycine. Glycine is the smallest amino acid and, most suitable candidate to provide flexibility (Argos, 1990). Serine residues help in providing both flexible and stability to the linker, the latter achieved by forming hydrogen bonds in an aqueous solution. As for the rigid linker, the length of the flexible linker can be optimised to ensure the proper folding and the biological function of the fusion protein. The GS linker consisting of four repeats (n=4) has been tested and shown to have no functional impairment due to proteolytic digestion. In addition to the GS linker, other flexible linkers have been designed incorporating other small amino acids such as glutamic acid and lysine primarily to improve the solubility in water (Argos, 1990, Bird *et al.*, 1988). Having a heterogeneity in the constituent amino acids in the linker also reduces the homologous repeats in the DNA coding sequence, thereby preventing the loss of the linker by homologous recombination.

Both rigid and flexible linkers establish a covalent attachment between the connecting proteins to function as a protein complex. This type of permanent connection could sometimes create problems such as a reduction in the biological activity and improper protein folding or assembly due to the steric hindrance. The choice of the linker type depends on the function of the protein, and the explicit design can be often unpredictable. Although, each of these linker types have their pros and cons; generally, all of them have the potential to help to improve the biological activity by ensuring the correct folding of the protein. With the advancement of fusion protein design, computational tools and databases such as LINKER are now available to help design the optimum linkers (Chen, Zaro and Shen, 2013). This chapter describes the attempts we made to optimise the different linker types to construct functional CetZ1 fusions with fluorescent proteins.

4.1.5 Aims and the content of the results chapter

In this chapter, we made attempts to understand the CetZ1 localisation dynamics in *H. volcanii* during morphogenesis. The approaches that were taken to create the new CetZ1 knockout stain, ID181 (a CetZ1 in frame knockout strain) will be discussed as the previously published ID59 failed to complement the CetZ1 function (Duggin *et al*., 2015).

Furthermore, CetZ1 localisation in *H. volcanii* H98 WT motile cells differentiated on a soft agar medium has previously been tested using CetZ1-smRSGFP (pIDJL40-*cetZ1*) in which CetZ1 displayed a cell envelope associated localisation. However, this fluorescent fusion was not fully functional as it has failed to induce rod formation during overexpression in the WT background, limiting its use in characterising CetZ1 localisation (Duggin *et al*., 2015). Therefore, in the present study we adopted a new CetZ1-mturquoise2 (CetZ1-mTq2) fusion with a flexible linker in between CetZ1 and mTq2 allowing the fusion to maintain function by 81%. The next sections will also cover, the approaches that have been taken to construct this improved fluorescent fusion protein. Finally, the CetZ1 localisation under the rod cell formation conditions will be explored using ID181 expressing CetZ1-mTurquoise2.

4.2 Results

To characterise the CetZ1 localisation dynamics during cell shape changes, development of a *cetZ1* knockout strain that can be complemented, and a functional CetZ1-fluorescent protein fusion were crucial.

4.2.1 Design, construction and complementation of CetZ1 knockout strains

The complete *cetZ1* gene, HVO_2204 was deleted in the previous *cetZ1* knock strain, *H. volcanii* ID59 used in the study by Duggin *et al.*, 2015. However, plasmid-borne *cetZ1* was unable to complement the motility defect in *H. volcanii* ID59.

Attempts were made to construct a new *cetZ1* knockout strain that can complement the CetZ1 function via an expression of plasmid-borne *cetZ1*. The *cetZ1* gene is 1118 bp long, and this includes a potential overlapping region of 32 bp with the downstream HVO_2203 gene (a hypothetical protein) according to NCBI annotations. As the annotation of HVO_2203 is based on many gene prediction algorithms, the exact gene length of HVO_2203 is not clearly defined. Based on the assumption *cetZ1* and HVO 2203 might be a part of an operon, two new knockout strains were designed, confining the deletion into the middle part of the *cetZ1* gene. Generally, gene promoters are located upstream on the genes, near the transcription start sites. Therefore, the first seven amino acids of the gene were kept intact in both knockouts to prevent the disruption of a possible promoter region. The predicted overlapping region with the downstream HVO_2203 gene was also retained to prevent any interruption for the expression of this hypothetical protein (Figure 4.5). Thus, if *cetZ1* and HVO_2203 are part of an operon and have a functional correlation, this current *cetZ1* knockout design would not hinder the complementation of cell shape control by plasmid-borne *cetZ1* in the new Δ*cetZ1*. The transcriptional coupling is a common phenomenon seen among many prokaryotes. For instance, in *E. coli*, there are several examples where one mRNA molecule codes for more than one protein (Levin-Karp *et al.*, 2013). Therefore, the transcription of the mRNA molecule with the correct reading frame is essential for the ribosomes to accurately read

the mRNA code and move along the mRNA during translation. In order to test whether there is crosstalk in gene expression between HVO_2203 and HVO_2204, first, an in-frame (IF) deletion within *cetZ1*was designed.

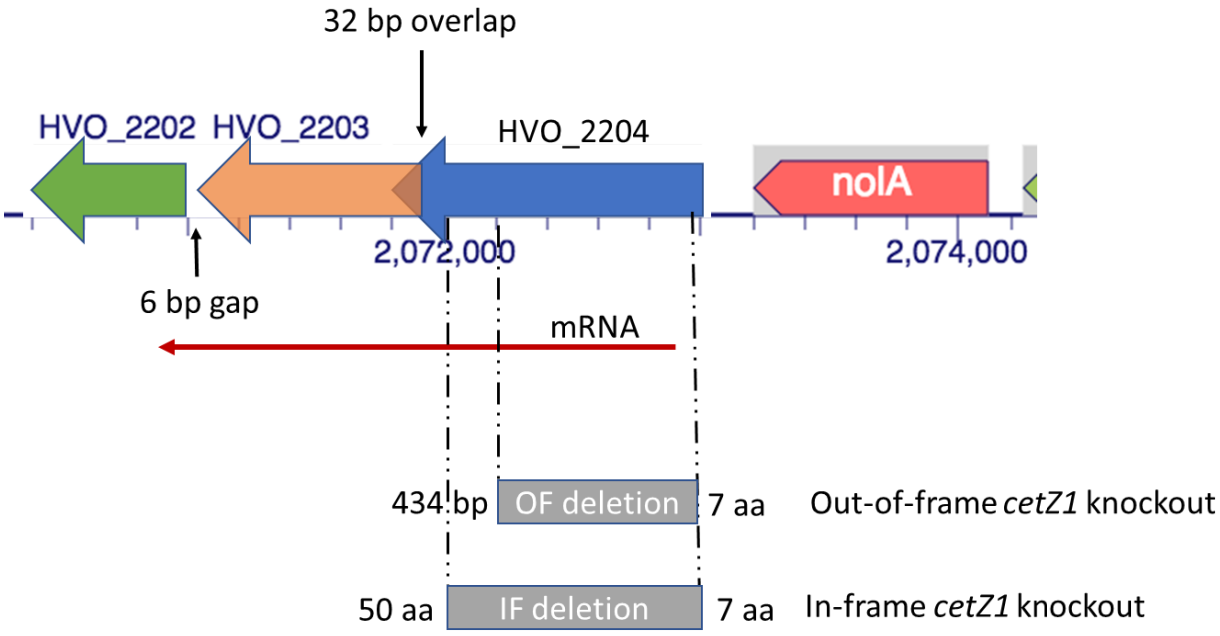

Figure 4.5: *Schematic representation of the cetZ1 (HVO_2204) deletion construct.*

Dark red arrow indicates the assumed direction of ribosome handover on the predicted mRNA molecule. The black arrow shows the predicted overlap (32 bp) region between HVO_2204 with HVO_2203. The image also highlights that HVO_2204 IF deletion region is larger than the OF deletion region.

In IF deletion, the correct reading frame was maintained to minimise any possible effects on ribosome handover to the closely linked downstream gene during translation. The HVO_2204 (cetZ1) IF deletion was designed to disrupt the core N-terminal GTPase domain and the C-terminal domain of CetZ1 protein while the last 50 amino acids remained which includes the whole C-terminal tail (Helix 11). It was hoped that the remaining parts would not interfere with normal CetZ1 functions during complementation. An out-of-frame (OF) deletion within HVO_2204 was also made to explore the transcriptional coupling between HVO_2203 and HVO_2204 genes. If these two genes are translated from the same mRNA molecule, OF deletion would disrupt the correct translation of HVO_2203. The OF deletion could also help to avoid any potential

dominant-inhibitory activity that the in-frame deletion may have. The IF deletion disrupted a larger proportion of the cetZ1 gene than the OF deletion (Figure 4.5). The construction of plasmids containing the deletion regions, followed by the construction of the knockout strains is described in 4.1.2 and 4.2.2, respectively.

First the regions (~700 bp long) that flanks the deletion region were PCR amplified. These upstream and downstream flanks were then joined by the overlap extension PCR to create the deletion region which subsequently cloned into a suicide plasmid, pTA131 (Table 2.3). The plasmids with *cetZ1* deletion regions were confirmed using digestion analysis and sanger sequencing before being introduced into *H. volcanii* (Figure 4.6). The plasmid with the deletion sequence could incorporate into *H. volcanii* genome via natural homologous recombination. The plasmid sequence would eventually "pop-out" retaining the deletion sequence when the cells grow in a non-selective medium for a few generations. Although *H. volcanii* displays efficient homologous recombination, the PCR amplification of the homologous flanking regions of the *cetZ1* deletions was troublesome most probably due to the high (65%) GC content in the *H. volcanii* genome. This problem was overcome by using high annealing temperature (72 ºC) and PCR additives such as betaine and magnesium, which generally increase the PCR efficiency with GC-rich templates.

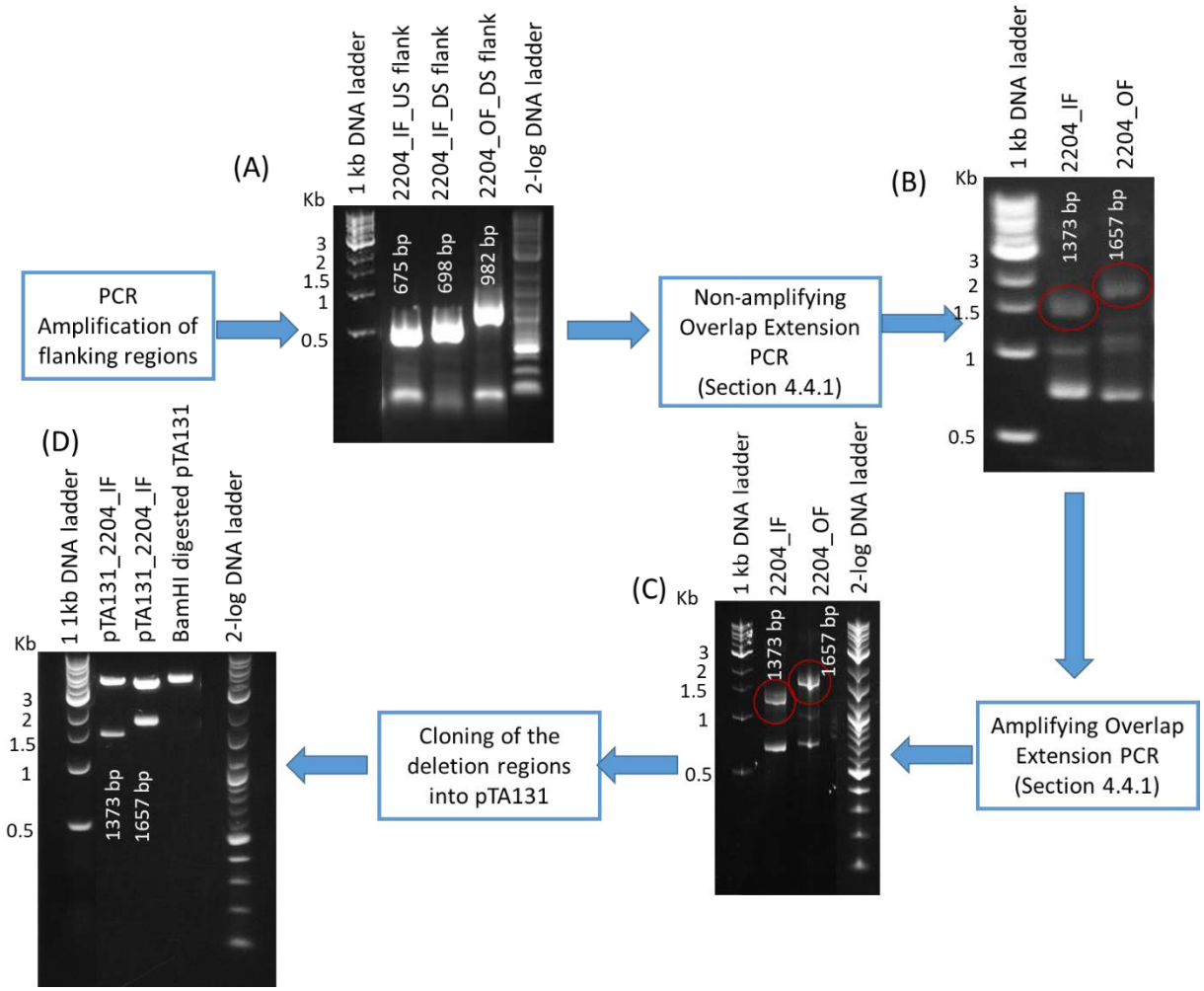

Figure 4.6: *Schematic representation showing the steps in the construction of new cetZ1 knockout strains.*

Each blue box describes the experimental step, followed by an agarose gel electrophoresis analysis of the results. (A) The PCR amplified flanking regions of cetZ1 and their expected sizes, to make the cetZ1 deletion. The annotations US and DS represent the up-stream and down-stream, respectively. (B) The joined flanks by non-amplifying overlap extension PCR, to create the complete deletion sequence. (C) The enriched deletion sequence by amplifying overlap extension PCR using end primers. These bands were gel purified and cloned into pTA131 using BamHI and HindIII restriction sites. (D) The digestion analysis (BamHI/HindIII) that confirms the insertion of the expected size (as indicated) into the plasmid which was subsequently subjected to homologous recombination inside the H. volcanii to create the deletion strain.

Following the completion of constructing the knockout strains, the deletion of the *cetZ1* gene in *H. volcanii* was confirmed by a PCR analysis using primers outside of the deletion region (End primers in Figure 4.7) and within the overlap region (overlap primers in

Figure 4.7, Primers listed in Table 4.2) and compared the size of the amplified products in the Δ*cetZ1*strain and the WT. With End primers, larger fragments were amplified from WT gDNA than from knockout gDNA (Figure 4.7). Also, the absence of CetZ1 protein inside the Δ*cetZ1* cells was confirmed by a Western blot analysis (Section 2.9.2).

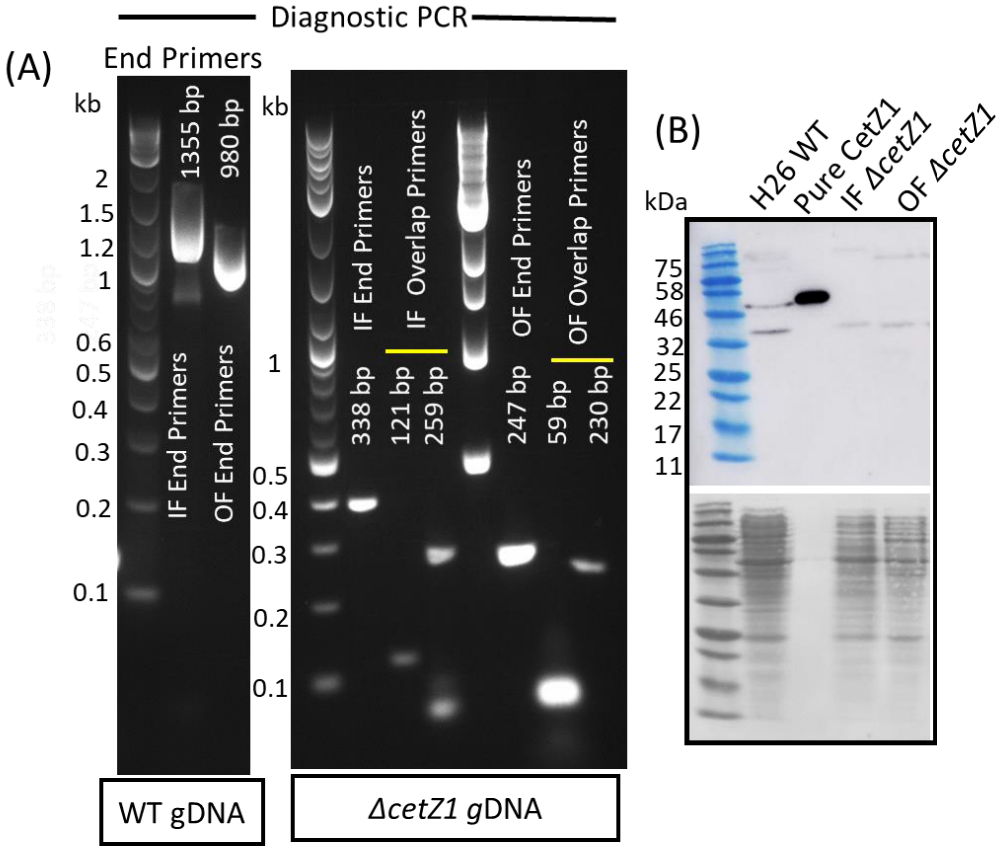

Figure 4.7: *Diagnostic tests to confirm the ΔcetZ1 strains*

(A) Electrophoresis gel showing correctly sized fragments resulting from the diagnostic PCR during pop-out selection. First gel indicates the PCR amplification with end primers when WT H. volcanii gDNA was used as the template. PCR in the second gel was done with gDNA from ΔcetZ1 strains. Electrophoresis gel indicates the correct sized bands resulted from PCR with end primers and overlap primers. (B) Western blot analysis for ΔcetZ1 strains to confirm the deletion of cetZ1. Pure CetZ1(Duggin lab stock) was loaded at 10 μM concentration.

Proteins often display the optimum function at a critical concentration inside the cell. When expressing a protein from a synthetic inducible promoter, it can be important to regulate the induction to maintain the correct expression level. Production of the protein

lower than its critical concentration would prevent establishing the proper function and the overproduction of a protein could sometimes result in unwanted artefactual effects. The rescue of CetZ1 function—cell shape differentiation—from a plasmid-borne *cetZ1* in the Δ*cetZ1* strains was essential to explore the structure-function correlations (Chapter 05). In the present study, *cetZ1* was expressed using the pTA962 expression plasmid (Table 2.3), which uses the tryptophanase inducible promoter to regulate the gene expression (Large *et al.*, 2007). Initially, the suitable tryptophan concentration was screened by expressing *cetZ1* in the IF Δ*cetZ1* strain using a tryptophan concentration gradient and then these expression levels were compared to the CetZ1 protein level in WT H26. According to the Western blot analysis, WT CetZ1 expression level was approximated by 2 mM tryptophan induction (Figure 4.8). Therefore, 2 mM tryptophan was used for all the experiments expressing *cetZ1* via this tryptophanase promoter unless otherwise indicated. Next, to compare the complementation of *cetZ1* in the new in-frame and out-of-frame deletions using the pTA962-*cetZ1* plasmid, motility assays (Section 4.4.5) and the TE depletion rod development assay introduced in chapter 3 (Section 4.4.6) were used. Motility assay screens CetZ1 function by the spread of the colony and TE depletion result in CetZ1-dependent cell elongation.

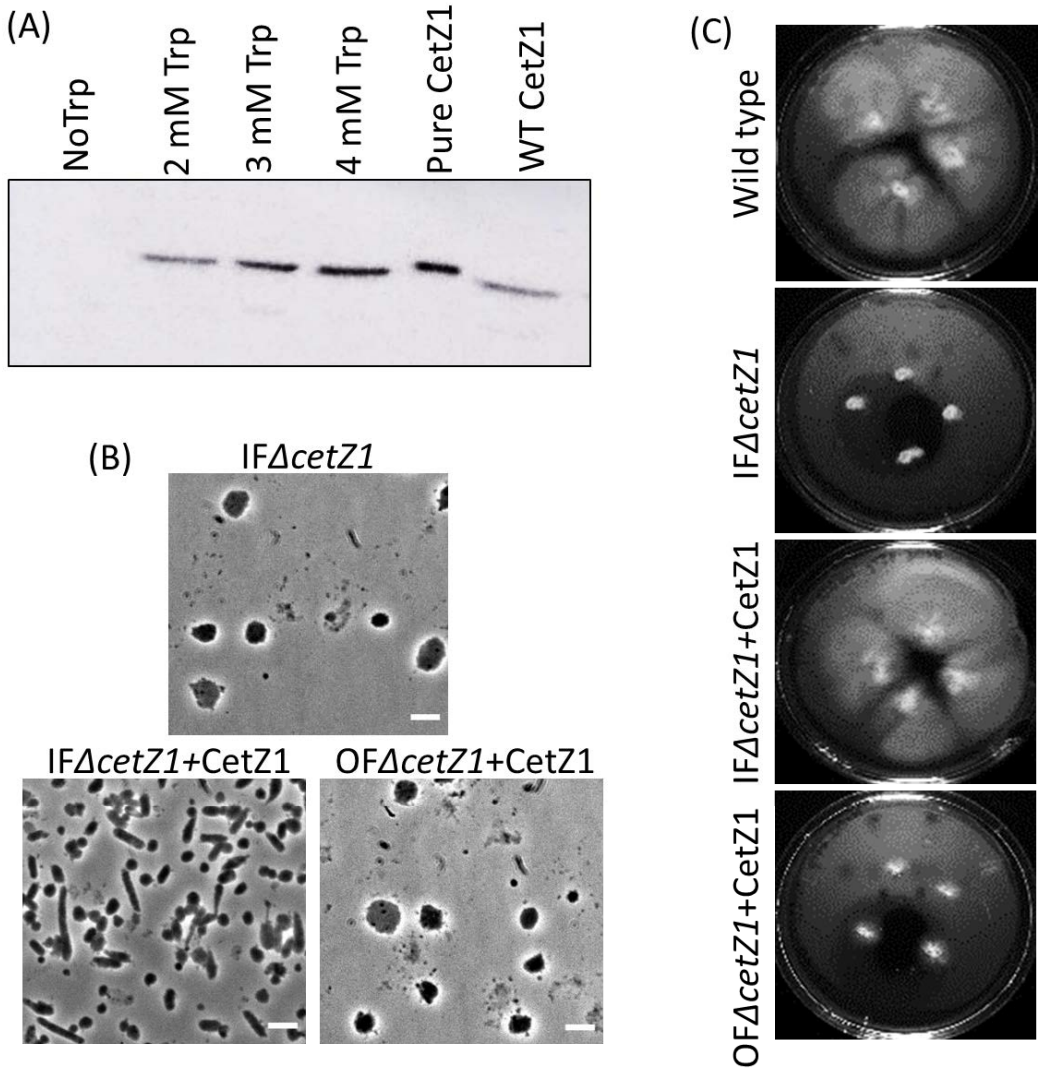

Figure 4.8: *Complementation of CetZ1 function in cetZ1 in-frame and out-of-frame knockouts compared to H. volcanii H26 (WT) strain.*

(A) Western blot analysis comparing CetZ1 expression in WT H26 at mid-log phase and IF ΔcetZ1 strain at mid-log phase when pTA962-cetZ1 was expressed using different tryptophan concentrations. Cells were grown in Hv-Cab liquid medium with the given concentration of tryptophan for 4 days before the Western blot analysis. The concentration of the purified His tagged CetZ1 sample (from Duggin lab stock, UTS) loaded on the gel was 10 µM. (B) The complementation of rod cell formation by pTA962.cetZ1 in ΔcetZ1 strains from TE depletion rod assay (3.5.4). The assay was carried out in Hv-Ca (-TE+2 mM tryptophan), and cells were imaged after 15 hours after the dilution into the liquid medium (Chapter 03, Methods Section). (C) Motility agar plates of WT and ΔcetZ1 strains after 10 days, indicating the rescue of CetZ1 function in the motility assay.

Interestingly, the IF Δ*cetZ1* was successfully complemented by pTA962_*cetZ1* in both functional assays tested—motility assay and trace metal depletion assay—while *cetZ1* completely failed to complement the OF Δ*cetZ1* in both functions—rod cell development and motility (Figure 4.8 and 4.9). These results supported our initial assumption; the transcription of HVO_2203 gene and *cetZ1* are probably coupled. Therefore, the correct ribosome handover that resulted in the correct translation of the downstream gene(s) is essential for the CetZ1 function. Another functional—early-log phase assay—was introduced in Chapter 3 to quantify CetZ1 function. In this assay, CetZ1-dependent rods that peak at 10 h after diluting into a fresh liquid medium from an agar-based medium can be collected for further analysis. A quantitative analysis of cell circularity in the early-log phase assay (Section 4.4.6) was carried out to compare (Figure 4.9C) *cetZ1* complementation in IF Δ*cetZ1*+pTA926_*cetZ1* to the WT H26+pTA962 and the IF Δ*cetZ1*+pTA962. The cell circularity values represent how much a cell can fill up a perfect circle (a perfectly round cell has a cell circularity value of 1). In the analysis, the cell circularity values of three independent technical trials were pooled. The data were compared by normalising the mean cell circularity of WT to 100% and mean cell circularity of Δ*cetZ1* to 0%. According to this analysis, the data for IF Δ*cetZ1*+pTA926_*cetZ1* indicated a 86% complementation of its ability form rods, compared to the WT h6+pTA962 in the early log phase assay (Figure 4.9). Moreover, complementation of IF Δ*cetZ1* by overexpression of pTA926_*cetZ1* was tested by growing the cells in HvCab+4 mM tryptophan at mid-log phase continuously for 4 days. IF Δ*cetZ1*+ pTA926_*cetZ1* displayed an induction in rod formation compared to IF Δ*cetZ1*+pTA962 (Figure 4.9 A and B).

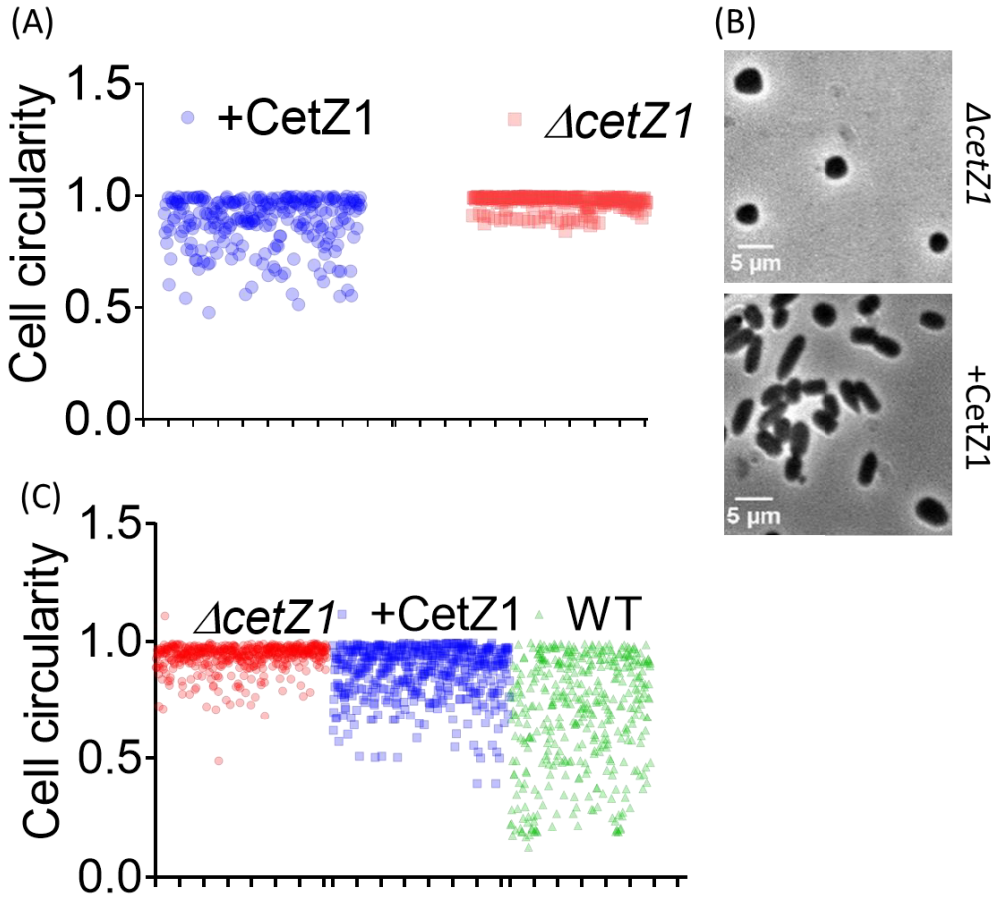

Figure 4.9: *Complementation of rod cell formation by cetZ1 overexpression (4 mM tryptophan) during mid-log growth and cetZ1 WT level expression (2 mM tryptophan) during early-log phase rod assay in the cetZ1 in-frame knockout strain.*

A perfectly round cell has the cell circularity value of 1, and this (Section 2.10.2) number decreases with the elongation of the cell. (A) The decrease in the cell circularity when cetZ1 is overexpressed (continuous mid-log growth in Hv-Cab, with 4 mM tryptophan) in IF ΔcetZ1 background compared to the ΔcetZ1. N=250. (B) Representation of the phase-contrast images of cells after CetZ1 overexpression. (C) Comparison of the cell circularity changes of IF ΔcetZ1+pTA962_cetZ1 to the that of WT (H26+pTA962) in the early-log phase assay. The cells from the early-log phase assay (Section 4.4.6) grown in Hv-YPCab+2 mM tryptophan were imaged at the rod-peak time point (10 h), and cell circularities were analysed using Microbej. The sample size N~500.

4.2.2 Design, construction and complementation of CetZ1 fluorecent protein fusions

The CetZ1 localisation studies were previously carried out in a WT background expressing plasmid-bourne CetZ1-smRSGFP, CetZ1-smRSGFP.A206K (mutation, which blocks the GFP self-association) and CetZ1-mCherry in the study by Duggin *et al*., 2015. All these fusions were cloned at the C-terminal end of CetZ1 with a short spacer. However, these fluorescent fusions were not fully functional as they were unable to induce rod-shaped cells during overexpression in WT cells similar to the untagged CetZ1. Therefore, attempts were made to construct a functional CetZ1-fluorescent protein fusion to express in the above IF *cetZ1* knockout background. This would allow us to characterise the CetZ1 dynamics during cell shape changes in a strain in which all the CetZ1 is fluorescently labelled.

Conventionally, the DNA sequence of the fluorescent protein is cloned to a selected site of the protein of interest by introducing restriction sites. This approach limits the number of insertion sites that can test as the cloning process could be time-consuming. To maximise the number of insertion sites that can screen, GFP was inserted into *cetZ1* using Tn5 transposon insertion approach. GFP was amplified with the primers containing mosaic ends for the binding of Tn5 transposase, and the GFP-Tn5 transposase complex was assembled *in vitro* as described in Picelli *et al*., 2014. The large size of the insert could decrease transposon insertion efficiency. Therefore, 40% PEG8000 was added as a crowding agent to improve the efficiency of *in vitro* transposon assembly. However, this approach was unsuccessful, possibly due to the low concentration of the insert after gel purification of the correct sized *in vitro* transposon assembly, which resulted in inefficient ligation (data not shown).

Secondly, CetZ1- GFP fusions that had GFP sandwiched into a few selected positions based on the crystal structure—D386GFP, Y22GFP, P51GFP, S61GFP, P94GFP, R159GFP, T175GFP, G247-T253GFP, L285GFP, G336GFP, N351GFP—in CetZ1 were tested in IF Δ*cetZ1* by expressing them from the pTA962 expression plasmid. These positions were originally selected, aiming to avoid interruption to the domains that are essential for the function, such as the GTPase active site in the N terminal domain (I.G. Duggin, unpublished). However, all these fusions failed to complement the motility

function in the new IF Δ*cetZ1* background (data not shown), suggesting that none of these internal inserts was fully functional.

As predicting a suitable fluorescent tag is challenging, a method was explored to screen multiple and improved fluorescent fusions efficiently. Many studies have shown that using linkers improves the function of fusion proteins. In order to screen multiple forms of fluorescent fusions, a set of vectors were created with 6 different fluorescent tags and 3 different linkers as described in Section 4.2.3. Fluorescent proteins usually have mix of advantages and disadvantages concerning the key factors such as brightness, maturation time, bleaching time and lifetime that effects imaging process. The slow maturation (the time it takes the fluorescent protein to fold correctly) could reduce bleaching and increase the lifetime of a fluorescent tag. But during imaging of a fast cellular process, a protein with a fast maturation time would be beneficial despite its relatively fast bleaching. Therefore, the choice of the fluorescent protein could depend on the type of the imaging experiment. Moreover, having fluorescent proteins with distinct excitation and emission spectrums would prevent the cross-talk between emission spectra when using multiple fluorescent tags in an experiment. Considering these factors, six different types of fluorescent proteins—mScarlet-I, smRSGFP, mNeonGreen, mCherry, mTurquoise2 and YPet—were chosen.

Next, three linkers were used to separate CetZ1 and fluorescent proteins. The first was flexible, as it was rich in glycine (G linker). The second was rigid, as it was rich in alanine (E linker), and the third was semi-flexible as it contained a combination of glycine and alanine (EG linker). The primary DNA sequence of fluorescent proteins and the linkers were optimised using the OptimumGene^{TM} algorithm (Genscript) to optimise the codon usage bias and avoid restriction sites that may interfere with the cloning, to enhance the efficiency of gene expression in *H. volcanii*.

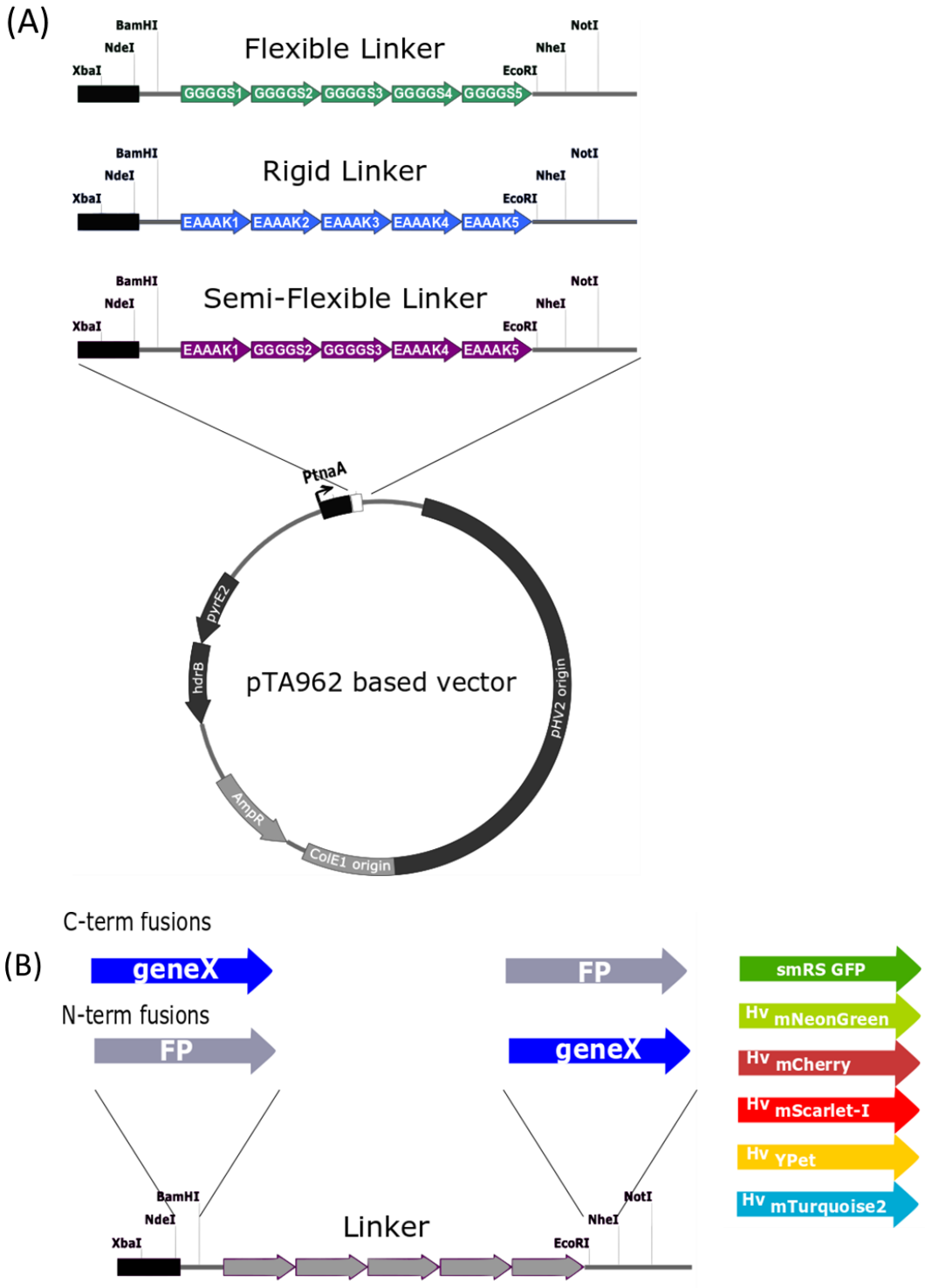

Figure 4.10: *Plasmid design of the fluorescent vectors.*

(A) The design of the basic pTA962 vector and the position of the three different linkers in it. (B) The exact cloning positions of the gene of interest and the fluorescent proteins separated by the linker in the plasmid shown in (A). With appropriate restriction ends, these vectors allow tagging a fluorescent protein into either C terminus or N terminus of a given protein. The plasmid figures were created by Solenne Ithurbide.

The basic plasmid structure was based on the pTA962 expression plasmid, and the primary features are illustrated in Figure 4.10. Also, this vector design allows the duel expression of fusion proteins. A second fusion protein digested using XbaI and NotI can be cloned into the plasmid using NheI and NotI restriction sites (XbaI and NheI have compatible ends for cloning). Although this plasmid design allows both N terminal and C terminal fusions of a given protein, all the fluorescent proteins were cloned to the C terminus of CetZ1. C-terminal fusion has shown a higher apparent functionality in the WT background than the N- terminal fusion during previous trials in developing a functional CetZ1-fluorescent fusion (I.G. Duggin unpublished data). CetZ1 was cloned into these 18 different plasmid constructs (3 linkers x 6 fluorescent proteins), as described in 4.2.3 and then initially screened for function using the motility assay (outlined in Section 4.2.5).

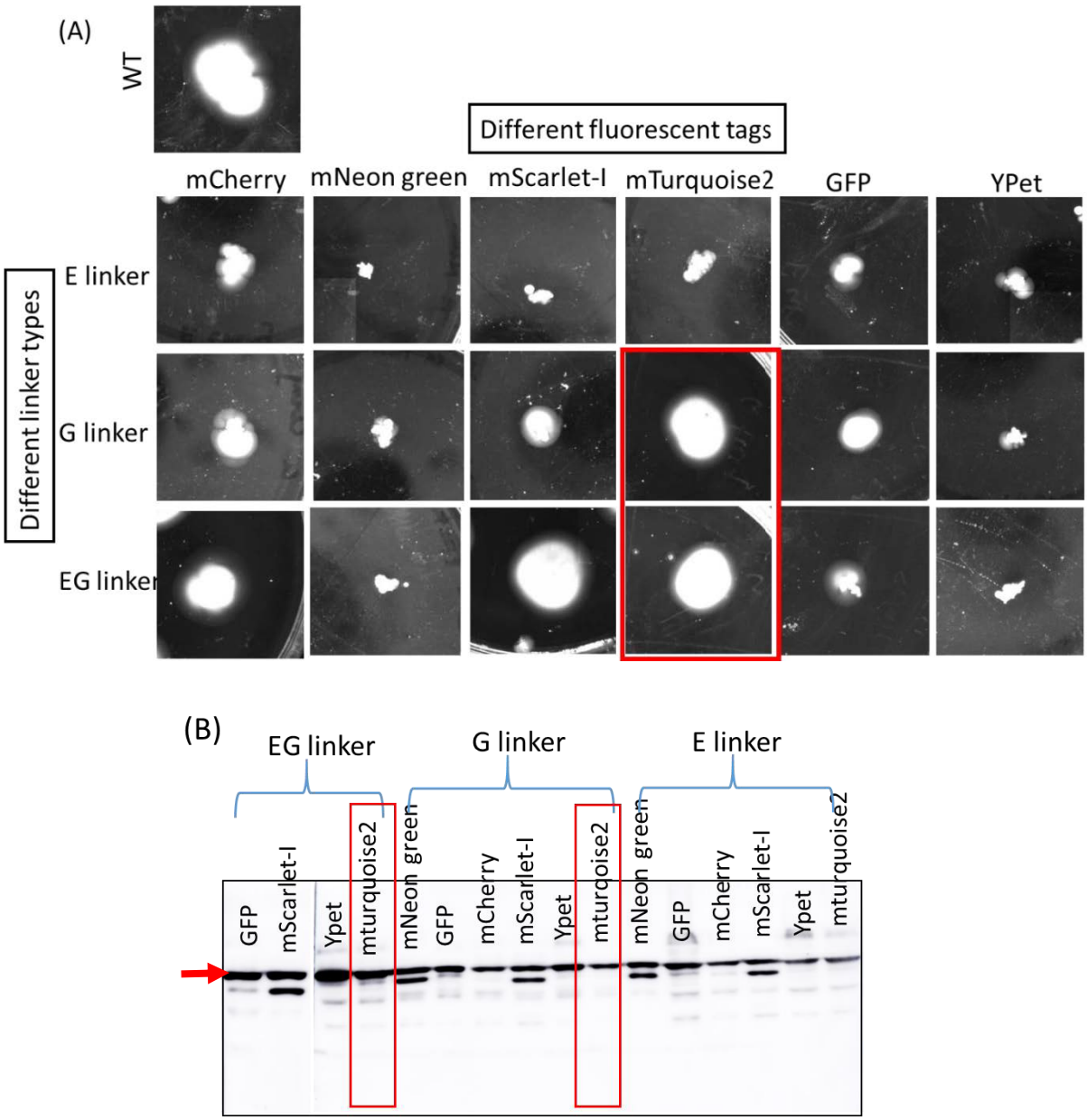

Figure 4.11: *Screening of IF ΔcetZ1 complementation by the fluorescently labelled CetZ1.*

(A) Representative images of the motility screen carried out (in triplicate) for all the CetZ1 fusion constructs. All the fusions were maintained at a mid-log growth (OD_{600} ~0.4) in Hv-Cab liquid media with 2 mM tryptophan for 4 days before subsequent stab-inoculation into the same type of motile agar medium. (B) Western blot analysis of IF ΔcetZ1 cells expressing CetZ1 fluorescent fusions. The cells were grown at mid-log phase for 4 days in Hv-YPCab+2 mM tryptophan before the Western blot analysis. The red arrow indicates the intact fusion protein. The second distinct band below indicates a proteolytic cleavage in some fusion proteins.

All the codon optimised fluorescent fusions were expressed well in *H. volcanii*. However, according to the motility assay screen (Figure 4.11 and 4.12), the highest motility was observed in mScarlet-I, while the mTurquoise2 fusions and mCherry fusions appeared moderately functional. Since the function of the fluorescently tagged protein cannot be predicted prior testing, having this spectrum of vectors would allow screening functional fluorescent fusions of any *Haloferax* protein efficiently.

Consistent with the motility results, mTurquoise2 and mScarlet-I fusions produced rods in early log-phase rod assay as well (Figure 4.12). It is also imperative to ensure the protein fusions are not damaged by any proteolytic cleavage. Therefore, a Western blot analysis was performed using the cells subjected to continuous mid-log induction with 2 mM tryptophan for four days in a Hv-Cab liquid culture expressing each of the fusion proteins. Proteolytic cleavage was detected in all mScarlet-I fusions, while mTurquoise2 fusions remained intact (Figure 4.11). Although all the other fusions were non-functional, they were stable against the proteolytic cleavage, except the mNeonGreen fusion, which also indicated a clipping similar to the mScarlet-I fusion. In the previous study by Duggin *et al*., 2015, CetZ1-GFP displayed a cell envelop associated localisation in *H. volcanii*. Despite the wide differences in functionality of these fusion proteins, many fusions indicated a similar cell envelope associated localisation (Figure 4.12). These results suggest that the fluorescent tags probably interrupt the proper function of CetZ1 by hindering the protein's active domains, but CetZ1 might still be expressed correctly. As many prokaryotic cytoskeletal proteins possess the ability to identify and localise into cell curvatures (Cannon *et al.*, 2019), these fusions probably exhibit similar localisation patterns as the WT. However, mNeonGreen and GFP indicated a slightly different localisation with intense foci.

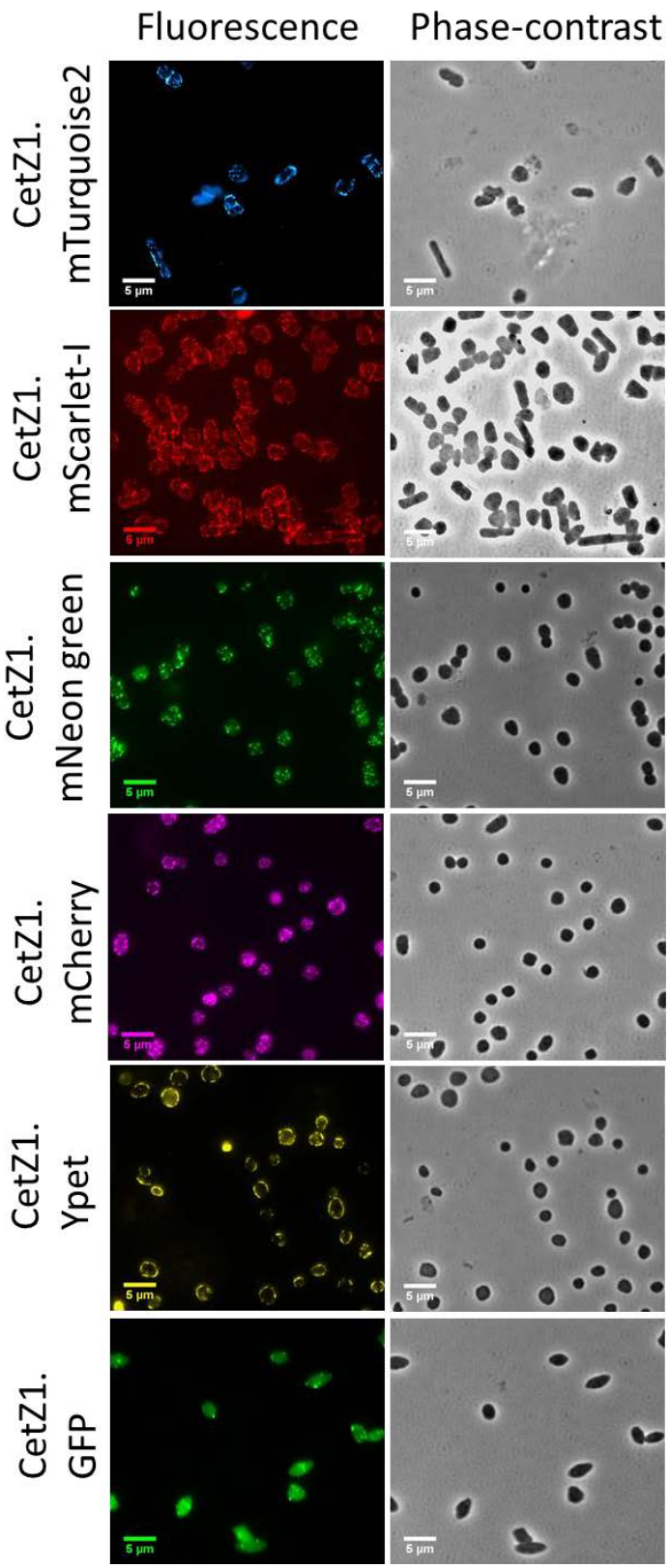

Figure 4.12: *The fluorescent (left) and phase-contrast (right) images of the cells from the early-log phase assay in Hv-YPCab+2 mM tryptophan for all CetZ1 fusions with G linker in IF ΔcetZ1.*

Scale bar = 5 µm.

The ability to develop rods by sole expression of a fluorescently labelled CetZ1 protein in a Δ*cetZ1* background is an important step to continue the characterisation of CetZ1 function. The above results indicated that mTurquoise2 fusions with either a G linker and EG linker could have the highest functionality. The early log-phase rod assay (outlined in Section 3.5.4) was used to quantitatively analyse the complementation of CetZ1 by these two fusion proteins. The test was performed by expressing CetZ1-mTurquoise2 with G linker and EG linker in *H. volcanii* H26 IF Δ*cetZ1* at 2 mM Tryptophan induction.

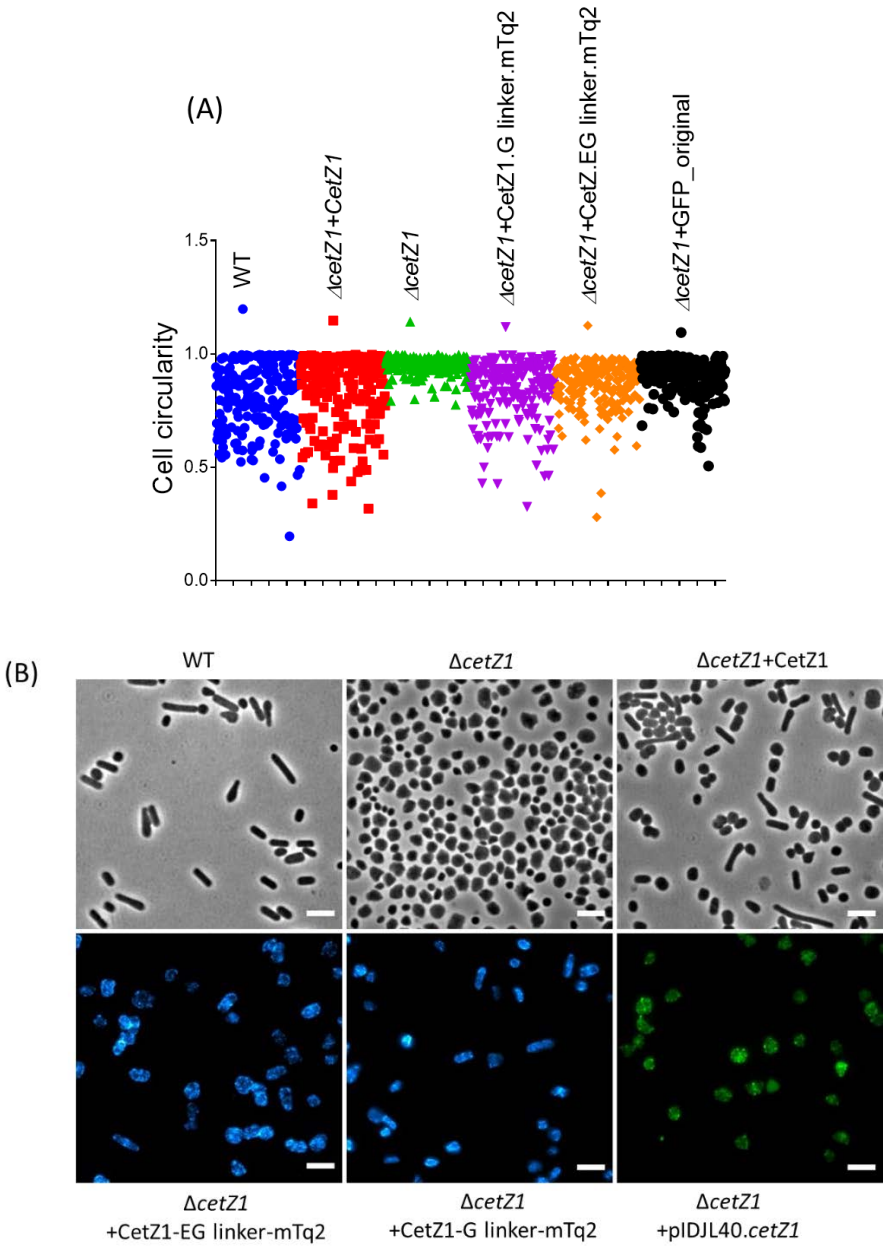

Figure 4.13: *Comparison of the complementation of ΔcetZ1 by CetZ1-mTurquoise2 fusions and the original GFP fusion; pIDJL40.CetZ1.*

(A) A comparison of the cell circularity distributions between the fluorescent fusions and the untagged CetZ1 in IF ΔcetZ1 background to the H26 WT in the early log-phase assay. All cells were grown in Hv-YPCab+2 mM tryptophan and imaged at the "rod peak" time; 10h. The control strains IF ΔcetZ1, and H26 WT contained the EG linker plasmid expressing mTurquoise2 without CetZ1. The sample size N~ 250. (B) The example images of the cells in early-log phase assay for each strain given in (A). Top row- phase-contrast images and bottom row- fluorescence images.

Because the previously reported CetZ1-smRS GFP fusion; CetZ1-pIDJL40 by Duggin *et al*., 2015 was partially functional, the complementation of rod cell formation by this fusion (2 mM tryptophan induction) in the new IF Δ*cetZ1* background was compared with the new CetZ1-mTurquoise2 fusions expressed in the same IF Δ*cetZ1* background. As the controls for this comparison, early-log phase rod formation in Hv-YPCab (+ 2 mM tryptophan) by WT H26+pTA962, IF Δ*cetZ1*+pTA962_CetZ1 (untagged) and the IF Δ*cetZ1*+pTA962 were analysed along with cells expressing the fluorescent fusion proteins. The complementation of rod cell formation was compared by normalising the mean cell circularity from early log-phase rod assay of the WT cells to 100% and that of IF Δ*cetZ1* to 0%. The quantification was carried out using pooled cell circularity data from two technical replicates. Both CetZ1-mTurquoise2 fusions with G linker and EG linker demonstrated an 81% and 70% complementation respectively compared to the WT while this was 86% in the untagged CetZ1 (Figure 4.13). The previous CetZ1-GFP fusion exhibited 50% complementation of *cetZ1* compared to the WT, suggesting that the new mTurquoise2.CetZ1 fusions are more suitable to continue the CetZ1 localisation studies than the previous GFP fusion (Figure 4.13). Finally, this new *cetZ1* knockout strain and the fluorescent fusions would now allow us to understand the CetZ1 dynamics and important interactions during *H. volcanii* morphogenesis.

4.2.3 The localisation of CetZ1 in *Haloferax volcanii* during morphogenesis

As the CetZ1_G-linker_mturquoise2 fusion displayed the highest CetZ1 function (~81% complementation), this fusion was expressed with 2 mM tryptophan in the new *cetZ1* knockout strain and was used initially to compare the CetZ1 localisation in the conditions that have been previously studied, i.e. during supplementary expression and in motility assay (Duggin *et al*., 2015). For clarity, the new IF Δ*cetZ1* was denoted as ID181.

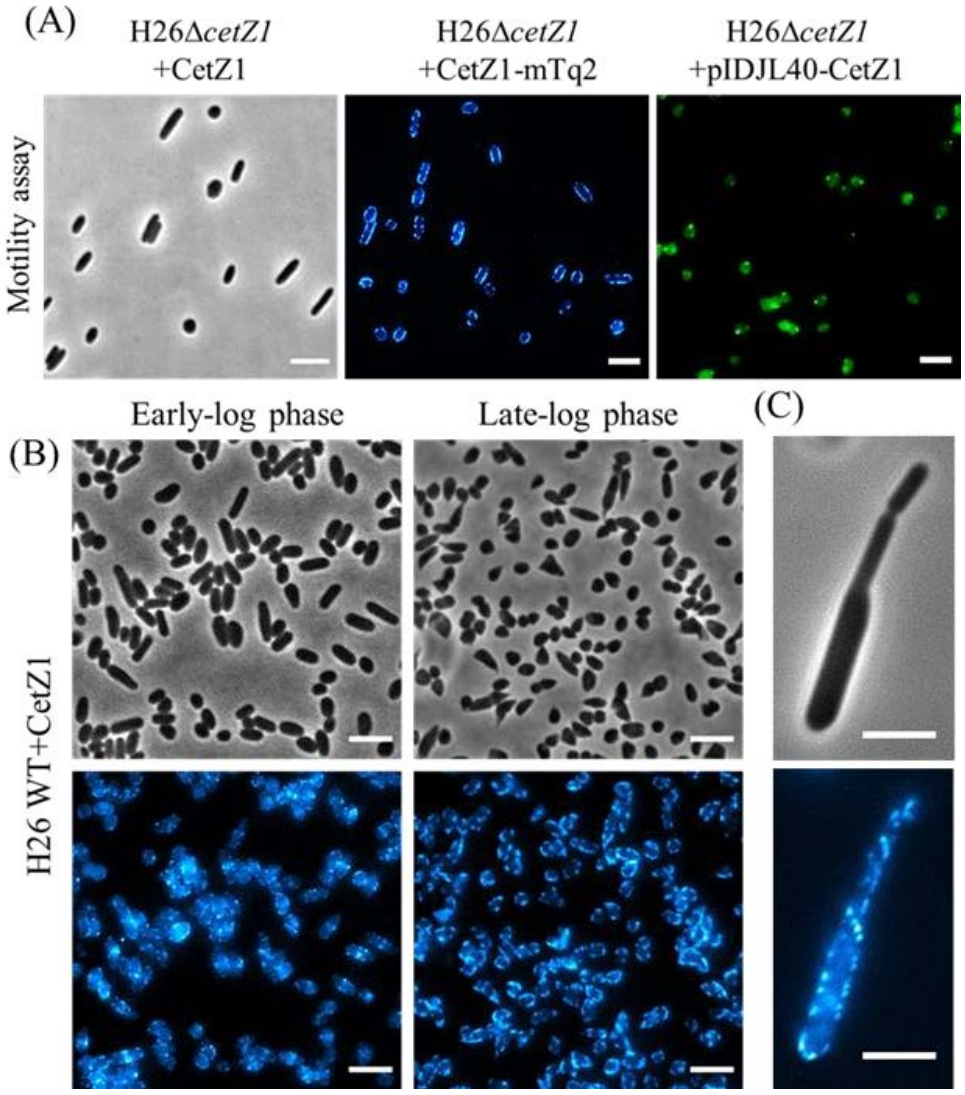

Figure 4.14: *The localisation of new CetZ1-mTurquoise2 in motile rods and during supplementary expression.*

(A) CetZ1 localisation in cells of the newly constructed cetZ1 deletion strain H26 ΔcetZ1 (ID181) produced in the motility assay. The first phase-contrast image shows the complementation of ID181 by untagged CetZ1. The fluorescence images show the CetZ1 localisation in motile rods and compare the complementation of ID181 by CetZ1-mTurquoise2 and original pIDJL40-cetZ1. The cells were grown in Hv-Cab+2 mM tryptophan. (B) H26 WT cells were supplemented with additional CetZ1-mTurquoise2 at 2 mM tryptophan concentration in Hv-YPCab. Top images show the phase-contrast images during the early-log phase and late-log phase respectively. Bottom images give the CteZ1-mTurquoise2 localisation of the same cells shown in the top phase-contrast images. (C) A magnified view of a dividing cell of the H26 WT strain expressing CetZ1-mTurquoise2 during the late-log phase. The scale bar in (A) and (B) indicates 5 µm, and in (C) indicates 2 µm.

In contrast to the previously observed (Duggin *et al.*, 2015) fixed intense foci at the cell poles in the cells at the leading edge of the motile halo in the motility assay, the expression of CetZ1-mTurquoise2 in ID181 displayed a patchy cell envelop associated localisation in motile cells (Figure 4.14). Although the original GFP fusion was failed to induce rod formation in WT cells during a supplementary CetZ1 expression (2 mM tryptophan), the new CetZ1-mTurquoise2 fusion was able to induce rods in the mid-log phase and late-log phase H26 WT culture at the same tryptophan concentration (Figure 4.14, B). Similar cell envelop-associated localisation was observed in these cells expressing CetZ1-mTurquoise2 (at 2 mM tryptophan) in the WT background consistent with the previous localisation pattern observed (Duggin *et al.*, 2015) in H98 WT during the overexpression of partially functional original GFP fusion.

Rod cells formed during both TE depletion and early-log phase assay also displayed similar patchy cell envelope-associated localisation as observed in the motile rods and during supplementary expression in the WT background (Figure 4.15). Moreover, the CetZ1-mTurquoise2 fusion was able to form CetZ1-induced stalk-like structures and peculiar cell shapes in the TE depletion rod assay similar to the untagged WT cells.

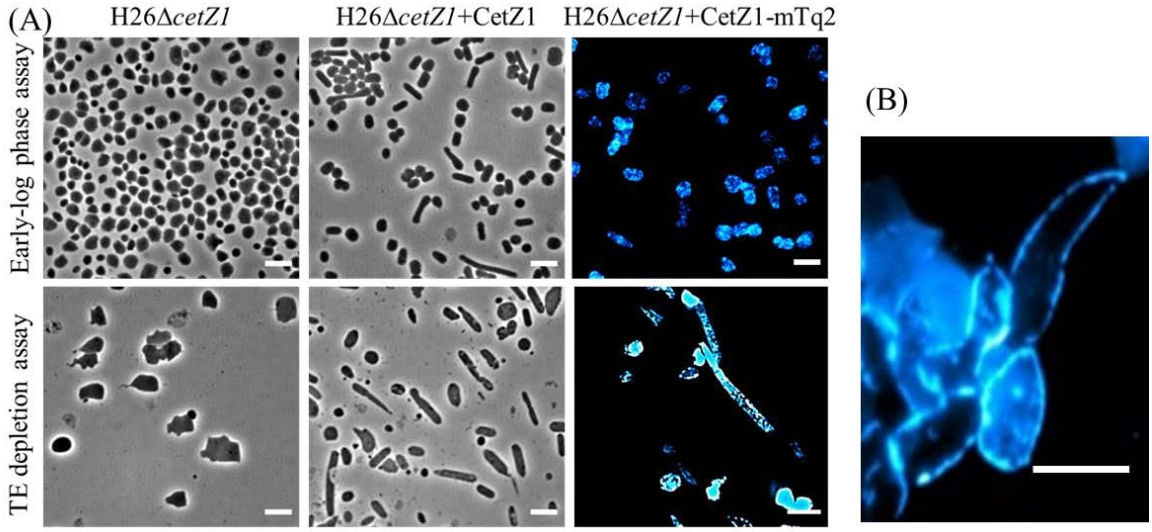

Figure 4.15: *CetZ1 localisation during early-log phase assay and trace elements (TE) depletion assay.*

(A) The first two phase-contrast images of the top row and the bottom row indicate the complementation of ID181 by untagged CetZ1 during early-log phase assay (top) and TE depletion assay (bottom). The last two fluorescence images in this panel show the CetZ1-mTurquoise2 localisation in early-log phase assay (top) and TE depletion assay (bottom). Scale bar shows 5 µm. (B) A zoomed image was showing CetZ1-mTurquoise2 localisation in a cell that displays an atypical cell shape during TE depletion. Scale bar shows 2 µm.

The sporadic localisation of CetZ1 was highlighted in the 3D cells imaged using 3D-structured illumination microscopy (3D-SIM) (Figure 4.16, Supplementary Video 10 A and B). *H. volcanii* has a flat cell shape. Using the middle slice of the Z-stack series taken from 3D-SIM allowed much clearer localisation of CetZ1 in 2D images without the interference from the fluorescence signal coming from top and bottom planes. The middle slice indicated a clear peripheral localisation suggesting CetZ1 has a cell-envelope associated localisation (Figure 4.16).

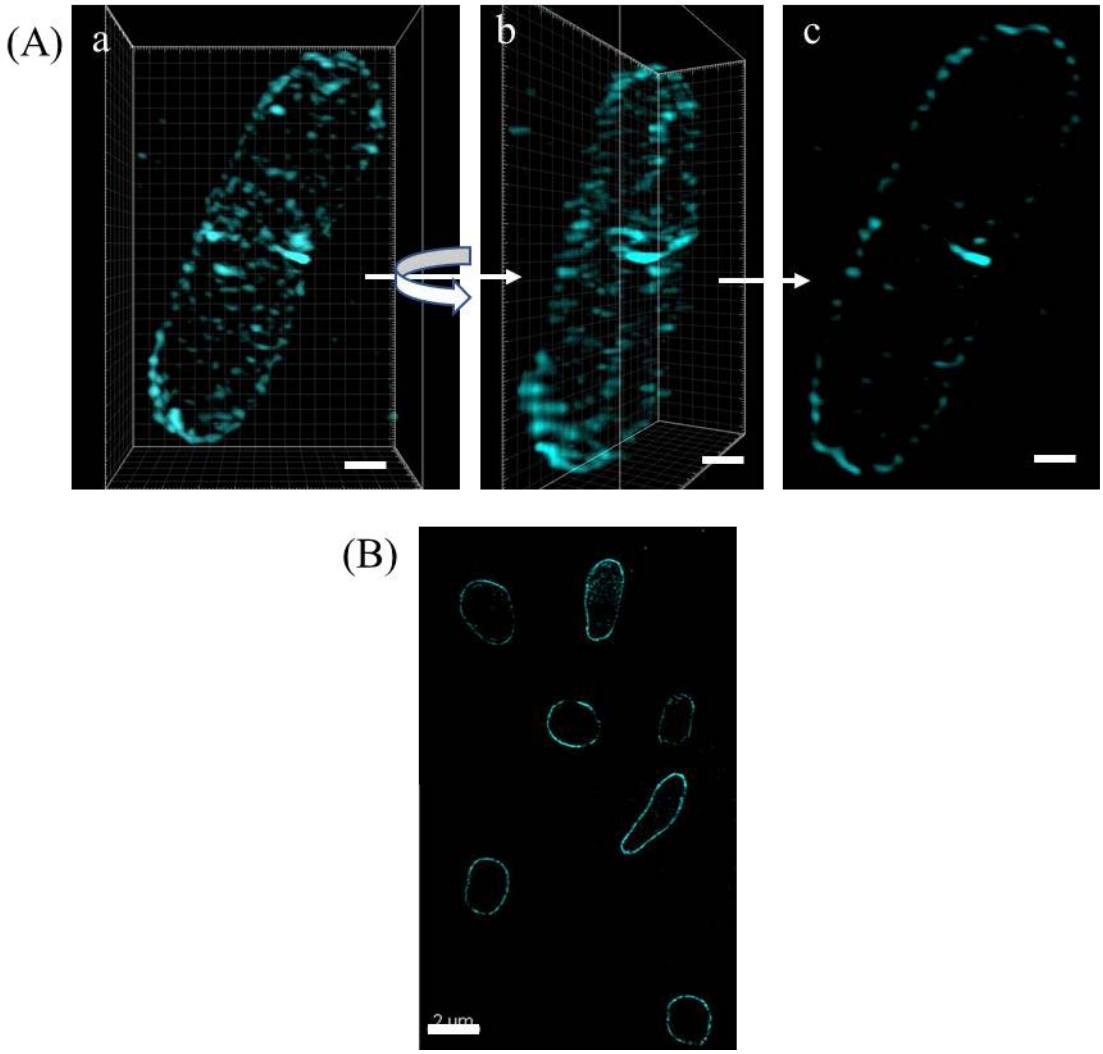

Figure 4.16: *CetZ1 localisation imaged by 3D-SIM.*

(A) A rod cell expressing CetZ1-mTurquoise2 in ID181 during early-log phase assay. a and b show the front view, and the 45^0 rotated view of the 3D-SIM reconstructed image. c, shows the middle slice (from front view) of the same cell. Scale bar shows 0.5 µm. (B) A middle slice of a 3D-SIM image of more cells expressing CetZ1-mTurquoise2 in ID181 during early-log phase assay. Scale bar shows 2 µm.

Live-cell imaging during early-log phase assay was carried out using the CellASIC microfluidic platform to understand the relation of CetZ1 dynamics to the developing cell shape changes. Cells were inoculated into Hv-YPCab (+2 mM tryptophan) liquid medium from the same type of agar-based medium and loaded into the CellASIC bacterial plate that was pre-treated with BSA followed by 18% w/v BSW and pre-warmed to 45 ^{0}C. The pre-treatment reduced the toxic effect to the *H. volcanii* growth by the original CellASIC plate. Morphogenesis in ID181 (H26Δ*cetZ1*) cells expressing CetZ1-mTurquoise2 was

imaged at 10 minutes intervals for 18 hours while cells were continuously treated with fresh media at 45 ^{0}C.

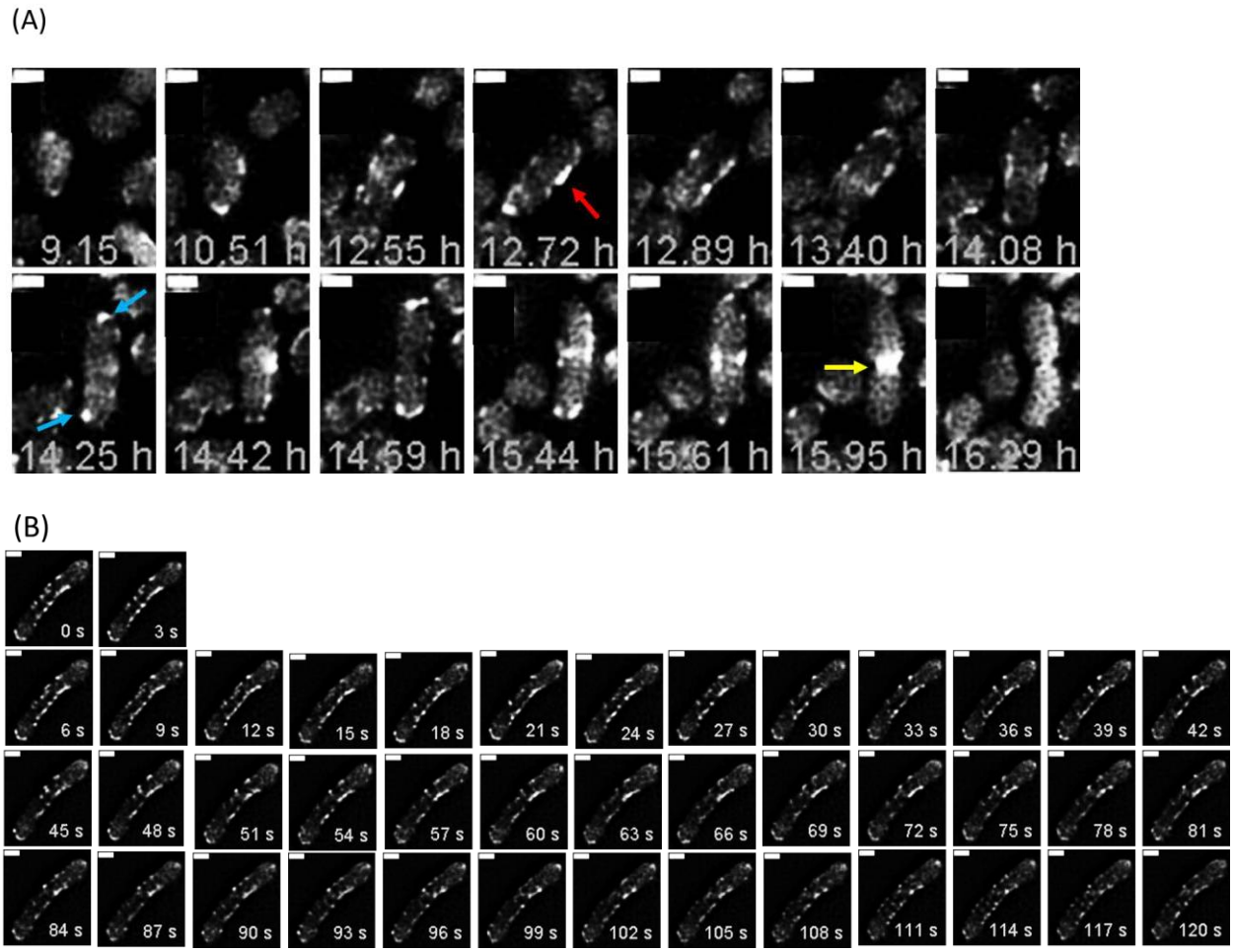

Figure 4.17: *Selected time frames showing CetZ1 localisation dynamics during morphogenesis.*

(A) ID181 expressing CetZ1-mTurquoise2 were imaged at 10 minutes intervals for 20 hours during early-log phase assay (Hv-YPCab+2 mM tryptophan). The arrows indicate the common features observed in CetZ1 dynamics. First, the formation of short filaments along the axis (red arrow), second, the polar cap localisation (blue arrow) and finally the localisation at the division furrow (yellow arrow). (B) The short-term CetZ1 localisation dynamics in a rod cell (ID181+CetZ) in early-log phase assay. The cell imaged in 3 s intervals for 2 minutes.

Although the localisation pattern appeared to be complex (Supplementary Video 5 A and B), it revealed some common features during plate to rod shape transition. Primarily, cells displayed an initial patchy and dynamic localisation in discoid cells, then, during rod formation, displayed short dynamic filaments along the edges of the cell's long axis. This was followed by dynamic polar-envelope localisation in rods, and then—during the division of these cells—at the envelope around the division furrow; this differed significantly from the FtsZ1 pattern, which forms a division ring and constricts with the division furrow, similar to bacterial FtsZ (Figure 4.17). Since CetZ1 deletion in *H. volcanii* does not affect cell division, it may recognise the envelope shape at the poles and division furrow rather than playing an essential role in the division. This transition from plate to rod shape cell was a slow process which consumed about 5 h. However, highly dynamic diffusional and treadmilling-like localisation of CetZ1 in time frames of seconds was evident from a short-term localisation (3s intervals for 2 mins) analysis in early-log phase assay (Figure 4.17, Supplementary Video 6). The localisation dynamics are primarily associated with the cell edges suggesting CetZ1 is actively remodel the cell envelop to exert the cell shape change from plate to a rod.

4.3 Discussion

Creation of gene knockouts has been used widely to study gene function with increased confidence as this approach completely inactivates the gene. This can be accomplished by several methods such as using homologous recombination, transcription activator-like effector nucleases (TALENs), Zinc-finger nucleases, site-specific nucleases and by gene knock-in (Hauschild-Quintern *et al.*, 2013, Joung and Sander, 2013, Lombardo *et al.*, 2011). The choice of method that improves the rate of success in making a gene knockout depends on the cell type and its genetic structure. In the present study, homologous recombination was used to create *cetZ1* gene knockouts in *Haloferax volcanii*. Single gene knockouts can be best (Nakashima and Miyazaki, 2014) achieved by homologous recombination without any off-target gene damages. In this study, homologous DNA sequences of ~2 kb were used to incorporate the deletion regions into the *H. vocanii* genome as the as this length has been shown to improve the homologous recombination. (Inbar *et al.*, 2000).

As seen previously (Duggin *et al.*, 2015), knocking out *cetZ1* did not exhibit a significant effect on cell division or growth in *H. volcanii,* suggesting that CetZ1 is not essential for *H. volcanii* survival. The failed attempt of complementing this *cetZ1* knockout when the whole gene was knocked out was overcome by avoiding the deletion of the potential region of overlap with the downstream gene; HVO_2203. Furthermore, the perpetuation of the correct reading frame in the deletion suggests that the correct expression of the downstream gene is important for the function of CetZ1. The function of HVO_2203 is currently unknown. According to NCBI BLAST search, homologous genes of HVO_2203 can be found in closely related haloarchaea such as *Haloferax gibbonsii*, and *Haloferax mediterranei*. The further downstream gene HVO_2202 expresses 2-phospho-L-lactate guanylyltransferase, homologous to enzymes involved in the biosynthesis of coenzyme F420, a hydride carrier cofactor. Both HVO_2202 and HVO_2203 genes are often positioned next to a cell division gene. The data presented in this chapter suggest that HVO_2203 and *cetZ1* genes might be functioning as an operon.

Expression of a fluorescently labelled protein inside a cell, that has the labelled protein knocked out could be informative to study the correlations of protein localisation and function. However, the expression of tagged proteins can often result in problems such as

aggregation or steric interference, thereby destroying its proper biological activity. Several probes have been developed over the years for direct labelling (e.g., expressing improved fluorescent proteins (Yu *et al.*, 2014, Yang *et al.*, 2013)) and indirect labelling (e.g., Halotag (Los *et al.*, 2008)) of proteins.

In previous studies, the utilisation of linkers between the fusion protein has shown to improve the function of fusion proteins. The present study developed a collection of vectors that can be used to screen a functional fluorescent fusion protein to express in *H. volcanii*. These vectors connect different types of fluorescent proteins to the protein of interest via 3 types of linkers—E, EG and G—that have a varied amount of flexibility. CetZ1 indicated improved function with mTurquoise2 fused via both G (flexible) and EG (semi-flexible) linkers and E (rigid) linker was non-functional. The other two tags—mScarlet-I and mCherry—displayed a functionality and were linked via the G (flexible) linker. This suggests that having flexibility in the linker increased the function of CetZ1 fusion protein via avoiding the obstruction in the active sites during polymerisation and other protein dynamics. However, GFP. YPet and mNeonGreen fused via the G linker were non-functional indicating that in addition to the properties of the linker, the type of the fluorescent protein also plays a major role in determining the functional rescue of the fluorescent protein.

Furthermore, this highly dynamic localisation suggests that previously observed fixed, polar cap localisation in WT motile cells during CetZ1-GFP supplementary expression (Duggin *et al*., 2015) was probably an artefact due to the reduced functionality of the fusion protein.

The regulation of cell shape is crucial for normal cell division and growth. In eukaryotic cells, the interplay between microtubule organisation to establish the cell polarity and the cell shape determines the correct cell growth and division. In yeast cells, interruption in the polarised growth of microtubules from the nucleus to the cell tips, resulted in branched cell shapes while, the cells with deliberately blemished cell shapes indicated aberrant microtubule growth (Haupt and Minc, 2018). In bacteria, the actin homolog MreB mediates the cell shape changes by identifying the local curvature. In well-studied bacteria, *E. coli*, MreB assists the insertion of cell wall material to maintain the rod shape by localising into the newly forming positive curvature, thereby promoting the cell growth along the cylindrical part which appears as a helical localisation to straighten the rod cell (Chang and Huang, 2014). However, CetZ1 appears to exert a complex

localisation pattern as the CetZ1 localised to both polar ends and along the cylindrical section. Consistent with the localisation pattern observed in the other non-long-range filaments (Haupt and Minc, 2018), CetZ1 localisation displayed a positive correlation with the local curvature during the overexpression of CetZ1 GTPase mutant E218A (Duggin *et al.*, 2015). Furthermore, in the localisation dynamics during morphogenesis, the localisation of CetZ1 into the division furrow immediately before the cell division indicates that CetZ1 localisation is linked to the local curvature of the cell. However, it remains uncertain whether CetZ1 triggers this morphogenesis by actively remodelling the cell envelop or assisting the positioning of the cell wall synthesis machinery. Despite the dissimilarity in shape, having a similar cell volume in both WT cells and CetZ1 knockout strain (ID181) during the early-log phase assay where cells are triggered to form rods (Figure 3. 6C and 5.4B), suggests CetZ1 is plausibly remodelling the cell envelope to modulate the cell shape. Also, we still have a little understanding of the functionally important polymer dynamics of CetZ1 to exert cell shape changes.

4.4 Methods

4.4.1 Construction of plasmids containing the knock-out regions

The two flanking regions (~700 bps) of the *cetZ1* deletions (in-frame/IF and out-of-frame/OF deletions) were amplified using PCR (Section 2.8.5) with site-specific primers (Table 4.1) and *Haloferax volcanii* gDNA as the template. Each flank was designed with a region of 21 bp overlap which contains the restriction sites BglII and EcoRI in it to allow for insertion of an additional selection marker if required.

Table 4.1 Primers Used for Amplification of Flanking Regions of *cetZ1* Deletions.

Name	Sequence forward (5'-> 3')	Source
2204_IF_US_F	ccggccaagcttgcgagttcgtctccttcacga	I. G. Duggin
2204_IF_US_R	gaattcgccgcccgaagatcttccgatcattgcgagcttc	This study
2204_IF_DS_F	agatcttcgggcggcgaattctcgggcgtgacgaacg	This study
2204_IF_DS_R and 2204_OF_DS_R	ccccggatccgtccggtcgctctccagttc	I. G. Duggin
2204_OF_DS_F	agatcttcgggcggcgaattctgacgggcggcgacgag	This study

Note: In the primer notations, "US" and "DS" represent primers for up-stream and down-stream flanks respectively and "F" and "R" represent the primer forward and primer reverse respectively.

An equimolar ratio of both flanks was mixed in a PCR reaction and a non- amplifying overlap extension PCR (without primers) for 18 cycles followed by amplifying overlap extension PCR (with end-primers/ 2204_US_F and 2204_DS_R in Table 4.1) for another 30 cycles to join the two flanks. The full-length insertions (joined flanks, ~1.18kb) were gel purified as outlined in Section 2.8.4. The purified inserts representing the *cetZ1* deletions were cloned (as described in Section 2.8.6) into pTA131 (Table 2.3) plasmid

using HindIII and BamHI sites. The ligation was transformed into *E. coli* DH5α (Table 2.10) as outlined in Section 2.5.1 and clones were selected for ampicillin resistance on LB agar. The plasmid DNA was extracted as outlined in 2.8.2 and correct insertions were initially screened by digestion analysis with subsequent confirmation by Sanger sequencing (Section 2.8.7).

4.4.2 Construction of Knockout strains

The sequence-confirmed pTA131 plasmids with *cetZ1* (HVO_2204) deletions were demethylated by transforming (protocol outlined in Section 2.5.2) into *E. coli* C2925 (Table 2.1). Demethylated plasmid DNA was extracted (Section 2.8.2) and transformed into *H. volcanii* DS70 *ΔpyrE2* (H26) strain (outlined in Section 2.7) which is auxotrophic for uracil. Transformants (or the "pop-ins") were selected using Hv-Cab without uracil (Table 2.5). These "pop-ins" were allowed to grow in Hv-YPC (Table 2.5) for ~10 generations, and the "pop-out"s were subsequently selected using Hv-Cab with uracil and 5-FOA. gDNA was extracted from cultures grown using randomly selected single colonies to select the "pop-out"s with the correct *cetZ1* deletion. Then, these were screened by a PCR analysis with primers listed in Table 4.2.

Table 4.2 Primers Used in Diagnostic PCR of *cetZ1* Deletion Strains

Name	Sequence forward (5'-> 3')	Source
OverlapP_Popout_F	agatcttcgggcggcgaattc	This Study
OverlapP_PopOut_R	gaattcgccgcccgaagatct	This Study
2204_IF_PopOut_F	gtggttcgacacgtccccat	I.G Duggin
2204_IF_PopOut_R	*gaattcgccgcccgaagatct*ctcgtcggggacgtcg	This Study
2204_OF_PopOut_F	gcgaggggactgaacctatg	This Study
2204_OF_PopOut_R	ctgctcctcgatccacttcc	This Study

4.4.3 Construction of vectors with CetZ1 fluorescent protein fusion

The vectors were designed (by Solenne Ithurbide) to test the functionality of CetZ1 fused into six different fluorescent proteins—smRS GFP, mNeonGreen, mScarlet-I, mCherry, YPet and mTurquoise2— separated by three different types of linkers. All the fluorescent proteins were codon optimised for *H. volcanii* using OptimimGene^{TM} algorithm and synthesised by GenScript, USA (these sequences were received in a simple pUC57 plasmid from GenScript). All the fluorescent proteins except smRS GFP were digested from pUC57 using NheI and ECoRI restriction sites and purified using gel purification. GFP was amplified by PCR using primers with NheI and ECoRI restriction ends and pIDJL40 as the template. The linkers listed in Table 4.3 with the tryptophanase (*tna*) inducible promoter (*P.tna*) were synthesized by GenScript, USA and extracted from a pUC57 plasmid using ApaI and NotI restriction digestion followed by gel purification.

Table 4.3 Sequences of the Three Types of Linkers Used in This Study

Linker name	Amino acid Sequence	Properties
G linker	(GGGGS)5	Flexible (330 bp)
E linker	(EAAAK)5	Rigid (330 bp)
EG linker	EAAAK-(GGGGS)2-(EAAAK)2	Semi-flexible (330 bp)

The basic vector design was based on the expression plasmid pTA962 (T Allers *et al.*, 2010). The new plasmid design consists of an XbaI restriction site in between the *tnA* promoter and the linker to permit dual expression of tagged proteins if necessary. The XbaI sites on the *pyrE2* marker region and the multiple cloning site (MCS) in the original pTA962 were removed to prevent multiple digestions during cloning. The XbaI site on the MCS was removed by cloning the *H. volcanii* FtsZ2 gene, a gene that is involved in cell division. The *pyrE2* region was replaced by cloning a PCR amplicon which has NheI,

and HindIII restriction ends into pTA962 digested with XbaI and HindIII (NheI has compatible ends with XbaI). The sequence of the XbaI sites removed pTA962 plasmid was confirmed using Sanger sequencing before the cloning of three gel-purified linkers using ApaI and NotI restriction sites.

Table 4.4 Primer Sequences Used for GFP Amplification and the Plasmid Sequence Confirmations

Primer name	Sequence (5'->3')	Description
SI32_EcoRI	tgcaGAATTCagtaaaggagaagaactttt	Forward primer for amplification of smRS_GFP from pIDJL40. Contains 5' EcoRI site
SI33_NheI	gtctGCTAGCttatttgtatagttcatcca	Reverse primer for the amplification of smRS_GFP from pIDJL40. Contains 5' NheI site and the stop codon is conserved
pUC/M13-Fwd	CAGGGTTTTCCCAGTCACGAC	Universal forward primer for pUC plasmid. For sequencing smRS GFP
pUC/M13-Rvs	CACACAGGAAACAGCTATGAC	Universal reverse primer for pUC plasmid. For sequencing smRS GFP

The promoter region of the EG linker was swapped with the *tna* promoter of the G linker using NcoI, and NdeI restriction sites as the *tna* promoter region of the EG linker synthesised by GenScript was designed with a mutation to facilitate gene overexpression. Each fluorescent fusion protein 'construct' digested with NheI and EcoRI were then cloned into the plasmids with three different linkers. The sequence of the smRS GFP cloned into the plasmids containing linkers was confirmed by the Sanger sequencing using universal forward primer and universal reverse primer (Table 4.4). The *cetZ1* was digested from a previously sequenced plasmid using BamHI and NdeI restriction

enzymes and purified by gel purification. Using the same restriction sites stop codon removed *cetZ1* was cloned into the 18 different plasmids containing six different fluorescent proteins separated by three different types of linkers.

4.4.4 Testing the complementation of CetZ1 fluorescent fusion proteins

The above 18 different plasmid constructs of CetZ1 fluorescent fusions were demethylated by transforming into *E. coli dam*$^{-}$*dcm*$^{-}$ c2925. Demethylated plasmids were transformed into IF Δ*cetZ1* constructed in 4.2.2. Transformants were isolated by uracil prototrophy selection using Hv-Cab medium. The cells were grown in Hv-YPcab with 2 mM tryptophan at mid-log phase for four days prior to being subjected to any complementation assays. Complementation was tested using the motility assay, early-log rod assay in Hv-YPCab and TE depletion rod assay.

4.4.5 Motility assay

Hv-Cab + 0.3 % (w/v) agar was used to prepare the soft agar plates (20 mL of media per plate) for the motility assay. *H. volcanii* cultures were grown into mid-log phase as described in 2.6 and 2 µl was stab-inoculated into the subsurface of the soft agar plate. A maximum of four inoculations per plate was used during qualitative screening, and one inoculum per plate with appropriate replicates was used during quantitative screening. Equal cell densities of the inoculum were used for comparison of multiple strains. Plates were incubated with minimal disturbance in a sealed plastic bag at 45 °C for 6 days. Images of the plates were acquired using a transilluminator (Ingenius3; Syngene) and recorded as a digital image using a charge-coupled device (CCD) camera (Synoptics CAM-FLXCM; Syngene) linked to GeneSys molecular imaging software, version 1.5.0.0 (Syngene).

4.4.6 Early-log phase rod assay

The *H. volcanii* strain was streaked onto an agar plate made from the same medium as chosen for the assay (e.g. Hv-YPCab, Chapter 3), and then the plate was incubated in a humidified bag at 45°C for 3-5 days. Colonies were collected from the surface with a microbiological loop, and suspended in 5 ml of the liquid medium, sufficient to give an optical density (OD - 600 nm) > 0.05. The OD was immediately adjusted to 0.05 by dilution with fresh medium. This culture (5 mL in a 50 mL Falcon tube) was then immediately incubated at 45°C at 200 rpm in a GFL1092 rotary-shaking water bath (the tube's lid was loosened to allow gas exchange), marking the start of the growth curve (t=0 h). Samples were withdrawn at t=10 h for microscopy or other analyses. For the TE depletion assay, the same steps were followed in Hv-Ca (-TE) media and the cells were collected for analysis at t= 15 h.

CHAPTER 5

IN VIVO CHARACTERISATION OF CETZ1 VIA SITE-DIRECTED MUTAGENESIS

5.1 Introduction

The cytoskeleton primarily serves as both a scaffold and force generator to maintain the mobility and structural integrity of the cell. Tubulin superfamily proteins are one of the main components in the cytoskeleton across all domains of life. The primary feature of tubulin superfamily proteins is the GTP-dependent polymerisation and depolymerisation of protein subunits, which ultimately leads to the dynamic instability of the cytoskeleton (Scheffers *et al.*, 2002). Therefore, the primary amino acid sequence at the GTP binding active site is highly conserved throughout the family (Scheffers *et al.*, 2002). Although these proteins share a common basic monomeric crystal structure, their quaternary structures and mechanism of action have diverged. Human tubulin exists as microtubules which typically comprise of thirteen protofilaments formed by the polymerisation of alpha and beta-tubulin dimers bundled into a hollow cylinder. These microtubules are essential for the formation and dynamics of the mitotic spindle during cell division (Nogales, 2001). Additionally, maintenance of cell shape, positioning of organelles, and molecular transportation within the cell are facilitated by a complex tubulin network (Richards *et al.*, 2000). The prokaryotic homolog of tubulin; FtsZ forms a ring-like structure at the mid-cell called the "Z ring" to organise the constrictive force required for cell division (Strauss *et al.*, 2012).

The FtsZ ring consists of four or more FtsZ protofilaments arranged into a ring shape with varying inter-protofilament distances (Osawa, Anderson and Erickson, 2008). Although cell shape regulation and cell division are closely associated, the cell shape in many bacteria is controlled by an actin homolog, MreB which exhibits approximately helical localisation along the length of the cell (Carballido-Lopez, 2006b, Carballido-Lopez, 2006a). Despite the similarities between homologues, the functional and structural divergence of the tubulin superfamily proteins prevails, hindering the appreciation of microtubule structure to the cell physiology. Archaea have been instrumental in understanding the evolution of many complex biological processes such as DNA replication in eukaryotes (Nunoura *et al.*, 2011). We believe the recently discovered third group of tubulin superfamily protein, CetZ, which is distributed mainly among methanogenic and halophilic archaea, may provide insights into the evolution of tubulin (Duggin *et al.*, 2015). The primary function reported for the CetZ homologue in model archaeon *Haloferax volcanii*, CetZ1, was the requirement in cell differentiation from

plates to rods during motility assays. We have recently identified additional culture conditions that result in CetZ1 dependent rod development, including trace elements (TE) depletion, and early-log phase growth curve (Chapter 03).

Nature tends to conserve functionally important features of biological molecules during evolution. The identification of functionally important regions in a protein's structure is crucial to understand how higher-order structures emerged during functional evolution to exert diverse biological functions (Otey *et al.*, 2004). Understanding the molecular design created by nature would not only help us to understand the evolution of complex molecular reactions in eukaryotic cells but could also assist in the design of new biological molecules with useful applications. Therefore, in the present study, the structural regions of CetZ1 that are important for cell shape control were explored via structure-guided site-directed mutagenesis. Moreover, attempts were made to compare the CetZ1 localisation and dynamics in mutants to those of WT during rod cell development.

5.2 Results

5.2.1 Use of CetZ1 site-directed mutants for identification of structural components in CetZ1 important for *Haloferax volcanii* motility and morphogenesis

The crystal structures of a CetZ1 monomer and a CetZ2 sheet-like polymer have been resolved in the study by Duggin *et al*., 2015. As CetZ1 and CetZ2 share 80% primary amino acid sequence similarity, both these structures were used to select regions for point mutations. Mutations were designed to disrupt the GTP dependent polymer formation, possible membrane interactions and lateral interactions between protofilaments that appear in the CetZ2 sheet structure.

The resolved CetZ1 crystal structure contains a GDP molecule on the 'top' side of the monomer, typical of the tubulin superfamily. The study by Duggin *et al*., 2015 revealed that a dominant-negative mutation, E218A (glutamate 218 changed to alanine), at the bottom surface of the T7 synergy loop impairs CetZ1 function probably due to the disruption of GTPase activity (Duggin *et al.*, 2015). Furthermore, CetZ1.E218A displayed an intense 'locked-in' localisation in vivo, suggesting this mutation might result in hyper stable protein filaments. In this study, we also made a mutation, G108S, on the top surface (nucleotide-binding T4 region) of CetZ1 which resembles the temperature-sensitive *ftsZ84* mutation in FtsZ (Lu, Stricker and Erickson, 2001), to explore the functional importance of this region in CetZ1 (Figure 5.1). According to the studies that had been carried out on tubulin and FtsZ, the T4 region is involved in GTP binding, and thus polymerisation (Bramhill and Thompson, 1994).

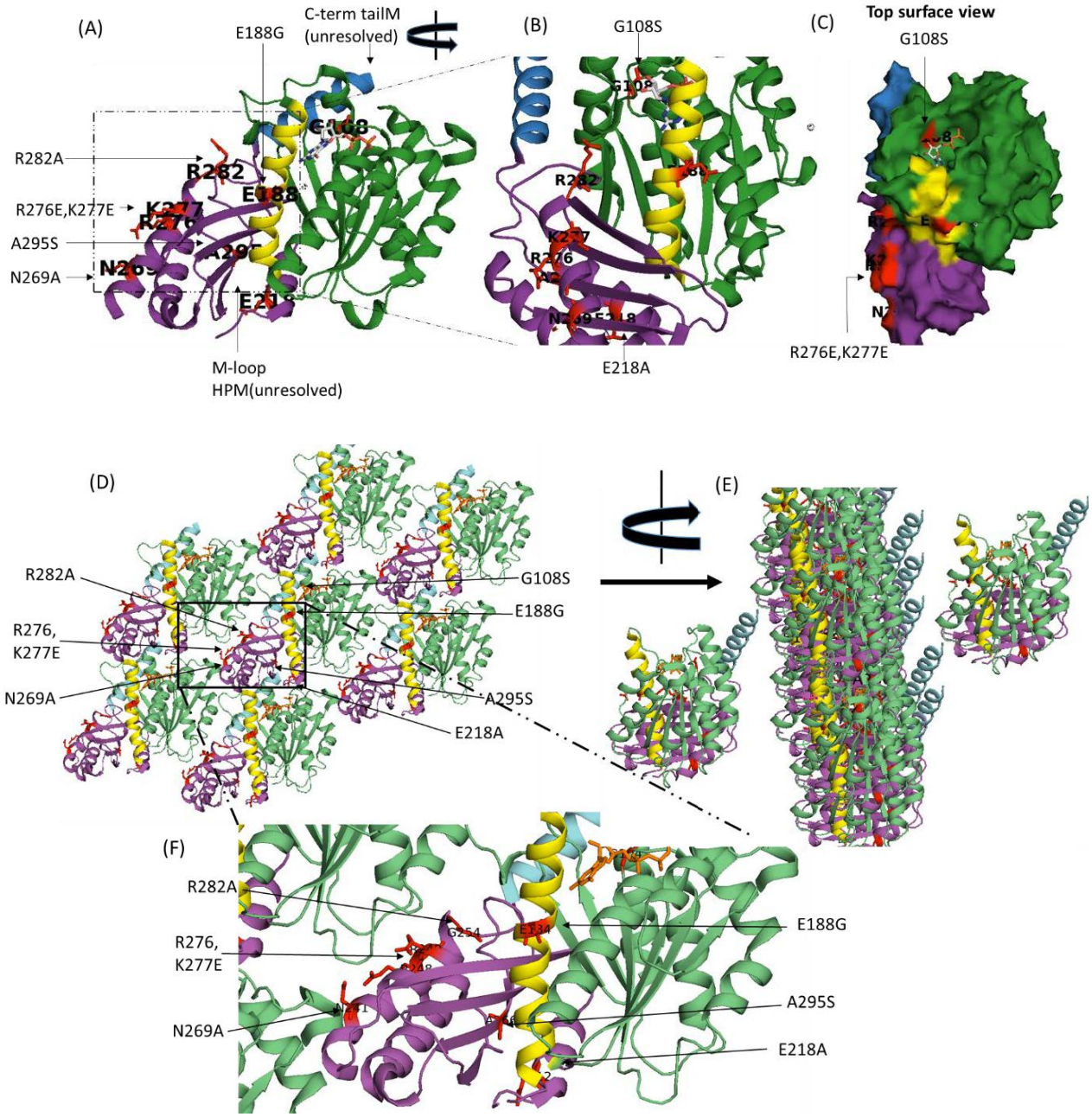

Figure 5.1: *Locations of the CetZ1 point mutations designed to disrupt the lateral interaction, membrane interaction and GTP contact.*

(A) marks the positions of all the point mutations in the CetZ1 monomer (front view). (B) rotates (A) by 45^0 and zooms on the purple C-terminal domain showing mutations assumed to disrupt the CetZ1 lateral interactions and the GTP binding site mutation in the green N-terminal domain. (C) The surface view of the monomer from 'topside'. This highlights the GTP binding site mutation inside the GTP binding pocket and the positions of lateral contact mutants on the surface. (D) The positions of point mutations in the CetZ2 sheet-like structure (front view) (E) The rotation of (D) by 90^0. (F) The zoomed view showing the position of the point mutation in the polymer structure, mainly the selected residues in the C-terminal domain sticks into the N-terminal domain of the adjacent monomer.

We also believe that CetZ1 may be capable of assembling into a higher-order structure involving lateral interactions between CetZ1 protofilaments, primarily based on evidence from 3D-SIM and cryo-electron microscopy (cryo-EM) that indicated the formation of an extra layer in patches of about 300 nm length on the inner surface of the cell envelope during overexpression of the depolymerisation mutant of CetZ1, E218A (Duggin *et al.*, 2015). In order to asses this hypothesis, we made mutations in CetZ1 to disrupt the possible lateral interactions. In microtubules, mainly the surface loops on the C-terminal domain are involved in lateral interaction (Mitra and Sept, 2008). Therefore, the mutations R282A, N269A and a double-mutant (R276E, K277E) were made in the C-terminal domain (purple domain in the Figure 5.1A) because they appeared to have the closest contact with the adjacent subunit. The residues at this lateral interface were chosen assuming they could make ionic interactions with the residues in the adjacent subunit. If these disrupt the possible CetZ1 lateral interactions, the localisation, function (Figure 5. 1), and polymerisation properties of the mutants would reflect this, supporting the hypothesis

Another mutation, E188G, was made on the front surface of CetZ1. The mutation A295S was also made, located slightly inside from the backside of the C-terminal domain (Figure 5.1) assuming this mutation might interrupt the interactions in the C-terminal domain core, similar to those studied previously in *B. subtilis* FtsZ (Monahan *et al.*, 2009), thus resulting in phenotypic effects when this part of the protein—known to be involved in lateral associations in other tubulin superfamily proteins—loses its structural integrity. The amino acid residues on the surface of the protein are usually involved in facilitating inter-molecular interactions. Therefore, the remaining mutations were located on the surface of the protein to increase the probability of having phenotypic effects due to the mutation itself, rather than the inability of the protein to fold properly (Figure 5.1).

As the CetZ1-mTq2 fusion displayed a high cell envelope associated localisation (Chapter 04), the regions in CetZ1 that might be important for membrane interactions were explored. Membrane association of FtsZ has been widely studied, and it has been reported that the flexible C-terminal tail region of FtsZ is important for its membrane interaction via cell division associated proteins, FtsA and ZipA (Hale, Rhee and de Boer, 2000, Pichoff and Lutkenhaus, 2005). Therefore, we made mutations in the CetZ1 C-terminal tail by changing the sequence ^{390}LESLF^{394} to AESGG (unresolved in the crystal structure) to disrupt the potential membrane interactions. Interestingly, in CetZ1 we found

a hydrophobic surface loop rich in leucine, between S7 and H9 of its structure. This loop structure called the “M-loop” is located at the same position within tubulin and has been shown to be crucial to the maintenance of lateral interactions of the microtubule (Mitra and Sept, 2008). However, similar to the C-terminal tail, the M-loop region has also not been resolved in the CetZ1 crystal structure due to its intrinsically disordered nature (Figure 5.1). This M-loop region of CetZ1 could be involved in the stabilisation of lateral interactions in CetZ1 polymeric organisation, equivalent to the M-loop in tubulin (Löwe *et al.*, 2001). Additionally, as this region contains a patch of hydrophobic residues, it may be involved in membrane association of CetZ1. In order to investigate the functional importance of the M-loop, a mutation was made substituting the sequence ^{248}LLSRL^{252} with SASRA to decrease the hydrophobicity (arginine is hydrophilic).

All the mutations were constructed using site-directed mutagenesis as described in Section 5.4.1 and expressed from pTA962 plasmid (Table 2.3) expression system in *H. volcanii* H26 Δ*cetZ1* (ID181, Chapter 04). With this expression system, a concentration of 2 mM tryptophan-induced expression at a similar level of CetZ1 in ID181 as the WT H26 (Chapter 04). The level of expression of the mutant proteins was analysed by a Western blot carried out) using cells continuously grown at the mid-log phase in Hv-YPCab for 4 days in the presence and absence of 2 mM tryptophan induction (Figure 4.2). Initially, the rescue of CetZ1 function of the point mutants was screened by motility assay (Section 4.4.5) and the trace element (TE) depletion assay (Section 5.4.3). Motility assays were performed by first, growing ID181 expressing each mutant on pTA962 in Hv-Cab+2 mM tryptophan at mid-log phase, then, inoculating onto the same media condition containing 3% w/v agar. The spread of the colony was analysed after incubation at 42 ^{0}C for 5 days.

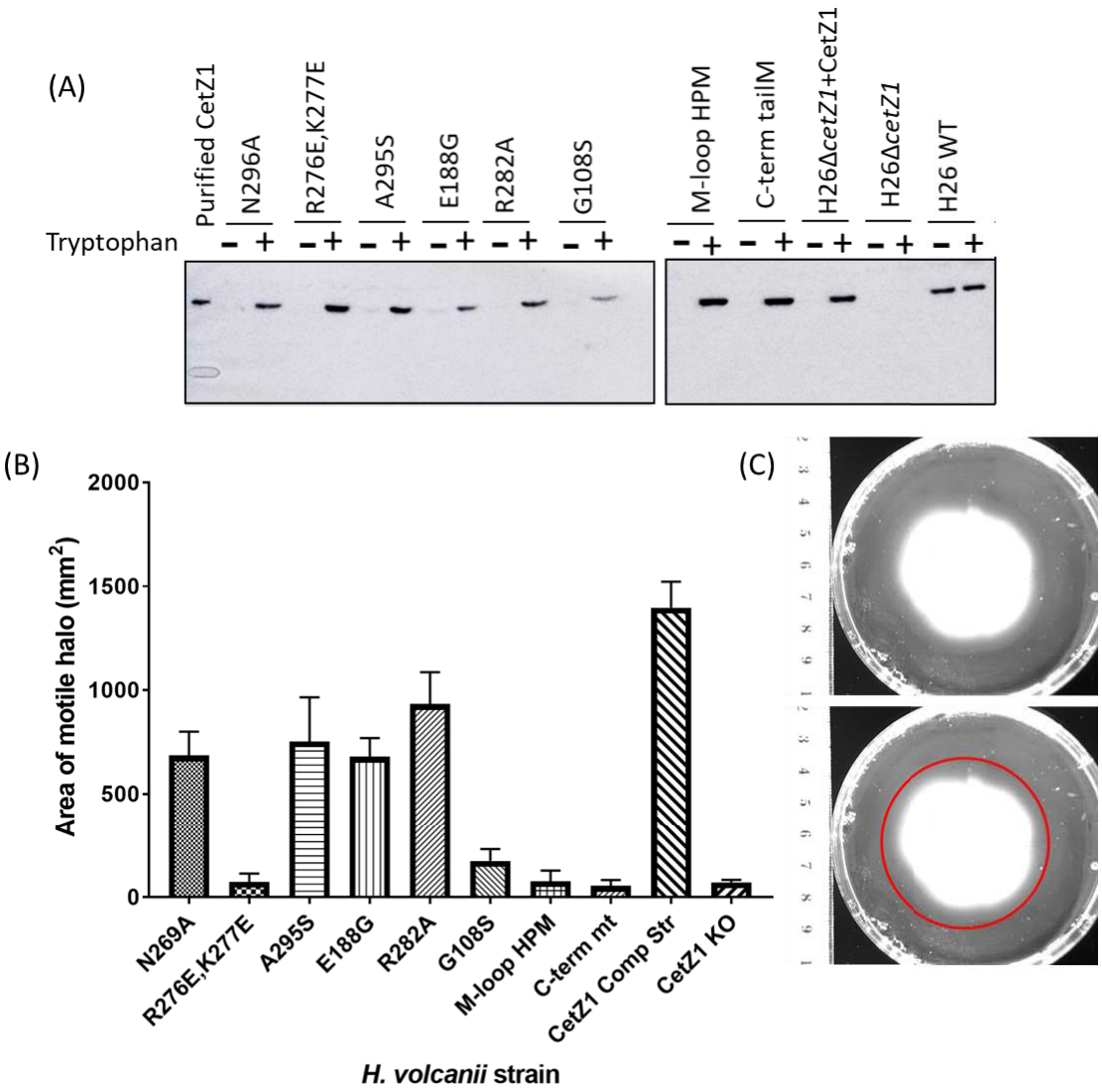

Figure 5.2: *Expression and motility assays of strains expressing CetZ1 point mutants.*

(A) A Western blot showing the regulation of expression of CetZ1 mutant proteins in the presence and absence of 2 mM tryptophan. All the mutant proteins were expressed in ID181 (ΔcetZ1, from a plasmid-based on pTA962). The cells were continuously grown at the mid-log phase in Hv-YPCab+2 mM tryptophan prior to the Western blot. (B) A screen for the capacity to support motility in the mutant-expression. Each bar indicates the mean area of the motile colony in 10 independent motility assays in H-vCab+2 mM tryptophan. Error bars represent the standard deviation. (C) An example of a motility assay plate. The top figure is the original image, which shows the halo around the motile colony. The area of the motile colony was measured indicated with a red circle in the bottom image (note that the red circle defines the outer edge of the expanding halo, which is fainter than the central region where cell growth has occurred).

Mutations were identified in the predicted CetZ1 self-association domain ((R276E, K277E) and M-loop hydrophobic patch mutant (HPM)), the GTP contact domain (G108S) and the membrane interaction domain (C-terminal tail mutant (C-term tailM) and M-loop HPM) that were essentially less motile (Figure 5.2) compared to the control CetZ1 complementation strain (i.e. *H. volcanii* ID181 (Δ*cetZ1*)+pTA962_*cetZ1*). The motility defect of the point mutants was compared by measuring the area of the motile halo (using ImageJ) of ten technical replicates (Figure 5.2). Each replicate contained 25 ml of soft agar medium per plate and was carried out at the same incubation conditions with one stab inoculation (2 µl) per plate. Maintaining these experimental conditions would minimise the variations in the spread of the colony due to the dehydration of the agar medium during incubation and possible effects on the growth by the sibling colonies. Next, the inability to form rods in point mutants during TE depletion assay was observed in technical duplicates. The TE depletion assay was performed in Hv-Ca (-TE) media and cells were collected for microscopy 15 h after inoculating into the liquid medium.

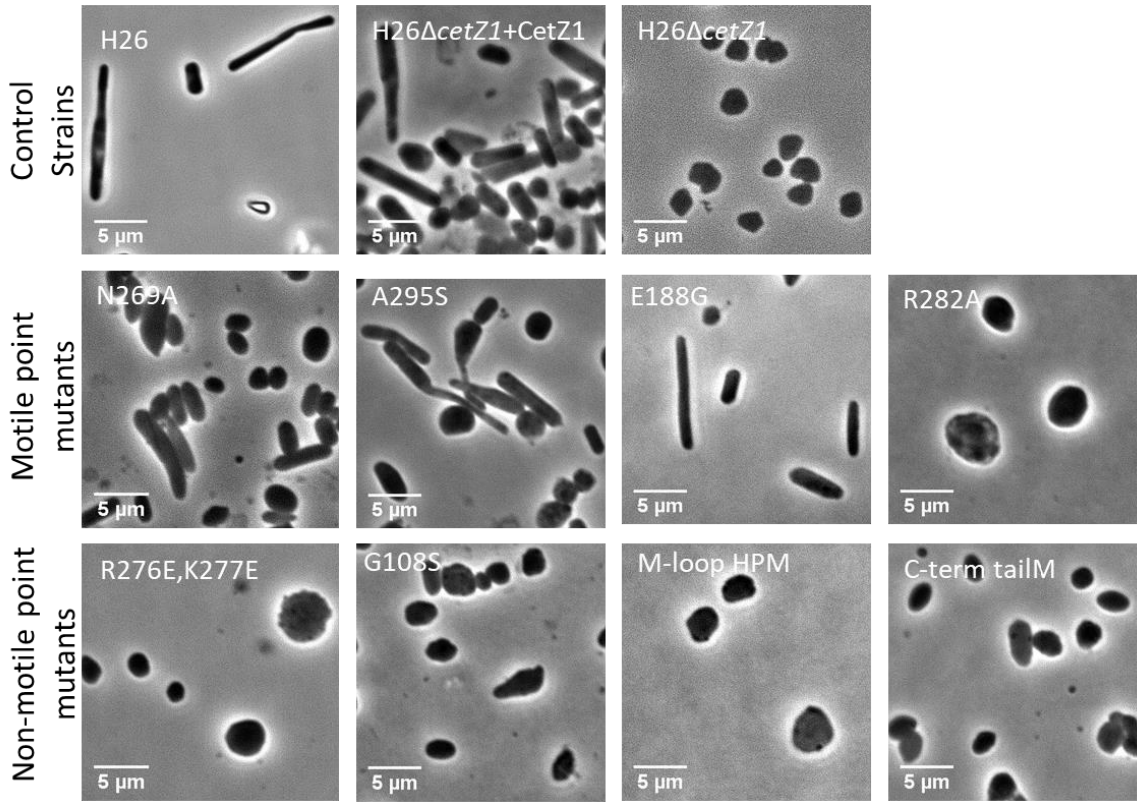

Figure 5.3: *Cell shapes observed in ID181 expressing the indicated CetZ1 site-directed mutants (on pTA962) in the TE depletion assay.*

The cells were imaged 15 h after inoculating into Hv-Ca (-TE)+2 mM tryptophan. The first row shows all the control strains: H26WT+pTA962, ID181+pTA962_cetZ1, ID181+pTA962. The second row indicates all the mutants that could form rods during TE depletion except R282A. The bottom row shows all the less-motile mutants that completely failed to form rods during TE depletion. The scale bar indicates 5 µm.

All the point mutants with motility defects—G108S, M-loop HPM, C-terminal tail mutant and (R276E, K277E)—failed to form rods during TE depletion. All the mutants that were motile, were able to form rods except R282A. The mutant CetZ1.R282A produced fewer rods and often contained large round cells (Figure 5.3). Despite having these mutations, CetZ1 appeared to have quite high stability and maintained its correct folding as the mutation, A295S, that was located partially inside the core of the protein exhibited the normal CetZ1 function.

A quantitative comparison of these point mutants' function was carried out using the early-log phase assay (Section 5.4.3). The assay was conducted in Hv-YPCab (+2 mM tryptophan), and cell samples were taken from ID181 expressing each point mutant on pTA962 at the rod-peak point (10 h after inoculation). Cell samples were then subjected

to microscopy for cell shape analysis. Furthermore, cell volume analysis of the same early-log phase cell samples was carried out using the coulter counter to investigate whether these mutations result in cell division defect (increase in the cell volume is a hallmark of a cell division defect).

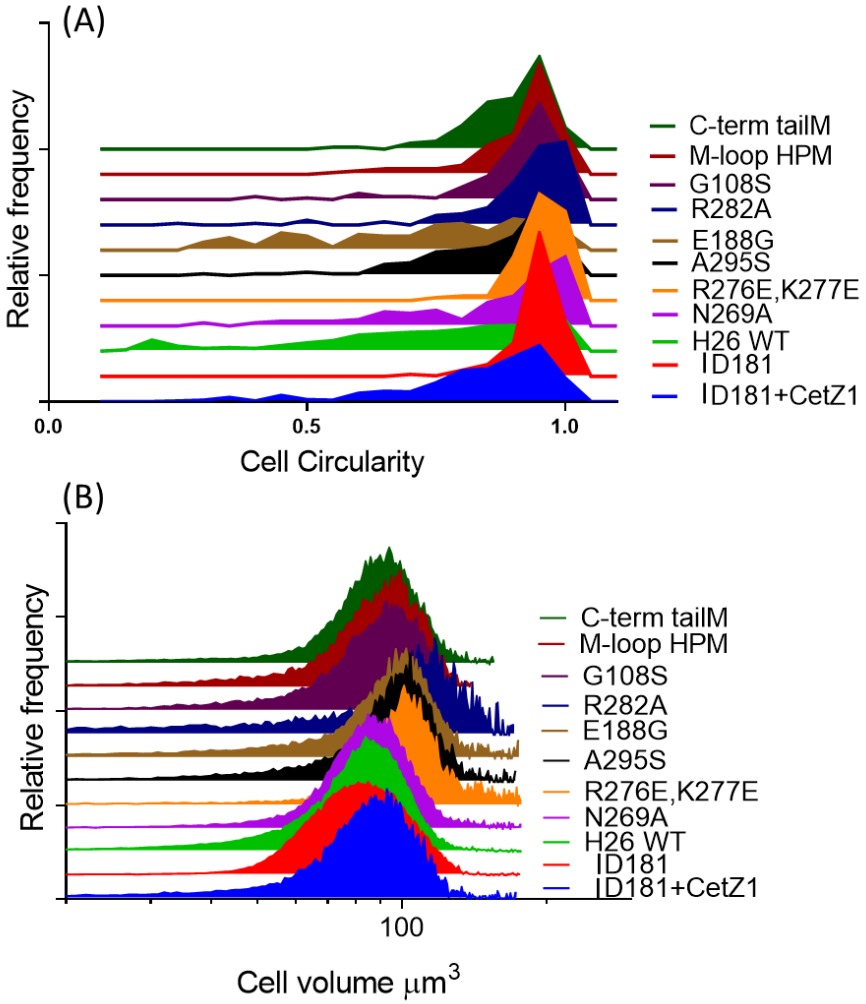

Figure 5.4: *Rod formation by CetZ1 point mutants in the early-log phase assay.*

(A) and (B) compares histograms of the cell circularity distribution (sample size N~200) and cell volume distribution (N>3000) respectively of the mutant cells to the WTH26+pTA962, ID181+pTA962 and ID181+pTA962_cetZ1.The mutants were expressed using pTA962 expression vector. The cells growing in Hv-YPCab+2 mM tryptophan were collected after 10 h for analysis. The cell circularities were analysed using ImageJ based tool Microbej (Ducret, Quardokus and Brun, 2016). A perfectly round-shaped cell has a cell circularity value of 1, with this number decreasing with the cell elongation.

The shape change quantification of the mutant-expressing strains was done by combining the cell circularity values (calculated from MicrobeJ) of three technical replicates. The mean cell circularity value of complementation strain (ID181+pTA962_*cetZ1*) was normalised to 100%, and the mean cell circularity of the *cetZ1* knockout (ID181+pTA962) was normalised to 0%. The CetZ1 point mutants that displayed motility showed an increased percentage of rod formation compared to the less-motile mutants, during the early-log phase assay except for R282A (Table 5.1). Although motile, R282A produced remarkably a smaller number of rods in both TE depletion and early-log phase assays (~8%).

Table 5.1 Rod Formation of ID181 by CetZ1 with Point Mutations During Early-log Phase Assay.

Mutant	**Normalised mean cell circularity%**	**Motility (Spread of colony after 5 days)**
E188G	125%	Yes
N295A	78%	Yes
A295S	68%	Yes
C-terminal tail mutant	30%	No
G108S	25%	No
M-loop HPM	16%	No
R282A	8%	Yes
(R276E, K277E)	1%	No

Note: The mean cell circularity of ID181+pTA962_*cetZ1* was normalised to 100% and that of ID181+pTA962 was normalised to 0% to calculate the values indicated in the above table.

Interestingly, E188G that is located on the front surface of the central H7 helix displayed a higher rod cell formation than the complementation strain, ID181+pTA962_*cetZ1*. All the point mutants that had a motility defect failed to form rods in the early-log phase assay equivalent to ID181 (Figure 5.4). However, the GTP binding site mutant G108S was jagged in shape compared to the other less-motile mutants. Similar cell shape was previously observed (Duggin *et al.*, 2015) for the CetZ1 GTPase mutant E218A,

suggesting these pointy cell shapes could be a characteristic feature that implies the impairment of the GTPase activity in CetZ1.

The cell volumes of the mutants during the "rod peak" in early-log phase revealed that despite the cell shape, the *cetZ1* knockout strain (ID181+pTA962) and the complementation strain (ID181+pTA962_*cetZ1*) displayed a similar cell volume as the H26 WT+pTA962. However, the CetZ1 mutants, A295S, E188G, R282A and the double-mutant (R276E, K277E) displayed a slight increase in cell volume compared to the H26 WT rod cells (Figure 5.4B). The highest cell volume was observed in R282A, the mutant that displayed motility but was unable to form rods during early-log phase assay. Comparable cell volume distributions were observed between the duplicates of the early-log phase assay carried out for these point mutants. Since CetZ1 does not play an essential role in cell division, we believe the aberration in the cell shape might have affected the proper cell division of the mutants during the early-log phase.

5.2.2 CetZ1 localisation dynamics in the point mutants

A close association with the cell envelope and a highly dynamic nature were the primary features observed in the WT CetZ1 localisation analysis (Chapter 04). In order to understand the significance of this localisation pattern for CetZ1 function and the important regions of the protein that help with such localisation, it is imperative to study the *in vivo* localisation of the point mutants. For this, we cloned all the CetZ1 point mutation sequences (without the stop codon) into the same expression plasmid, pTA962 with mTurquoise2 (mTq2) which was used to study the WT CetZ1 localisation. These plasmids were transformed into ID181 and the localisation patterns, and dynamics were mainly analysed during "rod peak" time (10 h) in the early-log phase assay. The assay was carried out in Hv-YPCab with 2 mM tryptophan.

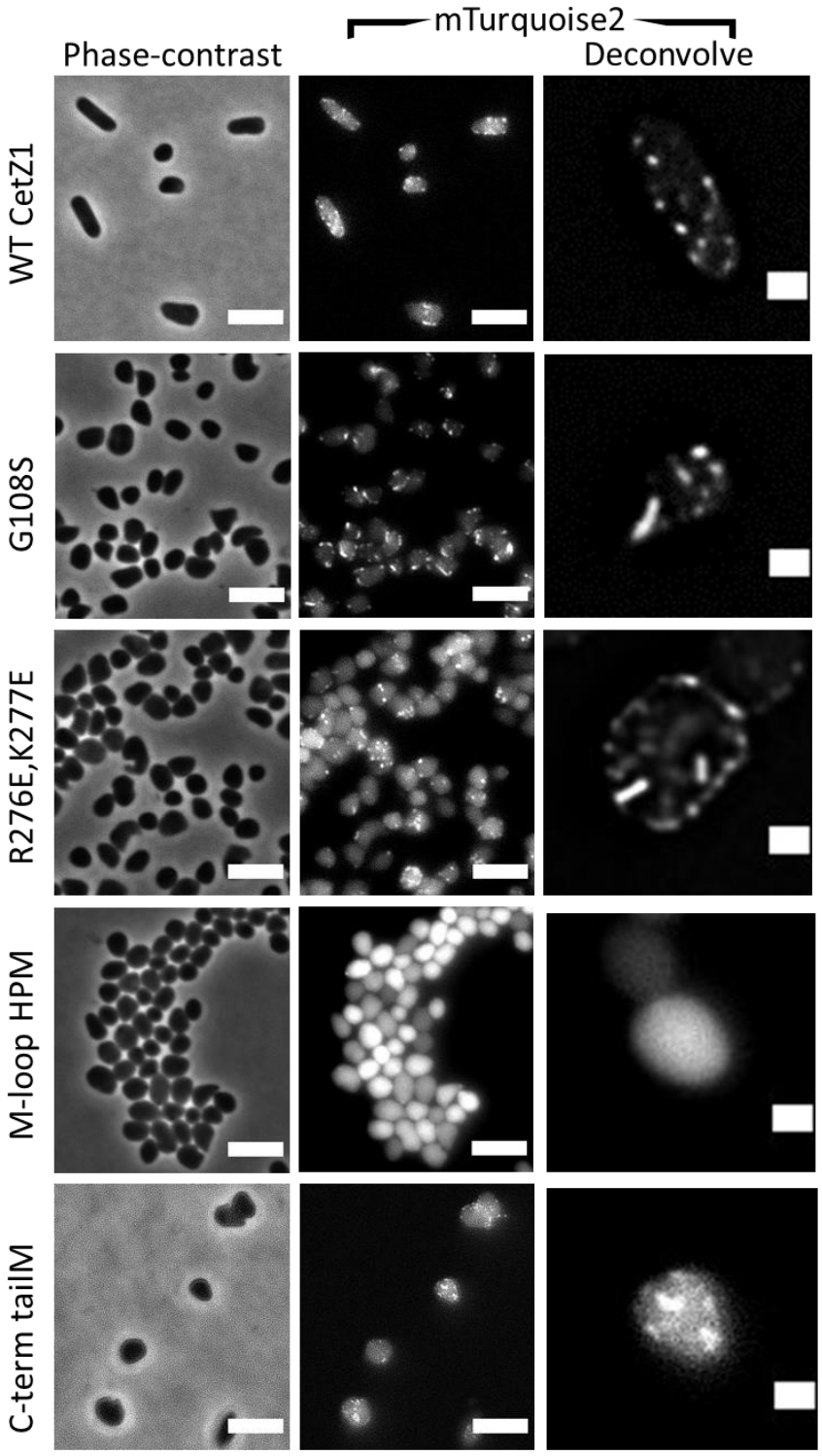

Figure 5.5: *CetZ1-mTurquoise2 localisation during early-log phase assay for point mutants that displayed decreased motility.*

The phase-contrast (first column) and the fluorescence (the next two columns) images of ID181 expressing WT and mutant CetZ1s on pTA962 based mTq2 plasmid. The cells growing in Hv-YPCab+2 mM tryptophan were imaged after 10 h. The last column (scale bar 1 µm) zooms the deconvolved cells of the images shown in the second row. The scale bar is 5 µm unless indicated otherwise.

The mutants with dysfunctional CetZ1s typically displayed an intense and less dynamic (Supplementary video 6, 7, 8 and 9) localisation compared to the WT CetZ1 except for the M-loop HPM. The M-loop mutation displayed a strikingly different localisation than the other mutants *in vivo*. CetZ1.M-loop HPM-mTq2 was highly diffuse (Figure 5.5) throughout the cytoplasm, thereby increasing the global fluorescence intensity inside the cells compared to the background intensity (mean fluorescence signal in the areas without distinct localisations) inside the WT and other mutants. The fluorescence signal in the control strain which expressed only mTurquoise2 in ID181, was quite weak (Figure 5.6) indicating that the intense diffuse fluorescence signal was due to the expression of CetZ1.M-loop HPM-mTq2 fusion. The GTP binding site mutant displayed an intense peripheral localisation while the double-mutant (R277E, K276E) displayed an intense filament-like localisation. The C-terminal tail mutation indicated a mix of localisation patterns. Although it showed a peripheral localisation, some cells displayed a diffuse localisation and others had CetZ1 localised away from the cell edges.

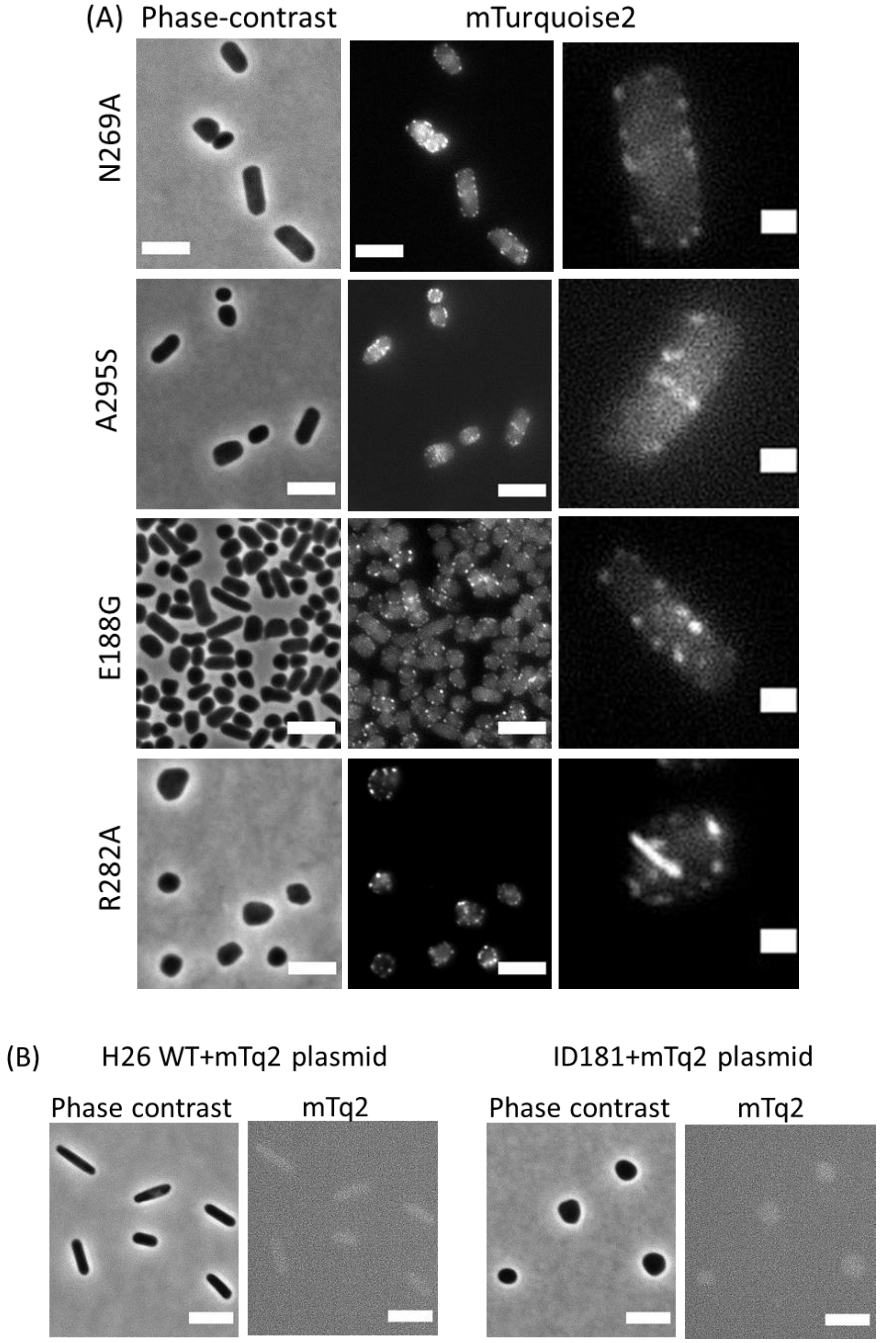

Figure 5.6: *CetZ1-mTurquoise2 localisation during early-log phase assay for point mutants that displayed normal motility.*

The phase-contrast (the first column) and the fluorescence (the next two columns) images of ID181 expressing mutants on pTA962 based mTq2 plasmid. The cells were grown in Hv-YPCab+2 mM tryptophan. The last column (scale bar is 1 µm) zooms the cells shown in the second column. (B) The phase-contrast and fluorescence images of the control strains, H26 WT and ID181 respectively expressing the mTurquoise2 expression plasmid without CetZ1. The fluorescence signal was extremely weak when there is an absence of a gene cloned before the mTq2 sequence. The scale bar is 5 µm (unless indicated otherwise).

All the point mutants that could form rods in the early-log phase assay displayed a similar patchy and peripheral localisation as the WT CetZ1. The majority of cells expressing the mutation CetZ1_R282A, which displayed motility and a significantly (P <0.000l) smaller number of rods than ID181+pTA962_*cetZ1* in early-log phase assay, showed intense and filament-like localisations rather similar to R276E, K277E.

In order to further compare the different localisation arrangements, a Fiji ImageJ based tool was developed to analyse the localisation distribution (in collaboration with Dr Christian Evenhuis). As shown in Figures 5.7A and Supplementary Figure 5, the new analysis tool can identify the local curvature (Duggin *et al.*, 2015) of the cell contour (positive curvature shown in shades of blue and negative curvatures shown in shades of red). Then localisations (marked in yellow line) were detected by acquiring foci that had 75% higher intensity than the background of the 40-pixel radius. The red lines in Figures 5. 7 give the shortest distance of these detected localisations to the cell outline.

CetZ1 with the mutation E218A disrupts the GTPase activity. Although overexpression of this mutant indicated a positive relationship with the cell curvature (Duggin *et al.,* 2015), no remarkable correlation was observed between CetZ1 localisation and the local curvature of the rod cells formed under WT level of expression (Figures 5.7A and Supplementary Figure 5). In rods, CetZ1 indicated localisation into both positive and negative curvatures, and also into the cell outline of the middle part of the long axis, although no increased curvature was detected in 2D images.

The analysis further indicated that all the strains expressing functional CetZ1 have a common localisation distribution.

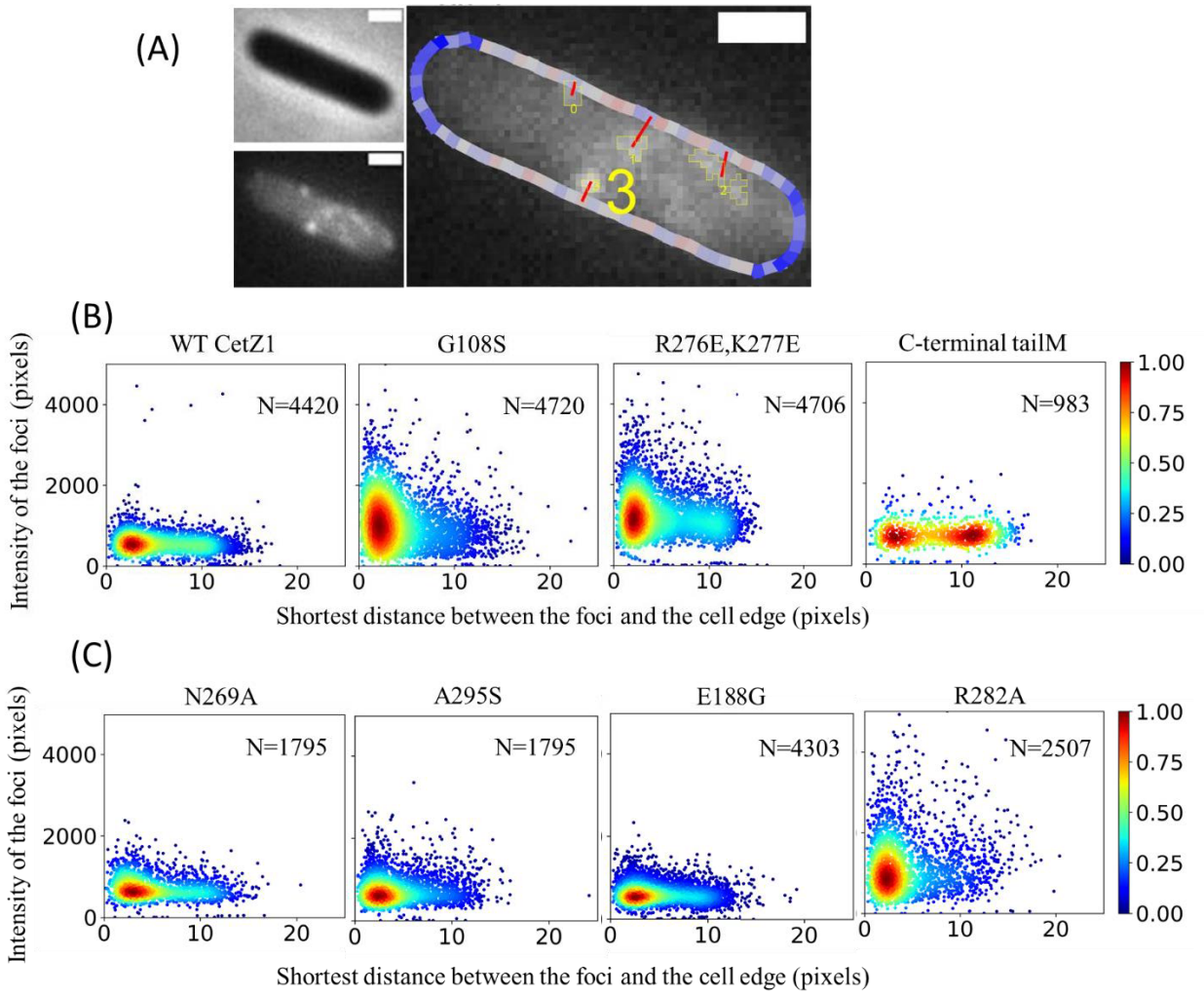

Figure 5.7: *Comparison of distances of CetZ1 localisations to the cell edge in different point mutants.*

(A) is an example of a cell showing how the Fiji based analysis tool detects the highest intensity localisations in the cell, the distance of the localisation (foci) from the cell edge and the local curvature changes on the cell outline (increase in red colour shows the increase in negative curvature, increase in blue shows the increase in positive curvature). (B) and (C) show the distribution of foci intensity and the shortest distance they located from the cell edge in ID181 expressing WT and mutant CetZ1s on pTA962-mTq2 in Hv-YPCab (+2 mM tryptophan) in early-log phase assay (10 h). The mutants given in the bottom row displayed higher motility than the mutants in the top row. N gives the sample size. The colour spectrum indicates the density of the data points.

In order to form a rod-shaped cell, CetZ1 was primarily localised close to the cell periphery. However, the smearing of this distribution (Figure 5.7) to the mid cell suggests that the localisation was not limited to the cell edges. Remarkably intense, strong peripheral localisation was displayed by the mutants expressing dysfunctional CetZ1s

(Figure 5.7) except for the M-loop HPM (localisation analysis is not shown for M-loop HPM). The intense and less dynamic (Figure 5.7, Supplementary Video 8 A and B) localisation pattern in the mutation at the GTP binding domain, G108S, was previously observed in E218A, the depolymerisation mutation which is expected to make hyper stable filaments. When the GTPase function is disrupted, the filaments polymerise with no shrinkage events. When all the elongation sites are saturated, and the GTP bound subunits in the polymer come into equilibrium with the free GTP bound subunits in the cytoplasm, the polymer growth stops, resulting in a hyper stable filament (Dougherty *et al.*, 2001). Although G108S locates on the GTP binding pocket, this mutation possibly hyper stabilises the binding of the GTP molecule, thereby resulting in hyper stable CetZ1 filaments. Furthermore, the strong cell envelope associated localisation of G108S and E218A suggests that holding a filament structure helps to enhance the envelope-binding of CetZ1 (Supplementary video 11 shows a Z-stack image of a cell expressing CetZ1.G108S-mTq2).

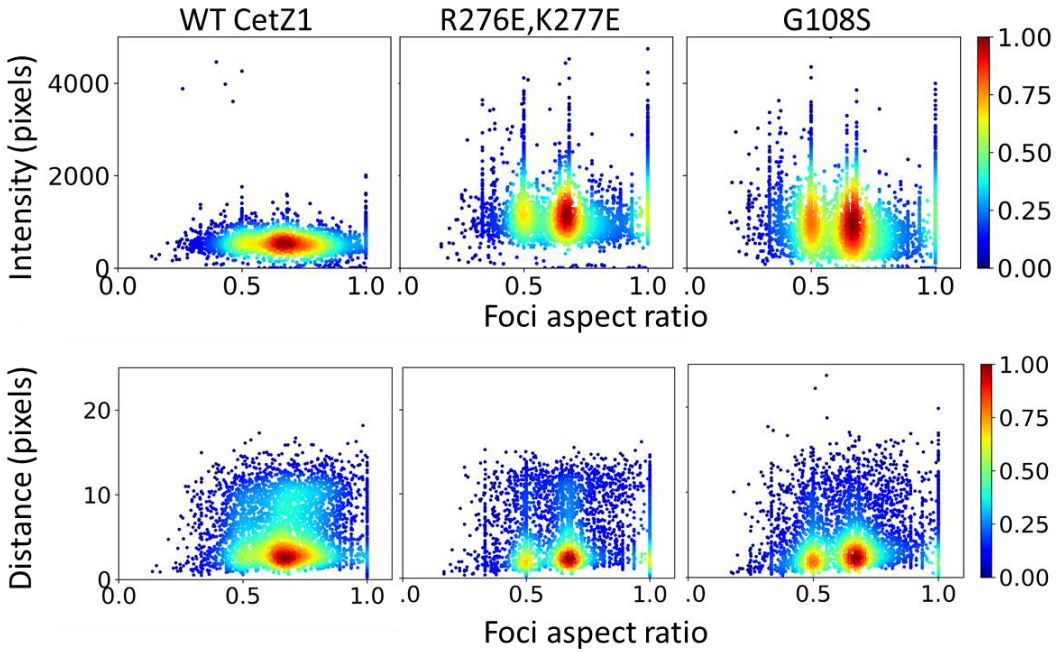

Figure 5.8: *A comparison of the aspect ratio of the localisations in the double mutant (R726E, K277E) and G108S to the that of WT CetZ1.*

The strain ID181 expressing (2 mM tryptophan) mTq2 tagged mutants on pTA962 were analysed in early-log phase. The top row compares the intensity and the aspect ratio of the foci between the strains mentioned above. The bottom row shows a comparison of the distribution of foci that has different aspect ratios inside the cell, between the above mentioned two mutants and the WT. The sample size N~4700. The colour spectrum indicates the density of the data points

Mutation in the lateral contact domain, (R276E, K277E), resulted in reduced peripheral localisation (Figure 5.8) compared to G108S and often contained distinct filament-like structures at the mid-cell (Figure 5.5). The majority of the peripherally associated fraction of this mutant protein displayed a higher intensity (Figure 5.7) than the WTcell envelope-associated localisation. This was mainly due to the distinct and less dynamic filament structures formed by the (R276E, K277E) mutant, which exhibited a high fluorescence intensity. The analysis of aspect ratio of the localisations indicated both (R276E, K277E) and G108S mutants have two distinct populations of intense foci whereas WT CetZ1 indicated a smeared aspect ratio distribution of low intense foci (Figure 5.8). Increased density of the localisations with a low aspect ratio in both these mutants compared to the WT CetZ1 further supports the indication of decreased GTPase activity in these mutants.

However, the reason for the decreased GTPase behaviour in the C-terminal domain surface mutant, (R276E, K277E) is obscure.

Furthermore, the cell envelope-associated localisation of (R276E, K277E) was different to that of the WT as the intense filament-like structures located close to the cell envelope were pointed inwards towards the cell cytoplasm (Figure 5.5. Supplementary video 7 A and B). This is unlike the treadmilling-like localisation on the cell envelope which was observed for the WT (Supplementary video 6). The reduced cell envelope localisation of (R276E.K277E) was potentially due to the disruption of lateral interactions within the CetZ1 quaternary structure that might be required for stable cell envelope interaction. The alternative possibility is that these filament structures observed under the super-resolution light microscope could be an assemblage of multiple protofilaments, and these failed in cell envelope remodelling as the double mutant region, (R276E, K277E) is involved in facilitating the cell envelope interaction of CetZ1. However, to confirm the individual filament structures, it is essential to observe these using cryo-electron microscopy.

The C-terminal tail mutant indicated a decreased cell envelope localisation (Figure 5.7, Supplementary video 9) suggesting the disordered C-terminal region could be useful for the membrane interaction of CetZ1 similar to the membrane interactions of FtsZ.

5.3 Discussion

This chapter explores the structure-function relationships of the cytoskeletal protein, CetZ1 during *H. volcanii* cell shape changes induced by different environmental conditions. The highly dynamic cell envelope associated localisation of CetZ1 during morphogenesis implies that CetZ1 might play a crucial role in the active remodelling of the cell envelope to ensure a cell shape change.

In tubulin superfamily proteins, dynamic instability is established by GTP dependent polymerisation and depolymerisation. Therefore, the amino acids at the GTP contact site, loop T1, T4 and T7, are highly conserved throughout the family. In CetZ1 T7 mutation, E218A and T4 mutation G108S, a comparable localisation pattern was displayed. Although we assumed G108S would result in diffuse localisation due to the impairment in polymerisation, both E218A and G108S mutations indicated a formation of less dynamic hyper-stable filaments (similar to tubulin) which ultimately resulted in complete functional impairment. A point mutation T143G, at the T4 GTP contact region of tubulin, indicated a significant reduction in GTP binding at the E site (in β tubulin) and microtubule growth both *in vivo* and *in vitro*. In addition to the slow growth, this mutation resulted in slow depolymerisation as well suggesting that the rate of polymerisation is probably associated with the rate of depolymerisation (Dougherty *et al.*, 2001). In *E. coli*, the analogous mutation G104S (*ftsZ84*) in the phosphate-binding signature motif (T4 region) of FtsZ increases the temperature sensitivity of the cells. The *ftsZ84* mutant exerts a normal cell division at 30^0C and a defective growth at 42ºC. Although the top surface T4 region is mainly associated with the polymerisation, it reduced the FtsZ depolymerisation by 4-fold compared to the WT (Lu, Stricker and Erickson, 2001). The bottom surface of the tubulin superfamily proteins is known to facilitate the depolymerisation. A mutation at the bottom surface residue D212 in T7 region of *E. coli* FtsZ results in a 90-fold reduction in the GTPase activity compared to the WT (Lu, Stricker and Erickson, 2001, Scheffers *et al.*, 2002). A mutation in the amino acid residue E254 in tubulin T7 region also displays a similar and severe impairment of GTPase activity. These mutations in the T7 region, however, did not affect the GTP binding or polymerisation significantly (Anders and Botstein, 2001a). The hyper stable localisation in G108S indicates that this residue in the T4 region could be either involved in

facilitating the depolymerisation or this mutation probably stabiles the GTP binding, thereby reducing its hydrolysis.

The above data also revealed a CetZ1 mutation that increases the complementation of rod cell formation in ID181. This mutation E188G is located on the H7 central helix that separates the core N-terminal and C-terminal domains. The mechanism of how it acts to improve the complementation is obscure. In contrast, a mutation located on the top part of the H7 region, β:T238A in yeast β-tubulin has been shown to uncouple the conformational changes in the microtubule from its nucleotide state, thereby maintaining a straight tubulin conformation which reduces the microtubule shrinkage (Geyer *et al.*, 2015). In the FtsZ of *Bacillus subtilis*, the mutation R191A in the FtsZ region has shown to reduce the level of polymerisation by instigating a conformational change that disrupts the interactions between the adjacent monomers via T7 loop (Dhaked *et al.*, 2016). However, both these mutations do not have a severe dominant effect on the function.

The present study also explored the other functionally important regions in CetZ1. Interestingly, we identified a few regions in CetZ1 such as the C-terminal tail, M-loop hydrophobic region and R276, K277 that are essential for rod formation in *H. volcanii*. The complete obstruction of the CetZ1 function due to the mutations on the surface loops, especially the M-loop region, suggests that CetZ1 is possibly assembling into a quaternary structure that might be essential to exert its activity. It is unlikely that this mutation destabilises the core of the protein as the M-loop region is a surface loop and, the expression of the mutation appeared normal in the Western blot analysis (Figure 1.2).

Furthermore, CetZ1_M-loop HPM was purified as a monomer protein via a gel filtration column (Chapter 6) and was soluble at 1.5 mM concentration. Therefore, it is plausible to assume this diffuse localisation pattern was due to the actual mutation in the context of a correctly folded protein, and not due to the loss of structural integrity of the protein monomer. According to our initial prediction, this region could be involved in either stabilising a CetZ1 higher-order structure or interaction with the cell membrane. In tubulin, the M-loop region is involved in stabilising the lateral interactions of the microtubule (Amos, 2004). The highly diffuse localisation pattern of CetZ1 M-loop mutation prompts two possible involvement of this region in CetZ1 function. First, the M-loop could be needed for the membrane interaction; thus, it facilitates the nucleation of the polymers that is essential for the structural dynamics. However, the actual structure of the visible filament-like fluorescent localisations for WT CetZ1 has not been confirmed

as a single protofilament. Therefore, this diffuse localisation also supports the second possibility, that the M-loop could be stabilising a possible quaternary structure of CetZ1 similar to tubulin which might functionally active in the ultimate remodelling of the cell envelope. However, carrying out appropriate *in vitro* analysis for the purified mutant proteins is imperative to confirm the exact role of the functionally important regions we have identified in this study.

5.4 Methods

5.4.1 Construction of point mutants

The forward primers containing the point mutations and EndP_CetZ1_R were used to amplify the flanks containing regions upstream of the point mutation. The reverse of the former primers and EndP_CetZ1_F were used to amplify the corresponding downstream flanks. These were then joined using overlap extension PCR (18 cycles at T_m 60^0 followed by 30 cycles at T_m 72^0C). The whole CetZ1 gene was amplified using EndP_CetZ1_F and reverse end-primer containing the mutation: CetZ1_C-term tailM_R 1o make the C-terminal tail mutant. All the primers are listed in Table 5.2. The PCR amplified CetZ1 sequences with the point mutations were gel purified and cloned (Section 2.8.6) into the pTA962 expression plasmid (Table 2.3) using BamHI and NdeI restriction sites. The plasmids were initially purified using *E. coli* DH5α and then, de-methylated by transforming into *E. coli* c2925 (Table 2.5). The sequences of de-methylated pTA962 plasmids carrying the CetZ1 point mutations were confirmed by sanger sequencing and then, transformed (Section 2.7) into *Haloferax volcanii* H26 CetZ1 in-frame knockout strain (ID181).

Table 5.2 Primers used to amplify the CetZ1 point mutations. The mutations are denoted by the uppercase letters.

Primer name	Sequence 5'>3'
CetZ1_N269A_F	caccgcccacacgaccGCGcgaatcacgagcctc
CetZ1_N269A_R	gaggctcgtgattcgCGCggtcgtgtgggcggtg
CetZ1_R276E,K277E_F	gaatcacgagcctcgtcGAGGAGgccgcgctcggtc
CetZ1_R276E,K277E_R	gaccgagcgcggcCTCCTCgacgaggctcgtgattc
CetZ1_A295S_F	gaaggcgcggagcgcTCGctgctcgtgctcgctg
CetZ1_A295S_R	cagcgagcacgagcagCGAgcgctccgcgccttc
CetZ1_E188G_F	gatacgacgagatcaacGGCgaaatcgtcaaccg
CetZ1_E188G_R	cggttgacgatttcGCCgttgatctcgtcgtatc
CetZ1_R282A_F	aaggccgcgctcggtGCGctcacgctcccgtg
CetZ1_R282A_R	cacgggagcgtgagCGCaccgagcgcggcctt
CetZ1_G108S_F	Cgtgtccgggctctcgggcggcaccggctc
CetZ1_G108S_R	Gagccggtgccgcccgagagcccggacacg
CetZ1_M-loop HPM_F	Ggaagaacaacggcggcggctcggcgtctcgggcgacgggcggcgacgagc
CetZ1_M-loop HPM_R	Gctcgtcgccgcccgtcgcccgagacgccgagccgccgccgttgttcttcc
CetZ1_C-term tailM_R	cgcggatccTTAgccgcccgactccgcttcgtcctcgtcatcgtttatgagg
CetZ1_C-term tailM2_R	cgcggatccGccgcccgactccgcttcgtcctcgtcatcgtttatgagg
EndP_CetZ1_F	CCCCCGGGAATTCATatgaagctcgcaatgatcggattcggg
EndP_CetZ1_R	CGCGGATCCttagaaaagcgactccagttcgtcctcg
EndP_CetZ1_2_R	CGCGGATCCgaaaagcgactccagttcgtcctcg

5.4.2 Construction of fluorescent fusion proteins of CetZ1 point mutants

The stop codon of each CetZ1 point mutants was removed by amplifying them (30 cycles at T_m 72^0C) using the primers EndP_CetZ1_F and EndP_CetZ1_2_R. For the amplification of the CetZ1 C-terminal tail mutant, the later primer was replaced with CetZ1_C-term tailM2_R. The stop codon removed point mutants were then cloned into pTA962_EGlinker_mTurquoise2 and pTA962_Glinker_mTurquoise2 plasmids (Chapter 04) using BamHI and NdeI restriction sites. The CetZ1 sequences were confirmed by sanger sequencing.

5.4.3 Early-log phase rod development

The *H. volcanii* strain was streaked onto an agar plate made from the same medium as chosen for the assay (e.g. Hv-YPCab, Chapter 3), and then the plate was incubated in a humidified bag at 45°C for 3-5 days. Colonies were collected from the surface with a microbiological loop, and suspended in 5 ml of the liquid medium, sufficient to give an optical density (OD - 600 nm) > 0.05. The OD was immediately adjusted to 0.05 by dilution with fresh medium. This culture (5 mL in a 50 mL Falcon tube) was then immediately incubated at 45°C at 200 rpm in a GFL1092 rotary-shaking water bath (the tube's lid was loosened to allow gas exchange), marking the start of the growth curve (t=0 h). Samples were withdrawn at t=10 h for microscopy or other analyses. For the TE depletion assay, the same steps were followed in Hv-Ca (-TE) media and the cells were collected for analysis at t= 15 h.

5.4.4 Live cell imaging

The CellASIC ONIX B04A-03 Microfluidic Plate with the CellASIC ONIX Microfluidic System and CellASIC ONIX F84 Manifolds which enable perfusion-based, long-term, live-cell imaging were used. The four chambers in the CellASIC ONIX B04A-03 Microfluidic Plate were initially washed with 1mg/mL Bovine Serum Albumin in phosphate-buffered saline followed by 18% BSW (Table2.5). The cells were loaded as

per user manual. Then, the chambers were perfused at 2 psi for 20 hours with Hv-YPCab, and 10 minutes time-lapse analysis was carried out using a Nikon Ti.

5.4.5 Cell volume and cell count analysis by Coulter counter

Culture samples were diluted (x1000) with 18% BSW, and then, analysed with a Multisizer 4 Coulter Counter (Beckman Coulter) in the constant volume mode (1 ml), with a 30 mm aperture tube and 18% BSW as the electrolyte. A 2 mm bead standard (Beckman Coulter), diluted in 18% BSW, was used for prior calibration

CHAPTER 6

IN VITRO CHARACTERISATION OF CETZ1

6.1 Introduction

Despite the weak homology in the primary amino acid sequence, proteins in the tubulin superfamily share many similarities in their polymer dynamics. The most conserved feature of all tubulin superfamily proteins is the GTP-dependent polymerisation of the subunits. Although CetZs belong to the tubulin superfamily due to its primary sequence homology, a little known about the polymer dynamics of these proteins. CetZ1 is the most conserved member of all CetZs with a known function, i.e. cell shape control. The *in vivo* characterisation of CetZ1 using site-directed mutagenesis revealed the regions in CetZ1 structure that are important for the cell shape control were analogous to those required in tubulin and FtsZ function. For example, mutations in the T7 region in all three proteins indicated features of interference in the GTPase activity (Duggin *et al.*, 2015, Scheffers *et al.*, 2002, Anders and Botstein, 2001b).

In FtsZ and tubulins, *in vitro* studies confirm that the polymer assembly significantly increases with the addition of GTP (Lu, Stricker and Erickson, 2001, Deng *et al.*, 2017). Furthermore, these proteins are more prone to make bundles, tubes or sheet-like structures (Lowe and Amos, 2000). However, no in vitro characterisation has been done so far to analyse CetZ1 polymer dynamics. Therefore, the present study aims to optimise and identify the conditions for CetZ1 GTP-dependent polymerisation *in vitro*. Moreover, The mechanisms by which FtsZ and tubulin assemble their subunits possess a few differences. The following sections describe the key differences and similarities discovered in FtsZ and tubulin polymerisation.

6.1.1 Models for subunit polymerisation

Two main models have been proposed to explain the different modes of subunit polymerisation; isodesmic polymerisation and cooperative polymerisation (Figure 6.1) (**Figure 6.1**(Miraldi, Thomas and Romberg, 2008). Single-stranded polymers are formed via isodesmic assembly of polymers. In an isodesmic reaction, the type of chemical bonds broken in the reactant are the same as the type of bonds formed in the reaction product. A linear increase in polymer elongation is observed when the monomer surface exposed to the elongation site is constant during isodesmic elongation. Moreover, during

isodesmic assembly, initiation of elongation can rapidly occur at a minimum subunit concentration, and the elongation is usually linearly proportional to the subunit concentration in the medium (Miraldi, Thomas and Romberg, 2008). It has been observed that FtsZ bound to GDP can undergo isodesmic polymerisation (Rivas *et al.*, 2000). However, in the presence of GTP, both FtsZ and tubulin exert a cooperative polymerisation (Yaodong Chen and Erickson, 2005).

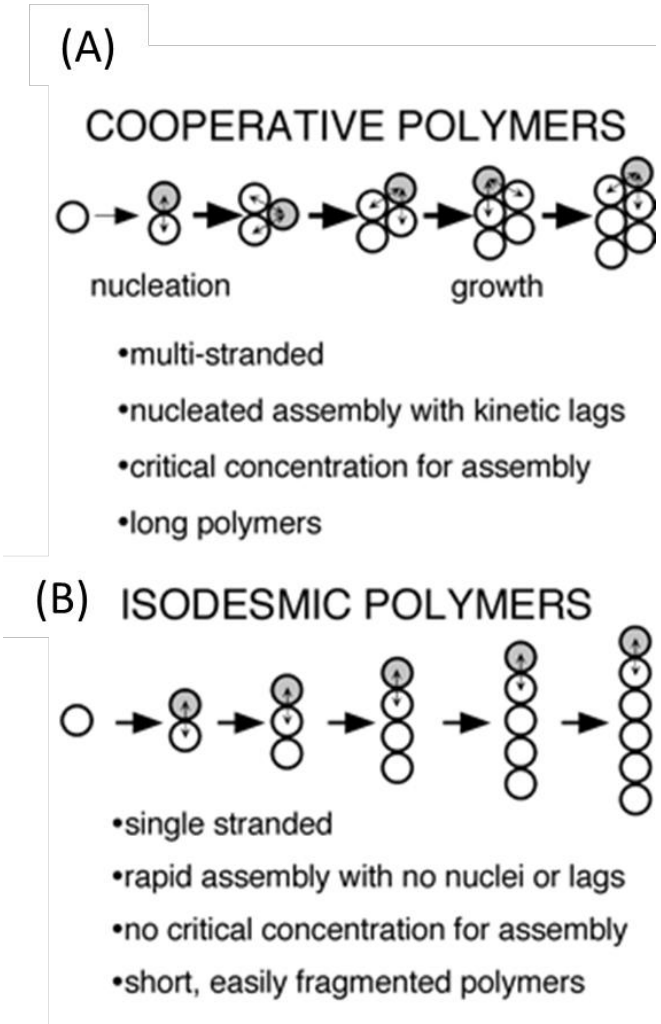

Figure 6.1: *A schematic showing the differences in subunit assembly between*

(A) Corporative assembly (B) isodesmic assembly. Taken from (Romberg, Simon and Erickson, 2001)

In cooperative polymerisation, subunits interact with each other to form the initial polymer nucleus which subsequently provides multiple interaction sites to grow the polymer. As a result, at low subunit concentrations, lagging of the nucleation causes a delay in the assembly of the polymers. Furthermore, the polymerisation initiation requires

a “critical” concentration of subunits, which refers to the minimum subunit concentration needed for the polymerisation (Miraldi, Thomas and Romberg, 2008). During cooperative assembly, polymerisation will terminate when the number of free subunits reaches to the critical concentration. In both FtsZ and tubulin, this value is approximately 1 μM (Yaodong Chen and Erickson, 2005). However, the critical concentration could be altered by other constituents present in the medium. For example, the presence of glycerol could significantly reduce the critical concentration required for tubulin polymerisation (Grego, Cantillana and Salmon, 2001). The reason for the improvement in the polymerisation via glycerol is unclear. Some studies show glycerol stabilises the hydrophobic interactions of the proteins (Vagenende, Yap and Trout, 2009), thus stabilising the correct protein fold. These variations of polymerisation suggest the *in vitro* critical concentration may not reflect the *in vivo* critical concentration as there are many regulatory proteins that affect both FtsZ and tubulin polymerisation *in vivo*.

During the polymerisation cycle, polymers of FtsZ and tubulin could be at one of the three nucleotide-bound states, i.e. GTP, GDP-P_i and GDP (Huecas and Andreu, 2003). And these polymers change the conformation of their subunits depending on the nucleotide bound state. In the monomeric state, the curved conformation is preferred independent from the bound nucleotide type (Lu, Reedy and Erickson, 2000). In an FtsZ polymer, the GTP bound state has a straight conformation while the GDP bound polymer to adopt a curved confirmation (via a conformational switch in loop T3 and helix H3). It is believed that this conformational change might be the basis for the cooperative polymerisation observed in single-stranded FtsZ polymers, whereas an increased number of interaction sites could contribute to the polymer elongation in multistrand polymers like tubulin in addition to the subunit conformational change (Miraldi, Thomas and Romberg, 2008).

6.1.2 The polarity of the cytoskeletal filaments

Both tubulin and FtsZ possess an intrinsic polarity due to the conformational changes upon GTP hydrolysis into GDP. *In vivo*, microtubules establish a polarity across the cell by having a minus-end attached to the microtubule-organising centre (the location of microtubule nucleation) and a fast-growing plus end that grows out to the cell periphery. Therefore, the GTP bound ‘top’ surface of the β-tubulin is always oriented toward the plus end. The stochastic stall of the polymerisation, which results in depolymerisation

and rescue of the depolymerising polymers are features of the characteristic dynamic instability of microtubules (Burbank and Mitchison, 2006). In FtsZ, the polar growth of FtsZ protofilaments assembled at the Z ring exerts a treadmilling behaviour to drive cell division in prokaryotes. The word treadmilling was introduced to this phenomenon as although it appeared as if the protofilaments are moving around the division plane, it is created by the polar growth of FtsZ filaments. The subunits are added to the polymer at one end while dissociation occurs at the other end.

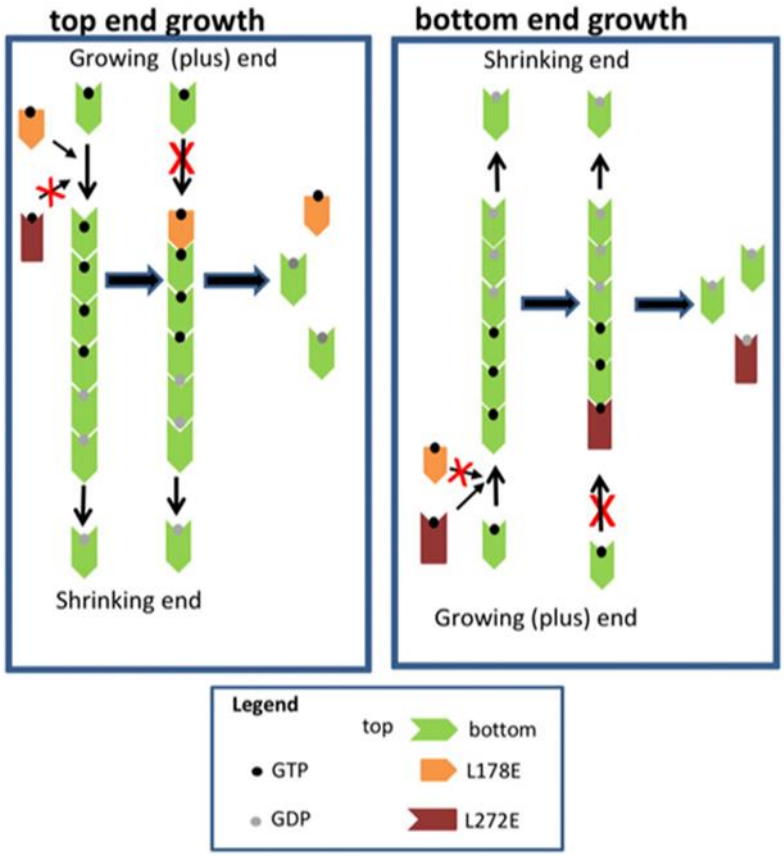

Figure 6.2: *The two possible kinetic polarities for polymer growth. Tubulin shows the first top-end growth kinetics in which subunits add to the GTP-bound end of the polymer.*

Using the two FtsZ mutations, L178E and L272E, it has been shown FtsZ has the opposite kinetic polarity shown in bottom end growth as the addition of FtsZ.L178E could not block FtsZ polymerisation like FtsZ.L272E. Taken from (Du et al., 2018)

By introducing mutant versions of FtsZ, FtsZL178E (Figure 6.2, top-end growth) and FtsZL272E (Figure 6.2, bottom-end growth), on the top and the bottom surface of FtsZ, it has been found that FtsZ and tubulin have opposite kinetic polarities (Du *et al.*, 2018).

FtsZ polymerisation occurs from the bottom of the protofilaments while it depolymerises at the top end (Figure 6.2).

In the present study, we made attempts to understand the *in vitro* polymer dynamics and molecular interactions of CetZ1, a third group of tubulin superfamily protein discovered in archaea. Analysing *in vitro* interactions would allow us to test CetZ1 dynamics under controlled conditions.

6.2 Results

6.2.1 Optimisation of CetZ1 purification

A method for purification of CetZ1 was previously reported by Duggin *et al.*, 2015. The cell lysate was first purified by ion exchange followed by gel filtration chromatography steps. During ion exchange, CetZ1 eluted at around 450 mM KCl in the salt gradient concentration and the fractions that contained a high amount of CetZ1 were pooled (Figure 6.5). The subsequent gel filtration further improved the purity of the protein (Figures 6.4, 6.5).

However, this method was ineffective in purifying the CetZ1 in the monomeric form. Comparison of the gel filtration chromatograms of BSA (66.5 kDa) and CetZ1 (42 kDa) indicated that the CetZ1 elution peak appears before the BSA elution peak (Figure 6.4) suggesting CetZ1 was eluted in a non-nucleotide-dependent multimeric form. Aggregation of proteins can obstruct the active sites, thereby hindering its proper function. Therefore, it is important to purify CetZ1 in the monomeric form, so that its nucleotide-dependent polymerisation dynamics and molecular interactions can be characterised meaningfully. The multimeric CetZ1 was incubated with reagents known to prevent protein aggregation such as reducing agents (β-mercaptoethanol, Dithiothreitol), detergents (0.1% v/v), 10% glycerol and 1 mM EDTA. These incubations were performed for both 30 mins and overnight to test the dissociation of the aggregates (Bumagina *et al.*, 2010, Bondos and Bicknell, 2003). The appearance of the CetZ1 peaks before the BSA peak in all these reactions during a subsequent gel filtration analysis indicated these protein aggregates were not dissociated satisfactorily once they were formed. Therefore, the purification was carried out using three types of additives in all the buffers used from the first step, i.e. lysis of the cells, throughout to the end. The first set of buffers contained the chelating agent 1 mM EDTA, the second had 1 mM EDTA and the kosmotrope 10%v/v glycerol and, the third set had the surfactant 0.1% v/v Triton X-100.

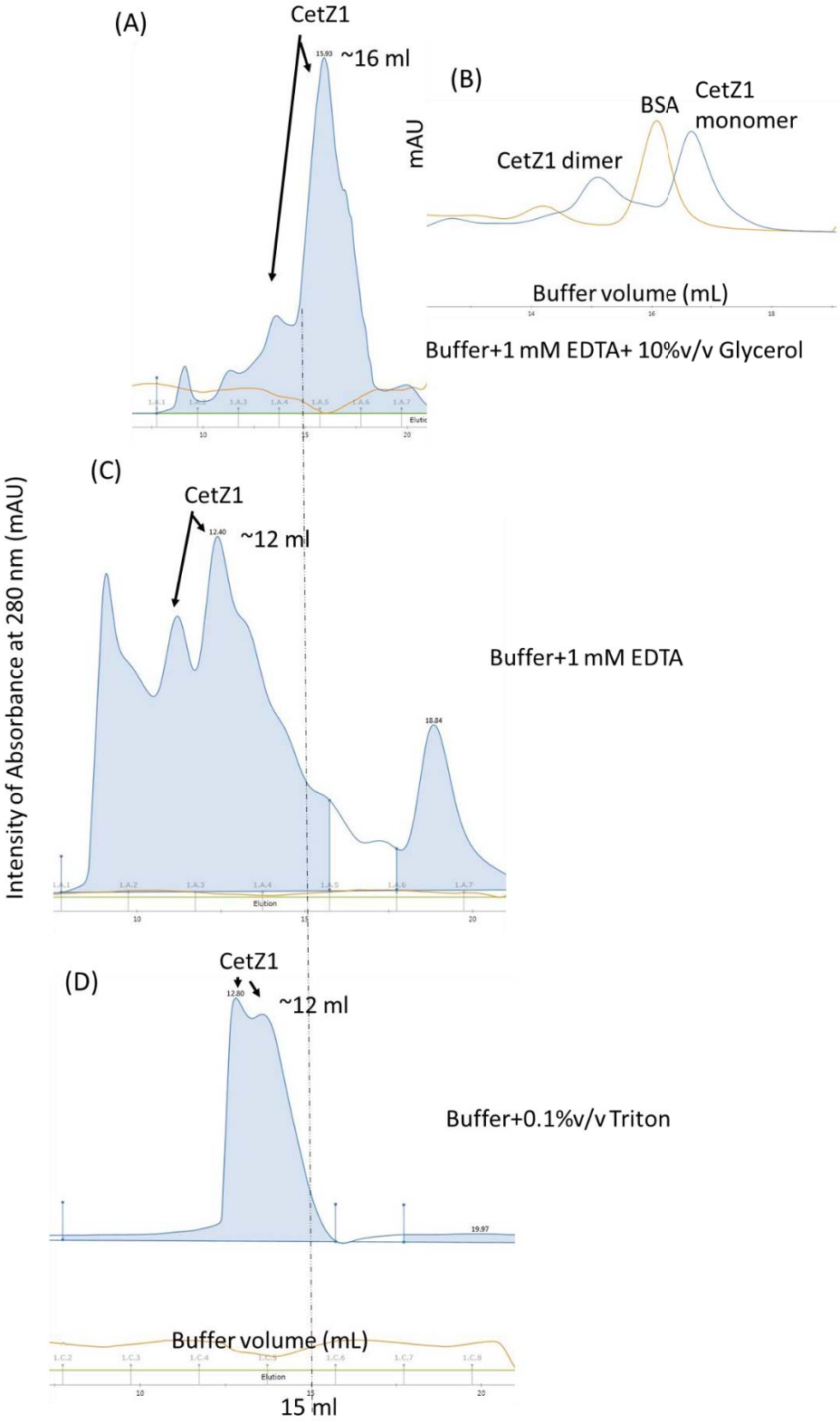

Figure 6.3: *The optimisation of the protein purification buffer with different additives.*

The figure compares the gel filtration chromatograms of CetZ1 purification using 25 mM Tris-HCl, 200 mM KCl, pH8.5 with (A) 1 mM EDTA+10%v/v Glycerol, (C) 1 mM EDTA and (D) 0.1%v/v Triton. (B) Comparison of CetZ1 elution with BSA from gel filtration when 1 mM EDTA+10% Glycerol was added to the buffer.

Having 1 mM EDTA or 0.1% Triton was unable to prevent the aggregation (Figure 6.3). Also, the control chromatographic run without the protein in the buffer containing 0.1% Triton indicated the buffer itself gives a peak that overlaps with the CetZ1 peak making Triton an unsuitable additive. Inclusion of both 1 mM EDTA and 10% glycerol improved the purification remarkably (Figure 6.4) by resulting in a higher monomeric peak between the peaks of BSA (66.5 kDa) and the truncated version (32 kDa) of *Bacillus subtilis* FtsZ (obtained from K. Kusuma, UTS) and, a small dimeric peak just before the BSA peak (Figure 6.4).

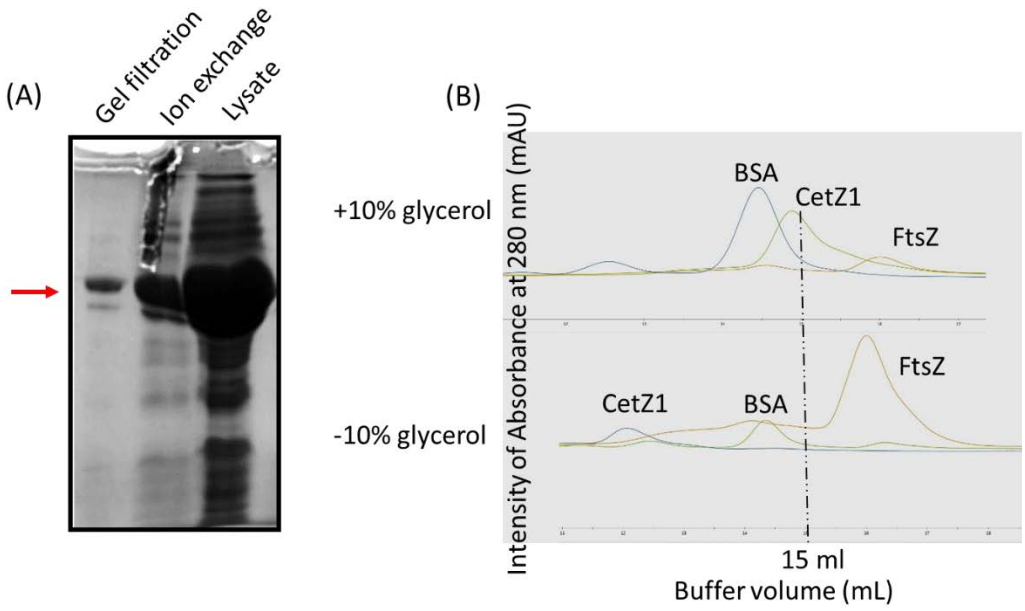

Figure 6.4: *Buffer optimisation improved CetZ1 purification.*

(A) SDS-PAGE showing CetZ1 purified after ion exchange and subsequent gel filtration. Red arrow indicates the CetZ1 band. (B) A diagnostic gel filtration chromatogram showed the improvement of CetZ1 elution in the monomeric form after incorporation of 10%v/v glycerol into the buffer. In the top figure, CetZ1(42 kDa) peak appeared between BSA (66.5 kDa) and FtsZ (32 kDa) peaks. In the bottom figure which shows initial purification without 10% glycerol, CetZ1 peak appeared before the BSA peak.

The cytoskeleton proteins possess an intrinsic tendency to aggregate together. Magnesium-induced polymerisation in the absence of nucleotides has been previously observed in FtsZ (Rivas *et al.*, 2000). The presence of 1 mM EDTA might aid to chelate the metal ions that could trigger this type of aggregation. Moreover, the lysate might contain ample amount of NTPs that triggers the oligomerisation of CetZ1. The amphiphilic nature of glycerol helps to interact with the hydrophobic surfaces of the

protein, thereby preventing the stabilisation of unwanted intermediates and unfolding of the protein (Vagenende, Yap and Trout, 2009). CetZ1 fractions purified during each chromatography step with the buffers containing 10% glycerol and 1 mM EDTA are shown in Figure 6.5. The pooled fractions from gel filtration were concentrated using Vivaspin20 (MWCO 10 0000) molecular concentrators and stored at -80 ^{0}C in aliquots for subsequent use in CetZ1 *in vitro* assays.

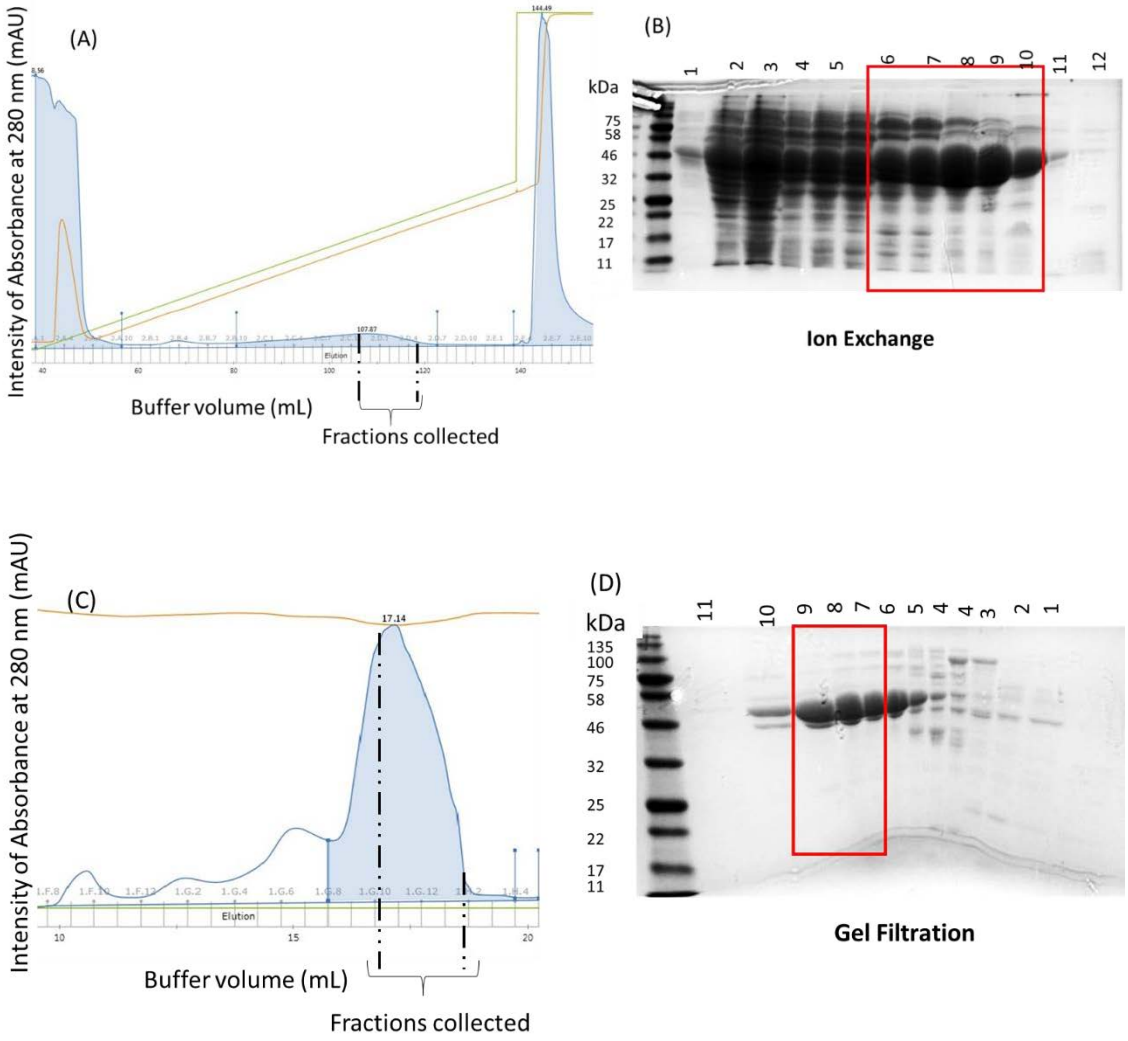

Figure 6.5: *SDS-PAGE analysis of the collected fractions from Ion Exchange and subsequent Gel Filtration.*

(A) and (C) are the ion exchange and gel filtration chromatograms, respectively. The fractions between the black dotted lines are highlighted by the red square in (B) and (D) SDS-PAGE gels, respectively. These fractions (band size~42 kDa) were pooled and concentrated using Vivaspin20. Concentrated fractions from the Ion Exchange was used for the Gel Filtration, and concentrated CetZ1 from Gel filtration were stored at -80 ^{0}C in small aliquots.

6.2.2 Optimised condition for CetZ1 polymerisation

Although CetZ1 indicated a higher similarity to tubulin according to the primary sequence conservation at the GTP active site, the overall backbone of its primary structure is more similar to FtsZ (Duggin *et al.*, 2015). Therefore, the buffer conditions that have previously been shown to facilitate FtsZ *in vitro* polymerisation were initially used. FtsZ has shown an increased polymerisation in 50 mM 4-morpholineethane-sulfonate (MES) buffer, pH 6.5 and increased GTPase activity in 50 mM 4-(2-hydroxyethyl)-1-piperazineethanesulfonic (HEPES) buffer, pH 7.5 with 1 mM GTP at 12 μM FtsZ concentration. The presence of Mg^{2+} facilitates FtsZ polymerisation. Furthermore, FtsZ has a higher GTPase activity at 300 mM KCl concentration compared to the lower KCl concentrations (Król and Scheffers, 2013). Therefore, the polymerisation of 12 μM CetZ1 in MES buffer and HEPES buffer at both pH 6.5 and pH 7.5 with 1 mM GTP (+10 mM Mg^{2+}) were explored. In addition to the 300 mM KCl ionic strength, 3 M KCl concentration was also tested as FtsZ in *Haloferax* has previously shown an increased polymerisation under 3 M KCl concentration (Wang and Lutkenhaus, 1996). However, no polymerisation was observed under all these conditions during both co-pelleting and 90^0 light scattering assays, which were tested with triplicates (data not shown). Although some studies indicate that Ca^{2+} could increase the FtsZ polymerisation *in vitro* (Lowe and Amos, 2000), no polymerisation was detected in CetZ1 with the presence of Ca^{2+}. As the currently reported FtsZ polymerisation buffer conditions (even with 3 M KCl, to approximate the intracellular concentration KCl) failed to facilitate CetZ1 polymerisation, it was decided to test polymerisation using previously established buffers used for tubulin polymerisation.

1,4-Piperazineethanesulfonate (PIPES) buffer and tubulin polymerisation PEM buffer (80 mM PIPES pH 6.9, 2 mM MgCl2 and 0.5 mM EGTA, 5% glycerol) have been commonly used for tubulin *in vitro* polymerisation (Waxman *et al.*, 1981). It was previously demonstrated that the concentration of the PIPES buffer could change the degree of polymerisation in tubulin. In this study, the highest tubulin polymerisation was achieved by using 800 mM PIPES at pH 6.9 (Waxman *et al.*, 1981). Therefore, using 800 mM PIPES at pH 6.9, the ionic strength needed for maximal CetZ1 polymerisation at 12 μM CetZ1 concentration was investigated using a KCl concentration gradient of 0.5 M, 1 M, 2 M and 3 M by 90^o light scattering assay. 1 mM GTP with 10 mM Mg^{2+} was added for

all the reactions as these concentrations have shown to give the optimum polymerisation *in vitro* in both FtsZ and tubulin.

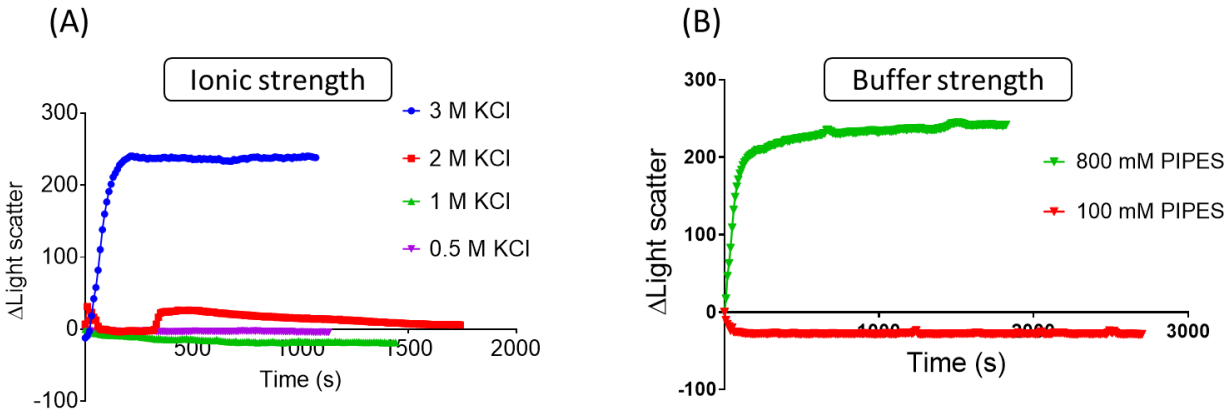

Figure 6.6*: Optimisation of CetZ1 (12 µM) in vitro polymerisation condition using the 90º light scattering assay.*

(A) CetZ1 polymerisation with 1 mM GTP (+10 mM Mg^{2+}) in 800 mM PIPES, pH 6.9 buffer with different KCl concentrations, 0.5 M, 1 M, 2 M and 3 M. (B) CetZ1 polymerisation with 1 mM GTP (+10 mM Mg^{2+}) in 800 mM PIPES and 100 mM PIPES. Both buffers were prepared at pH 6.9 and 3 M KCl concentration.

Interestingly, CetZ1 was able to polymerise in the 800 mM PIPES buffer, and the highest scattering was observed in the buffer that contained 3 M KCl (Figure 6.6). 2 M KCl concentration induced CetZ1 polymerisation at a very low magnitude after a lag time of about 7 min and KCl concentrations lower than 1 M were unable to induce a visible CetZ1 polymerisation (Figure 6.6). The results were confirmed by independent duplicates (not shown). These observations suggest that having the optimum ionic strength in the reaction is critical and might help the amino acid residues in the active sites of CetZ1 to maintain the correct charge, thereby facilitating the interactions that are essential for self-association during polymerisation. The importance of the buffer strength was then tested by comparing the light scattering during CetZ1 (12 µM) polymerisation in 800 mM PIPES, pH 6.9, 3M KCl and 100 mM PIPES, pH 6.9 supplemented with 3 M KCl. The low 100 mM PIPES concentration could not induce CetZ1 polymerisation while CetZ1 displayed a good polymerisation in 800 mM PIPES buffer (Figure 6.6B). The results were confirmed by independent duplicates. These results suggest that the choice of buffer and the buffer strength clearly can have a substantial direct effect on CetZ1 polymerisation.

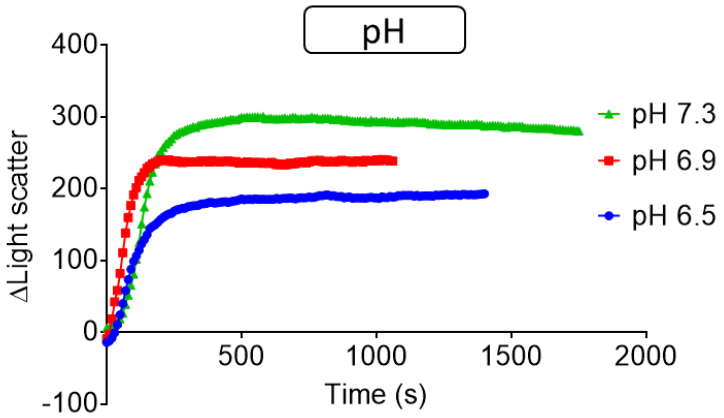

Figure 6.7: *The effect of pH on CetZ1 (12 µM) polymerisation.*

90º light scattering assay was performed mixing CetZ1 with 1 mM GTP (+10 mM Mg^{2+}) in 800 mM PIPES, 3M KCl buffer with different pHs, 6.5, 6.9 and 7.3.

Next, we explored the optimum pH for CetZ1 (12 µM) polymerisation by testing the light scattering at pH 6.5, 6.9 and 7.3 in 800 mM PIPES, 3 M KCl. Unlike FtsZ, which has shown to display an increased polymerisation with the reduction of the pH, CetZ1 displayed the best polymerisation at pH 7.3; the highest pH tested (Figure 6.7).

After finding the optimum polymerization conditions, the GTP dependence of CetZ1 polymerisation was explored by introducing a few further controls—1 mM GDP instead of GTP in the reaction, without any nucleotides in the reaction, and replacing CetZ1 with BSA (12 µM)— and comparing them to the optimized CetZ1 polymerisation with GTP in light scattering and co-pelleting assays.

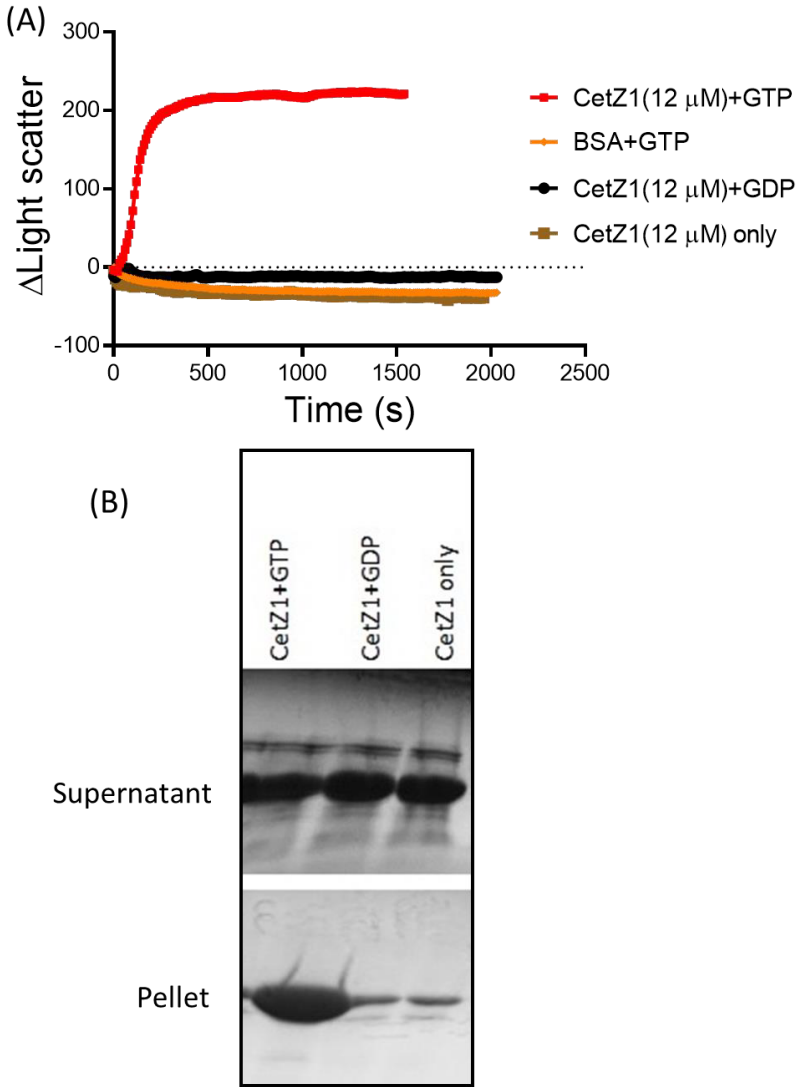

Figure 6.8: *Analysis of CetZ1 GTP dependent polymerisation.*

In all the reactions CetZ1(12 μM) was mixed with 1 mM GTP or 1 mM GDP with 10 mM Mg^{2+} in 800 mM PIPES, pH 7.3, 3 M KCl. (A) 90º light scattering assay indicated no light scattering on the control reactions tested. (B) The co-pelleting assay detected a higher amount of CetZ1 in the pellet fraction when GTP was present in the reaction.

Compared to CetZ1 with GTP, there was no scattering observed in the controls (Figure 6.8). The polymerisation was also explored by performing a co-pelleting assay using the same controls. This was followed by SDS-PAGE analysis which revealed increasing amounts of CetZ1 in the pellet of the reaction containing GTP (Figure 6.8). Both light scattering assay and the co-pelleting assay were confirmed by independent triplicates. All these results suggest that CteZ1 has a GTP dependent polymerisation.

Most biological polymers that are multistranded assemble cooperatively. As the nucleation steps of single subunits are energetically unfavourable, it is usually the rate-limiting step and at low protein, concentrations nucleation may not occur frequently enough to promote extension polymerisation. However, at high concentrations, assembly of the polymer nucleus is sufficient to allow extension and polymerisation to then proceed approximately exponentially, as each subunit can contribute to the formation of multiple bonds during the polymer growth (Miraldi, Thomas and Romberg, 2008). At a certain protein concentration, nucleus assembly is sufficient to lead to polymer extension. This concentration is known as the critical concentration for polymer assembly (Miraldi, Thomas and Romberg, 2008). In order to test the effect of concentration for CetZ1 polymerisation, the light scattering assay was performed with increasing concentrations of CetZ1. The polymerisation of CetZ1 at 3 µM, 6 µM, 12 µM and 18 µM concentrations in 800 mM PIPES, pH 7.3, 3 M KCl were compared.

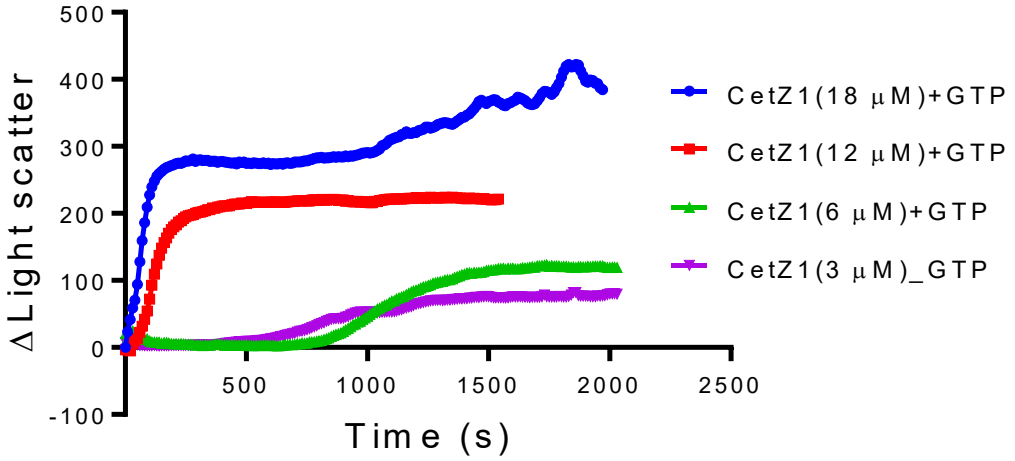

Figure 6.9: *CetZ1 displays cooperative polymerisation.*

The polymerisation of CetZ1 at different concentrations in 800 mM PIPES, pH 7.3, 3 M KCl with 1 mM GTP (+10 mM Mg2+) measured via 90º light scattering assay.

At low CetZ1 concentrations, 3 µM and 6 µM, there was a lag time prior to a visible polymerisation with a low magnitude of light scattering suggesting the polymers formed in these samples were probably shorter than the polymers formed at high protein concentration (Figure 6.9). At 12 µM CetZ1 concentration, rapid polymerisation was observed without a lag time (within the resolution of these assays), indicating that 12 µM

concentration is a suitable concentration for CetZ1 polymerisation under these buffer conditions. Furthermore, the increase in the scattering of light during 6 µM to 12 µM CetZ1 concentration increment is much larger than that during 12 µM to 18 µM CetZ1 concentration increment (Figure 6.9). This non-linear concentration-dependent polymerisation pattern suggests that CetZ1 assemble via cooperative polymerisation.

Then, the GTPase activity of CetZ1 was investigated using a Malachite Green phosphate assay. The complex formed between Malachite Green, molybdate and the orthophosphate causes the development of green colour proportional to the available orthophosphate in the solution. This colour intensity was measured using a microtiter-plate spectrophotometer at 630 nm. This assay has been previously used to measure the GTPase activity in FtsZ (Król and Scheffers, 2013). *Bacillus subtilis* FtsZ was used as a positive control. The GTPase activity was tested by two different ways as outlined in the Methods section of the current chapter.

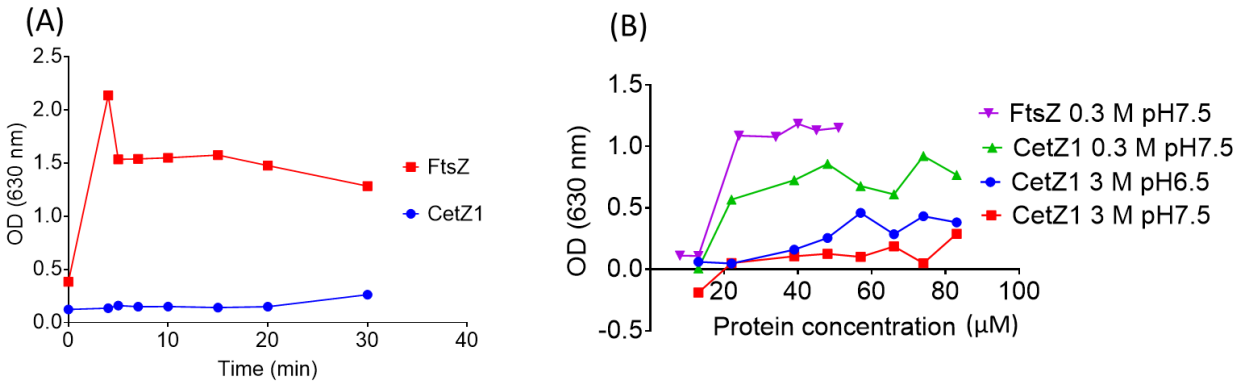

Figure 6.10: *Malachite Green Phosphate assay cannot detect CetZ1 GTPase activity.*

Reactions were carried out in 50 mM MES, pH 7.5. Reaction buffer for FtsZ had 300 mM KCl and that for CetZ1 had 3M KCl. All the absorbance values plotted were subtracted from the absorbance of the control reaction that had 1 mM GTP (+10 mM Mg2+) and no proteins. (A) Absorbance (630 nm) measurements of reaction mixtures containing 12 µM FtsZ and CetZ1 at different time points after 1 mM GTP (+10 mM Mg2+) was added. (B) The proteins at different concentrations (µM) and 1 mM GTP (+10 mM Mg2+) were mixed and incubated for 30 min prior to performing the Malachite Green Phosphate assay.

First, the release of orthophosphate was measured at different time points after mixing GTP and the protein of interest. Second, the release of orthophosphate was measured after a fixed incubation period when GTP was mixed with different protein concentrations. Although FtsZ displayed a GTPase activity under the conditions tested, the Malachite Green phosphate assay failed to detect the GTPase activity of CetZ1 at 3 M KCl concentration as the negative control which contained only GTP indicated a colour development. The graph shown in Figure 6.10 does not indicate a significant increase in the absorbance as all the absorbance values plotted in this graph were subtracted from the absorbance of the GTP only control. It was hypothesised that having a high KCl concentration destabilises one of the constituents contribute to the green colour complex. Therefore, Malachite Green phosphate assay cannot be used to measure the CetZ1 GTPase activity under these conditions.

6.2.3 *In vitro* polymerisation of selected CetZ1 point mutants

In Chapter 05, we have identified CetZ1 point mutants that disrupt the CetZ1 function *in vivo*. Investigation of *in vitro* polymer dynamics of these point mutants would further highlight the importance of regions in CetZ1 structure that is responsible for the function and molecular interactions. *In vivo*, WT CetZ1 displayed a highly dynamic, filament-like localisations during morphogenesis suggesting that formation of CetZ1 cytoskeletal structures are needed for the function. Interestingly, the non-functional CetZ1.M-loop mutant that was assumed to disrupt the lateral interactions displayed a strikingly diffuse CetZ1 localisation *in vivo*. The non-functional CetZ1.E218A mutation alters the T7 region, which is usually involved in exerting the GTPase activity. It displayed an intense and less dynamic localisation consistent with protofilament hyper-stability. Initially, the untagged CetZ1.M-loop and CetZ1.E218A mutants were purified following the same method used to purify the WT CetZ1.

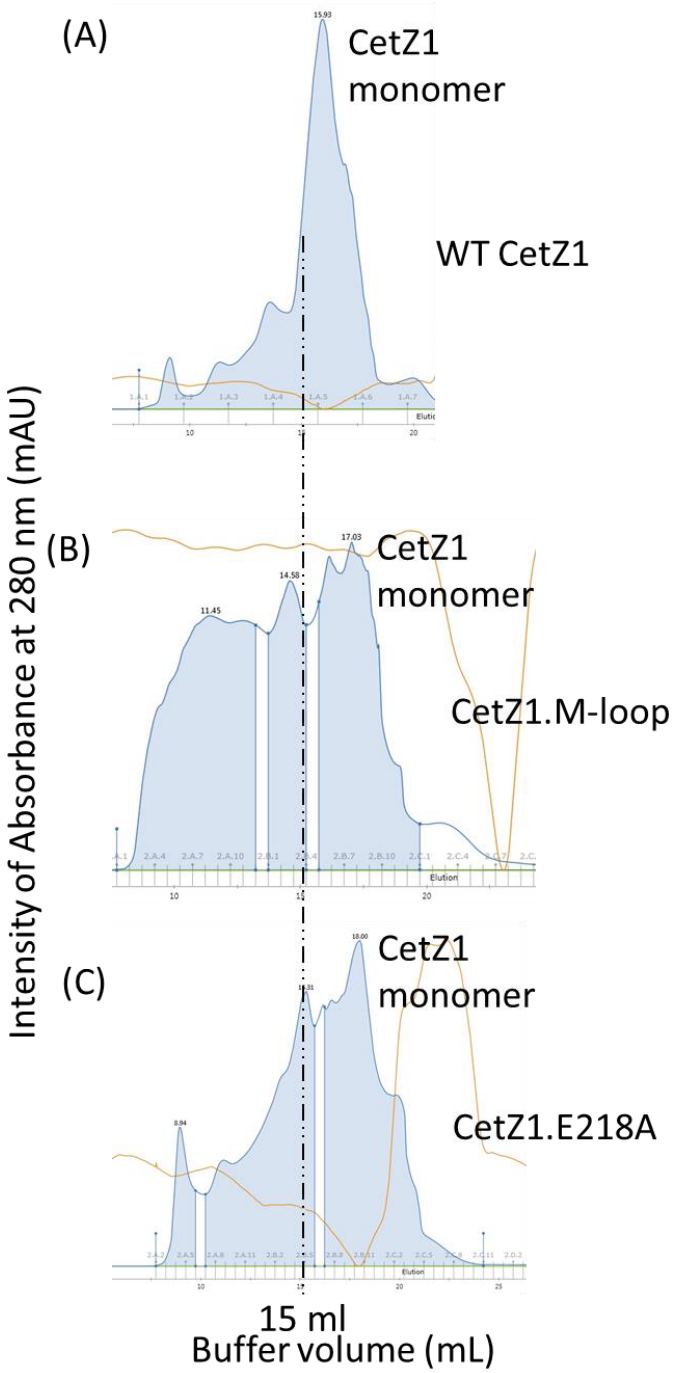

Figure 6.11: *Comparison of gel filtration chromatograms between (A) WT CetZ1 and CetZ1 point mutants, (B) CetZ1.M-loop, (C) CetZ1.E218A resulted during their purification.*

Both mutations displayed higher oligomeric peak compared to the WT CetZ1 during gel filtration (Figure 6.11). However, a high amount of protein was eluted in the monomeric form suggesting these mutations do not destabilise the proper fold of the protein. Instead, the mutation might inflict a change in the normal monomeric conformation that might

increase unspecific oligomerisation compared to the WT CetZ1 monomer. The light scattering assay was carried out with both purified monomeric CetZ1.M-loop, and CetZ1.E218A mutant proteins (supplemented with 1 mM GTP+10 mM Mg^{2+}) using the previously optimised conditions for WT CetZ1.

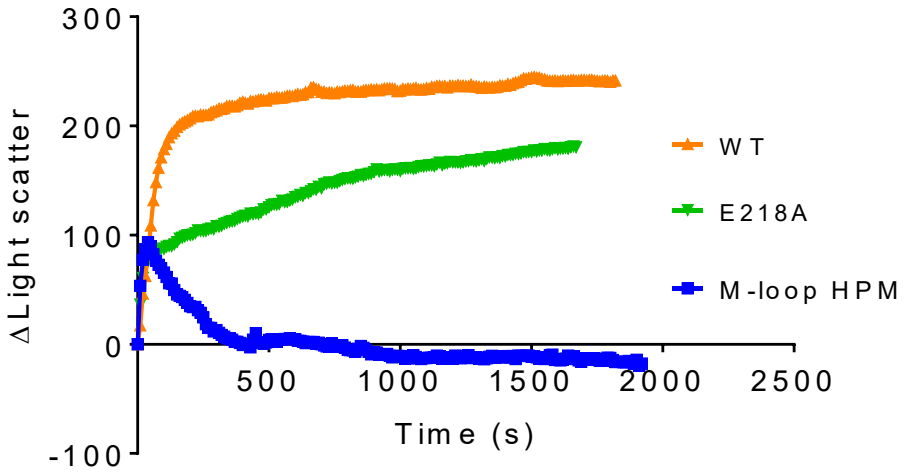

Figure 6.12: *Analysis of the polymerisation of CteZ1 point mutants, CetZ1, M-loop and CetZ1.E218A, via light scattering assay.*

Interestingly, the CetZ1.M-loop protein showed a rapid initial rise in light scattering after GTP addition but then fell to zero by about 500 s (Figure 6.12). This *in vitro* polymerisation results in combination with the diffuse *in vivo* localisation observed in Chapter 05 suggests that CetZ1 is probably assembling into a complex higher-order quaternary structure and this M-loop region which locates on the surface in the C-terminal domain is probably involved in stabilising the lateral interactions of this polymeric structure. Purified CetZ1.E218A indicated initiation of polymerisation to a similar magnitude as the CetZ1.M-loop when the GTP was added to the reaction. Following a similar initiation of polymerisation, CetZ1. E218A displayed a continuous increase in polymerisation at a slower rate than the WT CetZ1 for ~30 min (Figure 6.12). This slow *in vitro* polymer dynamics was comparable with the less dynamic localisation observed *in vivo*. We assumed CetZ1.E218A would form hyper-stable filament by disrupting the depolymerisation while preserving its polymerisation rate. However, the *in vitro* behaviour suggests that the mutation might be affecting the rate of polymerisation as well. Both the mutant polymerisation assays were confirmed by independent triplicates.

Further cryo-EM analysis of the *in vitro* polymers is needed to further understand these polymer dynamics.

6.2.4 CetZ1 aggregated multimers can directly bind to the lipids

CetZ1 displayed a high cell envelope-associated (peripheral) localisation during the morphogenesis. Furthermore, point mutants such as the CetZ1 C-terminal tail mutant that had decreased peripheral localization, failed to show CetZ1 function (Chapter 05). Therefore, the ability of CetZ1 to interact directly with the cell membrane was explored. *H. volcanii* lipids were extracted as described in the Method Section of the current chapter and the liposomes were prepared by sonication.

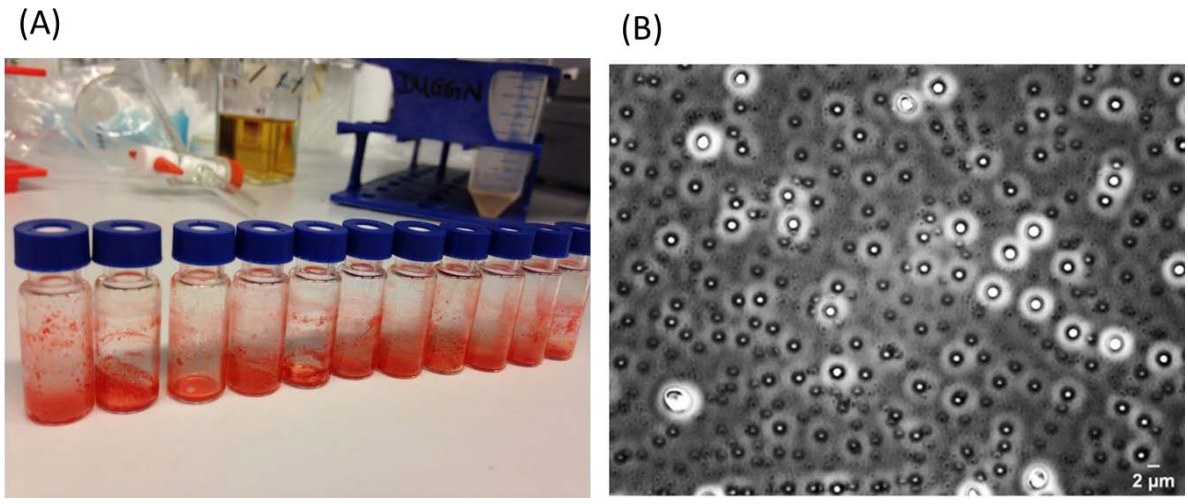

Figure 6.13: *Haloferax volcanii lipids.*

(A) The H. volcanii lipid extracts after the organic solvents were evaporated under the N_2 gas. Membrane-bound carotenoids give them a pink colour. (B) Phase-contrast image of liposomes prepared by sonication.

Liposomes are thought to resemble biological lipid membranes. Sonication usually results in liposomes with a myriad of sizes, and this could be advantageous when the liposome size favoured by the protein is unknown. Sonication of *H. volcanii* lipids mainly resulted in two populations (~2 µm and ~1 µm) of liposomes that had satisfactory uniformity

independently according to the phase-contrast images (Figure 6.13). There was a small number of large liposomes which had an approximate size of 3 μm.

CetZ1 lipid-binding activity was tested by the co-sedimentation assay as described in the Method Section of this chapter. Liposomes were prepared in 800 mM PIPES, pH 7.3, 3M KCl buffer and lipid binding were tested in the same buffer by mixing 5 μM monomeric CetZ1 and 0.7 mg/ml liposomes. No lipid binding was observed with the monomeric CetZ1 and increasing the monomeric CetZ1 lipid concentration showed no lipid binding (data not shown). Then, the lipid binding was tested with addition of 1 mM GTP (+10 mM Mg^{2+}) into the same reaction conditions (5 μM monomeric CetZ1 and 0.7 mg/ml liposomes). [Note: these conditions were trialed before the PIPES buffer system above had been identified and developed.]

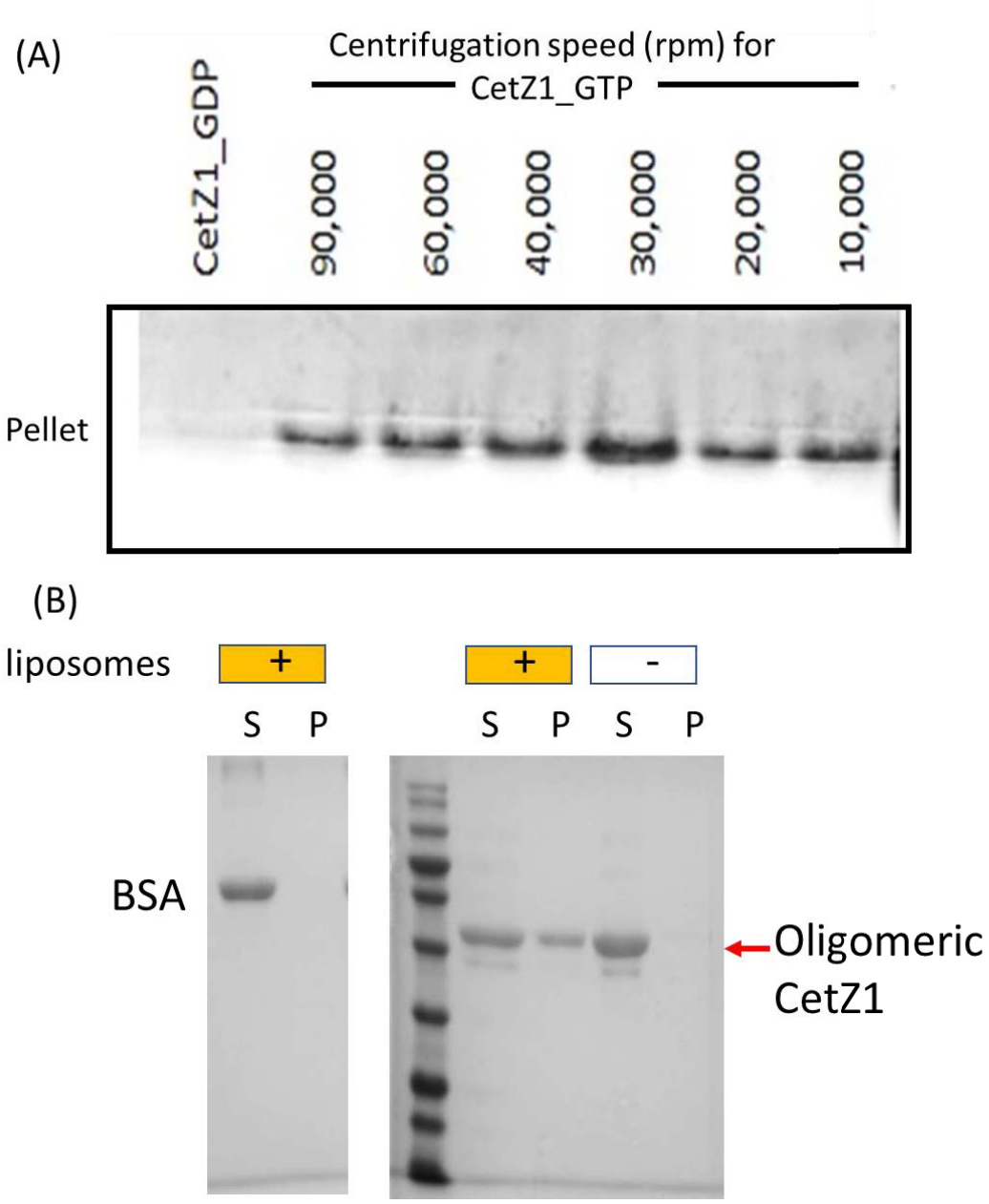

Figure 6.14: *Analysis of CetZ1 lipid-binding via ultracentrifuge co-sedimentation assay.*

(A) SDS-PAGE of CetZ1 polymers formed in the reactions containing CetZ1 (12 µM) with 1 mM GTP (+10 mM Mg^{2+}) in 800 mM PIPES, pH 7.3, 3 M KCl when centrifuged at different speeds. This was done to screen centrifugation speeds that would not precipitate the polymeric CetZ1 in order to test the binding of lipids with CetZ1 polymers. (B) SDS-PAGE for ultracentrifuge co-sedimentation assay carried out with oligomeric CetZ1 (5 µM) from the initial purification with 0.7 mg/ml liposomes in 25 mM TrisCl, 200 mM KCl, pH 8.5, 1 mM EDTA buffer.

.

In order to perform the co-sedimentation assay, the centrifugation speed should allow sedimentation of the lipids (and lipid-bound proteins) but not the unbound proteins.

However, pelleting of CetZ1 polymers without the lipids, even at a low centrifugation speed of 10 000 rpm (the minimum speed that requires to pellet all liposomes was 10 000 rpm) hindered us from testing the lipid-binding ability of polymers using co-sedimentation assay.

In our initial studies of CetZ1 purification (without 10% glycerol), we observed that CetZ1 predominantly existed in a non-nucleotide-dependent oligomeric form (Figure 6.4). As this oligomeric form was unable to form a pellet at high speed (55 000 rpm) without the lipids, the lipid-binding ability of the oligomeric CetZ1 (5 μM) was tested in 25 mM TrisCl, 200 mM KCl, pH 8.5, 1 mM EDTA (the buffer the protein was stored in) with the liposomes (0.7 mg/ml) made in the same buffer. Interestingly, direct binding of CetZ1 to the liposomes was observed with the oligomeric CetZ1 but not in the pellet of the control reactions—with BSA instead of CetZ1 in the reaction and CetZ1 without lipids in the reaction—performed under the same conditions (Figure 6.14). The results were confirmed with triplicates. This shows CetZ1 is directly capable of binding to the *H. volcanii* lipids, at least when it is in the aggregate multimeric form.

6.3 Discussion

Studying *in vitro* polymer dynamics with purified proteins could unravel how the proteins subunits assemble into cytoskeletal structures. The above study mainly provides evidence of the cooperative GTP dependent polymerisation of CetZ1. In addition, the results also suggest that CetZ1 could assemble into a higher-order quaternary structure that might be important for the CetZ1 function. In addition, we developed successful purification procedures for monomeric CetZ1 from the E. coli expression system and identified and developed robust buffer and assay conditions for investigation of CetZ1 polymerisation studies in vitro. Some studies of CetZ1 mutants, particularly the polymerisation-defective M-loop mutation are also presented in this chapter. Further potential studies of CetZ1 mutants that have been studied in vivo in other chapters, are discussed further below in relation to future directions and could not be studied in the present work due to time constraints.

The purification of the protein in the monomeric state is necessary to understand the pure polymer dynamics. Most cytoskeletal proteins are prone to aggregate as they possess an intrinsic ability to make polymers (Rivas *et al.*, 2000). The protein aggregation during purification can be minimised via several methods. A few such examples are, introducing a fusion tag such as Maltose binding protein to increase the stability of the protein or modification of culture conditions such as reducing the growth temperature during overexpression and reduction of protein concentration using for the purification (Zhao, Li and Liang, 2013). Furthermore, introducing additional reagents into the purification buffers have been demonstrated to improve prevention of the protein aggregation. For example, the reducing agents (β-mercaptoethanol, DTT), chaotropes (urea, guanidium hydrochloride), kosmotropes (ammonium sulfate, glycerol), detergents (Tween, CHAPS), amino acids (arginine, glutamine) and ligand/co-factors at low concentrations (Bondos and Bicknell, 2003, Ghahghaei and Mohammadian, 2014). The aggregation of CetZ1 was reduced by incorporating 10%v/v glycerol into the purification and storage buffers.

Moreover, running the chromatographic columns at a very low speed improved the purity of the purified CetZ1. Usually, proteins can be stored at -80 ^{0}C for approximately a year (duration could change depending on the protein). However, subjecting proteins into

continuous freeze-thaw cycles are known to reduce protein activity via denaturation. CetZ1 was stored at -80 ^{0}C with 10% glycerol and at a CetZ1 concentration higher than 1 mM. We noted that storage at a low protein concentration and storage of the thawed samples at 4 ^{0}C more than 4 days gave rise to a loss of its activity during *in vitro* assays.

Generally, biological molecules are expected to exert near-natural activity *in vitro* when the reaction conditions are approximately similar to the cytoplasmic conditions (Wright *et al.*, 2002). However, both tubulin and FtsZ have displayed a variation in polymerisation depending on the type of buffer and additives such as Mg^{2+} (Waxman *et al.*, 1981, Huecas and Andreu, 2003). The addition of glycerol into the reaction has shown to decrease the critical concentration of the protein and the buffer strength needed for the tubulin polymerisation (Waxman et al., 1981). Incorporation of macromolecular crowding agents such as Ficoll 70 (200 g/L) into the reaction has shown to increase the FtsZ polymerisation; incorporation of these additives probably assists to resemble the crowded natural environment in the cytoplasm (Negi et al., 2003). The dependence of CetZ1 polymerisation on the type of the buffer and the buffer strength suggested that some attributes of *in vitro* polymerisation such as protein concentration, might not resemble the *in vivo* polymerisation. How these sulfonate buffers mediate the polymerisation is yet unclear. However, according to the 90^0 light scattering assay, tubulin and CetZ1 facilitates polymerisation (Figure 6.6 and 6.7) under similar *in vitro* conditions (except for the high ionic concentration needed in CetZ1) while for FtsZ these conditions are different. *H. volcanii* has a high cytoplasmic KCl concentration, as an adaptation to their high salt habitats (Wright et al., 2002). Therefore, the 3 M KCl concentration required for CetZ1 polymerisation would better resemble the natural reaction conditions of CetZ1.

The disruption of the GTP binding domain on the top T4 region (CetZ1.G108S) and the GTPase active site on the bottom T7 region (CetZ1.E218A) resulted in a similar *in vivo* localisation pattern (Chapter 05). Both mutants displayed an intense, less dynamic peripheral localisation that is consistent with the polymer hyper-stability. The slow and continuous *in vitro* polymer growth displayed by CetZ1.E218A during light scattering assay suggest that this mutation is therefore probably affecting both polymerisation and depolymerisation of CetZ1 polymers. This *in vivo* hyper stable filament-like localisations in both ‘top’ and ‘bottom’ surface mutants and slow *in vitro* polymer growth in the ‘bottom’ surface mutant might suggest CetZ1 can add and remove subunits in the polymer

from both ends. Therefore, it would be intriguing to explore the kinetic polarity of these CetZ1 polymers in future studies.

The polymerisation of the potential lateral surface-interaction mutant was explored by measuring the light scattering of CetZ1.M-loop. This revealed, consistent with the *in vivo* localisation studies, that the CetZ1.M-loop mutation destabilises the CetZ1 polymeric structures. In future, a cryo-EM analysis for the *in vitro* reactions carried out by WT CetZ1 and CetZ1.M-loop could help us to understand the polymeric structure formed by CetZ1 and the possible role of M-loop region in stabilising lateral interactions of CetZ1. The initial attempts made to analyse CetZ1 *in vitro* polymers by cryo-EM (data not shown) were unsuccessful due to technical that challenges arise due to the need for high glycerol and KCl concentration in the reaction.

Many prokaryotic cytoskeletal proteins that modulate the cell envelope have been shown to assemble on liposomes. FtsZ could form a Z ring-like structure on liposomes to exert a direct constrictive force (Szwedziak *et al.*, 2014, Ramirez-diaz *et al.*, 2019). Mreb, a bacterial actin homologue that helps in maintaining the cell shape, could directly modulate the shape of liposomes (Maeda *et al.*, 2012). The tests performed with aggregated CetZ1 indicated that CetZ1 can directly bind to *H. volcaii* liposomes. However, this may be an unspecific binding that may not occur *in vivo*. Therefore, it is essential to examine the ability of CteZ1 to modulate the shape of liposomes *in vitro* using cryoEM followed by a comparison of this to the mutations that possibly disrupt the lipid-binding (eg: C-terminal tail mutation).

The *in vitro* polymerisation conditions discovered from this study would allow exploring CetZ1 polymer dynamics in future. Finally, the discoveries from this chapter in combinations with the mutation identified from Chapter 05 provide a solid foundation to identify the *in vitro* polymer dynamics and CetZ1 lipid interaction in future.

6.4 Methods

6.4.1 Overproduction of the protein and preparation of the cell lysate

The insert, which is the required CeZ1 gene sequence (WT or mutant) was digested (BamHI/NdeI) from a previously constructed pTA962 expression system-based plasmid (Chapter 05). The vector, pHis17 was digested using the same restriction sites, BamHI and NdeI. Then the gel-purified insert was cloned into the gel-purified pHis17 vector following the general cloning protocol (Section 2.8.6). Chemically competent *E. coli* DH5α (Section 2.4.2) was used to amplify the cloned plasmid. In order to overexpress the protein, purified pHis17 with the CetZ1 (or mutated CetZ1) was transformed into *E. coli* C41 via electroporation (day 01). On day 02 the transformed colonies were scraped off from the agar plate and inoculated into 50 ml of 2TY (table 2.4) media containing 0.1 mg/ml ampicillin. First, this culture was incubated at 37ºC for 1 h with 200 rpm shaking. After 1 h, the culture was transferred to a 5 L flask containing 1.6 L of 2TY (with 0.1 mg/ml ampicillin). The flask was incubated further at 37ºC with 200 rpm shaking. After the culture reached OD (600 nm) of 0.4, it was placed in an incubator at 18ºC with 150 rpm shaking. A 1 ml sample was taken at this point as the "pre-induction" sample, and its cell pellet was stored at -20ºC for the later SDS-PAGE comparison. The flask was left at 18ºC for 15 minutes to cool, and then, 1 mM IPTG was added to induce the culture. This was left overnight (~18 h) at 1 ºC with 150 rpm shaking. On day 03 (after ~18 h), OD (600 nm) was checked by diluting the sample by 1:10 and a cell pellet of 1 ml sample was stored as the "post-induction" sample. The cells were then centrifuged using a Hitachi R9A rotor at 9000 rpm for 30 min at 4°C before proceeding onto disruption of the pellet, resuspended in 40 ml of 25 mM TrisCl buffer (pH 8.5, with 1 mM EDTA and 10% glycerol), using sonication on ice (10 mins in 1 min intervals, 50% maximum output, VC 50T) followed by centrifugation at 18 000 rpm (using Hitachi R18A rotor) for 30 min at 4°C. The supernatant was subjected to the subsequent chromatographic purification.

6.4.2 The purification of untagged CetZ1

Purification was carried out using the AKTA pure chromatography system (GE Healthcare Life Sciences) at 4 ^{0}C. All the solutions used were filter-sterilised (by 0.2 µm membrane filter) and pre-chilled. Before each purification, all the chromatography columns and the system were washed first with 20% v/v ethanol, second with MiliQ water and finally with the buffer used as buffer A. All the buffers used for the purification contained 1 mM EDTA and 10% glycerol in them. The CetZ1 was purified from the final supernatant by ion exchange with a HiTrap Q column HP (GE Healthcare) running in 25 mM Tris-Cl pH 8.5, 1 mM EDTA, 10% glycerol, with a 0-500 mM KCl gradient t 0.4 ml/min speed. The fractions containing CetZ1 were screened by SDS PAGE. These were pooled and concentrated in 20 ml capacity, 10 kDa cut-off centrifugal concentrators (Vivaspin) to obtain a final volume of 0.5 ml. The concentrated proteins were further purified by size exclusion chromatography using a Superdex 200 Increase 10/300 GL column (GE Healthcare), running in 25 mM Tris-Cl pH 8.5, 200 mM KCl, 1 mM EDTA, 10% glycerol at 0.2 ml/min speed. High yielding fractions were pooled and concentrated to ~1.5 mM after size exclusion chromatography in 20 ml capacity, 30 kDa cut-off centrifugal concentrators (Vivaspin). Protein concentrations were measured using Thermofisher nanodrop spectrophotometer at 280 nm.

6.4.3 Purification of archaeal membrane lipids and liposome preparation

The cells from *H. volcanii* DS2 WT culture (typically 1-2 litres in late exponential phase) were harvested by centrifugation at 7 000 rpm for 10 mins. These cells were washed by resuspending in 50 mL of 18% BSW and then, spun at 6,500 rpm for 10 min. The supernatant was carefully discarded, and the washing step with 50 mL 18% BSW was repeated. All the supernatant was removed carefully, and the tubes stored at -80, until frozen (usually 24 h). On the next day, the frozen cell sample was Freeze-dried for 24 h. Next, a mixture of methanol, dichloromethane (DCM), and phosphate buffer (8.7 g/L KH2PO4, pH 7.4) at a ratio of 2: 1: 0.8 (v/v) was prepared, ensuring that the solvent mixture is well mixed and not in separate phases. The lipid extraction was carried out by adding this solvent mixture into the freeze-dried cells (5 ml per gram of dry cell mass)

and then resuspending briefly by vortex followed by sonication in a water bath sonicator (40 kHz, 700 W) for 5 mins. The cell suspension was centrifuged at 6 500 rpm for 5 min, and the supernatants (organic and aqueous together) were collected in a separate tube. The extraction was repeated on the pellet and pooled the supernatant with the first extract. Two further extractions were carried out by using 0.8 volumes of 5% trichloroacetic acid (pH 2) instead of the phosphate buffer in the solvent mixture (TCA improves extraction of glyceroldialkylglyceroltetraethers). Next, 0.5 volumes of DCM and 0.5 volumes of MiliQ water were added into the pooled extracts, vortexed and spun at 6 500 rpm for 5 min. The solution was kept still to separate the phases, and the organic phase was collected to a different tube. The aqueous phase was then washed by adding DCM (5 mL per g of original dry mass) followed by vortex and centrifugation. This second DCM phase was pooled with the main organic phase. Next, the organic phase was washed with an equal volume of pure water, centrifuged and collected the organic phase. The final organic phase in aliquots in glass vials was evaporated under a stream of dry N_2 in a fume hood. The vials were sealed while under N_2 flow (to minimize oxygen in the vial), and stored the total lipid extract (TLE) at −20 °C.

To prepare liposome, extracted lipids were resuspended in liposome buffer (filter sterilised 50 mM Tris-HCl, 200 mM KCl, 1mM EDTA, pH 8.5) by vortexing (5 ml of liposome buffer per 10 mg of lipids). This was then sonicated in a water bath sonicator (PowerSonic420, 40 kHz, 700 W) for 30 min. Liposomes were stored at 4 ^{0}C and used within 7 days.

6.4.4 Ultracentrifuge co-sedimentation assay

The co-sedimentation assay was carried out using *H. volcanii* liposomes prepared using sonication as outlined in Section 6.6.3. The reaction was carried out in 25 mM TrisCl buffer, 200mM KCl, pH 8.5, 1 mM EDTA (unless given otherwise). Liposomes (0.7 mg/mL) were mixed with pre-spun CetZ1 at final concentrations of 5 µM and centrifuged at 55 000 rpm at 20ºC for 15 min in a Beckman TLA100 rotor. The supernatants were removed for analysis, the pellets washed and solubilised with SDS –LB (Table 2.7) (same volume as for the supernatants) and samples were analysed by SDS–PAGE (Section 2.9.1).

6.4.5 Ultracentrifuge co-pelleting assay

In order to carry out the co-pelleting assay, purified CetZ1 at the final concentration of ~1.5 mM was pre-spun at 90 000 rpm in a Beckman TLA100 rotor for 30 min at 4 ^{0}C. The supernatant was transferred to a new tube. Pre-spun CetZ1 was diluted in 800 mM PIPES buffer pH 7.3 containing 3 M KCl to a final concentration of 12 µM (unless given otherwise) and then 1 mM GTP (+10 mM Mg^{2+}) was added. The reaction was incubated at 45 ^{0}C for 2 min. Next, the tubes were centrifuged at 90 000 rpm at 20ºC for 10 min. The supernatants were removed for analysis, and the pellets were solubilised with SDS-LB (Table 2.7) (same volume as for the supernatants), and samples were analysed by SDS–PAGE (Section 2.9.1).

6.4.6 90º Light scattering assay

The fluorescence spectrophotometer (Shimadzu RF-6000 Spectrofluorophotometer) was switched on 10 min prior to the assay to avoid the thermal fluctuation. The light scattering measurements were taken at room temperature. The parameters of the detector with 300 V was adjusted as follows. Emission and excitation wavelengths were set to 350 nm, slit width was 4 nm and the time-based acquisition for ~2000 sec was chosen. The quartz cuvettes (Thorlabs, 100 µL Super Micro Fluorescence Cuvette with Cap, 8.5 mm Beam Height) with 10 mm path length were used and cleaned them thoroughly with water between each measurement. Total reaction volume used for the assay was 200 µl. Protein (CetZ1 or mutants) was added to 800 mM PIPES, pH 7.3, 3 M KCl buffer heated to 45 ºC (during optimisation MES and HEPES buffers were used as described in the above Results Section) to achieve 12 µM final protein concentration (unless specified otherwise). This solution was used as the blank for the spectrophotometric measurements. Then GTP was added to this reaction mixture at 1 mM (+10 mM Mg^{2+}) final concentration and mixed briefly by pipetting up and down with a larger volume pipette prior start collecting data.

6.4.7 Malachite Green GTPase assay

Malachite green working reagents and phosphate standard (0-40 µM) were prepared as described in the Sigma Aldrich Malachite Green Phosphate Assay Kit user guide. A 96 well qPCR plate was used to carry out the GTPase assay, and the plate was kept on a thermocycler which was maintained at 37ºC. *B. subtilis* FtsZ at 12 µM concentration in 50 mM MES pH 7.5, 300 mM KCl was used as the positive control. CetZ1 was mixed at 12 µM concentration in 50 mM MES pH 7.5, 3M KCl. Reaction mixtures with 10 mM EDTA added and no protein added were used as the negative control. GTP was added at 1 mM (+10 mM Mg^{2+}) final concentration to each parallel reaction mixtures simultaneously using a multi-channel pipette. Then the GTP was added at the time points of 0 (start point), 10, 16, 21, 25,27,29 and 30 min into the row below each time up to 8 rows in the 96-well plate. The plate was incubated for 30 min. Then the samples were taken out at the time intervals from each in the same order as the GTP was added and mixed with the malachite green working solution in a 96-well plate. The sample volume was chosen so that the final GTP concentration in the malachite green mixture was 0.25 mM. The plate was incubated at room temperature for 30 min for the colour development. The absorbance at 630 nm of the reactions in the 96-well plate was measured using Tecan plate reader in 30-sec intervals as the same order the GTP was added.

The effect of protein concentration on GTPase activity was measured by mixing different concentrations of *B. subtilis* FtsZ and CetZ1 with the malachite green working reagent in a 96-well plate. The following protein concentrations were used.

Table 6.1 Protein Concentration Gradient used in Malachite Green Phosphate Assay

CetZ1 conc (µM)	13	22	39	48	57	66	74	83
FtsZ conc (µM)	13	24	30	34	40	45	51	-

CetZ1 GTPase activity was tested in MES buffer with 3 M KCl pH 7.5, 3 M KC pH 6.6 and 0.3 M KCl pH 7.5. Measurements using FtsZ were carried out in MES buffer 0.3 M KCl, pH 7.5. The reactions without GTP and “without proteins” were used as the negative controls. The reactions were incubated for 1 hour and then added into the malachite green working solution. The volume of the reaction was chosen to achieve the final GTP concentration in the malachite green solution to 0.25 mM GTP. The absorbance at 630 nm was measured after incubation for 30 min to allow colour development.

CHAPTER 7

DISCUSSION AND FUTURE DIRECTIONS

Microbial cell shape is a key attribute that affects survival, and the cytoskeleton plays a prime role in modulating the cell shape. Despite the growing knowledge of the cytoskeleton due to the recent advancements in biotechnology and microscopy, we still have a limited understanding of how these nano-scale molecular assemblies function at the micron-scale. Many species change their morphology to adapt to environmental changes and stresses. *H. volcanii* cells transition from plates to rods, to optimise swimming motility, which requires the tubulin-like cytoskeletal protein CetZ1 (Duggin *et al.*, 2015). However, the triggers for the rod cell development were obscure. This rod shape is a commonly observed cell shape in many organisms that possess a cell wall. This shape conservation and recurrence through evolution demonstrates the importance of this morphology for many different species and survival in their environments. For instance, maintaining a rod shape increases the surface to volume ratio of the cell, improving the ability to exchange materials (e.g. nutrients) with the environment (Gonin *et al.*, 2000). Furthermore, a rod shape has many other advantages such as ensuring the efficient cell division by introducing a better cell polarity across the cell length. Rod cells also allowing efficient packing during biofilm formation and when swarming in motile rafts of microbes (Huang, Mukhopadhyay and Wingreen, 2006, Huang, Meir and Wingreen, 2003, Young, 2006).

In the present study, we aimed to identify some environmental triggers that induce the rod formation in *H. volcanii*, characterise CetZ1 dynamics during this cell shapeshift and identify the important functional region of CetZ1 molecule.

7.1 External signals that induce the *H. volcanii* rod formation

In Chapter 03, we aimed to understand the signals that trigger cell shape elongation via CetZ1 in *H. volcanii*. Cell shape changes in various nutrient-depleted media were analysed and it was discovered that cells developed highly irregular elongated forms in response to depletion of metal nutrients (Figure 3.1). These shapes were substantially more diverse compared to the regular rod-shaped cells seen in motile cells (formed in soft-agar swimming motility assays). The formation of elongated cells during trace elements (TE) limitation was dependent on CetZ1 (Figure 3.6). Remarkably, the addition of a solution containing eight metals to the complex growth medium (Hv-YPC)

significantly improved culture growth, and the cells showed a uniform plate-shaped morphology compared to non-supplemented Hv-YPC that produced mixed elongated- and plate-cell types. Early decline in the growth rate of Δ*cetZ1* compared to the WT during TE depletion suggested that CetZ1 or having a rod shape benefits *H. volcanii* to survive during metal starvation (Supplementary Figure 4F). This might be achieved via increasing the surface-to-volume ratio to enhance the uptake of an alternate nutrient component that might compensate the metals deprivation. Similar behaviour has previously been observed in the bacterium *Caulobacter crescentus,* which usually lives in a phosphorus limited aquatic environment (Paerl, 1982). It displayed an asymmetric cell division resulting in one cell with a polar flagellum, and the other contains a stalk formed from an extension of the cell envelope (Brun, 1994). *C. crescentus* has shown to increase this stalk length as a response to phosphorus starvation. These long and thin cell envelope extensions are proven to be advantageous in enhancing the nutrient uptake while maintaining a low cell volume (Gonin *et al.*, 2000, Wagner *et al.*, 2006).

Moreover, phase-contrast images displayed a seeming increase in inclusion bodies when *H. volcanii* cells were transferred from a TE depleted agar medium into a liquid medium containing TE compared to the vice versa (Supplementary Figure 3). We speculate that these inclusion bodies might form as a way of removing waste built up during starvation, released out of the cytoplasm when ample amount of nutrients is available in the medium. These inclusion bodies could be aggregates of proteins that were upregulated or mineralisation of extra nutrients that were gained during starvation. In bacteria, inclusion bodies with a similar appearance are formed via aggregation of proteins (Rinas *et al.*, 2017). However, further quantitative microscopy analysis followed by *in vitro* studies (to understand their structure and constituents) of these inclusion bodies are needed to investigate the above hypothesis in future.

Different species maintain the rod cell shape by very different mechanisms. Usually, this involves molecular polymerisation and dynamics that position the cell wall synthetic machinery to insert the new cell wall material or directly remodel the cell envelope (Teeffelen *et al.*, 2011). When the synthesis is involved, some species maintain the rod shape by growing the cell wall from the middle cylindrical part of the long axis (De Pedro, Schwarz and Koch, 2003) and some do this by growing the new cell wall from the tips (Brown *et al.*, 2012). However, the peculiar cell shapes and asymmetric cell divisions observed during *H. volcanii* metal starvation challenge these existing modes of cell shape

modulations for this species. It suggests that archaea probably possess very different and more complex mechanisms to sense or influence cell geometries. Moreover, we observed that the final culture density ($OD_{600\ nm}$) in the stationary phase of the culture increased proportionally with the starting optical density during TE depletion (Supplementary Figure 4). This suggested that metal deprivation is mainly a nutritional signal that directly affects their growth depending on the available metal nutrients in the medium. Carrying out well-controlled high-throughput genetic screens during the metal starvation conditions would allow identification of the metabolic pathways or other changes associated with the CetZ1 dependant cell shape modulation.

Secondly, we observed *H. volcanii* producing a "peak" of rods during the early-growth phase of their growth curve (Figure 3.4). Some studies predict having a rod shape during initial division stages helps cells to establish better polarity, thus improving the subsequent exponential cell division in the log phase (Mishra *et al.*, 2012, Brian D. Corbin, Yu and Margolin, 2002). We also observed that the width of this "rod peak" was slightly different depending on the culture media condition. In bacteria, it has been shown the gene expression profile in the lag and early log phases is very dynamic based on the history of the starting culture (Pin *et al.*, 2009). Therefore, the discrepancy of this "rod peak" duration could be a result of the nutrient status of different media conditions. Additionally, the study by Pin *et al*, 2009 suggests the history of the "mother culture" could also influence the width (the duration cells remain as rods) and the height (the elongation of the cells) of this "rod peak". Furthermore, we have presented preliminary evidence suggesting that this effect might also be a result of a quorum-sensing signal (Supplementary Figure 2). Identification of these two conditions—TE depletion and early-log rod formation—provided two new functional assays to quantify the CetZ1 function and characterise *H. volcanii* cell differentiation.

As all these cell elongation responses were dependent on the expression of CetZ1, next, we investigated the localisation dynamics of CetZ1 during the morphogenesis.

7.2 CetZ1 in modulating *H. volcanii* cell shape

In Chapter 4, we developed a new *cetZ1* knockout strain (ID188) that can be complemented by the reintroduction of functional CetZ1. This was achieved by avoiding disruption to the expression of the downstream gene, HVO_2203, and by maintaining the wild-type reading frame between HVO-2204 (CetZ1) and HVO_2203. This process also revealed that the transcription and translation of these genes is probably coupled and that correct expression of HVO_2203 is important for the *cetZ1*-dependent rod formation (figure 4.8 and 4.9). Carrying out functional assays of CetZ1 in an HVO_2203 knockout strain followed by a comparison of localisation and dynamics of CetZ1 and the hypothetical protein produced by HVO_2203 could help to unravel the other genes involved in CetZ1 function.

Next, a new CetZ1-mTurquoise2 fusion protein was developed that can complement the CetZ1 function by ~80% compared to the WT strain (Figure 4.13), compared to only 50% for the original CetZ1-GFP (Duggin *et al.*, 2015). The functional complementation of this fusion protein was improved by using a flexible linker to connect the fluorescent tag with CetZ1. The previous characterisation of CetZ1 localisation was carried out in *H. volcanii* H98 WT cells using the partially functional CetZ-GFP fusion (Duggin *et al.*, 2015). The expression of the CetZ1-mTurquoise2 fusion in ID188 allowed us to understand the CetZ1 dynamics during *H. volcanii* cell differentiation and, compare the effects of different CetZ1 structural mutants without the presence of a CetZ1 WT copy.

It has been shown that the cytoskeletal proteins that modulate cell shape can usually identify positive or negative local curvatures to direct cell synthesis to straighten or curve the cell shape. For example, the bacterial actin homologue, Mreb can identify both positive and negative curvatures to recruit the cell wall synthetic machinery in rod-shaped bacteria (Ursell *et al.*, 2014, Hussain *et al.*, 2018). Overexpression of CetZ1.E218A in H98 WT cells resulted in pointy, jagged shaped cells. Moreover, CetZ1.E218A indicated an increased localisation into both positive and negative curvatures (Duggin *et al.*, 2015). However, the combination of fluorescence and phase-contrast 2D images used in the present study did not reveal any obvious correlation between the local curvatures and the subcellular CetZ1 localisation in rods formed during the early-log phase (Supplementary Figure 5). In a 3D context, CetZ1 indicated a patchy peripheral localisation (Figure 4.16

and Supplementary Video 10 A, B). Therefore, it would be useful to measure the 3D cell curvatures to understand the correlation of curvature and CetZ1 localisation during plate to rod transition. Initially, the major technical obstacle that hindered this step was the unavailability of a non-toxic membrane dye for *H. volcanii*. The staining methods available involved either fixation (Leuko *et al.*, 2005) of the cells or utilisation of DNA-intercalating dyes which are usually associated with cytotoxicity (Fröls, Dyall-Smith and Pfeifer, 2012). The recent identification of the use of non-toxic dyes such as Mito Tracker for halophiles (Maslov *et al.*, 2018) would now allow tracking of CetZ1 localisation concerning the 3D cell curvature. A normal growth pattern has been observed in *H. volcanii* DS2 stained with Mito Tracker Orange (Yan Liao, unpublished data).

In chapter 5, we revealed important regions in CetZ1 structure for the function via structure-guided site-directed mutagenesis. The point mutations in the GTPase active site (T7 loop) (Duggin *et al.*, 2015) and GTP binding site (T4 loop) of CetZ1 prevented the cell shape transition from plates to rods (Figures 5.2, 5.3, and 5.4). Mutations in the analogous regions in both FtsZ (Bramhill and Thompson, 1994) and tubulin (Dougherty *et al.*, 2001) have also resulted in functional impairment. These results further confirm the functional significance of highly conserved primary sequence homology in the tubulin superfamily proteins. The GTP-dependent cooperative polymerisation of CetZ1 was further confirmed in Chapter 6 via *in vitro* assays (Figures 6.9 and 6.8). Identification of the CetZ1 *in vitro* polymerisation conditions in Chapter 6 allows us to test CetZ1 dynamics under controlled conditions. Furthermore, we discovered a non-functional surface mutation in CetZ1 that is located at a similar position as the microtubule loop (M-loop). The M-loop is important in lateral interactions between protofilaments in the microtubule (Prota *et al.*, 2013). It has been shown that weak lateral interactions between FtsZ protofilaments are required for Z ring assembly and its cell division function (Guan *et al.*, 2018). Unlike microtubule polymerisation which requires the formation of both longitudinal and lateral interaction (Tovey and Conduit, 2018), FtsZ can polymerise as single protofilaments (Guan *et al.*, 2018). The weak lateral interactions are formed between the existing protofilaments of FtsZ to stabilise the Z ring formation. However, the FtsZ sheets, ribbons, and bundles that have been shown to form *in vitro* might not reflect any functional association *in vivo* (Guan *et al.*, 2018). The defective *in vitro* polymerisation (Figure 6.12) and diffuse localisation (Figure 5.5) observed in CetZ1M-

loop mutation suggests that CetZ1 is possibly assembling into a complex higher-order structure that is required in cell shape modulation.

In summary, this thesis introduces two new assays, TE depletion assay and early-log phase assay, to quantify *H. volcanii* CetZ1-dependent cell differentiation. These assays performed under controlled conditions can be utilised to explore other genes involved in cell shape regulation. The new *cetZ1* knockout strain and the CetZ1-mTurquoise2 fluorescent fusion developed in this study opened the door for observing CetZ1 protein localisation and dynamics in living cells using the fusion protein as the sole source of CetZ1. The live-cell imaging using these also revealed CetZ1 forms dynamic filament-like structures that align the long axis of rod cells during initial cell elongation. The dynamic localisation of CetZ1 at cell edges was a characteristic feature observed during *H. volcanii* cell shapeshift. And we discovered mutations in C-terminal domain and the disordered C-terminal tail region reduced this peripheral localisation, thereby disrupting CetZ1function.

Furthermore, this thesis presented data showing that CetZ1 can display a GTP-dependent polymerisation, and the GTPase activity is essential for the dynamic localisation *in vivo*, thus the cell shape modulation. An important discovery of this study was the identification of the functional importance of CetZ1 'M-loop' region. A mutation in this region supported our initial hypothesis, CetZ1 protofilaments probably interact laterally to form a higher-order polymer that is essential for CetZ1 function. The present study provides optimised conditions for the untagged CetZ1 purification in the monomeric form. And by identifying the conditions for the *in vitro* polymerisation of CetZ1, based on those of microtubule assembly and high salt, we showed that it can polymerise in a GTP-dependent manner and required the M-loop region for polymer stability, in future, the cryo-EM analysis of the *in vitro* polymers and other interactions formed by CetZ1, and the comparison of the mutant proteins identified from this study would provide further important insights into the function and mechanisms of the CetZ family and tubulin superfamily evolution generally.

APPENDIX

SUPPLEMENTARY DATA

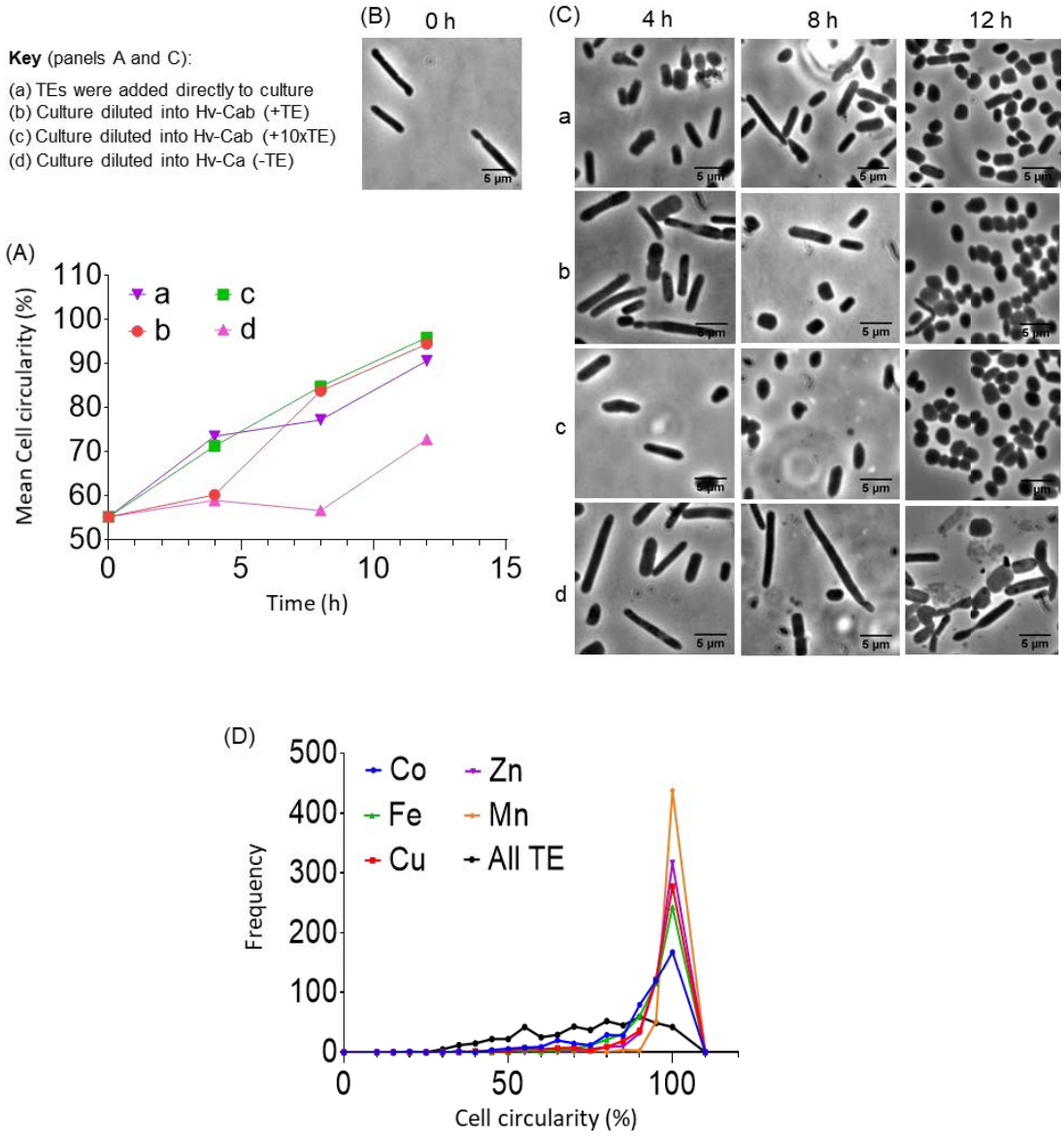

Supplementary Data Figure 1. Reversal and specificity testing of TE starvation. *H. volcanii* (H98 + pTA962) colonies from Hv-Ca agar were resuspended in Hv-Ca liquid medium. After 15 h of incubation, the culture was treated as indicated in the key, and then each new culture was monitored by sampling at 3 h intervals for microscopy over 12 hours. (A) The mean cell circularity vs time. (B) Representative phase-contrast image of the Hv-Ca (-TE) culture at 15 h, immediately prior to introducing TE. (C) Images containing cells after 4 h, 8 h and 12 h incubation under the conditions given in the key. Scale bars represent 5 microns. (D) To test the effect of individual TEs, *H. volcanii* (H98 + pTA962) was resuspended in liquid Hv-Cab lacking Co, Fe, Cu, Zn, Mn or all TEs, from colonies grown on the same drop-out agar medium. The cell circularity histograms are based on the indicated TE-dropout media, 15 hours after inoculation into the liquid media (45°C at 200 rpm shaking).

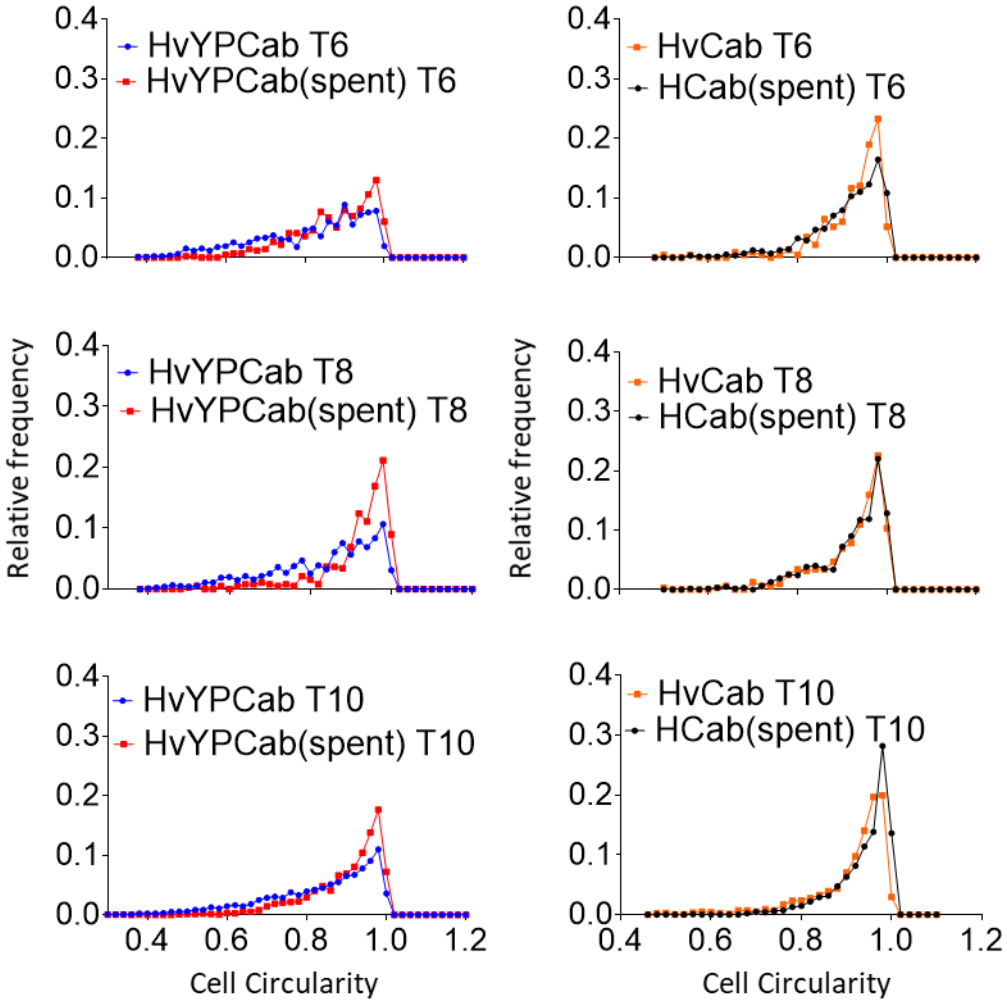

Supplementary Data Figure 2. Effect of spent media on *H. volcanii* cell shape during onset of rod formation.To prepare the conditioned medium, the cells in a late-log phase *H. volcanii* culture were removed using centrifugation (at 18,000 rpm for 30 mins) followed by filtration by (0.2 µm membrane filter). Then, the nutrients—Casamino acids, TEs and vitamins—were added to the amounts used for the fresh media, to avoid the effect from nutrient stress on the cell shape. Final pH was adjusted to 7.4. Cell circularities were compared in conditioned or fresh medium at 3 selected time points within the "rod peak". Panels A-C show the cell circularity histograms for Hv-YPCab fresh medium and conditioned medium, at 6 h, 8 h and 10 h respectively after inoculation. Panels D-F show the cell circularity in Hv-Cab fresh and conditioned medium at 6 h, 8 h and 10 h respectively after inoculation. For 6 h and 8 h time points N~1000 and for 10 h time point N~3000.

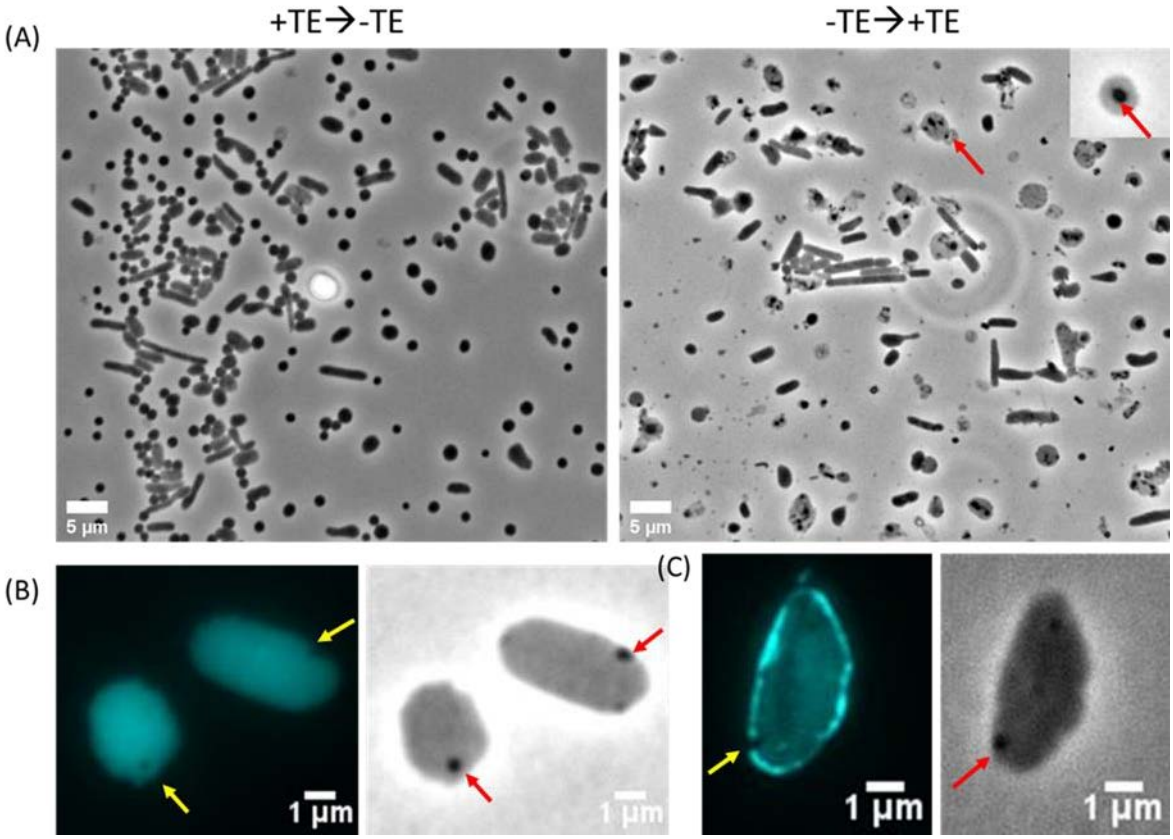

Supplementary Data Figure 3. Inclusion body formation depending on the cells' history of starvation. (A) Phase-contrast images of *H. volcanii* H98 cell when they were sub-cultured into Hv-Cab liquid medium without (left) or with (right) TEs form an agar-based medium that has opposite TE availability. Red arrow indicates the formation of inclusion bodies. (B) and (C) shows the absence of fluorescence signal on spots (yellow arrow) with inclusion bodies (red arrow) formed when CetZ1-mturquoise2 was expressed in ID181 in Hv-Cab (-TE). (B) shows cells that have diffuse CetZ1 localisation and (C) indicates a cell with peripheral CetZ1 localisation. These results suggest the inclusion bodies are not aggregates of CetZ1 protein.

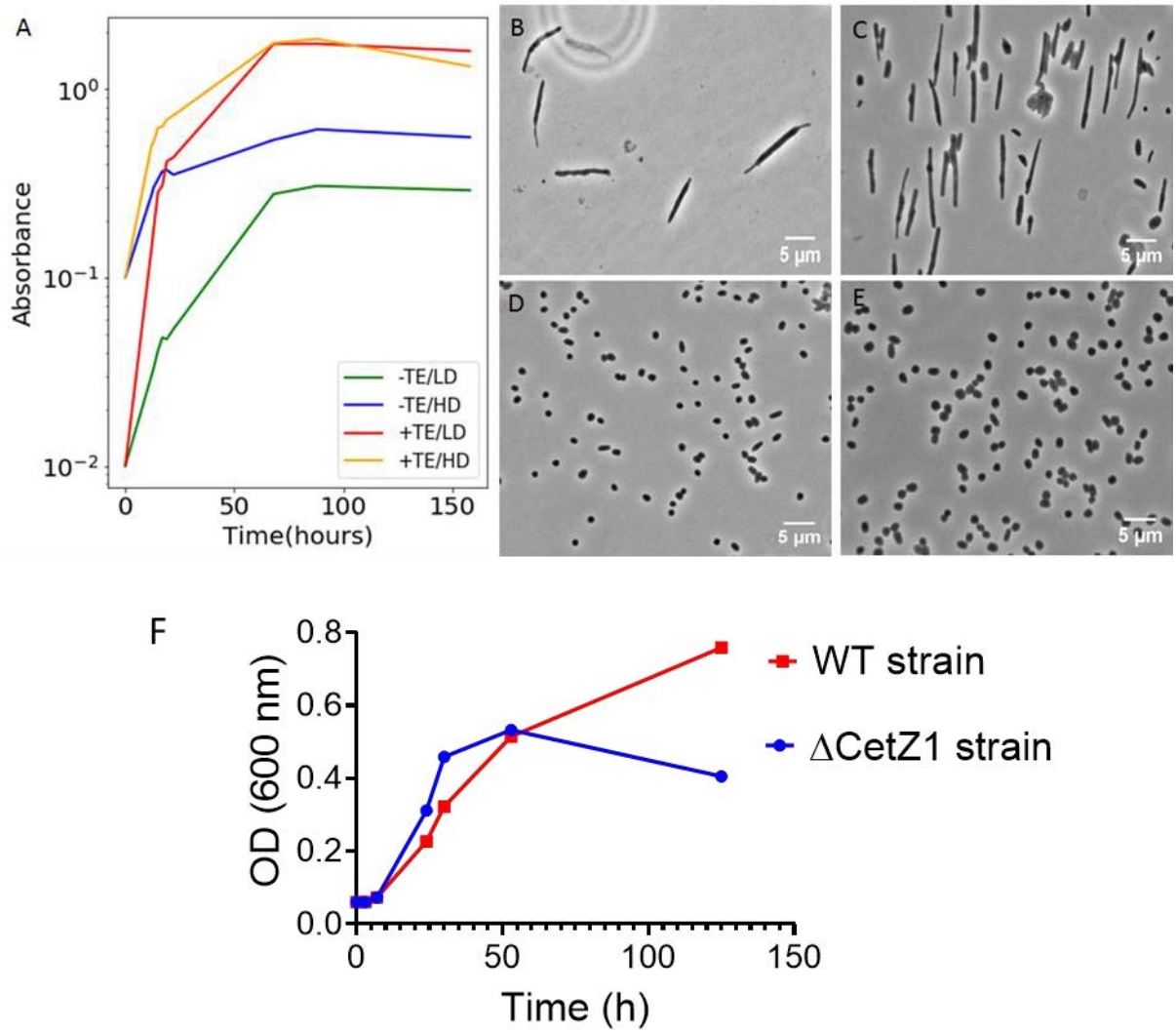

Supplementary Data Figure 4. The growth differences in *H. volcanii* during TE depletion. (A) A comparison of *H. volcanii* H98 growth curves starting with high cell density/ HD (OD600 = 0.1) and low density/ LD (OD600= 0.01) with the presence and absence of TEs in the growth medium. OD (600 nm) was measured at the selected time point for 150 hours. (B), (C), (D) and (E) are the phase-contrast images taken 15 hours after cells were inoculated into the liquid Hv-Ca (+ or – TE) liquid medium from the respective agar-based medium. (B) and (C) show the cell shapes of cells in low-density and high-density cultures respectively during metal starvation. (D) and (E) show the low-density and high-density cultures respectively grown in the presence of TEs. (F) A growth curve comparison between H98 WT strain and Δ*cetZ1* (ID59) in Hv-Ca (-TE).

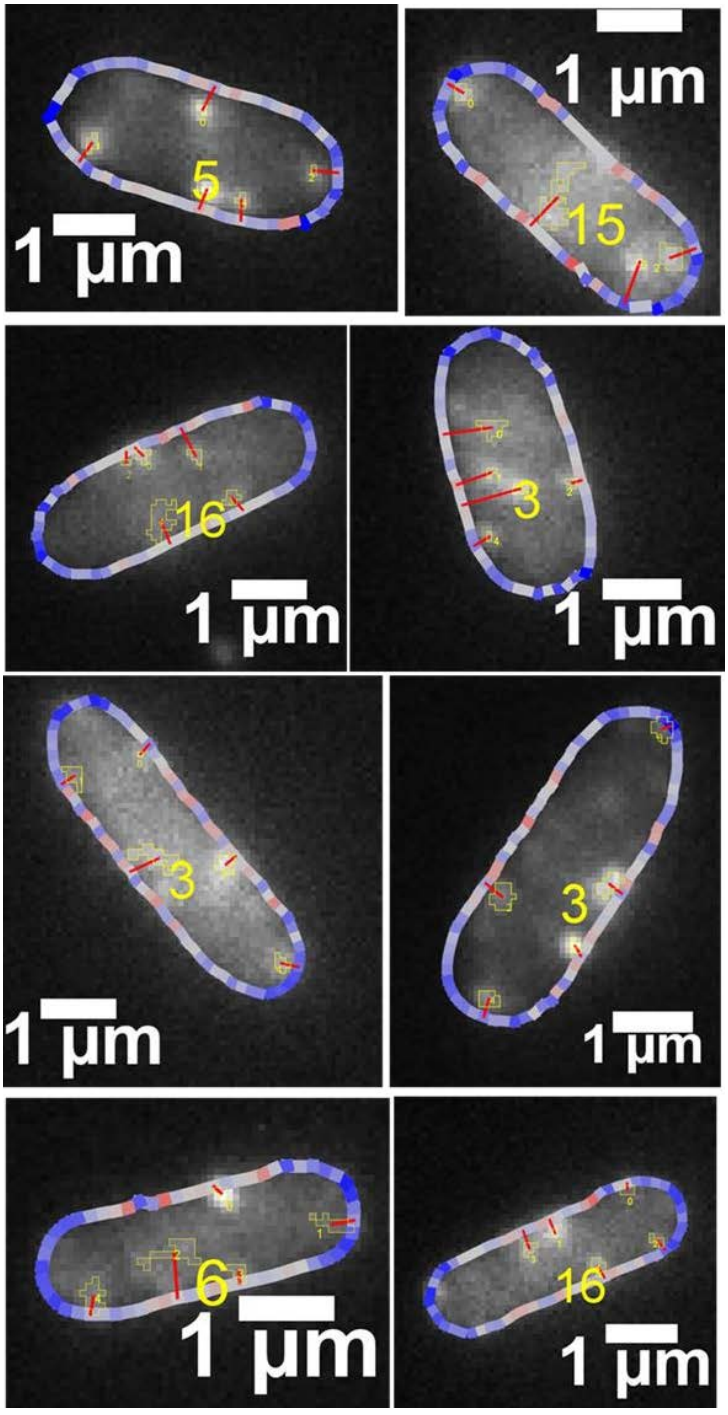

Supplementary Data Figure 5. The CetZ1 localisation concerning the local curvature of the cell. Example images of ID181 expressing pTA962_cetZ1-mTq2 in Hv-YPCab (+2 mM tryptophan) during early-log phase assay (10 h). Cell outlines resulting from the ImageJ cell detection process in phase-contrast images were used to analyse the local curvature of the cell (Duggin et al., 2015). The shades of red colour in the line at the cell outline gives the negative curvature (highest intensity of red had the highest negative curvature), and the shades of blue in that shows the positive curvature (the intensity of blue increases with the positive curvature). The corresponding fluorescence images were used to detect the localisation that has 75% higher intensity above the 40-pixel radius inside the cell. The detected localisations are marked by a yellow line.

The legends for the Supplementary Video:

Supplementary Video 1. *H. volcanii* cell shape change in Hv-Cab (+TE). The CellASIC chambers with *H. volcanii* H98 +pTA962 were perfused at 2 psi for 20 h with Hv-Cab (+TE), and 10 min interval time-lapse imaging was carried out.

Supplementary Video 2. *H. volcanii* cell shape change in Hv-Ca (-TE). The CellASIC chambers with *H. volcanii* H98+pTA962 were perfused at 2 psi for 20 hours with Hv-Cab (-TE), and 10 minutes time-lapse imaging was carried out.

Supplementary Video 3. *H. volcanii* cell shape change in Hv-YPC (-TE). The CellASIC chambers with *H. volcanii* H98+pTA962 were perfused at 2 psi for 20 hours with Hv-YPCab (-TE), and 10 minutes time-lapse imaging was carried out.

Supplementary Video 4. *H. volcanii* cell shape change in Hv-YPCab (+TE). The CellASIC chambers with *H. volcanii* H98+pTA962 were perfused at 2 psi for 20 hours with Hv-YPCab (+TE), and 10 minutes time-lapse imaging was carried out.

Supplementary Video 5. The localisation of CetZ1-mTq2 expressed in ID181 during early-log phase assay. Cells were grown at 42 ^{0}C in CellASIC microfluidic plate while HvYPCab+2mM tryptophan was flowing through the system at 2psi/min speed. Images were taken in 10 min intervals for 18 h.

Supplementary Video 6. The localisation of CetZ1-mTq2 expressed in ID181 during early-log phase assay. Cells were grown on a liquid culture at 42 ^{0}C water bath prior to imaging. Images were taken at 3 sec intervals for ~2 min on a 1% agarose pad in an incubator at 42 ^{0}C. All images were taken within 20 min.

Supplementary Video 7. The localisation of CetZ1.R276E, K277E-mTq2 expressed in ID181 during early-log phase assay. Cells were grown on a liquid culture at 42 ^{0}C water bath prior to imaging. Images were taken at 3 sec intervals for ~2 min on a 1% agarose pad in an incubator at 42 ^{0}C. All images were taken within 20 min. (A) Field view 01 (B) Field view 02

Supplementary Video 8. The localisation of CetZ1.G108S-mTq2 expressed in ID181 during early-log phase assay. Cells were grown on a liquid culture at 42 ^{0}C water bath prior to imaging. Images were taken at 3 sec intervals for ~2 min on a 1% agarose pad in an incubator at 42 ^{0}C. All images were taken within 20 min. (A) Field view 01 (B) Field view 02

Supplementary Video 9. The localisation of CetZ1.C-terminal tail mutant-mTq2 expressed in ID181 during early-log phase assay. Cells were grown on a liquid culture at 42 ^{0}C water bath prior to imaging. Images were taken at 3 sec intervals for ~2 min on a 1% agarose pad in an incubator at 42 ^{0}C. All images were taken within 20 min.

Supplementary Video 10. 3D-SIM images showing localisation of CetZ1-mTq2 expressed in ID181 during early-log phase assay.

Supplementary Video 11. Z-stack of a 3D-SIM image showing localisation of CetZ1.G108G-mTq2 expressed in ID181 during early-log phase assay.

REFERENCES

1) Abdul Halim, M. F. *et al.* (2016) 'Permuting the PGF signature motif blocks both archaeosortase-dependent C-terminal cleavage and prenyl lipid attachment for the *Haloferax volcanii* S-layer glycoprotein', *Journal of Bacteriology*. doi: 10.1128/JB.00849-15.
2) Adams, D. W. and Errington, J. (2009) 'Bacterial cell division: assembly, maintenance and disassembly of the Z ring', *Nature reviews. Microbiology*, 7(9), pp. 642–653. doi: 10.1038/nrmicro2198.
3) Addinall, S. G., Erfei, B. and Lutkenhaus, J. (1996) 'FtsZ ring formation in fts mutants', *Journal of Bacteriology*. doi: 10.1128/jb.178.13.3877-3884.1996.
4) Addinall, S. G. and Lutkenhaus, J. (1996) 'FtsZ-spirals and -arcs determine the shape of the invaginating septa in some mutants of *Escherichia coli*', *Molecular Microbiology*. doi: 10.1046/j.1365-2958.1996.00100.x.
5) Al-Bassam, J. *et al.* (2010) 'CLASP promotes microtubule rescue by recruiting tubulin dimers to the microtubule', *Developmental Cell*. doi: 10.1016/j.devcel.2010.07.016.
6) Albers, S. V. and Meyer, B. H. (2011) 'The archaeal cell envelope', *Nature Reviews Microbiology*. doi: 10.1038/nrmicro2576.
7) Alfaro-Aco, R., Thawani, A. and Petry, S. (2017) 'Structural analysis of the role of TPX2 in branching microtubule nucleation', *Journal of Cell Biology*. doi: 10.1083/jcb.201607060.
8) Allers, T *et al.* (2004) 'Development of additional selectable markers for the halophilic archaeon *Haloferax volcanii* based on the leuB and trpA genes', *Applied and environmental microbiology*. 2004/02/10, 70(2), pp. 943–953.
9) Allers, Thorsten *et al.* (2004) 'Development of Additional Selectable Markers for the Halophilic Archaeon *Haloferax volcanii* Based on the leuB and trpA Genes', *Applied and Environmental Microbiology*. doi: 10.1128/AEM.70.2.943-953.2004.
10) Allers, T *et al.* (2010) 'Improved strains and plasmid vectors for conditional overexpression of His-tagged proteins in *Haloferax volcanii*', *Applied and Environmental Microbiology*. 2010/01/26, 76(6), pp. 1759–1769. doi: 10.1128/aem.02670-09.
11) Allers, Thorsten *et al.* (2010) 'Improved strains and plasmid vectors for conditional overexpression of His-tagged proteins in *Haloferax volcanii*', *Applied and Environmental Microbiology*. doi: 10.1128/AEM.02670-09.
12) Alushin, G M *et al.* (2014) 'High-resolution microtubule structures reveal the structural transitions in alphabeta-tubulin upon GTP hydrolysis', *Cell*, 157(5), pp. 1117–1129. doi: 10.1016/j.cell.2014.03.053.
13) Alushin, Gregory M. *et al.* (2014) 'High-Resolution microtubule structures reveal the structural transitions in αβ-tubulin upon GTP hydrolysis', *Cell*. doi: 10.1016/j.cell.2014.03.053.
14) Amet, N., Lee, H. F. and Shen, W. C. (2009) 'Insertion of the designed helical linker led to increased expression of Tf-based fusion proteins', *Pharmaceutical Research*. doi: 10.1007/s11095-008-9767-0.
15) Anders, K. R. and Botstein, D. (2001a) 'Dominant-Lethal alpha -Tubulin Mutants Defective in Microtubule Depolymerization in Yeast', *Molecular Biology of the Cell*. doi: 10.1091/mbc.12.12.3973.
16) Anders, K. R. and Botstein, D. (2001b) 'Dominant-lethal α-tubulin mutants defective in microtubule depolymerization in yeast', *Molecular Biology of the Cell*. doi: 10.1091/mbc.12.12.3973.
17) Anderson, D. E., Gueiros-Filho, F. J. and Erickson, H. P. (2004) 'Assembly dynamics of FtsZ rings in *Bacillus subtilis* and *Escherichia coli* and effects of

FtsZ-regulating proteins', *J Bacteriol*. 2004/08/20, 186(17), pp. 5775–5781. doi: 10.1128/JB.186.17.5775-5781.2004.
18) Arai, R. *et al.* (2001) 'Design of the linkers which effectively separate domains of a bifunctional fusion protein', *Protein Engineering Design and Selection*. doi: 10.1093/protein/14.8.529.
19) Argos, P. (1990) 'An investigation of oligopeptides linking domains in protein tertiary structures and possible candidates for general gene fusion', *Journal of Molecular Biology*. doi: 10.1016/0022-2836(90)90085-Z.
20) Aurora, R. *et al.* (1997) 'Local interactions in protein folding: Lessons from the α-helix', *Journal of Biological Chemistry*. doi: 10.1074/jbc.272.3.1413.
21) Bagchi, S. *et al.* (2008) 'Intermediate filament-like proteins in bacteria and a cytoskeletal function in Streptomyces', *Molecular Microbiology*. doi: 10.1111/j.1365-2958.2008.06473.x.
22) Baumann, P. and Jackson, S. P. (1996) 'An archaebacterial homologue of the essential eubacterial cell division protein FtsZ', *Proceedings of the National Academy of Sciences of the United States of America*. 1996/06/25, 93(13), pp. 6726–6730.
23) Beber, A. *et al.* (2019) 'Membrane reshaping by micrometric curvature sensitive septin filaments', *Nature Communications*. doi: 10.1038/s41467-019-08344-5.
24) Bernhardt, T. G. and de Boer, P. A. (2005) 'SlmA, a nucleoid-associated, FtsZ binding protein required for blocking septal ring assembly over Chromosomes in E. coli', *Mol Cell*, 18(5), pp. 555–564. doi: 10.1016/j.molcel.2005.04.012.
25) BHANDARI, D. G. *et al.* (1986) '1H-NMR study of mobility and conformational constraints within the proline-rich N-terminal of the LC1 alkali light chain of skeletal myosin: Correlation with similar segments in other protein systems', *European Journal of Biochemistry*. doi: 10.1111/j.1432-1033.1986.tb09978.x.
26) Bieling, P. *et al.* (2007) 'Reconstitution of a microtubule plus-end tracking system in vitro', *Nature*. doi: 10.1038/nature06386.
27) Bird, R. E. *et al.* (1988) 'Single-chain antigen-binding proteins', *Science*. doi: 10.1126/science.3140379.
28) Bitan-Banin, G., Ortenberg, R. and Mevarech, M. (2003) 'Development of a gene knockout system for the halophilic archaeon Haloferax volcanii by use of the pyrE gene', *Journal of Bacteriology*. doi: 10.1128/JB.185.3.772-778.2003.
29) Bolhuis, H. *et al.* (2006) 'The genome of the square archaeon Haloquadratum walsbyi : life at the limits of water activity', *BMC genomics*, 7, p. 169. doi: 10.1186/1471-2164-7-169.
30) Bondos, S. E. and Bicknell, A. (2003) 'Detection and prevention of protein aggregation before, during, and after purification', *Analytical Biochemistry*. doi: 10.1016/S0003-2697(03)00059-9.
31) Bramhill, D. and Thompson, C. M. (1994) 'GTP-dependent polymerization of Escherichia coli FtsZ protein to form tubules', *Proceedings of the National Academy of Sciences of the United States of America*. doi: 10.1073/pnas.91.13.5813.
32) Brouhard, G. J. *et al.* (2008) 'XMAP215 Is a Processive Microtubule Polymerase', *Cell*. doi: 10.1016/j.cell.2007.11.043.
33) Brown, P. J. B. *et al.* (2012) 'Polar growth in the Alphaproteobacterial order Rhizobiales', *Proceedings of the National Academy of Sciences of the United States of America*. doi: 10.1073/pnas.1114476109.
34) Brun, Y. (1994) 'The Expression of Asymmetry During Caulobacter Cell Differentiation', *Annual Review of Biochemistry*. doi:

10.1146/annurev.biochem.63.1.419.
35) Bumagina, Z. M. *et al.* (2010) 'Mechanism of suppression of dithiothreitol-induced aggregation of bovine α-lactalbumin by α-crystallin', *Biophysical Chemistry*. doi: 10.1016/j.bpc.2009.11.002.
36) Burbank, K. S. and Mitchison, T. J. (2006) 'Microtubule dynamic instability', *Current Biology*. doi: 10.1016/j.cub.2006.06.044.
37) Burns, D. G. *et al.* (2007) 'Haloquadratum walsbyi gen. nov., sp. nov., the square haloarchaeon of Walsby, isolated from saltern crystallizers in Australia and Spain', *International journal of systematic and evolutionary microbiology*. 2007/02/03, 57(Pt 2), pp. 387–392. doi: 10.1099/ijs.0.64690-0.
38) Cannon, K. S. *et al.* (2019) 'An amphipathic helix enables septins to sense micrometer-scale membrane curvature', *Journal of Cell Biology*. doi: 10.1083/jcb.201807211.
39) Carballido-Lopez, R. (2006a) 'Orchestrating bacterial cell morphogenesis', *Molecular Microbiology*, 60(4), pp. 815–819. doi: 10.1111/j.1365-2958.2006.05161.x.
40) Carballido-Lopez, R. (2006b) 'The bacterial actin-like cytoskeleton', *Microbiol Mol Biol Rev*, 70(4), pp. 888–909. doi: 10.1128/MMBR.00014-06.
41) Chang, F. and Huang, K. C. (2014) 'How and why cells grow as rods', *BMC Biology*. doi: 10.1186/s12915-014-0054-8.
42) Charlesworth, J. C. and Burns, B. P. (2015) 'Untapped Resources: Biotechnological Potential of Peptides and Secondary Metabolites in Archaea', *Archaea*. doi: 10.1155/2015/282035.
43) Chen, X., Zaro, J. L. and Shen, W.-C. (2013) 'Fusion protein linkers: property, design and functionality.', *Advanced drug delivery reviews*. doi: 10.1016/j.addr.2012.09.039.
44) Chen, Y and Erickson, H. P. (2005) 'Rapid in vitro assembly dynamics and subunit turnover of FtsZ demonstrated by fluorescence resonance energy transfer', *J Biol Chem*. 2005/04/14, 280(23), pp. 22549–22554. doi: 10.1074/jbc.M500895200.
45) Chen, Yaodong and Erickson, H. P. (2005) 'Rapid in vitro assembly dynamics and subunit turnover of FtsZ demonstrated by fluorescence resonance energy transfer', *Journal of Biological Chemistry*. doi: 10.1074/jbc.M500895200.
46) Chinen, A., Uchiyama, I. and Kobayashi, I. (2000) 'Comparison between Pyrococcus horikoshii and Pyrococcus abyssi genome sequences reveals linkage of restriction-modification genes with large genome polymorphisms', *Gene*. doi: 10.1016/S0378-1119(00)00459-5.
47) Chrétien, D., Flyvbjerg, H. and Fuller, S. D. (1998) 'Limited flexibility of the inter-protofilament bonds in microtubules assembled from pure tubulin', *European Biophysics Journal*. doi: 10.1007/s002490050159.
48) Corbin, B D, Yu, X. C. and Margolin, W. (2002) 'Exploring intracellular space: function of the Min system in round-shaped Escherichia coli', *The EMBO journal*, 21(8), pp. 1998–2008. doi: 10.1093/emboj/21.8.1998.
49) Corbin, Brian D., Yu, X. C. and Margolin, W. (2002) 'Exploring intracellular space: Function of the Min system in round-shaped Escherichia coli', *EMBO Journal*. doi: 10.1093/emboj/21.8.1998.
50) Cordell, S. C. and Löwe, J. (2001) 'Crystal structure of the bacterial cell division regulator MinD', *FEBS Letters*. doi: 10.1016/S0014-5793(01)02216-5.
51) Delmas, S., Duggin, I. G. and Allers, T. (2013) 'DNA damage induces nucleoid compaction via the Mre11-Rad50 complex in the archaeon Haloferax volcanii',

Molecular Microbiology. doi: 10.1111/mmi.12091.
52) Deng, X. *et al.* (2017) 'Four-stranded mini microtubules formed by Prosthecobacter BtubAB show dynamic instability', *Proceedings of the National Academy of Sciences of the United States of America*. doi: 10.1073/pnas.1705062114.
53) Dhaked, H. P. S. *et al.* (2016) 'Mutation of Arg191 in FtsZ Impairs Cytokinetic Abscission of Bacillus subtilis Cells', *Biochemistry*. doi: 10.1021/acs.biochem.6b00493.
54) Dominguez, R. and Holmes, K. C. (2011) 'Actin structure and function', *Annu Rev Biophys*.
55) Dougherty, C. A. *et al.* (2001) 'Mutation in the β-tubulin signature motif suppresses microtubule GTPase activity and dynamics, and slows mitosis', *Biochemistry*. doi: 10.1021/bi010070y.
56) Dráber, P. and Dráberová, E. (2012) 'Microtubules', in *Cytoskeleton and Human Disease*. doi: 10.1007/978-1-61779-788-0_2.
57) Du, S. *et al.* (2018) 'FtsZ filaments have the opposite kinetic polarity of microtubules', *Proceedings of the National Academy of Sciences*. doi: 10.1073/pnas.1811919115.
58) Ducret, A., Quardokus, E. M. and Brun, Y. V. (2016) 'MicrobeJ, a tool for high throughput bacterial cell detection and quantitative analysis', *Nature Microbiology*. doi: 10.1038/nmicrobiol.2016.77.
59) Duggin, Iain G. *et al.* (2015) 'CetZ tubulin-like proteins control archaeal cell shape', *Nature*. doi: 10.1038/nature13983.
60) Duggin, Iain G *et al.* (2015) 'CetZ tubulin-like proteins control archaeal cell shape', *Nature*, 519(7543), pp. 362–365. doi: 10.1038/nature13983.
61) Dyall-Smith, M. L. *et al.* (2011) 'Haloquadratum walsbyi: Limited Diversity in a Global Pond', *PLoS ONE*. doi: 10.1371/journal.pone.0020968.
62) Van den Ent, F., Amos, L. A. and Löwe, J. (2001) 'Prokaryotic origin of the actin cytoskeleton', *Nature*. doi: 10.1038/35092500.
63) Erickson, H. P. (1997) 'FtsZ, a tubulin homologue in prokaryote cell division', *Trends in Cell Biology*. doi: 10.1016/S0962-8924(97)01108-2.
64) Ettema, T. J. and Bernander, R. (2009) 'Cell division and the ESCRT complex: A surprise from the archaea', *Communicative & integrative biology*, 2(2), pp. 86–88. Available at: http://www.ncbi.nlm.nih.gov/pubmed/19704896.
65) Fraipont, C. *et al.* (2011) 'The integral membrane FtsW protein and peptidoglycan synthase PBP3 form a subcomplex in Escherichia coli', *Microbiology*. doi: 10.1099/mic.0.040071-0.
66) Freedman, H. *et al.* (2011) 'Molecular dynamics modeling of tubulin C-terminal tail interactions with the microtubule surface', *Proteins: Structure, Function and Bioinformatics*. doi: 10.1002/prot.23155.
67) Fröls, S., Dyall-Smith, M. and Pfeifer, F. (2012) 'Biofilm formation by haloarchaea', *Environmental Microbiology*. doi: 10.1111/j.1462-2920.2012.02895.x.
68) George, R. A. and Heringa, J. (2003) 'An analysis of protein domain linkers: their classification and role in protein folding', *Protein Engineering, Design and Selection*. doi: 10.1093/protein/15.11.871.
69) Geyer, E. A. *et al.* (2015) 'A mutation uncouples the tubulin conformational and GTPase cycles, revealing allosteric control of microtubule dynamics', *eLife*. doi: 10.7554/eLife.10113.
70) Ghahghaei, A. and Mohammadian, S. (2014) 'The effect of Arg on the structure

perturbation and chaperone activity of α-crystallin in the presence of the crowding agent, dextran', *Applied Biochemistry and Biotechnology*. doi: 10.1007/s12010-014-1092-y.

71) Gonin, M. *et al.* (2000) 'Regulation of stalk elongation by phosphate in Caulobacter crescentus', *Journal of Bacteriology*. doi: 10.1128/JB.182.2.337-347.2000.
72) Grego, S., Cantillana, V. and Salmon, E. D. (2001) 'Microtubule treadmilling in vitro investigated by fluorescence speckle and confocal microscopy', *Biophysical Journal*. doi: 10.1016/S0006-3495(01)75680-9.
73) Gregoretti, I. (2007) 'Modeling Microtubule Dynamic Instability', *Dissertation*.
74) Guan, F. *et al.* (2018) 'Lateral interactions between protofilaments of the bacterial tubulin homolog FtsZ are essential for cell division', *eLife*. doi: 10.7554/eLife.35578.
75) Guesdon, A. *et al.* (2016) 'EB1 interacts with outwardly curved and straight regions of the microtubule lattice', *Nature Cell Biology*. doi: 10.1038/ncb3412.
76) Hale, C. A., Rhee, A. C. and de Boer, P. A. (2000) 'ZipA-induced bundling of FtsZ polymers mediated by an interaction between C-terminal domains', *J Bacteriol*, 182(18), pp. 5153–5166. Available at: http://www.ncbi.nlm.nih.gov/pubmed/10960100.
77) Hartman, A. L. *et al.* (2010) 'The complete genome sequence of Haloferax volcanii DS2, a model archaeon', *PLoS One*. 2010/03/25, 5(3), p. e9605. doi: 10.1371/journal.pone.0009605 [doi].
78) Haupt, A. and Minc, N. (2018) 'How cells sense their own shape – mechanisms to probe cell geometry and their implications in cellular organization and function', *Journal of Cell Science*. doi: 10.1242/jcs.214015.
79) Hauschild-Quintern, J. *et al.* (2013) 'Gene knockout and knockin by zinc-finger nucleases: Current status and perspectives', *Cellular and Molecular Life Sciences*. doi: 10.1007/s00018-012-1204-1.
80) Hohmann and Dehghani (2019) 'The Cytoskeleton—A Complex Interacting Meshwork', *Cells*. doi: 10.3390/cells8040362.
81) Huang, K. C., Meir, Y. and Wingreen, N. S. (2003) 'Dynamic structures in Escherichia coli: Spontaneous formation of MinE rings and MinD polar zones', *Proceedings of the National Academy of Sciences of the United States of America*. doi: 10.1073/pnas.2135445100.
82) Huang, K. C., Mukhopadhyay, R. and Wingreen, N. S. (2006) 'A curvature-mediated mechanism for localization of lipids to bacterial poles', *PLoS Computational Biology*. doi: 10.1371/journal.pcbi.0020151.
83) Huecas, S. and Andreu, J. M. (2003) 'Energetics of the cooperative assembly of cell division protein FtsZ and the nucleotide hydrolysis switch', *The Journal of biological chemistry*, 278(46), pp. 46146–46154. doi: 10.1074/jbc.M307128200.
84) Hussain, S. *et al.* (2018) 'MreB filaments align along greatest principal membrane curvature to orient cell wall synthesis', *eLife*. doi: 10.7554/eLife.32471.
85) Inbar, O. *et al.* (2000) 'The relationship between homology length and crossing over during the repair of a broken chromosome', *Journal of Biological Chemistry*. doi: 10.1074/jbc.C000133200.
86) Jarrell, K. F. *et al.* (2011) 'Major players on the microbial stage: Why Archaea are important', *Microbiology*. doi: 10.1099/mic.0.047837-0.
87) Joung, J. K. and Sander, J. D. (2013) 'TALENs: A widely applicable technology for targeted genome editing', *Nature Reviews Molecular Cell Biology*. doi: 10.1038/nrm3486.

88) Kapitein, L. C. *et al.* (2010) 'Probing intracellular motor protein activity using an inducible cargo trafficking assay', *Biophysical Journal*. doi: 10.1016/j.bpj.2010.07.055.
89) Kavallaris, M. (2010) 'Microtubules and resistance to tubulin-binding agents', *Nature reviews cancer*, 10(3), pp. 194–204.
90) Keskin, O. *et al.* (2002) 'Relating molecular flexibility to function: A case study of tubulin', *Biophysical Journal*. doi: 10.1016/S0006-3495(02)75199-0.
91) Klein, E. A. *et al.* (2013) 'Physiological role of stalk lengthening in caulobacter crescentus', *Communicative and Integrative Biology*. doi: 10.4161/cib.24561.
92) Kollman, J. M. *et al.* (2011) 'Microtubule nucleation by gamma-tubulin complexes', *Nature Reviews Molecular Cell Biology*.
93) Król, E. and Scheffers, D. J. (2013) 'FtsZ polymerization assays: Simple protocols and considerations', *Journal of Visualized Experiments*. doi: 10.3791/50844.
94) Kuchnir Fygenson, D. *et al.* (1995) 'Spontaneous nucleation of microtubules', *Physical Review E*. doi: 10.1103/PhysRevE.51.5058.
95) Large, A. *et al.* (2007) 'Characterization of a tightly controlled promoter of the halophilic archaeon Haloferax volcanii and its use in the analysis of the essential cct1 gene', *Molecular Microbiology*. 2007/11/02, 66(5), pp. 1092–1106. doi: MMI5980 [pii]10.1111/j.1365-2958.2007.05980.x [doi].
96) Leube, R. E. and Schwarz, N. (2015) 'Intermediate Filaments', in *Encyclopedia of Cell Biology*. doi: 10.1016/B978-0-12-394447-4.20056-4.
97) Leuko, S. *et al.* (2005) 'Isolation of Viable Haloarchaea from Ancient Salt Deposits and Application of Fluorescent Stains for in Situ Detection of Halophiles in Hypersaline Environmental Samples and Model Fluid Inclusions', in *Adaptation to Life at High Salt Concentrations in Archaea, Bacteria, and Eukarya*. doi: 10.1007/1-4020-3633-7_7.
98) Levin-Karp, A. *et al.* (2013) 'Quantifying translational coupling in E. coli synthetic operons using RBS modulation and fluorescent reporters', *ACS Synthetic Biology*. doi: 10.1021/sb400002n.
99) Li, G. *et al.* (2016) 'Construction of a linker library with widely controllable flexibility for fusion protein design', *Applied Microbiology and Biotechnology*. doi: 10.1007/s00253-015-6985-3.
100) Liao, Y. *et al.* (2018) 'Archaeal cell biology: diverse functions of tubulin-like cytoskeletal proteins at the cell envelope', *Emerging Topics in Life Sciences*. Dec 14, 20, 2(4), pp. 547–559. doi: 10.1042/ETLS20180026.
101) Lindas, A. C. *et al.* (2008) 'A unique cell division machinery in the Archaea', *Proceedings of the National Academy of Sciences of the United States of America*, 105(48), pp. 18942–18946.
102) Lindås, A. C. *et al.* (2008) 'A unique cell division machinery in the Archaea', *Proceedings of the National Academy of Sciences of the United States of America*. doi: 10.1073/pnas.0809467105.
103) Lombardo, A. *et al.* (2011) 'Site-specific integration and tailoring of cassette design for sustainable gene transfer', *Nature Methods*. doi: 10.1038/nmeth.1674.
104) Los, G. V. *et al.* (2008) 'HaloTag: A novel protein labeling technology for cell imaging and protein analysis', *ACS Chemical Biology*. doi: 10.1021/cb800025k.
105) Lowe, J. (1998) 'Crystal structure determination of FtsZ from Methanococcus jannaschii', *Journal of structural biology*, 124(2–3), pp. 235–243. doi: 10.1006/jsbi.1998.4041.
106) Löwe, J. *et al.* (2001) 'Refined structure of αβ-tubulin at 3.5 Å resolution', *Journal of Molecular Biology*. doi: 10.1006/jmbi.2001.5077.

107) Lowe, J. and Amos, L. A. (1998) 'Crystal structure of the bacterial cell-division protein FtsZ', *Nature*, 391(6663), pp. 203–206. doi: 10.1038/34472.
108) Lowe, J. and Amos, L. A. (2000) 'Helical tubes of FtsZ from Methanococcus jannaschii', *Biological chemistry*, 381(9–10), pp. 993–999. doi: 10.1515/BC.2000.122.
109) Löwe, J. and Amos, L. A. (2017) 'Erratum to: Prokaryotic Cytoskeletons : Filamentous Protein Polymers Active in the Cytoplasm of Bacterial and Archaeal Cells', *Sub-cellular biochemistry*. doi: 10.1007/978-3-319-53047-5_16.
110) Lu, C., Reedy, M. and Erickson, H. P. (2000) 'Straight and curved conformations of FtsZ are regulated by GTP hydrolysis', *J Bacteriol*. 1999/12/30, 182(1), pp. 164–170. Available at: https://www.ncbi.nlm.nih.gov/pubmed/10613876.
111) Lu, C., Stricker, J. and Erickson, H. P. (2001) 'Site-specific mutations of FtsZ - Effects on GTPase and in vitro assembly', *BMC Microbiology*. doi: 10.1186/1471-2180-1-7.
112) Lüders, J. and Stearns, T. (2007) 'Microtubule-organizing centres: A re-evaluation', *Nature Reviews Molecular Cell Biology*. doi: 10.1038/nrm2100.
113) Ludueña, R. F. and Banerjee, A. (2009) 'The Isotypes of Tubulin', in *The Role of Microtubules in Cell Biology, Neurobiology, and Oncology*. doi: 10.1007/978-1-59745-336-3_6.
114) Maeda, Y. T. *et al.* (2012) 'Assembly of MreB filaments on liposome membranes: A synthetic biology approach', *ACS Synthetic Biology*. doi: 10.1021/sb200003v.
115) Makarova, K. S. and Koonin, E. V. (2010) 'Two new families of the FtsZ-tubulin protein superfamily implicated in membrane remodeling in diverse bacteria and archaea', *Biology Direct*. doi: 10.1186/1745-6150-5-33.
116) Marteyn, B. S. *et al.* (2014) 'ZapE is a novel cell division protein interacting with FtsZ and modulating the Z-ring dynamics', *mBio*. doi: 10.1128/mBio.00022-14.
117) Maslov, I. *et al.* (2018) 'Efficient non-cytotoxic fluorescent staining of halophiles', *Scientific Reports*. doi: 10.1038/s41598-018-20839-7.
118) Maurer, S. P. *et al.* (2011) 'GTPγS microtubules mimic the growing microtubule end structure recognized by end-binding proteins (EBs)', *Proceedings of the National Academy of Sciences of the United States of America*. doi: 10.1073/pnas.1014758108.
119) Maurer, S. P. *et al.* (2012) 'EBs recognize a nucleotide-dependent structural cap at growing microtubule ends', *Cell*. doi: 10.1016/j.cell.2012.02.049.
120) Mauriello, E. M. F. *et al.* (2010) 'Bacterial motility complexes require the actin-like protein, MreB and the Ras homologue, MglA', *EMBO Journal*. doi: 10.1038/emboj.2009.356.
121) Megaw, J. and Gilmore, B. F. (2017) 'Archaeal persisters: Persister cell formation as a stress response in haloferax volcanii', *Frontiers in Microbiology*. doi: 10.3389/fmicb.2017.01589.
122) Minc, N., Burgess, D. and Chang, F. (2011) 'Influence of cell geometry on division-plane positioning', *Cell*, 144(3), pp. 414–426. doi: 10.1016/j.cell.2011.01.016.
123) Miraldi, E. R., Thomas, P. J. and Romberg, L. (2008) 'Allosteric models for cooperative polymerization of linear polymers', *Biophysical Journal*. doi: 10.1529/biophysj.107.126219.
124) Mishra, M. *et al.* (2012) 'Cylindrical cellular geometry ensures fidelity of

division site placement in fission yeast', *Journal of Cell Science*. doi: 10.1242/jcs.103788.
125) Mitchison, T. and Kirschner, M. (1984) 'Dynamic instability of microtubule growth', *Nature*, 312(5991), pp. 237–242.
126) Mitra, A. and Sept, D. (2008) 'Taxol allosterically alters the dynamics of the tubulin dimer and increases the flexibility of microtubules', *Biophysical Journal*. doi: 10.1529/biophysj.108.133884.
127) Monahan, L. G., Robinson, A. and Harry, E. J. (2009) 'Lateral FtsZ association and the assembly of the cytokinetic Z ring in bacteria', *Molecular Microbiology*. doi: 10.1111/j.1365-2958.2009.06914.x.
128) Moore, D. A. *et al.* (2017) 'Probing for Binding Regions of the FtsZ Protein Surface through Site-Directed Insertions: Discovery of Fully Functional FtsZ-Fluorescent Proteins', *J Bacteriol*. 2016/11/01, 199(1). doi: 10.1128/JB.00553-16.
129) Moriwaki, T. and Goshima, G. (2016) 'Five factors can reconstitute all three phases of microtubule polymerization dynamics', *Journal of Cell Biology*. doi: 10.1083/jcb.201604118.
130) Mostowy, S. and Cossart, P. (2012) 'Septins: The fourth component of the cytoskeleton', *Nature Reviews Molecular Cell Biology*. doi: 10.1038/nrm3284.
131) Mukherjee, A. and Lutkenhaus, J. (1998) 'Dynamic assembly of FtsZ regulated by GTP hydrolysis', *The EMBO journal*, 17(2), pp. 462–469. doi: 10.1093/emboj/17.2.462.
132) Mullakhanbhai, M. F. and Larsen, H. (1975) 'Halobacterium volcanii spec. nov., a Dead Sea halobacterium with a moderate salt requirement.', *Archives of microbiology*. 1975/08/28, 104(3), pp. 207–14. Available at: http://www.ncbi.nlm.nih.gov/pubmed/1190944.
133) Nakanishi, H. *et al.* (2009) 'Conservation and differences of the Min system in the chloroplast and bacterial division site placement', *Communicative and Integrative Biology*. doi: 10.4161/cib.2.5.8762.
134) Nakashima, N. and Miyazaki, K. (2014) 'Bacterial cellular engineering by genome editing and gene silencing', *International Journal of Molecular Sciences*. doi: 10.3390/ijms15022773.
135) Natale, D. A. *et al.* (2000) 'Towards understanding the first genome sequence of a crenarchaeon by genome annotation using clusters of orthologous groups of proteins (COGs)', *Genome Biol*, 1(5), p. RESEARCH0009. doi: 10.1186/gb-2000-1-5-research0009.
136) Nogales, E. *et al.* (1999) 'High-resolution model of the microtubule', *Cell*. doi: 10.1016/S0092-8674(00)80961-7.
137) Nogales, E. (2001) 'Structural Insights into Microtubule Function', *Annual Review of Biophysics and Biomolecular Structure*. doi: 10.1146/annurev.biophys.30.1.397.
138) Nunoura, T. *et al.* (2011) 'Insights into the evolution of Archaea and eukaryotic protein modifier systems revealed by the genome of a novel archaeal group', *Nucleic Acids Research*, 39(8), pp. 3204–3223. doi: 10.1093/nar/gkq1228.
139) Osawa, M., Anderson, D. E. and Erickson, H. P. (2008) 'Reconstitution of contractile FtsZ rings in liposomes', *Science*. 2008/04/19, 320(5877), pp. 792–794. doi: 10.1126/science.1154520.
140) Osawa, M. and Erickson, H. P. (2005) 'Probing the domain structure of FtsZ by random truncation and insertion of GFP', *Microbiology (Reading, England)*. 2005/12/13, 151(Pt 12), pp. 4033–4043. doi: 10.1099/mic.0.28219-0.
141) Osawa, M. and Erickson, H. P. (2006) 'FtsZ from divergent foreign bacteria can

function for cell division in Escherichia coli', *J Bacteriol*. 2006/10/04, 188(20), pp. 7132–7140. doi: 10.1128/JB.00647-06.
142) Otey, C. R. *et al.* (2004) 'Functional evolution and structural conservation in chimeric cytochromes P450: Calibrating a structure-guided approach', *Chemistry and Biology*. doi: 10.1016/j.chembiol.2004.02.018.
143) Paerl, H. W. (1982) 'Factors Limiting Productivity of Freshwater Ecosystems', in. doi: 10.1007/978-1-4615-8318-9_3.
144) De Pedro, M. A., Schwarz, H. and Koch, A. L. (2003) 'Patchiness of murein insertion into the sidewall of Escherichia coli', *Microbiology*. doi: 10.1099/mic.0.26125-0.
145) Pichoff, S. and Lutkenhaus, J. (2005) 'Tethering the Z ring to the membrane through a conserved membrane targeting sequence in FtsA', *Molecular Microbiology*, 55(6), pp. 1722–1734. doi: 10.1111/j.1365-2958.2005.04522.x.
146) Pin, C. *et al.* (2009) 'Network analysis of the transcriptional pattern of young and old cells of Escherichia coli during lag phase', *BMC Systems Biology*. doi: 10.1186/1752-0509-3-108.
147) Pollard, T. D. *et al.* (2016) *Cell Biology: Third Edition*, *Cell Biology: Third Edition*.
148) Prota, A. E. *et al.* (2013) 'Molecular mechanism of action of microtubule-stabilizing anticancer agents', *Science*. doi: 10.1126/science.1230582.
149) Ramirez-diaz, A. D. A., Merino-salomon, A. and Heymann, M. (2019) 'Bidirectional FtsZ filament treadmilling promotes membrane constriction via torsional stress', *bioRxiv*. doi: 10.1101/587790.
150) Rice, L. M., Montabana, E. A. and Agard, D. A. (2008) 'The lattice as allosteric effector: Structural studies of αβ- and γ-tubulin clarify the role of GTP in microtubule assembly', *Proceedings of the National Academy of Sciences of the United States of America*. doi: 10.1073/pnas.0801155105.
151) Richards, K. L. *et al.* (2000) 'Structure-function relationships in yeast tubulins', *Mol Biol Cell*. 2000/05/04, 11(5), pp. 1887–1903.
152) Rickman, J. *et al.* (2017) 'Steady-state EB cap size fluctuations are determined by stochastic microtubule growth and maturation', *Proceedings of the National Academy of Sciences of the United States of America*. doi: 10.1073/pnas.1620274114.
153) Rinas, U. *et al.* (2017) 'Bacterial Inclusion Bodies: Discovering Their Better Half', *Trends in Biochemical Sciences*. doi: 10.1016/j.tibs.2017.01.005.
154) Rivas, G. *et al.* (2000) 'Magnesium-induced linear self-association of the FtsZ bacterial cell division protein monomer. The primary steps for FtsZ assembly', *Journal of Biological Chemistry*. doi: 10.1074/jbc.275.16.11740.
155) Robinson, J. L. *et al.* (2005) 'Growth kinetics of extremely halophilic Archaea (family Halobacteriaceae) as revealed by arrhenius plots', *Journal of Bacteriology*. doi: 10.1128/JB.187.3.923-929.2005.
156) Rodrigues-Oliveira, T. *et al.* (2017) 'Archaeal S-Layers: Overview and Current State of the Art', *Frontiers in Microbiology*, 8. doi: 10.3389/fmicb.2017.02597.
157) Rodrigues, C. D. A. and Harry, E. J. (2012) 'The min system and nucleoid occlusion are not required for identifying the division site in bacillus subtilis but ensure its efficient utilization', *PLoS Genetics*. doi: 10.1371/journal.pgen.1002561.
158) Roll-Mecak, A. (2015) 'Intrinsically disordered tubulin tails: Complex tuners of microtubule functions?', *Seminars in Cell and Developmental Biology*. doi: 10.1016/j.semcdb.2014.09.026.
159) Romberg, L., Simon, M. and Erickson, H. p. (2001) 'Polymerization of FtsZ, a

bacterial homolog of tubulin. Is assembly cooperative?', *Journal of Biological Chemistry*. doi: 10.1074/jbc.M009033200.
160) Rothfield, L., Taghbalout, A. and Shih, Y. L. (2005) 'Spatial control of bacterial division-site placement', *Nature reviews. Microbiology*, 3(12), pp. 959–968. doi: 10.1038/nrmicro1290.
161) Sanfilippo, J. E. *et al.* (2019) 'Microfluidic-based transcriptomics reveal force-independent bacterial rheosensing', *Nature Microbiology*. doi: 10.1038/s41564-019-0455-0.
162) Satir, P. and Christensen, S. T. (2007) 'Overview of Structure and Function of Mammalian Cilia', *Annual Review of Physiology*. doi: 10.1146/annurev.physiol.69.040705.141236.
163) Scheffers, D J *et al.* (2002) 'GTP hydrolysis of cell division protein FtsZ: evidence that the active site is formed by the association of monomers', *Biochemistry*. 2002/01/10, 41(2), pp. 521–529. doi: bi011370i [pii].
164) Scheffers, Dirk Jan *et al.* (2002) 'GTP hydrolysis of cell division protein FtsZ: Evidence that the active site is formed by the association of monomers', *Biochemistry*. doi: 10.1021/bi011370i.
165) Schlieper, D. *et al.* (2005) 'Structure of bacterial tubulin BtubA/B: evidence for horizontal gene transfer', *Proceedings of the National Academy of Sciences of the United States of America*, 102(26), pp. 9170–9175. doi: 10.1073/pnas.0502859102.
166) Schmidt, K. L. *et al.* (2004) 'A predicted ABC transporter, FtsEX, is needed for cell division in Escherichia coli', *J Bacteriol*. 2004/01/20, 186(3), pp. 785–793. Available at: https://www.ncbi.nlm.nih.gov/pubmed/14729705.
167) Shemesh, J. *et al.* (2015) 'Flow-induced stress on adherent cells in microfluidic devices', *Lab on a Chip*. doi: 10.1039/c5lc00633c.
168) Sirajuddin, M., Rice, L. M. and Vale, R. D. (2014) 'Regulation of microtubule motors by tubulin isotypes and post-translational modifications', *Nature Cell Biology*. doi: 10.1038/ncb2920.
169) Snyder, J. T. *et al.* (2010) 'Structural features of rhogefs', in *Handbook of Cell Signaling, 2/e*. doi: 10.1016/B978-0-12-374145-5.00224-2.
170) Song, Y. and Brady, S. T. (2015) 'Post-translational modifications of tubulin: Pathways to functional diversity of microtubules', *Trends in Cell Biology*. doi: 10.1016/j.tcb.2014.10.004.
171) Strauss, M. P. *et al.* (2012) '3D-SIM super resolution microscopy reveals a bead-like arrangement for FtsZ and the division machinery: implications for triggering cytokinesis', *PLoS biology*, 10(9), p. e1001389. doi: 10.1371/journal.pbio.1001389.
172) Strelkov, S. V., Herrmann, H. and Aebi, U. (2003) 'Molecular architecture of intermediate filaments', *BioEssays*. doi: 10.1002/bies.10246.
173) Stretton, S. *et al.* (1997) 'Changes in cell morphology and motility in the marine Vibrio sp. strain S14 during conditions of starvation and recovery', *FEMS Microbiology Letters*. doi: 10.1016/S0378-1097(96)00387-4.
174) Szwedziak, Piotr *et al.* (2014) 'Architecture of the ring formed by the tubulin homologue FtsZ in bacterial cell division', *eLife*. doi: 10.7554/eLife.04601.
175) Szwedziak, P *et al.* (2014) 'Architecture of the ring formed by the tubulin homologue FtsZ in bacterial cell division', *eLife*, 3, p. e04601. doi: 10.7554/eLife.04601.
176) Van Teeffelen, S. *et al.* (2011) 'The bacterial actin MreB rotates, and rotation depends on cell-wall assembly', *Proceedings of the National Academy of Sciences*

of the United States of America. doi: 10.1073/pnas.1108999108.
177) Thawani, A., Kadzik, R. S. and Petry, S. (2018) 'XMAP215 is a microtubule nucleation factor that functions synergistically with the γ-tubulin ring complex', *Nature Cell Biology*. doi: 10.1038/s41556-018-0091-6.
178) Tovey, C. A. and Conduit, P. T. (2018) 'Microtubule nucleation by γ-tubulin complexes and beyond', *Essays in Biochemistry*. doi: 10.1042/EBC20180028.
179) Turner, S. L. *et al.* (1993) 'Restructuring an interdomain linker in the dihydrolipoamide acetyltransferase component of the pyruvate dehydrogenase complex of Escherichia coli', *Protein Engineering, Design and Selection*. doi: 10.1093/protein/6.1.101.
180) Ursell, T. S. *et al.* (2014) 'Rod-like bacterial shape is maintained by feedback between cell curvature and cytoskeletal localization', *Proceedings of the National Academy of Sciences of the United States of America*. doi: 10.1073/pnas.1317174111.
181) Vagenende, V., Yap, M. G. S. and Trout, B. L. (2009) 'Mechanisms of protein stabilization and prevention of protein aggregation by glycerol', *Biochemistry*. doi: 10.1021/bi900649t.
182) Vishniakov, I. E. and Borkhsenius, S. N. (2007) '[FtsZ and the division of bacterial cell]', *Tsitologiia*, 49(5), pp. 421–429. Available at: http://www.ncbi.nlm.nih.gov/pubmed/17654828.
183) Voter, W. A. and Erickson, H. P. (1984) 'The kinetics of microtubule assembly. Evidence for a two-stage nucleation mechanism', *Journal of Biological Chemistry*.
184) Wagner, J. K. *et al.* (2006) 'A nutrient uptake role for bacterial cell envelope extensions', *Proceedings of the National Academy of Sciences of the United States of America*. doi: 10.1073/pnas.0602047103.
185) Wang, H. W. and Nogales, E. (2005) 'Nucleotide-dependent bending flexibility of tubulin regulates microtubule assembly', *Nature*. doi: 10.1038/nature03606.
186) Wang, L. and Lutkenhaus, J. (1998) 'FtsK is an essential cell division protein that is localized to the septum and induced as part of the SOS response', *Molecular Microbiology*. 1998/09/02, 29(3), pp. 731–740.
187) Wang, W. *et al.* (2017) 'Insight into microtubule disassembly by kinesin-13s from the structure of Kif2C bound to tubulin', *Nature Communications*. doi: 10.1038/s41467-017-00091-9.
188) Wang, X. and Lutkenhaus, J. (1996) 'FtsZ ring: the eubacterial division apparatus conserved in archaebacteria', *Molecular Microbiology*. 1996/07/01, 21(2), pp. 313–319.
189) Waxman, P. G. *et al.* (1981) 'Induction of Polymerization of Purified Tubulin by Sulfonate Buffers: Marked Differences between 4-Morpholineethanesulfonate (Mes) and 1,4-Piperazineethanesulfonate(Pipes)', *European Journal of Biochemistry*. doi: 10.1111/j.1432-1033.1981.tb05679.x.
190) Wickstead, B. and Gull, K. (2011) 'The evolution of the cytoskeleton', *Journal of Cell Biology*. doi: 10.1083/jcb.201102065.
191) Wright, D. B. *et al.* (2002) 'The effect of salts on the activity and stability of Escherichia coli and Haloferax volcanii dihydrofolate reductases', *Journal of Molecular Biology*. doi: 10.1016/S0022-2836(02)00916-6.
192) Wu, L. J. and Errington, J. (2004) 'Coordination of cell division and chromosome segregation by a nucleoid occlusion protein in Bacillus subtilis', *Cell*, 117(7), pp. 915–925. doi: 10.1016/j.cell.2004.06.002.
193) Yang, C. *et al.* (2013) 'Direct and rapid quantum dots labelling of Escherichia coli cells', *Journal of Colloid and Interface Science*. doi:

10.1016/j.jcis.2012.10.036.
194) Yang, X. *et al.* (2017) 'GTPase activity-coupled treadmilling of the bacterial tubulin FtsZ organizes septal cell wall synthesis', *Science*. doi: 10.1126/science.aak9995.
195) Young, K. D. (2006) 'The Selective Value of Bacterial Shape', *Microbiology and Molecular Biology Reviews*. doi: 10.1128/mmbr.00001-06.
196) Young, K. D. (2007) 'Bacterial morphology: why have different shapes?', *Current Opinion in Microbiology*. doi: 10.1016/j.mib.2007.09.009.
197) Young, K. D. (2010) 'Bacterial Shape: Two-Dimensional Questions and Possibilities', *Annual Review of Microbiology*. doi: 10.1146/annurev.micro.112408.134102.
198) Yu, D. *et al.* (2014) 'An improved monomeric infrared fluorescent protein for neuronal and tumour brain imaging', *Nature Communications*. doi: 10.1038/ncomms4626.
199) Yu, I., Garnham, C. P. and Roll-Mecak, A. (2015) 'Writing and reading the tubulin code', *Journal of Biological Chemistry*. doi: 10.1074/jbc.R115.637447.
200) Zhang, R. *et al.* (2015) 'Mechanistic origin of microtubule dynamic instability and its modulation by EB proteins', *Cell*. doi: 10.1016/j.cell.2015.07.012.
201) Zhao, X., Li, G. and Liang, S. (2013) 'Several affinity tags commonly used in chromatographic purification', *Journal of Analytical Methods in Chemistry*. doi: 10.1155/2013/581093.